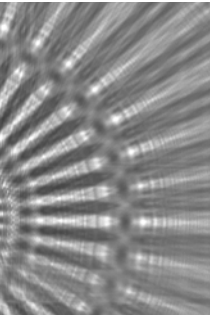


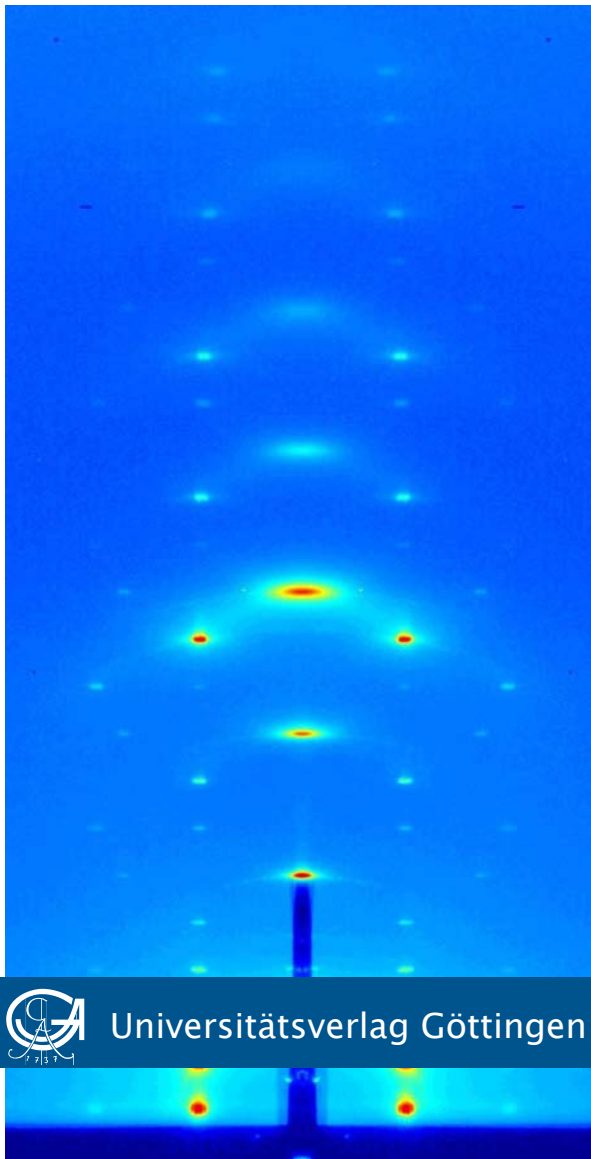


Göttingen Series in
X-ray Physics



Sebastian Aeffner

Stalk structures in lipid bilayer fusion
studied by x-ray diffraction



Universitätsverlag Göttingen

Sebastian Aeffner
Stalk structures in lipid bilayer fusion
studied by x-ray diffraction

This work is licensed under the [Creative Commons](https://creativecommons.org/licenses/by-nd/3.0/) License 3.0 “by-nd”, allowing you to download, distribute and print the document in a few copies for private or educational use, given that the document stays unchanged and the creator is mentioned. You are not allowed to sell copies of the free version.



Published in 2012 by Universitätsverlag Göttingen
as Volume 6 in the series „Göttingen series in x-ray physics“

Sebastian Aeffner

Stalk structures in lipid
bilayer fusion studied
by x-ray diffraction

Göttingen series in x-ray physics
Volume 6



Universitätsverlag Göttingen
2012

Bibliographische Information der Deutschen Nationalbibliothek

Die Deutsche Nationalbibliothek verzeichnet diese Publikation in der Deutschen Nationalbibliographie; detaillierte bibliographische Daten sind im Internet über <http://dnb.ddb.de> abrufbar.

This work has been supported financially by the DFG Collaborative Research Center SFB 803 "Functionality controlled by organization in and between membranes".

Address of the Author

Dr. Sebastian Aeffner

Email: Sebastian.Aeffner@web.de

Dissertation for the award of the degree
„Doctor rerum naturalium“
Division of Mathematics and Natural Sciences
of the Georg-August-Universität Göttingen
submitted by Sebastian Aeffner, Göttingen 2011

Supervisor: Prof. Dr. Tim Salditt
Thesis committee: Prof. Dr. Marcus Müller
Prof. Dr. Claudia Steinem

Date of the oral examination: 14.07.2011

This work is protected by German Intellectual Property Right Law.
It is also available as an Open Access version through the publisher's homepage and the Online Catalogue of the State and University Library of Goettingen (<http://www.sub.uni-goettingen.de>). Users of the free online version are invited to read, download and distribute it. Users may also print a small number for educational or private use. However they may not sell print versions of the online book.

Layout: Sebastian Aeffner
Cover: Jutta Pabst
Cover image: Sebastian Aeffner

© 2012 Universitätsverlag Göttingen
<http://univerlag.uni-goettingen.de>
ISBN: 978-3-86395-043-9
ISSN: 2191-9860

Preface of the series editor

The Göttingen series in x-ray physics is intended as a collection of research monographs in x-ray science, carried out at the Institute for X-ray Physics at the Georg-August-Universität in Göttingen, and in the framework of its related research networks and collaborations.

It covers topics ranging from x-ray microscopy, nano-focusing, wave propagation, image reconstruction, tomography, short x-ray pulses to applications of nanoscale x-ray imaging and biomolecular structure analysis.

In most but not all cases, the contributions are based on Ph.D. dissertations. The individual monographs should be enhanced by putting them in the context of related work, often based on a common long term research strategy, and funded by the same research networks. We hope that the series will also help to enhance the visibility of the research carried out here and help others in the field to advance similar projects.

Prof. Dr. Tim Salditt, Editor
Göttingen February 2011

Contents

Introduction	1
1 Elements of lipid bilayer fusion	5
1.1 Lipids	5
1.2 Phospholipid mesophases	7
1.3 Bilayer fusion pathways	10
1.4 Interaction potentials between lipid bilayers	11
1.5 Continuum theory and simulations of stalks	14
2 X-ray diffraction on lipid mesophases	17
2.1 Fundamentals of X-ray diffraction	17
2.2 Oriented samples	20
2.3 Experimental techniques	22
2.3.1 X-ray reflectivity	22
2.3.2 Grazing-incidence x-ray diffraction	23
2.3.3 Powder diffraction	25
2.4 Intensity correction factors	26
2.5 The phase problem	29
2.6 Resolution	31
3 Lyotropic lipid polymorphism	35
3.1 Hydration control by water vapour	35
3.2 Experimental	37
3.2.1 Sample preparation	37
3.2.2 Sample environment	38
3.2.3 In-house small-angle x-ray scattering setup	39
3.2.4 Phase diagram determination	41
3.3 Results	41
3.3.1 Characteristic diffraction patterns	41
3.3.2 Phase diagrams	42
3.3.3 Indexing of Diffraction patterns	48
3.4 Conclusions	55
4 Bilayer structure and interactions	57
4.1 Electron density profiles	57
4.2 Osmotic stress method	58
4.3 Motivation of our work	61
4.4 Experimental	62
4.4.1 X-ray reflectivity Instrument	62
4.4.2 Measurements	63
4.4.3 Data reduction	63
4.4.4 Fourier Synthesis of electron density profiles	66
4.4.5 Phase retrieval: The swelling method	66
4.5 Results and Discussion	72

4.5.1	Effects at close bilayer separation	72
4.5.2	Bilayer structure	72
4.5.3	Hydration force parameters	74
4.5.4	Hydration barrier for membrane fusion	79
4.6	Conclusions	81
5	Structure determination of stalks	83
5.1	Data collection and reduction	83
5.1.1	Synchrotron GIXD experiments	83
5.1.2	X-ray reflectivity experiments	93
5.1.3	Powder diffraction experiments	94
5.1.4	Combination of different X-ray geometries	98
5.2	Solving the phase problem	98
5.3	Results	106
5.4	Discussion	112
5.5	Conclusions	113
6	Analysis of the 3d electron density of stalks	115
6.1	Structural parameters of the stalk phase	115
6.1.1	Definitions	115
6.1.2	Results	117
6.2	Electron density isosurface analysis	119
6.2.1	Motivation	119
6.2.2	Differential geometry of implicit surfaces	121
6.2.3	Implementation	122
6.2.4	Results	124
6.3	Discussion and comparison to continuum theory	131
6.3.1	General remarks	131
6.3.2	Possible limitations of continuum theory	131
6.3.3	Comparison to continuum models	132
6.4	Conclusions	134
7	Summary	135
A	Appendix	137
A.1	Triplet relationship	137
A.2	Crystallographic data and swelling diagrams	139
A.3	Gauss-Bonnet theorem applied to stalks	156
A.4	MATLAB code: Examples	158
	References	171
	List of publications	183
	Danksagung	185
	Curriculum Vitae	187

Introduction

Biological membranes can be considered nature's most important interfaces. They constitute the physical barrier that separates each cell from its environment. In addition, membranes subdivide cells into cell organelles with different tasks and specific biochemical composition. This *compartmentalization* is a prerequisite for the development of living organisms [1].

Phospholipid bilayers constitute the structural matrix of biological membranes. They are formed by spontaneous self-assembly of lipids in aqueous solution, driven by the hydrophobic effect [2], and possess a typical thickness of about 5 nm. Their lateral extent can exceed this value by orders of magnitude, placing them among the largest structures in biology held together by noncovalent forces [3]. Membrane proteins are permanently embedded in or temporarily associated to the lipid bilayer matrix and fulfil tasks such as selective transport or cell signaling.

Membranes are flexible and soft and adapt to moderate mechanical deformations without losing their function as an impermeable barrier. Both lipids and proteins are laterally mobile and can diffuse within the bilayer plane. Therefore, membranes have been characterized as two-dimensional fluids [4]. More recently, the possibility of lateral segregation and formation of transient microdomains called *lipid rafts* has been considered [5, 6].

To assure compartmentalization and maintain concentration gradients, membranes are required to be stable and impermeable. At the same time, however, membranes must be able to merge. This process, membrane fusion, is ubiquitous in numerous events on the cellular and subcellular level. Examples include neurotransmission by synaptic vesicles, intracellular transport, exocytosis, fertilization, or entry of enveloped viruses. In each case, membrane fusion involves a complex and tightly concerted interplay of lipid bilayers, specific membrane fusion proteins, water and ions such as Ca^{2+} [7, 8, 9, 10, 11, 12]. Membrane fusion takes place on length scales of few nanometers and involves highly transient intermediates steps. This precludes the direct observation by existing methods [13]. Despite enormous interdisciplinary efforts, the exact mechanisms of membrane fusion are currently only poorly understood.

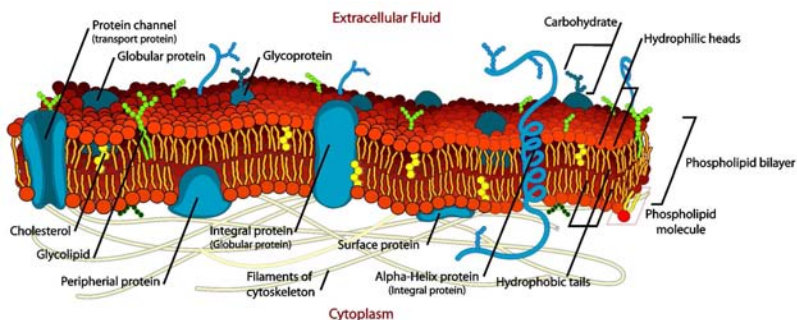


Figure 1: Schematic representation of a cell membrane [14].

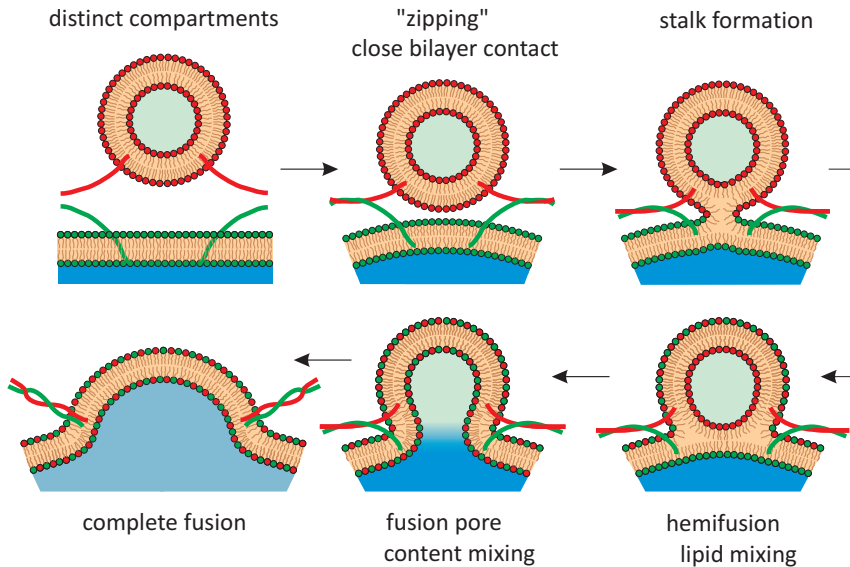


Figure 2: *Cartoon of SNARE-mediated membrane fusion. “Zipping” of the SNARE complexes forces lipid bilayers into close contact and, in addition, may create bilayer stresses and lipid disorder. This initiates stalk formation. The stalk develops into a hemifusion diaphragm, whose rupture leads to the opening of a fusion pore and finally to full fusion. Adapted from [15].*

By now, it is generally accepted that membrane fusion proceeds by formation of lipidic non-bilayer intermediates. Fig. 2 illustrates the so-called fusion-by-hemifusion mechanism for the case of SNARE-mediated fusion of a small vesicle and a flat membrane. Proteins mediate the initial recognition, bring membranes into close contact and eventually create mechanical stresses and perturb the bilayer structure. This results in formation of a so-called stalk: The two proximal lipid monolayers merge into one continuous, strongly curved monolayer, while the distal monolayers are still separated and intact. The stalk develops into a hemifusion diaphragm, which finally ruptures and leads to the opening of a fusion pore. The existence of a hemifused state, defined as the mixing of lipids without the mixing of contents, has been confirmed by electrophysiology and fluorescence assays [15, 16, 17, 18, 19, 20].

To tackle a problem as complex and inherently difficult to study as membrane fusion, complementary approaches addressing different aspects are required. One approach is to focus on properties of the lipid matrix and the putative non-bilayer intermediates and study protein-free lipid bilayer fusion in simplified models. In the present thesis, this strategy is pursued.

Formation of a lipid stalk as the first connection between two merging bilayers is a central element in the current conception of membrane fusion [13, 20]. The first quantitative analysis of stalks based on a continuum theory treating fluid bilayers as thin elastic sheets has been proposed almost 30 years ago [21]. This model has been revis-

ited several times [22, 23, 24, 25]. In addition, with the emergence of computational physics, the initial steps of membrane fusion have been studied by simulations (*e.g.* [26, 27]), in which stalk formation is observed. The goal of these efforts is to clarify the sequence of structural rearrangements which define the free energy barrier for membrane fusion. This would help to understand the mechanisms by which fusion proteins catalyze bilayer merger. However, experimental evidence for stalk formation failed to appear for a long time.

In excess water, the lipid composition found in biological membranes leads to bilayer formation. However, isolated lipid species display a large variety of lipid mesophases under different experimental conditions [3, 28, 29]. These preserve the fluid state and thermal disorder characteristic for biological membranes, but display a lattice order on larger length scales of several nanometers. This allows studies by diffraction methods. In contrast to conventional microscopy, these provide access to length scales relevant to fusion intermediates. Starting with the pioneering work of LUZZATI in the 1960s, lipid mesophases have been used as model systems for more complex biological membranes.

As recently as 2002, the first direct experimental evidence for the feasibility of stalk formation was given by the group of H. W. HUANG, who discovered a phospholipid mesophase consisting of an array of stalks in thermal equilibrium [30]. So far, this “stalk phase” is the only model system which allows to study the structure of bilayer fusion intermediates by experimental means. However, only little data exist. Open questions are for example: How does stalk structure vary with lipid composition? Can experimental data and existing continuum models be reconciled? Which lipid compositions optimize the propensity to stalk formation? Which are the decisive energetic contributions? Answers to these questions can contribute to a more thorough understanding of membrane fusion.

The aim of the present thesis is to further explore the use of stalk phases as a model system for lipid bilayer fusion and address several of the above questions. In particular, the goals are (*i*) to study phospholipid phase behaviour and identify further lipids and biologically relevant lipid mixtures which display the stalk phase, (*ii*) study the repul-

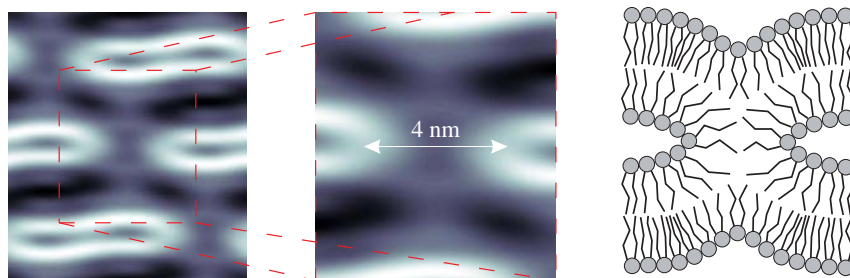


Figure 3: (left) 2d electron density maps of the rhombohedral phase reconstructed from data recorded by laboratory diffractometers [31]. The lipid headgroups indicated by high electron density (white) indicate strongly curved monolayers resembling those of a stalk (right).

sive forces opposing bilayer approach prior to stalk formation, (iii) to obtain stalk structures in different lipid systems with optimum resolution, (iv) to work towards a quantitative analysis and comparison of stalks formed by different lipids.

After this introduction, *chapter 1* discusses lipid mesophases as model systems and summarizes physical concepts to describe bilayer interaction and deformation. In addition, different pathways of bilayer fusion and the energies involved in stalk formation are presented.

The background in x-ray diffraction and electron density reconstruction required to study lipid mesophases is provided in *chapter 2*. This includes the different scattering geometries and corresponding correction factors used in this thesis.

Chapter 3 describes experiments on the hydration-dependent phase behaviour of a number of lipids and lipid mixtures with the goal to identify parameter ranges in which the stalk phase can be observed.

The knowledge of the phase boundaries is used in *chapter 4* to obtain the structure of lipid bilayers in close contact. This allows to quantify the repulsive interbilayer forces that oppose close bilayer contact and therefore stalk formation.

Chapter 5 focuses on the determination of stalk structure. Synchrotron experiments required for optimum data quality and additional in-house experiments as well as the applied methods to solve the crystallographic phase problem are described.

Chapter 6 presents the further analysis of the obtained stalk structures. A method to extract the curvatures of lipid monolayers from the experimental data is proposed. The results are discussed in light of existing continuum models.

Finally, *chapter 7* summarizes the main results obtained in this dissertation.

1 Elements of lipid bilayer fusion

This chapter introduces selected elements of membrane biophysics. The lipid compositions of biomembranes are highly complex, diverse and tightly regulated. Isolated lipid species display a variety of mesophases. These can be used as model systems to study lipid bilayers and their interactions, as well as structural transformations resembling those in bilayer fusion. Different pathways of bilayer fusion exist, but all require close bilayer contact and start by stalk formation. The involved bilayer interaction potentials and energies due to monolayer deformation are discussed.

1.1 Lipids

Along with proteins, sugars and nucleic acids, lipids are one of the four major groups of biomolecules [32]. The lipid composition of biological membranes is highly complex and can vary considerably for different cells or cell organelles [1]. However, three major groups can be distinguished [33]:

- **Glycerophospholipids:**

The most abundant group of lipids in most membranes consists of a glycerol backbone, which is linked to two fatty acids and one phosphate group. The latter, in turn, is esterified to one of the alcohols choline, ethanolamine, serine or inositol. The unpolar acyl chains constitute the hydrophobic interior of lipid bilayers, while the headgroup region is zwitterionic or charged and thus hydrophilic. Type and charge of the headgroup and length and number of double bonds of the hydrocarbon chains determine the physicochemical properties of each lipid, *e.g.* their phase behaviour or degree of fluidity when used in purified form [34]. Several lipids of this class are shown in Fig. 1.1. Dioleoylphosphatidylcholine (DOPC) and dioleoylphosphatidylethanolamine (DOPE) are widely used in studies involving model membranes. PIP₂ (phosphatidylinositol(4,5)-bisphosphate) is a possibly essential component in SNARE-mediated membrane fusion of synaptic vesicles. More details on this lipid can be found *e.g.* in [35] and references therein.

- **Sphingolipids:**

These are structurally similar to glycerophospholipids, but consist of a sphingosine molecule which is linked to one fatty acid. Since this lipid species is not used in the following, it is referred to the literature for further information.

- **Cholesterol:**

The structure of cholesterol (Chol) differs considerably from the two former groups. Its hydrophobic part consists of a planar and rigid ring system and a short hydrocarbon chain, while the hydrophilic region is made up of a single hydroxyl group (Fig. 1.1). Cholesterol is insoluble in water and does not form bilayers alone. When incorporated into a lipid bilayer, it can rather easily undergo a *flip-flop* movement from one monolayer leaflet to the other [36]. The effects of cholesterol on membranes are diverse: When incorporated into fluid bilayers,

cholesterol progressively increases chain order and leads to the so-called liquid-ordered phase, which is accompanied by an increase in bilayer thickness. On the contrary, when incorporated into gel-phase bilayers, it promotes membrane fluidity. Therefore, cholesterol stabilizes the degree of fluidity over a substantial temperature range. In ternary mixtures of unsaturated and saturated lipids and cholesterol, formation of raft-like domains enriched in the two latter compounds is observed [37, 38]. Cholesterol makes the spontaneous curvature of lipid monolayers more negative [39] and can modify the elastic properties of lipid bilayers [40, 41].

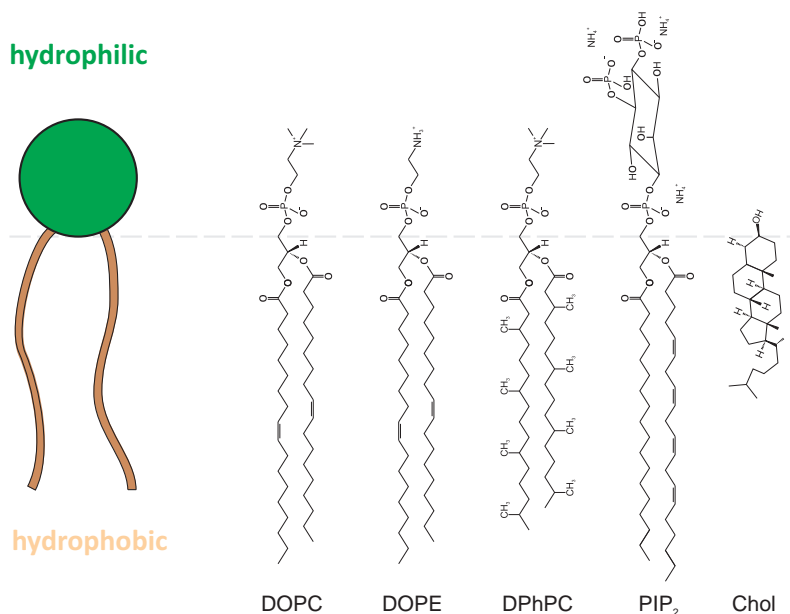


Figure 1.1: Sketch of the typical representation of a lipid molecule and structure formulas of some lipids used in this thesis. A covalently bound hydrophilic headgroup and hydrophobic acyl chains make phospholipids amphiphilic, causing lipid self-assembly driven by the hydrophobic effect. Cholesterol is structurally different and does not form bilayers on its own.

The lipid composition of biological membranes varies considerably. For example, cholesterol and sphingomyelin are predominantly localized in plasma membranes, whereas membranes surrounding most cell organelles are rather devoid of these species. In addition, the lipid composition of two monolayers constituting a bilayer is usually highly asymmetric [1]. For glycerophospholipids and sphingolipids, the movement from one monolayer to the other is associated with a considerable energy barrier. These findings suggest a correlation of lipid composition and functional tasks of a cell or cell organelle and a role of bilayers that goes beyond that of a passive barrier and matrix for proteins.

1.2 Phospholipid mesophases

In aqueous dispersions, lipids form a large variety of aggregates. This process, lipid self-assembly, is driven by the hydrophobic effect [2, 34, 42]. In dilute conditions, the lipid compositions found in biological membranes form vesicles. In the opposite case of relatively low water content, liquid-crystalline mesophases with long-range translational symmetry can be observed. Their structure can be studied by x-ray or neutron diffraction. Fig. 1.2 shows some of the most frequently encountered topologies. For a given lipid composition, phase transitions between different mesophases can often be observed if the degree of hydration or the temperature are changed. This phenomenon is known as lipid polymorphism. Since the pioneering work of LUZZATI and coworkers in the 1960s [43], lipid mesophases have been the subject of numerous studies [3, 28]. In the present thesis, structural changes and phase transitions induced by changes in lipid hydration, *lyotropic* lipid polymorphism, is employed to address questions related to membrane fusion.

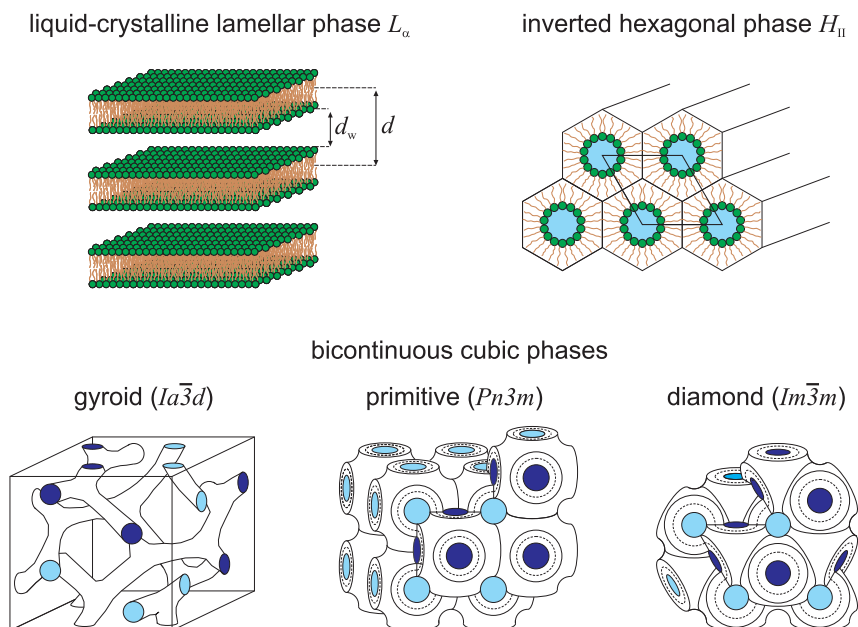


Figure 1.2: Sketch of a selection of lipid mesophases. Lamellar phases are used as model systems to study lipid bilayer structure. Bicontinuous cubic phases consist of two distinct interwoven water regions indicated in light and dark blue. Lipid mesophases are not static, but display considerable thermal disorder. This limits the resolution obtainable by diffraction experiments. Parts of the figure are adapted from [28, 42].

Fig. 1.2 shows some frequently observed lipid mesophases. Several lamellar phases consisting of stacked bilayers exist, e.g. different gel phases or the ripple phase [42].

Usually, only the liquid-crystalline L_α phase with fluid, disordered chains is considered biologically relevant. The lamellar repeat spacing d and the thickness d_w of the water layer separating adjacent bilayers are determined by the balance of several interbilayer forces (*cf.* section 1.4). The inverted hexagonal phase H_{II} consists of long aqueous channels surrounded by cylindrically curved lipid monolayers. Bicontinuous cubic phases consist of two distinct interwoven water regions. Their topology can be described by infinitely periodic minimal surfaces [44]. The transition from a lamellar to a bicontinuous cubic phase resembles the formation of an array of fusion pores [29]. In a simplifying, yet very popular model, ISRAELACHVILI *et al.* explained the propensity of lipids to form certain geometries by a mean or effective molecular shape [45]. As sketched in Fig. 1.3, the mean cross-sectional area a_0 of the polar headgroup in the interfacial region and the length l_c and volume V of the chains define a packing parameter $P = V/a_0 l_c$. If P is close to one, the effective molecular shape resembles a cylinder and lipids tend to pack into lamellar aggregates. Lipids with $P > 1$ have a propensity to form inverted phases in which the hydrocarbon region curls around the lipid headgroup region. Introduction of additional double bonds, branched chains or smaller headgroups increase P and hence is expected to increase the tendency to form inverted phases. Although only a very coarse description, this model gives a first qualitative idea *e.g.* about the strong tendency of PE lipids or the lipid diphytanoyl-PC used below to form inverted phases.

Lamellar phases are probably most widely used and constitute a model system to study lipid bilayer structure and interactions [46, 47, 48]. Since lipid compositions found *in vivo* readily form bilayers in the physiological condition of excess water¹, the biological relevance of nonlamellar mesophases is less obvious. Studying them can be motivated as follows [3]:

Lipid which show no tendency to form nonbilayer topologies would be sufficient to form fluid bilayers that assure compartmentalization and serve as the structural matrix for proteins. However, in addition to these, biomembranes often contain a considerable fraction of lipids that have a strong tendency to promote nonlamellar phase formation or even, like cholesterol, do not form bilayers at all (*cf.* section 1.1). This

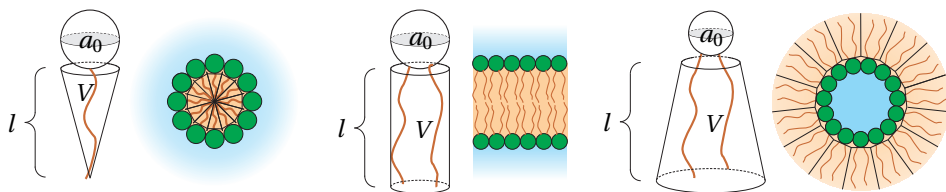


Figure 1.3: Mean geometrical shape of different lipid species and corresponding preferred lipid aggregates. Lipids with a single chain (*e.g.* lysolipids) tend to form aggregates of positive curvature, while lipids with two chains and small headgroup (*e.g.* PE lipids) rather form inverted mesophases.

¹ In some cases, several non-bilayer topologies have been identified in living organisms, indicating the possibility of direct biological relevance [28].

indicates a very specific role of lipid composition and presence of lipids facilitating nonlamellar phase formation. One function could be to assure bilayer properties that facilitate membrane fusion [3, 29, 49, 50]. Investigating the polymorphism of isolated lipid species or simple lipid mixtures is essential to understand their possible roles in complex biological membranes. To this end, nonlamellar lipid mesophases are useful model systems.

To learn more about the initial steps in membrane fusion, the most suitable phospholipid mesophase is probably the rhombohedral phase of space group $R\bar{3}$ discovered by the group of H. W. HUANG. It consists of a dense array of thermodynamically stable stalks and some residual water [30, 51]. Its observation was the first direct experimental evidence of the feasibility of stalk formation, at least in certain lipids and under certain conditions. However, only the stalk phases of the two lipids diphytanoylphosphatidylcholine (DPhPC) and dioleoylphosphatidylcholine (DOPC) have been characterized so far [30, 31, 51, 52]. One goal of this thesis is to extend the use of the stalk phase as a model system to a larger variety of lipid systems.

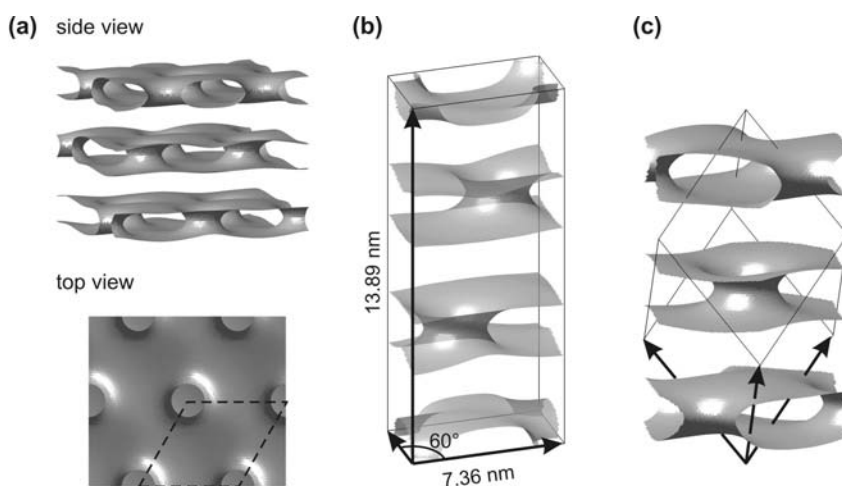


Figure 1.4: Different electron density isosurface representations of the stalk phase: (a) Stalks are arranged in layers in ABC stacking, within each layer they form a 2d hexagonal lattice. (b) Nonprimitive hexagonal unit cell containing three stalks and (c) primitive rhombohedral unit cell containing a single stalk in its center. (DOPC/-DOPE 1:1, RH = 70%, cf. chapter 5)

Stalk phase formation has been observed upon partial dehydration of lamellar lipid bilayer stacks. By some authors, only fully hydrated lipid assemblies in excess water conditions are considered “biologically relevant” [49]. However, the initiation of membrane fusion most likely requires close bilayer contact well below the equilibrium distance found in excess water. This is equivalent to at least local partial dehydration of lipid bilayers at the fusion site. Therefore, studying lyotropic lipid polymorphism in partially dehydrated mesophases can yield insights into the physics relevant to biological membrane fusion. Also in simulations of isolated stalks or stalk phase formation, lipid

bilayer patches are “prepared” in partially dehydrated conditions [53, 54]. A quantitative explanation for stalk phase formation has been given by the interplay of the energies due monolayer deformation on the one hand and a decrease of the energy due to hydration repulsion on the other hand [55]. These factors are explained further below.

1.3 Bilayer fusion pathways

In the classical fusion-through-hemifusion pathway sketched in Fig. 1.5, a sequence of structures with axial symmetry is assumed. After stalk formation, the stalk expands radially and develops into a hemifusion diaphragm or *trans* monolayer contact, *i.e.* a lipid bilayer composed of the two *trans* monolayers is formed. Rupture of this bilayer leads to formation of a fusion pore and finally to complete fusion. In this pathway, no leakage of content out of the compartments occurs [20].

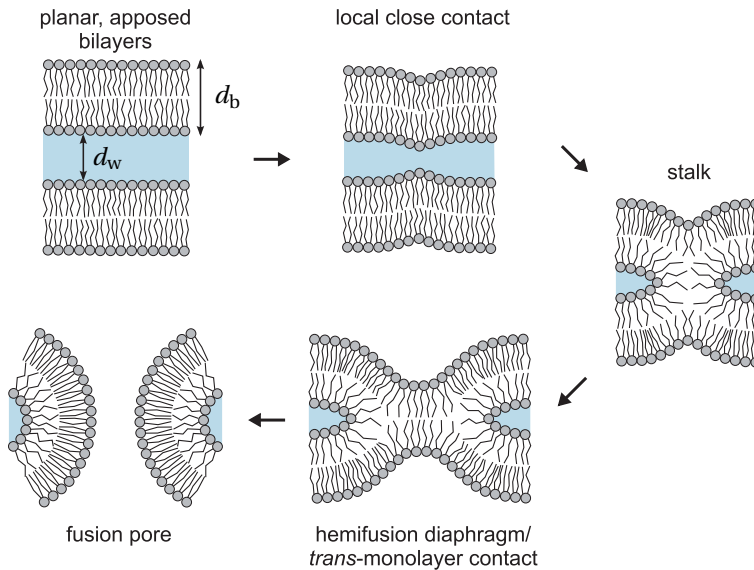


Figure 1.5: Cartoon of the classical hemifusion pathway. The structures possess axial symmetry. Figure taken from AEFNER *et al.* [31] and used with kind permission from Springer.

More recently, in addition to the classical pathway, a different pathway involving non-axially symmetric structures has been observed by simulations of bilayer fusion [56, 57, 58]. Recent reviews are given in [26, 27]. Importantly, simulations predict the sequence of bilayer rearrangements without making prior assumptions [59]. After stalk formation, the stalk does not expand axially, but elongates in one dimension in a worm-like fashion. Simultaneously, the bilayer structure in its proximity is destabilized, which facilitates formation of holes. If holes form rather easily, the elongating stalk encircles a hole formed in its vicinity in one bilayer, yielding a hemifusion diaphragm, or holes in each bilayer, directly yielding a fusion pore. In another variant without hole forma-

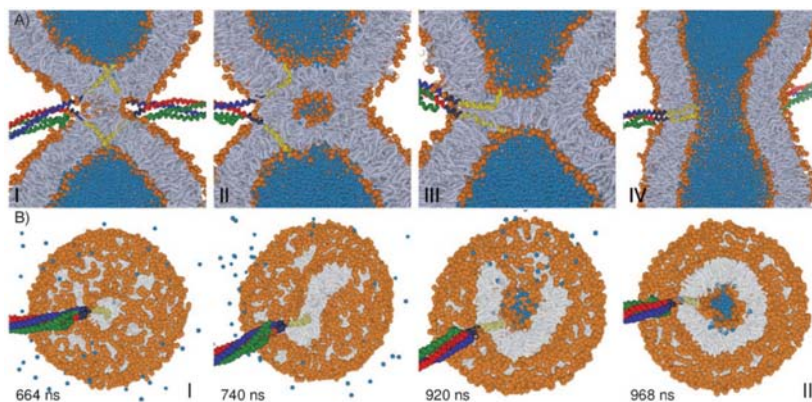


Figure 1.6: A simulation showing SNARE-mediated vesicle fusion by an alternative pathway involving non-axial stalk expansion into an inverted micellar intermediate (I→II). The lower panel shows different stages of this step in more detail. Subsequent rupture of the bilayers separating the IMI from the two vesicles result in a hemifusion diaphragm (III) and finally a fusion pore (IV). Figure taken from RISS-LADA *et al.* [60] and used with kind permission from John Wiley and Sons.

tion, the elongating stalk wanders on a closed path until its two ends meet, yielding a so-called inverted micellar intermediate (IMI) which contains some residual water. Rupture of one bilayer of the IMI yields a hemifusion diaphragm consisting of the remaining bilayer.

Unlike the classical pathway, the lipids constituting the hemifusion diaphragm in the alternative, non-axisymmetric pathway originate from both *cis* and *trans* leaflets. In addition, it allows transient leakage due to hole formation, which is in agreement with several experimental reports [58]. A very recent simulation of SNARE-mediated vesicle fusion in molecular detail displayed fusion by this alternative pathway involving IMI formation [60] (Fig. 1.6). Other recent simulations indicate that stalk formation at close bilayer contact is initiated by so-called splay intermediates formed by acyl chains extending into the separating aqueous layer [53, 61].

In the remainder of this chapter, energies involved in stalk formation are considered more closely. This comprises interactions between bilayers which oppose initial bilayer contact, as well as the energies due to deformation of lipid monolayers in highly curved structures.

1.4 Interaction potentials between lipid bilayers

In excess water conditions and absence of osmotic stressors, uncharged lipid bilayers interact by van der Waals attraction and several repulsive forces. Equilibrium of these forces leads to well-defined interbilayer distances. The corresponding water layer thickness between adjacent bilayers is typically between 10 and 30 Å, depending on the exact lipid composition.

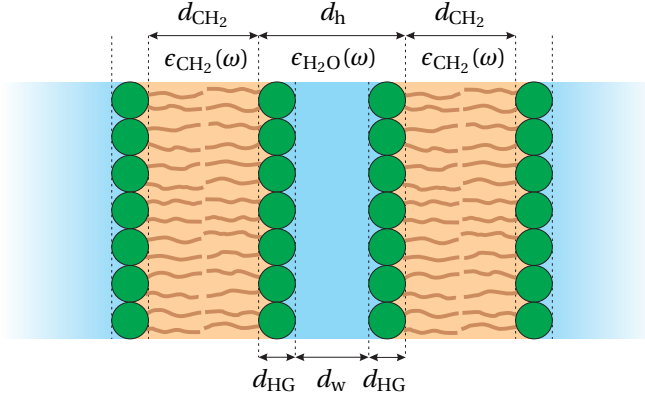


Figure 1.7: Sketch for derivation of the van der Waals interaction between two lipid bilayers. Lipid headgroup and water regions are grouped into one hydrophilic region, i.e. the interaction of two parallel hydrocarbon layers of thickness d_{CH_2} embedded in water and separated by a hydrophilic layer with a thickness $d_{\text{h}} = d_{\text{w}} + 2d_{\text{HG}}$ is considered.

Van der Waals attraction results from different polarizabilities of lipid and water molecules and can be calculated in the framework of Lifshitz theory [62, 63, 64]. To this end, two lipid bilayers are modeled as sketched in Fig. 1.7. The hydrophilic headgroup regions and the bulk water layer are modeled as one homogeneous layer of thickness d_{h} [65, 66]. Then, the van der Waals interaction potential between two parallel hydrocarbon layers of thickness d_{CH_2} embedded in an aqueous medium and separated by a water layer d_{h} is considered [63, 67]:

$$V_{\text{vdW}}(d_{\text{h}}) = -\frac{k_{\text{B}}T}{8\pi d_{\text{h}}^2} \sum_{n=0}^{\infty} ' \int_{r_n}^{\infty} dx x \ln \left[1 - \left(\frac{\Delta_n (1 - \exp(-(d_{\text{CH}_2}/d_{\text{h}}) \cdot x))}{1 - \Delta_n^2 \exp(-(d_{\text{CH}_2}/d_{\text{h}}) \cdot x)} \right)^2 e^{-x} \right] \quad (1.1)$$

The summation is carried out for frequency-dependent contributions where the expression $\Delta_n = (\epsilon_{\text{H}_2\text{O}}(i\omega_n) - \epsilon_{\text{CH}_2}(i\omega_n)) / (\epsilon_{\text{H}_2\text{O}}(i\omega_n) + \epsilon_{\text{CH}_2}(i\omega_n))$ contains the dielectric permittivities of water and hydrocarbon at angular frequencies $\omega_n = 2\pi n k_{\text{B}}T/\hbar$. The lower integration limit is denoted by $r_n = 2d_{\text{h}}\sqrt{\epsilon_{\text{H}_2\text{O}}}\omega_n/c$. The prime indicates that the term for $n = 0$ has to be multiplied by a factor $\frac{1}{2}$. A widely used approximation for the corresponding pressure has the form

$$P_{\text{vdW}}(d_{\text{h}}) = -\frac{\partial V_{\text{vdW}}}{\partial d_{\text{h}}} = \frac{H}{6\pi} \left[\frac{1}{d_{\text{h}}^3} - \frac{2}{(d_{\text{h}} + d_{\text{CH}_2})^3} + \frac{1}{(d_{\text{h}} + 2d_{\text{CH}_2})^3} \right], \quad (1.2)$$

where $H = \frac{3}{2}k_{\text{B}}T \sum_{n=0}^{\infty} ' \Delta_n^2$ denotes the Hamaker coefficient. FENZL argues that this approximation might lead to incorrect results for larger values of d_{h} [67]. However, for small d_{h} up to the equilibrium value in excess water as required throughout this thesis, Eq. (1.2) should suffice. In Fig. 1.8, $\epsilon_{\text{H}_2\text{O}}(i\omega)$ and $\epsilon_{\text{CH}_2}(i\omega)$ are parameterized by

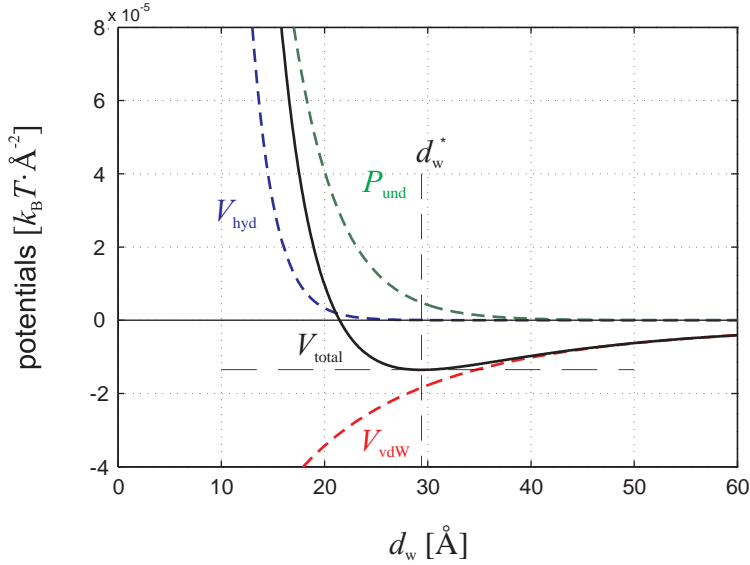


Figure 1.8: Interaction potentials of two DOPC bilayers in excess water for $P_0 = 0.55 \cdot 10^8 \text{ Jm}^{-3}$, $\lambda_h = 2.2 \text{ \AA}$, $\kappa = 8.0 k_B T$, $d_{CH_2} = 26.8 \text{ \AA}$, $d_{HG} = 9.0 \text{ \AA}$ [68].

an oscillator model following [67] and references therein. A very thorough introduction into van der Waals forces is given *e.g.* in [63].

The precise physical mechanism causing strong repulsive forces between lipid bilayers at small separation is still a matter of debate [61, 69, 70]. Application of an order-parameter formalism and Landau free energy expansion to the water layer between two parallel and smooth surfaces predicts a repulsive pressure

$$P_{\text{hyd}}(d_w) = \frac{P_h}{4 \sinh^2\left(\frac{d_w}{2\lambda_h}\right)} \quad (1.3)$$

resulting from the orientation of water molecules close to surfaces [71]. Due to this apparent relation to water structure, the interaction has been termed *hydration repulsion* [72]. P_0 has been related to the dipole density in the headgroup region [73]. The hydration force decay length is typically in the range of 1 to 3 Å. For $d_w \gg \lambda_h$, P_{hyd} can be approximated by

$$P_{\text{hyd}}(d_w) = P_h \exp\left(-\frac{d_w}{\lambda_h}\right). \quad (1.4)$$

An additional pressure term is used to account for enhanced bilayer repulsion due to undulatory modes. In the so-called soft confinement regime for multilamellar bilayer stacks,

$$P_{\text{und}}(d_w) = \frac{\pi k_B T}{32\lambda_h} \sqrt{\frac{P_0}{2\kappa\lambda_h}} \exp\left(-\frac{d_w}{2\lambda_h}\right) \quad (1.5)$$

with twice the decay length of P_{hyd} is used. In our notation, κ is the bending rigidity of one lipid monolayer, *i.e.* half the bending rigidity of the lipid bilayer. In our example in Fig. 1.8, P_{und} is the dominant repulsive interaction in excess water. In dehydrated conditions (*cf.* Fig. 4.2), it gives only a minor correction to the equilibrium value for partially dehydrated conditions d_w^* [74, 75].

In an alternative approach, it has been proposed that bilayer repulsion rather results from the rough, non-smooth structure and molecular protrusions in the lipid head-group region than from water structure [72, 76]. However, this view has been challenged [77].

If the partial volume v_w of a water molecule is modeled as a sphere, one obtains a diameter of about 3.8\AA . Typical bilayer separations d_w below 20\AA thus correspond to only very few molecular layers. Any description in terms of smooth interfaces and well-defined distances such as in Fig. 1.7 is to some extent arbitrary and limited in accuracy, since it neglects the molecular structure and thermal motions of lipid headgroups and water [74, 75]. Moreover, as will be seen below, bilayer structure changes upon dehydration. Therefore, the assumption of constant bilayer properties and a simple superposition of interaction potentials such as in Fig. 1.8 is only an approximation.

1.5 Continuum theory and simulations of stalks

While different pathways of bilayer fusion may exist, the formation of stalks at an early stage is generally accepted. Almost all simulations on membrane fusion include the formation of axially symmetric stalks between apposed bilayers [20, 59]. In addition, stalks or hemifusion intermediates have been observed between synaptic vesicles and the presynaptic membrane by conical electron microscopy with $\geq 3\text{ nm}$ resolution [78], as well as in the rhombohedral phospholipid phase [30]. These findings support the role of stalks as a conserved motif in membrane fusion.

Continuum theory

For almost 30 years, attempts have been made to determine the free energy of a stalk with respect to the initial state of two planar bilayers. The first quantitative analysis of stalks by KOZLOV *et al.* [21] was conducted by a continuum theory developed by HELFRICH and others for lipid bilayers [79, 80, 81]. The model has been revisited several times (*e.g.* [22, 23, 24, 25, 82]) and contributed considerably to the development of the current conception of membrane fusion [13]. Therefore, despite possible limitations addressed further below, its basic principles are sketched here.

Each monolayer of the stalk is described as a homogeneous elastic sheet, whose resistance to deformations is characterized by few elastic constants which effectively summarize the underlying molecular interactions. Deformations are described with respect to a neutral surface where the cross-sectional area of lipid molecules remains constant upon bending [83]. Its position is assumed close to the headgroup/hydrocarbon interface ([84] and references therein).

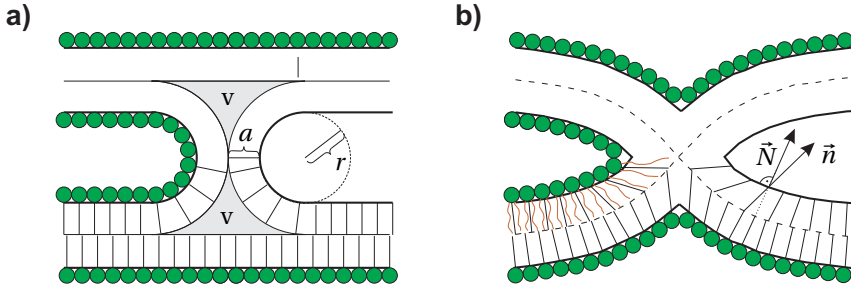


Figure 1.9: Different realizations of a stalk proposed and analyzed by continuum theory: (a) Original stalk model describing the bent monolayer as the figure of revolution of a semicircle and including void regions (v) [21, 22, 24]. (b) Stalk including lipid tilt, i.e. the unit vectors denoting the mean chain direction \vec{N} and the unit normal of the neutral plane \vec{n} are not collinear [25]. In both cases, solid black lines indicate the approximate location of the neutral surface.

As a $2d$ surface embedded in $3d$ space, the neutral surface can be described by differential geometry. Here, each point of a smooth and continuous surface is characterized by two principal curvatures c_1 and c_2 or, equivalently, the mean curvature H and the Gaussian curvature K :

$$H = \frac{c_1 + c_2}{2} \quad \text{and} \quad K = c_1 \cdot c_2. \quad (1.6)$$

In case of lipid monolayers, c_1 and c_2 are conventionally defined as positive if the polar lipid headgroups curve around the hydrocarbon chain region, and *vice versa*. Using this description, the elastic energy due to bending is expanded up to quadratic terms in c_1 and c_2 , which yields the widely used Hamiltonian [79]

$$F_{\text{bend}} = \frac{\kappa}{2} \int_A (2H - c_0)^2 dA + \kappa_G \int_A K dA. \quad (1.7)$$

Extensions of the model incorporate lipid tilt as an additional degree of freedom [25, 55] or terms up to fourth order in c_1 and c_2 [85]. However, the leading terms are still those of Eq. (1.7). The integration is carried out over the neutral surface of each monolayer of the stalk. c_0 denotes the spontaneous curvature, κ the bending rigidity and κ_G the Gaussian curvature modulus of a lipid monolayer. These are related to its lateral pressure profile [84, 86] and are assumed to be constant. The bending modulus κ can be determined *e.g.* by Fourier spectroscopy of vesicle fluctuations, micropipet aspiration or diffuse x-ray scattering [34, 41], the spontaneous curvature c_0 by lattice swelling experiments using H_{II} phases [39]. In general, a typical value for the bending modulus of a lipid monolayer is $\kappa \approx 10 k_B T$ and a quadratic dependence on the hydrocarbon chain length is assumed [86, 87].

The Gaussian curvature has been neglected in many earlier studies [24, 88]. As a result of the Gauss-Bonnet theorem, the integral over a surface of fixed topology is constant. The value $\int_A K dA = -4\pi$ is expected for a smooth *cis* monolayer of a single stalk connecting two planar bilayers, independent of the exact stalk shape [42]. In appendix A.3,

this is explicitly demonstrated for two surfaces that have been used to describe stalks or fusion pores [89]. The Gaussian curvature modulus is assumed to be negative and in the range $-\kappa \leq \kappa_G \leq -\kappa/2$ and can be determined by experiments on bicontinuous cubic phases [88, 89].

The first versions of this model assumed a fixed semitoroidal stalk shape shown in Fig. 1.9(a) [21]. Depending on c_0 and the parameters r and a , bending energies of $\approx 40 k_B T$ were found, neglecting the Gaussian curvature term. Later, as summarized in [25], it was realized that an additional contribution due to the “hydrophobic void” regions (v) in Fig. 1.9(a) lead to an additional energy penalty, resulting in values F_{bend} of up to several hundreds of $k_B T$. In the latest versions, the unjustified assumption of a fixed toroidal shape was dropped, leading to models of stress-free stalks [24] or a stalk with lipid tilt as an additional deformation (Fig. 1.9b) leading to values of about $40 k_B T$ [25, 82]. Lipid tilt is also observed in simulations of the stalk phase [54]. However, with the inclusion of Gaussian curvature, the condition $-\kappa \leq \kappa_G \leq -\kappa/2$ and $\kappa \approx 10 k_B T$, the Gaussian curvature term $-4\pi\kappa_G$ yields an additional contribution of at least $60 k_B T$, resulting in a minimum bending energy of about $100 k_B T$ in total [88].

Simulations

In contrast, stalk free energies predicted by recent simulations which take into account the microscopic structure of lipids, *e.g.* by coarse-grained molecular dynamics [53, 59] or self-consistent field theory [90], are typically below $15 k_B T$. This discrepancy between continuum models and simulations has not yet been resolved and is likely to result from the simplifying assumptions of continuum theory. The description by few elastic coefficients and expansion of bending energy up to quadratic terms have been developed *e.g.* to determine the shape of vesicles at a given ratio of area and contained volume [34, 42]. However, on length scales of fusion intermediates, the validity has been questioned repeatedly. This is discussed in more detail in section 6.3.

Stalks and lipid composition

The sensitivity of membrane fusion to lipid composition has been shown in a number of studies [16]. For example, certain viral fusion reactions can be inhibited if the target membrane are depleted of cholesterol [91, 92]. Phosphatidylethanolamines (PE) have been found to promote several fusion reactions [93]. Lysolipids affect fusion rates depending on their location either in the inner or the outer membrane leaflet [94].

A reason for the success of continuum theory is that it rationalizes these observations [93, 95]. In the packing parameter model described in section 1.2, these lipids would change the spontaneous curvature, thus changing the stalk bending energy. It has been hypothesized that the lipid composition of biomembranes is adjusted in a way that the spontaneous curvature of its monolayer is optimized for fusion [96]. Therefore, one of the goals of this thesis is to investigate if the shape of stalks changes with lipid composition in way that correlates with lipid geometry.

2 X-ray diffraction on lipid mesophases

Diffraction on lipid mesophases is currently the only experimental method which can provide structural information on model membrane systems down to sub-nanometer lengthscales and hence allows to study stalk structures. This chapter provides the required background in crystallography and electron density reconstruction and introduces the methods used in this thesis: Grazing-incidence x-ray diffraction, x-ray reflectivity and powder diffraction. For all three cases, the intensity correction factors required for data analysis in subsequent chapters are presented. The chapter closes with a brief discussion of the phase problem and the obtainable resolution.

2.1 Fundamentals of X-ray diffraction

This section is based on the textbooks [97, 98, 99]. X-rays are scattered by electrons and can thus be used to study the spatial distribution of electrons inside the scattering entities of a sample. In structural biology, x-ray diffraction is usually formulated within the kinematical or first-order Born approximation. This description neglects multiple-scattering effects, which is valid for weakly scattering imperfect crystals. For diffraction from macroscopically perfect crystals, the more general formalism of dynamical diffraction theory has to be applied. The distorted-wave Born approximation combines elements of both approaches. For the particular case of solid-supported samples, dynamical effects may occur due to reflection from the substrate if incidence and exit angles are close to the angle of total external reflection [98]. Diffraction from the lipid mesophases covering the substrate as a thin film is treated within kinematical theory.

A scattering event is described by the wavevector transfer or scattering vector

$$\vec{q} = \vec{k}_f - \vec{k}_i \quad (2.1)$$

defined as the difference between the final and initial wavevectors \vec{k}_f and \vec{k}_i of a photon. In case of elastic scattering,

$$|\vec{k}_f| = |\vec{k}_i| = \frac{2\pi}{\lambda} \quad (2.2)$$

holds, where λ denotes the wavelength of the incident x-ray beam. As the main result of kinematical theory, the scattering amplitude $A(\vec{q})$ of a sample corresponds to the Fourier transform of its electron density distribution $\rho(\vec{r})$:

$$A(\vec{q}) = \int \rho(\vec{r}) \exp(i\vec{q} \cdot \vec{r}) d^3r \quad (2.3)$$

The scattering vector \vec{q} is used as the transform variable and the integration extends over the entire sample. X-ray diffraction relies on the periodic arrangement of identical scattering entities in space. In case of a crystal, $\rho(\vec{r})$ can be written as the convolution of a point lattice spanned by vectors

$$\vec{R}_{uvw} = u \cdot \vec{a} + v \cdot \vec{b} + w \cdot \vec{c}, \quad u, v, w \in \mathbb{Z} \quad (2.4)$$

and the electron density $\rho_{\text{u.c.}}(\vec{r})$ inside the parallelepiped spanned by \vec{a} , \vec{b} and \vec{c} , the unit cell:

$$\rho(\vec{r}) = \sum_{\vec{R}_{uvw}} \delta(\vec{r} - \vec{R}_{uvw}) * \rho_{\text{u.c.}}(\vec{r}). \quad (2.5)$$

Importantly, there is no unique way to choose \vec{a} , \vec{b} , \vec{c} . For a choice which minimizes the unit cell volume $V_{\text{u.c.}} = \vec{a} \cdot (\vec{b} \times \vec{c})$, one obtains a so-called primitive unit cell, which can be regarded as the smallest repeating unit required to rebuild the crystal only by translations. As demonstrated in crystallography, each lattice can be classified according to its symmetries into seven crystal systems and fourteen Bravais lattices. The lengths a, b, c of the vectors $\vec{a}, \vec{b}, \vec{c}$ and the angles α, β, γ between them are the lattice parameters. Combined with 32 crystallographic point symmetries of the unit cell, there are 230 space groups describing any possible symmetry of a 3d crystal. Using the properties of the δ distribution and the convolution theorem, the scattering amplitude becomes

$$A(\vec{q}) = \underbrace{\sum_{\vec{R}_{uvw}} \exp(i\vec{q} \cdot \vec{R}_{uvw})}_{S(\vec{q})} \cdot \underbrace{\int_{V_{\text{u.c.}}} \rho_{\text{u.c.}}(\vec{r}) \exp(i\vec{q} \cdot \vec{r}) d^3r}_{F(\vec{q})}. \quad (2.6)$$

$S(\vec{q})$ is called the lattice sum or structure factor, and $F(\vec{q})$ the unit cell form factor. For a perfect crystal with fixed atomic positions, it is possible to write $F(\vec{q})$ as a sum over the scattering amplitudes of the single atoms inside the unit cell using the so-called atomic form factors. As discussed in detail in section 2.6, phospholipid mesophases are characterized by long-range lattice symmetry, but highly disordered unit cells [100]. Therefore, a continuous unit cell electron density distribution $\rho_{\text{u.c.}}(\vec{r})$ provides an appropriate description. In the following, the subscripts u.c. for unit cell electron density and volume are omitted. The observable intensity is the modulus square of the scattering amplitude,

$$I(\vec{q}) \propto |S(\vec{q})|^2 \cdot |F(\vec{q})|^2. \quad (2.7)$$

Proportionality is used to indicate that $I(\vec{q})$ depends on additional factors determined by the actual experimental conditions. These are considered in detail in section 2.4. All terms in $S(\vec{q})$ can be represented as unit vectors in the complex plane. $|S(\vec{q})|^2$ adopts maxima if these point all into the same direction. Since a global phase factor does not affect $I(\vec{q})$, this is fulfilled if

$$\exp(i\vec{q} \cdot \vec{R}_{uvw}) = 1 \quad \text{or} \quad \text{mod}(\vec{q} \cdot \vec{R}_{uvw}, 2\pi) = 0 \quad \forall u, v, w. \quad (2.8)$$

To this end, the reciprocal lattice spanned by vectors

$$\vec{a}^* = \frac{2\pi}{V} (\vec{b} \times \vec{c}), \quad \vec{b}^* = \frac{2\pi}{V} (\vec{c} \times \vec{a}), \quad \vec{c}^* = \frac{2\pi}{V} (\vec{a} \times \vec{b}) \quad (2.9)$$

is introduced. By definition, each linear combination $\vec{G}_{hkl} = h \cdot \vec{a}^* + k \cdot \vec{b}^* + \ell \cdot \vec{c}^*$ with Miller indices $h, k, \ell \in \mathbb{Z}$ is perpendicular to a set of lattice planes (hkl) of the corresponding direct lattice defined by Eq. (2.4) and fulfils condition (2.8), since

$$\vec{G}_{hkl} \cdot \vec{R}_{uvw} = 2\pi(hu + kv + \ell w) = 2\pi \cdot n, \quad n \in \mathbb{Z}. \quad (2.10)$$

For a large number N of unit cells, it can be shown that

$$\lim_{N \rightarrow \infty} |S(\vec{q})|^2 = NV^* \sum_{h,k,\ell} \delta(\vec{q} - \vec{q}_{hkl}) \quad (2.11)$$

where $V^* = \vec{a}^* \cdot (\vec{b}^* \times \vec{c}^*)$, independent of the actual crystal shape [97]. Hence, diffraction peaks only occur for scattering vectors which coincide with a vector of the reciprocal lattice,

$$\vec{q}_{hkl} = h \cdot \vec{a}^* + k \cdot \vec{b}^* + \ell \cdot \vec{c}^*, \quad h, k, \ell \in \mathbb{Z}. \quad (2.12)$$

This is known as the Laue condition. Due to finite crystallite size as well as divergence and wavelength spread of the x-ray beam in a real experiment, the description using delta functions should be regarded as an approximation. The equivalent condition for constructive interference in direct space is Bragg's law

$$2d_{hkl} \sin \theta = n \cdot \lambda, \quad n \in \mathbb{Z}. \quad (2.13)$$

Here, $d_{hkl} = 2\pi/|\vec{q}_{hkl}|$ denotes the spacing of a family of crystallographic planes and θ the glancing angle between these planes and the incident x-ray beam. Collecting these results together, the diffracted intensity from a crystallite in a lipid mesophase is

$$I(\vec{q}) \propto \sum_{hkl} \delta(\vec{q} - \vec{q}_{hkl}) \cdot \left| \int_V \rho(\vec{r}) \exp(i\vec{q} \cdot \vec{r}) d^3r \right|^2 \quad (2.14)$$

and thus proportional to the modulus square of the Fourier transform of the unit cell electron density $\rho(\vec{r})$ sampled at discrete values \vec{q}_{hkl} fulfilling the Laue condition. This provides an elegant connection between crystal structure and measured x-ray diffraction patterns. *Vice versa*, the form factors $F_{hkl} = F(\vec{q}_{hkl})$ are the coefficients of the Fourier series of $\rho(\vec{r})$,

$$\rho(\vec{r}) = \frac{1}{V} \sum_{h,k,\ell} F_{hkl} \exp(-i\vec{q}_{hkl} \cdot \vec{r}). \quad (2.15)$$

In general, the form factors are complex-valued quantities:

$$F_{hkl} = |F_{hkl}| \exp(i\phi_{hkl}) \in \mathbb{C} \quad \text{where} \quad \phi_{hkl} \in [0, 2\pi]. \quad (2.16)$$

From the measurable intensities $I_{hkl} = I(\vec{q}_{hkl})$, only the form factor amplitudes $|F_{hkl}| \propto \sqrt{I_{hkl}}$ are obtained on a relative scale. The phase angles ϕ_{hkl} are not directly accessible. This is the well-known phase problem of crystallography, which needs to be solved in order to obtain the structure $\rho(\vec{r})$. In the following, the experimental methods used to obtain the lattice constants and form factor amplitudes $|F_{hkl}|$ from solid-supported lipid bilayer stacks and nonlamellar phases are introduced. Subsequently, we will return to the phase problem for this particular case in section 2.5.

2.2 Oriented samples

The vast majority of experiments in this thesis is carried out using oriented lipid bilayer stacks. These are routinely prepared by deposition of lipids in organic solution on a substrate, from which highly aligned, hydrated bilayer stacks are obtained by pure self-assembly. This process is sketched in Fig. 2.1(a), a detailed protocol is provided in section 3.2.1. The number of bilayers in a stack is typically on the order of 10^3 , yielding a thin film of few μm thickness. The high degree of alignment is quantified by low mosaic distribution, *i.e.* narrow distribution of bilayer normal vectors as measured by a rocking scan shown in Fig. 2.1(c).

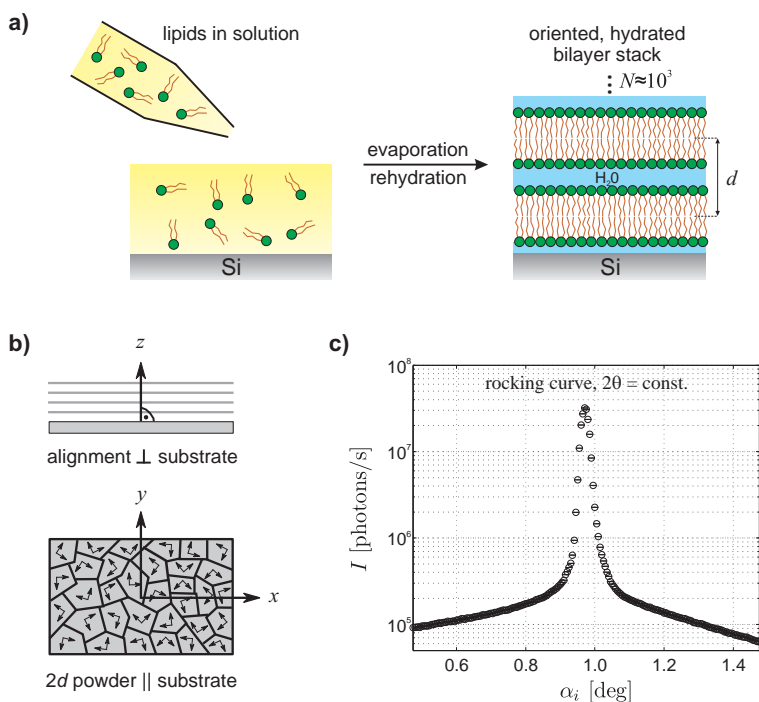


Figure 2.1: (a) Cartoon illustrating the preparation of oriented, solid-supported bilayer stacks. (b) Sketch of the 2d powder character of aligned samples and definition of coordinate axes. (c) Rocking curve of the 1. Bragg peak along q_z (di14:IPC, RH = 80%): The full width at half maximum (FWHM) is below 0.03° and thus considerably smaller than the primary beam width of 0.11° . Experimental parameters are given in section 4.4.1.

Compared to powder samples or multilamellar liposomes, oriented samples provide several advantages: Most obviously, components of the scattering vector \vec{q} corresponding to structural information in and perpendicular to the bilayer plane can be precisely distinguished. In addition, the scattering signal is amplified: In case of unoriented samples, only a small fraction of crystallites with suitable orientation give rise to

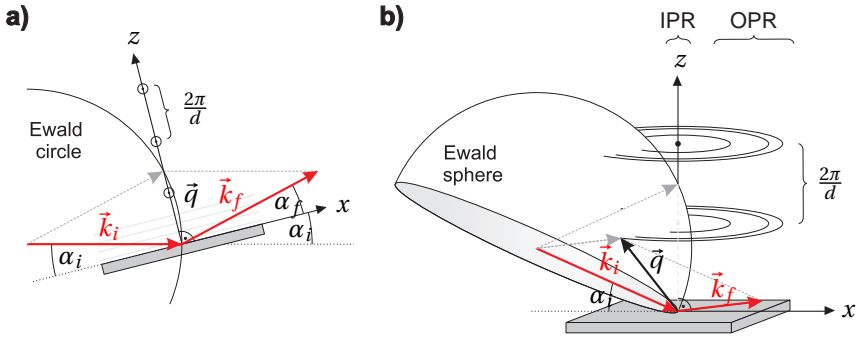


Figure 2.2: Diffraction on a solid-supported $2d$ powder sample described by the Ewald sphere. **(a)** For in-plane reflections (IPR), the Laue condition is fulfilled only for certain α_i . **(b)** Out-of-plane reflections (OPR) can be observed for all α_i (provided λ is small enough), since their reciprocal lattice points are distributed on rings centered about \vec{e}_z . Adapted from [52].

constructive interference and contribute to Bragg peak intensity. If oriented samples are used, all domains placed in the x-ray beam contribute simultaneously to constructive interference in case of reflections where \vec{q}_{hkl} is perpendicular to the substrate. Finally, when used in conjunction with the osmotic stress method (section 4.2), the small lipid film thickness of few μm enables a quick response of the entire sample to changes of water vapour pressure in the surrounding air.

In case of the lipids used in this thesis, the bilayer stacks transform into nonlamellar phospholipid phases upon dehydration. A lipid film with an area of the order of few cm^2 consists of a large number of crystallites which are randomly oriented parallel to the substrate, but still retain the alignment perpendicular to the substrate (Fig. 2.1b). This can be characterized as a $2d$ powder. It turns out that different geometries are required to measure all integrated Bragg peak intensities and lattice parameters of these samples correctly [51, 101].

In Fig. 2.2, diffraction from a $2d$ powder is explained by aid of the Ewald sphere construction [97]. The plane of incidence is defined by the initial wave vector \vec{k}_i and the surface normal of the substrate. \vec{k}_i points at the coordinate origin and center of rotation of the sample. In case of elastic scattering, the Laue condition for a reflection is fulfilled only if the corresponding reciprocal lattice point coincides with a sphere of radius $\frac{2\pi}{\lambda}$ drawn around the starting point of \vec{k}_i .

Fig. 2.2 (left) shows this situation for \vec{q} perpendicular to the substrate, *i.e.* \vec{k}_f is also located in the plane of incidence. The Laue condition for these *in-plane* reflections is only fulfilled if the corresponding reciprocal lattice point coincides with the Ewald circle. This condition can only be fulfilled for a single reflection at a time. Therefore, at fixed α_i , only diffuse *Bragg sheets* due to fluctuations or orientational defects in the bilayer stack [102] are observed if an area detector is placed behind the sample. The sample must be rotated about the axis $\vec{k}_i \times \vec{n}$ to successively excite all in-plane reflections. To this end, we use x-ray reflectivity scans as described in section 2.3.1.

Due to the $2d$ powder character, the reciprocal lattice sites corresponding to *out-of-plane*² reflections are distributed on concentric rings around the \vec{q}_z axis (Fig. 2.2, *right*). Provided λ is small and hence the radius of the Ewald sphere large enough, each ring intersects the Ewald sphere twice [51]. All out-of-plane reflections can be recorded using a single sample orientation and fixed area detector position. Since only a small fraction of crystallites with suitable orientation contributes to the diffracted intensity, out-of-plane reflections are in general much weaker than in-plane reflections. If α_i is varied, out-of-plane reflections are always excited as long as the intersection occurs. However, the corresponding directions of \vec{k}_f and thus locations of diffraction peaks on the detector change with α_i , and reflections corresponding to $\alpha_f < 0$ disappear below the sample horizon. Therefore, out-of-plane reflections are measured at fixed and sufficiently small α_i by grazing-incidence diffraction as described in section 2.3.2.

2.3 Experimental techniques

2.3.1 X-ray reflectivity

Reflections corresponding to momentum transfer perpendicular to the substrate can be recorded by x-ray reflectivity. The sample is aligned with the lipid film in the center of the beam and the substrate surface parallel to the incident beam (Fig. 2.3*a*). Then, α_i is successively increased. For each step, the point detector is moved to position $2\alpha_i$ with respect to the incident beam in order to measure the intensity corresponding to the momentum transfer perpendicular to the substrate,

$$\vec{q} = \begin{pmatrix} 0 \\ 0 \\ \frac{4\pi}{\lambda} \sin \alpha_i \end{pmatrix}. \quad (2.17)$$

The resulting reflectivity curve $I(\alpha_i)$ is the superposition of the Fresnel reflectivity

$$I_F = I_0 \cdot \left| \frac{\sin \alpha_i - \sqrt{\sin^2 \alpha_i - \sin^2 \alpha_c}}{\sin \alpha_i + \sqrt{\sin^2 \alpha_i - \sin^2 \alpha_c}} \right|^2 \quad (2.18)$$

from the silicon substrate³ [97] and the intensity diffracted from the lipid bilayer stack, which leads to Bragg peaks with a spacing defined by the periodicity d along the bilayer normal. The critical angle for total external reflection is

$$\alpha_c = \sqrt{\frac{\lambda^2}{\pi} r_0 \rho_S}, \quad (2.19)$$

² To avoid confusion, the following should be noted: In this thesis, *in-* and *out-of-plane* refer to the plane of incidence defined by \vec{k}_i and the surface normal $\vec{n} = \vec{e}_z$ of the substrate. In the literature, *in-plane* is also used in conjunction with lateral correlations in the sample, *i.e.* in the xy plane. *Out-of-plane* reflections arise from *in-plane* structures, while pure *out-of-plane* correlations (*i.e.* in z direction) give rise to *in-plane* reflections only.

³ Eq. (2.18) applies to the ideal case of vanishing absorption and surface roughness.

where $r_0 = 2.82 \cdot 10^{-5} \text{ \AA}$ denotes the Thomson scattering length and ρ_S the electron density of the substrate. The values α_c for x-ray energies used in this thesis are given in Tab. 2.1.

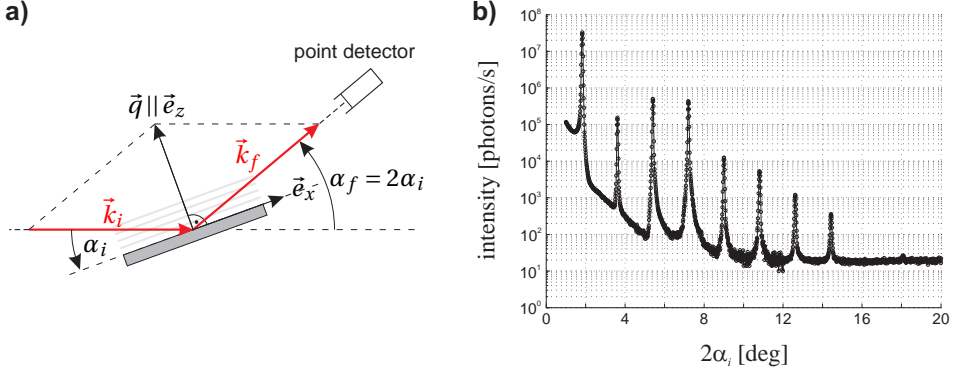


Figure 2.3: (a) Geometry of a reflectivity measurement. α_i is increased in steps of e.g. 0.005° . At each position, the reflected and diffracted intensity with \vec{q} perpendicular to the substrate is measured by rotating the point detector to $2\alpha_i$. (b) Typical reflectivity curve displaying 8 well-defined Bragg peaks (DOPC, RH = 80%, experimental details are given in section 4.4.1.)

photon energy E [keV]	wavelength λ [Å]	critical angle α_c [deg]
8.048	1.5406	0.223
17.000	0.7293	0.105
19.500	0.6358	0.091

Table 2.1: X-ray energies used in this thesis, corresponding wavelengths $\lambda = 2\pi\hbar c/E$ and critical angles of total external reflection α_c from the silicon substrate.

2.3.2 Grazing-incidence x-ray diffraction

Fig. 2.4 shows the grazing-incidence x-ray diffraction (GIXD) geometry. The incident angle α_i is fixed at a value close to zero, *i.e.* the x-ray beam is almost parallel to the substrate surface.⁴ An area detector is placed at a distance D behind the sample. Each pixel of the detector corresponds to a unique pair of angles (α_f, ψ) describing the corresponding scattering vector. With the conventions made in Fig. 2.4, the initial and final wavevectors are

$$\vec{k}_i = \frac{2\pi}{\lambda} \begin{pmatrix} \cos \alpha_i \\ 0 \\ -\sin \alpha_i \end{pmatrix} \quad \text{and} \quad \vec{k}_f = \frac{2\pi}{\lambda} \begin{pmatrix} \cos \alpha_f \cos \psi \\ \cos \alpha_f \sin \psi \\ \sin \alpha_f \end{pmatrix}, \quad (2.20)$$

⁴ The term *grazing* is often understood as an angle below the critical angle of total external reflection α_c from the substrate. We also use it for angles slightly above α_c .

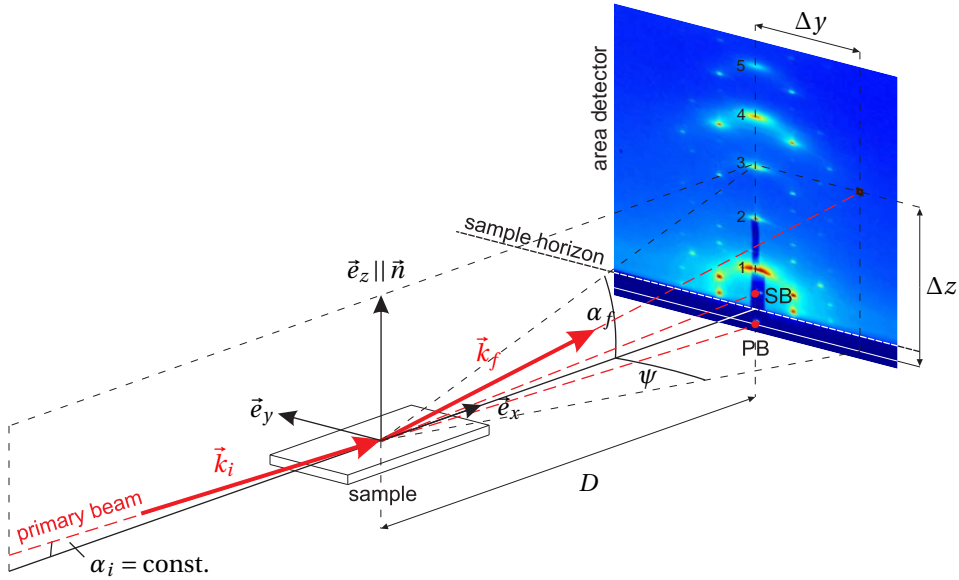


Figure 2.4: Scattering geometry for grazing-incidence diffraction. The positions of primary beam (PB) and specular beam (SB) on the detector are indicated by red circles. Scattered photons with $\alpha_f < 0$, i.e. below the sample horizon, are absorbed by the substrate. In the plane of incidence, five orders of diffuse Bragg sheets can be recognized. At $\psi \neq 0$, the characteristic out-of-plane diffraction peaks of the rhombohedral phase are visible (DOPC/Chol 70:30, RH=60%, ID01 measurement, cf. section 5.1.1).

yielding scattering vector components

$$q_x = \frac{2\pi}{\lambda} (\cos \alpha_f \cos \psi - \cos \alpha_i), \quad (2.21)$$

$$q_y = \frac{2\pi}{\lambda} (\cos \alpha_f \sin \psi), \quad (2.22)$$

$$q_z = \frac{2\pi}{\lambda} (\sin \alpha_i + \sin \alpha_f). \quad (2.23)$$

Due to random orientation of crystallites in the xy plane, the scattering vector components parallel and perpendicular to the substrate are of interest:

$$q_{\parallel} = \sqrt{q_x^2 + q_y^2} = \frac{2\pi}{\lambda} \sqrt{\cos^2 \alpha_i + \cos^2 \alpha_f - 2 \cos \alpha_i \cos \alpha_f \cos \psi} \quad (2.24)$$

$$q_z = \frac{2\pi}{\lambda} (\sin \alpha_i + \sin \alpha_f). \quad (2.25)$$

For the total scattering angle 2θ between \vec{k}_i and \vec{k}_f , one obtains

$$\cos 2\theta = \cos \alpha_i \cos \alpha_f \cos \psi - \sin \alpha_i \sin \alpha_f. \quad (2.26)$$

The angle α_i has to be chosen small enough to ensure that no detectable diffraction peaks disappear below the sample horizon. On the other hand, α_i should not be too small, since this reduces the number of photons impinging onto the lipid film (*cf.* section 2.4). As an additional effect for $\alpha_i < \alpha_c$, a second set of diffraction peaks may appear due to diffraction of the beam reflected from the substrate [103]. Due to the $2d$ powder character, the images recorded in GIXD possess mirror symmetry with respect to the plane of incidence.

2.3.3 Powder diffraction

Additional powder measurements are required to put the form factor amplitudes $\{F_{hkl}\}$ of in-plane reflections obtained from reflectivity scans and those of out-of-plane reflections measured in GIXD experiments on a common scale. As explained in detail in section 5.1.3, this is a highly nontrivial and important step for correct electron density reconstruction. The basic setup for powder diffraction is shown in Fig. 2.5. The scattering vector corresponding to a total scattering angle 2θ is

$$q = \frac{4\pi}{\lambda} \sin \theta. \quad (2.27)$$

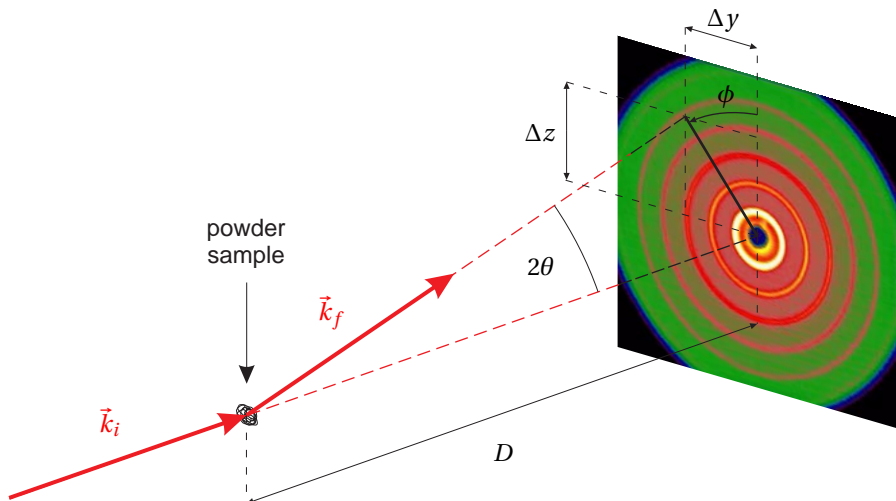


Figure 2.5: Powder diffraction geometry and typical powder pattern consisting of concentric rings (silver behenate calibration standard, SAXS instrument, Institute for X-ray Physics, *cf.* section 3.2.3).

2.4 Intensity correction factors

In addition to the proportionality $I_{hkl} \propto |F_{hkl}|^2$, the integrated Bragg peak intensities obtained from an experiment depend on further effects determined by the exact experimental conditions [99]. It is crucial to take these into account in order to obtain correct form factor amplitudes $|F_{hkl}|$. Considering absorption, polarization, and illumination effects as well as the Lorentz factor and peak multiplicities, the integrated intensity I_{hkl} and the corresponding unit cell form factor F_{hkl} are related by [51, 101]

$$I_{hkl} = K \cdot C_{\text{abs}} C_{\text{pol}} C_L C_{\text{ill}} C_m |F_{hkl}|^2. \quad (2.28)$$

The constant K summarizes all global experimental parameters such as primary beam intensity, scattering volume, detector efficiency and duration of the exposure and can usually be neglected, since it does not affect the ratio of intensities of different reflections. However, as discussed in detail in section 5.1.3, the special case of a $2d$ powder requires some effort to obtain the form factor amplitudes measured in two different geometries on a common scale. The origin and different functional forms of the remaining correction factors for grazing-incidence, reflectivity and powder measurements are explained in the following.

Absorption

In our experiments, scattered x-ray photons can be absorbed either in the lipid film or by the sample chamber and flight tube windows and by the remaining air between sample and detector. In the reflectivity measurements, the second contribution is identical for all angles α_i . Also in a grazing-incidence experiment where α_f and ψ are both small, it is very similar for all angles. Therefore, only absorption by the lipid film is taken into account.

Consider a photon which is scattered in a depth z inside the lipid film of total thickness d_f (Fig. 2.6a). The path length of the photon through the sample is

$$l(z) = \left[\frac{1}{\sin \alpha_i} + \frac{1}{\sin \alpha_f} \right] z, \quad (2.29)$$

the corresponding transmission probability is $\exp(-\mu(\lambda)l)$, where $\mu(\lambda)$ denotes the wavelength-dependent linear absorption coefficient of the lipid film. The absorption factor for a given pair of angles (α_i, α_f) is equivalent to the transmission probability averaged over all penetration depths,

$$C_{\text{abs}} = \frac{1}{d_f} \int_0^{d_f} \exp(-\mu l(z)) dz = \frac{1 - \exp\left(-\mu d_f \left[\frac{1}{\sin \alpha_i} + \frac{1}{\sin \alpha_f} \right]\right)}{\mu d_f \left[\frac{1}{\sin \alpha_i} + \frac{1}{\sin \alpha_f} \right]}. \quad (2.30)$$

This result is the same as in [101]. The linear absorption coefficient $\mu(\lambda)$ depends on the x-ray wavelength approximately *via* $\mu \propto \lambda^3$ [97], used values are listed in Tab. 2.2. For a stack of $N \approx 1400$ lipid bilayers as estimated below and a lattice constant of $d \approx 50 \text{ \AA}$, the resulting film thickness is $d_f \approx 7 \mu\text{m}$. For simplicity, this value is used for

all samples. In Fig. 2.6(b), the absorption factors for typical reflectivity and grazing-incidence measurements are shown as a function of q_z . In the latter case, C_{abs} is considerably more uniform in the required q_z range. Therefore, we apply absorption correction only to the reflectivity data, where it slightly increases the form factor amplitudes of the lower-order reflections. For the first Bragg peak, this effect is on the order of about 10%.

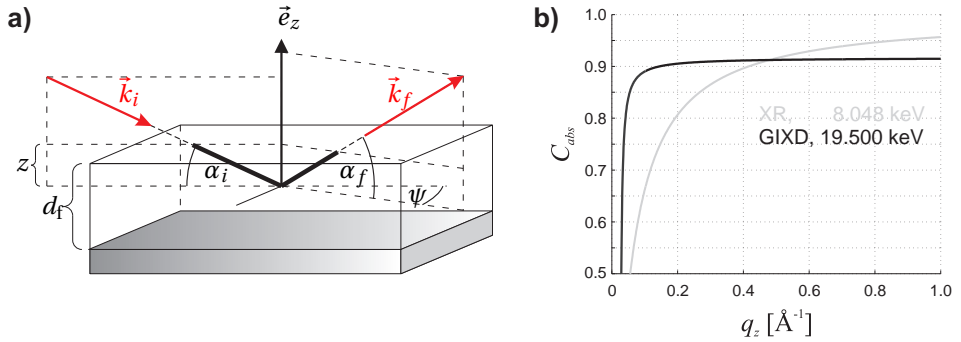


Figure 2.6: Absorption correction: (a) Sketch for derivation of the absorption correction factor C_{abs} . A photon is scattered in a depth of z inside the lipid film. The corresponding path through the sample is indicated by the solid black line. (b) C_{abs} as a function of q_z for an x-ray reflectivity (XR) and a GLXD ($\alpha_i = 0.15^\circ$) experiment ($d_f = 7 \mu\text{m}$, values of μ are given in Tab. 2.2).

E [keV]	μ [m^{-1}]
8.048	783
17.000	91
19.500	66

Table 2.2: Linear absorption coefficients μ for the three photon energies used in this thesis. Calculations were carried out by a tool on the CXRO web page [104] using the sum formula of DOPC, $C_{44}H_{84}NO_8P$, and a molecular volume of 1296\AA^3 [105] yielding a mass density of 1.007g cm^{-3} . The value obtained for Cu- K_α radiation (8.048 keV) is very close to the one in [106].

Polarization

The scattered intensity also depends on the angle between the final wavevector \vec{k}_f and the polarization of the x-ray beam, *i.e.* the direction of the electric field vector. In a synchrotron storage ring, electrons circulate in the horizontal plane and wigglers or undulators cause oscillations in horizontal direction. A synchrotron beam is thus linearly polarized. In contrast, a sealed tube provides an unpolarized x-ray beam. The polarization factors correcting for this effect are [97, 107, 108]

$$C_{\text{pol}} = \begin{cases} \cos^2 \alpha_f \cos^2 \psi + \sin^2 \alpha_f & \text{synchrotron (horiz. scattering geometry)} \\ \frac{1}{2} [1 + \cos^2(2\theta)] & \text{sealed tube.} \end{cases} \quad (2.31)$$

For a total scattering angle $2\theta = 10^\circ$, this leads to a correction of $|F_{hkl}|$ by less than 1%.

Lorentz factor

The number of crystallites which contribute to a certain reflection depends on the structure of the sample ($2d$ vs. $3d$ powder) and the experimental geometry. The Lorentz factor corrects for this effect. In contrast to the rather weak polarization and absorption corrections, it strongly affects the obtained $|F_{hkl}|$ [97, 101, 107, 108, 109, 110]:

$$C_L = \begin{cases} [\cos \alpha_i \cos \alpha_f \sin \psi]^{-1} & \propto q_{\parallel}^{-1} & \text{grazing-incidence diffraction} \\ [\sin 2\alpha_i]^{-1} & \propto q_z^{-1} & \text{reflectivity} \\ \cos \theta / \sin^2 2\theta & \propto q^{-2} & \text{powder diffraction} \end{cases} \quad (2.32)$$

The proportionality symbols are valid in the small-angle region, which is assumed throughout this thesis. It has been demonstrated that corrections by q_z^{-1} for oriented stacks and q^{-2} for unoriented multilamellar liposomes lead to the same results [87].

Illumination

In a reflectivity scan, the number of photons of the primary beam which reach the sample depends on the angle of incidence (Fig. 2.7). If α_i is small, a certain fraction misses the sample. Assuming a rectangular primary beam profile, the following illumination factor is used:

$$C_{\text{ill}} = \begin{cases} \frac{h}{l \sin \alpha_i} & \alpha_i < \arcsin\left(\frac{h}{l}\right), \\ 1 & \text{else.} \end{cases} \quad (2.33)$$

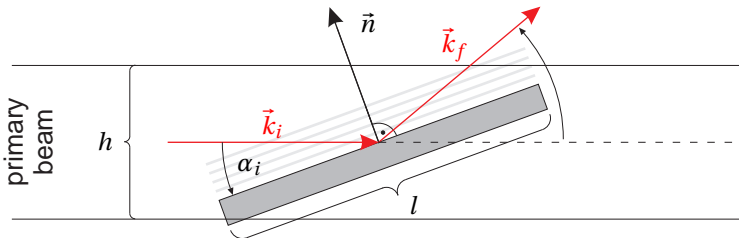


Figure 2.7: Illustration of the illumination correction. For small angles α_i , a part of the beam does not impinge on the sample.

Multiplicity factor

In case of nonlamellar lipid mesophases, symmetry-equivalent reflections occur. In the rhombohedral phase, e.g. the reflections denoted by Miller indices $(\bar{1}02)$, (012) and

$(\bar{1}\bar{1}2)$ ⁵ are symmetry-equivalent and coincide on the detector. The integrated intensity I_{hkl} of a Bragg peak then corresponds to a family of reflections denoted by curly brackets $\{hkl\}$, where any of the contained index triples can be used for hkl . The multiplicity m_{hkl} of a family of reflections $\{hkl\}$ denotes the number of its members. The multiplicity correction factor in Eq. (2.28) is

$$C_m = m_{hkl}. \quad (2.34)$$

For the rhombohedral phase, the families of reflections and their members are listed in Tab. A.1 in appendix A.2.

2.5 The phase problem

Now we return to the phase problem of crystallography and consider the special case of phospholipid mesophases.⁶ As introduced above, the unit cell form factors

$$F_{hkl} = \int_V \rho(\vec{r}) \exp(i\vec{q}_{hkl} \cdot \vec{r}) d^3r = |F_{hkl}| \cdot \exp(i\phi_{hkl}) \quad (2.35)$$

obtained by Fourier transform of the unit cell electron density $\rho(\vec{r})$ are, in general, complex-valued quantities. *A priori*, the crystallographic phase ϕ_{hkl} can assume any value between 0 and 2π . Without additional information, the number of possibilities to assign ϕ_{hkl} to a set of measured form factor amplitudes is infinite.

For lamellar phospholipid phases, it is sufficient to consider the one-dimensional electron density profile (EDP) $\rho(z)$ perpendicular to the bilayer plane. In bilayer stacks obtained by self-assembly from lipids in solution, the lipid composition of both monolayers composing each bilayer must be, at least on average, the same.⁷ In addition, $\rho(z)$ is the spatial and temporal average over all bilayers in the stack. Therefore, $\rho(z)$ must be symmetric with respect to the bilayer midplane. If the bilayer center is chosen as the origin $z = 0$, the electron density profile is centrosymmetric, $\rho(z) = \rho(-z)$ (Fig. 2.8).

Also in case of all studies of nonlamellar phospholipid mesophases we are aware of, be it inverted hexagonal, ripple, cubic (e.g. [111, 112, 113]) or the rhombohedral phase, the assumption of centrosymmetry has been made and yielded reasonable structural results. It has been attempted to motivate this by the fact that nonlamellar mesophases are obtained by phase transitions from symmetric lipid bilayers, and centrosymmetry should somehow be conserved [114]. However, there is no rigorous proof at hand to make this a universal rule.

In case of centrosymmetry, without loss of generality, the center of inversion can be chosen as the coordinate origin. Use of the Euler identity

$$\exp(ix) = \cos x + i \cdot \sin(x) \quad \forall x \in \mathbb{R} \quad (2.36)$$

⁵ In crystallography, a minus sign is often indicated as a bar above a Miller index.

⁶ Unfortunately, the word *phase* has to be used to characterize the sample state as well as for the property of a complex number. In this section, *lipid mesophase* and *crystallographic phase* are used for clarity.

⁷ Note that this does not apply to biological membranes *in vivo*, which are usually characterized by asymmetric lipid composition of the inner and outer leaflets [1].

yields

$$F_{hkl} = \int_V \rho(\vec{r}) \cos(\vec{q}_{hkl} \cdot \vec{r}) d^3r = (\pm 1) \cdot |F_{hkl}| \in \mathbb{R}, \quad (2.37)$$

since the integral of an odd function evaluated over a symmetric interval is zero. The Fourier series Eq. (2.15) for reconstruction of $\rho(\vec{r})$ turns into

$$\rho(\vec{r}) = \frac{1}{V} \sum_{h,k,\ell} v_{hkl} |F_{hkl}| \cos(\vec{q}_{hkl} \cdot \vec{r}) \quad \text{where} \quad v_{h,k,\ell} = \pm 1. \quad (2.38)$$

The crystallographic phase problem $\phi_{hkl} \in [0, 2\pi]$ is reduced to $\phi_{hkl} = 0$ or π , *i.e.* turns into a “sign problem” $v_{hkl} = \pm 1$. For N independent, not symmetry-related reflections, the number of possible sign combinations $\{v_{hkl}\}$ is 2^N . In case of a liquid-crystalline L_α phase, we typically observe $N = 8$ Bragg reflections, yielding $2^8 = 256$. For the rhombohedral phase, this increases to up to about 2^{30} . In comparison to the general non-centrosymmetric case, this already poses a considerable simplification. However, still some effort is required to solve the residual sign problem.

The structures $\rho(\vec{r})$ obtained after reconstruction must be compatible with some general features due to the physico-chemical properties of lipid mesophases [113]: As a result of the powerful hydrophobic effect, water and hydrocarbon do not mix. The obtained structures must be composed of continuous lipid monolayers [115], *i.e.* a lipid headgroup region indicated by elevated electron density (due to the phosphate groups, *cf.* chapter 4) must separate aqueous regions and the hydrophobic hydrocarbon region. The dimensions of features in the obtained electron density maps, *e.g.* the width of the polar headgroup region indicated by elevated electron density, must be consistent with the known molecular dimensions of the used lipids. In addition, as addressed more closely in the following section, the density maps must be rather smooth and display no sharp edges or features with sizes below few Å.

After these general considerations, a brief summary of several existing methods to solve the crystallographic phase problem for the case of diffraction from lipid mesophases is given:

- **Plausibility:** If the number of reflections is small, *e.g.* 4 in case of a lipid bilayer stack at full hydration, it is an accepted practice to select one of $2^4 = 8$ phase combinations as the correct one, since the others can be excluded based on arguments given above [116].
- **Model building:** A structural model is built and corresponding intensities are calculated. By comparison to the observed intensities, the model is then successively refined until convergence of model and observed intensities is achieved. However, this does not necessarily prove correctness of the model [112, 117].
- **Pattern recognition method:** Mesophases with a common phase boundary are often very similar in chemical composition. Therefore, both mesophases should possess very similar electron density histograms, since these do not depend on

the actual spatial distribution of lipid and water in the unit cell. If the structure of one mesophase has been solved, the crystallographic phases for reconstruction of the other mesophase can be chosen using close agreement of both electron density histograms as a criterion [113, 118].

- **Multiwavelength anomalous diffraction:** In the field of protein crystallography, this method is well-established and routinely applied. It has been demonstrated that it can be transferred to lipid mesophases using bromine-labeled lipids, where it allows to single out the distribution of the label atoms and determine the corresponding crystallographic phases [114, 119, 120]. However, the number of independent reflections sufficiently strong for further analysis in these studies was substantially lower than in our rhombohedral phase data. This could also be due to disorder caused by peptides. In addition, presence of heavy-atom labels in every lipid is highly unphysiological.⁸ In addition, for application of the MAD method, the use of synchrotron radiation for all measurements is mandatory, since the x-ray wavelength must be tunable.
- **Methyl trough search:** This method has been introduced for cubic phases containing infinite periodic minimal surfaces (IPMS) [44].
- **Swelling method:** The swelling method for lamellar phases as introduced already about 40 years ago is probably the most widely used phase retrieval method in membrane diffraction. As shown in [30, 51], it can be extended to the rhombohedral phase.

The swelling method is the method of choice used in this thesis. The underlying principles and its implementation are explained in detail both for the lamellar and the rhombohedral phase in sections 4.4.5 and 5.2. In case of the rhombohedral phase, we will use an additional criterion derived from direct methods of crystallography.

2.6 Resolution

After introduction of the basic principles required for reconstruction of the unit cell electron density of lipid mesophases, we briefly address the question for the obtainable resolution. In later chapters, the positions of electron density maxima indicative of lipid headgroup peaks will be used to define lipid bilayer and water layer thickness as well as stalk neck radii. Therefore, it is important to consider if observed small changes correctly reflect reality, or possibly are artifacts due to poor resolution. This section summarizes some considerations made by WHITE *et al.* [100, 121] and NAGLE *et al.* [47] for the case of bilayer stacks. They should apply to the stalk phase as well. In crystallography, resolution is usually defined as the lattice spacing corresponding to the largest measured wavevector transfer,

⁸ We briefly explored the possibility to use bromine-labeled cholesterol (synthesized and provided by P. SCHNEGGENBURGER), which strongly changed the phase behaviour when added to DOPC in a molar ratio of $X_{\text{Chol-Br}} = 0.3$

$$d_{\min} = \frac{2\pi}{q_{\max}}. \quad (2.39)$$

In case of diffraction on a lipid bilayer stack, where n_{\max} denotes the highest observed Bragg peak order corresponding to $q = n_{\max} \cdot 2\pi/d$, this *canonical* resolution [100] yields

$$d_{\min} = \frac{d}{n_{\max}}. \quad (2.40)$$

For the results presented in this thesis, $d \approx 40 - 55 \text{ \AA}$ and typically $n_{\max} = 8$ yield a canonical resolution of 5 to 7 \AA . This is considerably lower than in *e.g.* protein crystallography, where structures are currently often obtained with a resolution better than 1 \AA .

The reasons for this rather low resolution from lipid mesophases should be clarified. In a lipid mesophase, each unit cell contains a large number of noncovalently bound lipid and water molecules. These can diffuse at least along certain directions and display considerable disorder and thermal fluctuations. This makes lipid mesophases very different from what is usually understood as the crystalline state. Nevertheless, sharp Bragg peaks are observed in diffraction experiments. Therefore, it has been concluded that lipid mesophases are best described by “*convolution of a nearly perfect lattice with a highly disordered unit cell*” [100]. EDPs of lamellar phases have therefore been described by superposition of Gaussians representing several submolecular fragments such as lipid headgroups, water and terminal methyl groups, and the widths of these Gaussians characterize the degree of disorder.

As a general property of the Fourier transform, larger widths of Gaussian electron density distributions reduce the higher-order form factor amplitudes. Considering the following example given in [47], this becomes immediately apparent: For a hypothetical EDP composed of one pair of Gaussians placed symmetrically with respect to the origin,

$$\rho^{\text{model}}(z) = \frac{1}{2} [\delta(z - z_0) + \delta(z + z_0)] * \exp(-z^2/\sigma^2), \quad (2.41)$$

the form factor

$$F^{\text{model}}(q_z) = \cos(q_z z_0) \cdot \exp\left(-\left[\frac{q_z \sigma}{2}\right]^2\right), \quad (2.42)$$

decays more rapidly with q_z for broader distributions, *i.e.* larger σ . The rather low number of detectable reflections is a consequence of the inherent properties of lipid bilayers and not due to experimental shortcomings. In addition to disorder in the unit cell, long-range bilayer undulations can further reduce the number of observable reflections at or close to full hydration and change their lineshape [47]. However, in partially dehydrated conditions, this is a negligible effect [121]. Electron density reconstruction using all observable form factors therefore yields a correct and fully resolved representation of the true bilayer structure.

Fig. 2.8 serves to illustrate this by comparison of the gel and fluid L_α phases of two lipids. Samples were prepared and data measured under the same conditions. In case of the gel phase, the highest discernible order of diffraction in the measured interval is $n_{\max} = 14$ for gel-phase DPPC, but only $n_{\max} = 8$ for L_α -Phase DOPC. In the EDPs, which were reconstructed as described in chapter 4, the gel phase is indicated by a characteristic double peak in the lipid headgroup region [122, 123]. The widths of the headgroup peak and the methyl trough region around $z = 0$ are wider in case of the fluid phase, reflecting its more disordered structure.

From model calculations using Fourier synthesis of Gaussian distributions, WHITE and coworkers concluded that $\frac{d}{n_{\max}}$ is a measure for the $1/e$ half width σ of the Gaussian distributions of submolecular groups. According to their analysis, the positions of these groups can be determined with a “resolution precision” of up to 0.1 \AA in the fluid phase, which is substantially smaller than $d_{\min} = \frac{d}{n_{\max}}$ ([100, 121] and references therein).

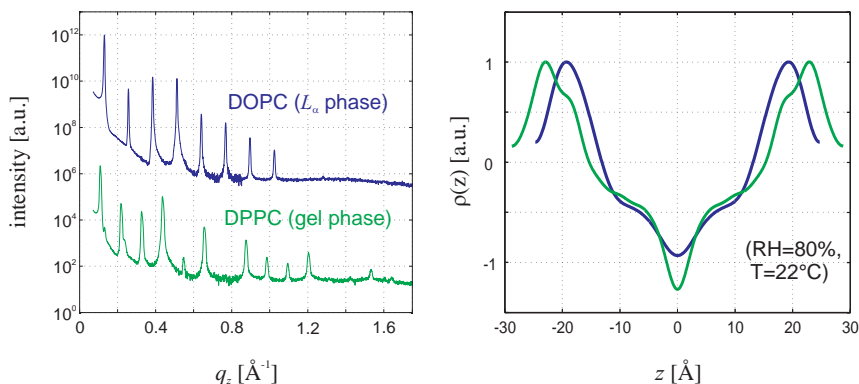


Figure 2.8: (left) X-ray reflectivity scans of a fluid phase (DOPC) and a gel phase (DPPC) sample displaying 8 or 14 Bragg peaks, respectively, reflecting the different degree of disorder in both phases. Experimental parameters are given in section 4.4.1. Curves are shifted vertically for clarity. (right) Corresponding EDPs $\rho(z)$ on arbitrary scale.

3 Lyotropic lipid polymorphism

As the first step towards structural analysis of stalks in model membrane systems, phospholipids and lipid mixtures which display the stalk phase must be identified. To this end, phase diagrams must be determined. Bringing lipid bilayers into close proximity is equivalent to removal of water from the interbilayer space. Therefore, a suitable experimental scheme for controlled dehydration is required. In membrane biophysics, this is achieved by the well-established osmotic stress method. After description of the basic concepts and the used experimental setup, the results of systematic studies on the phase behaviour of a series of lipids and lipid mixtures displaying the stalk phase are presented. In addition, as the first step towards electron density reconstruction, indexing of the observed diffraction patterns is described.

3.1 Hydration control by water vapour

In order to study phenomena which occur when two lipid bilayers are brought into close contact, the water layer separating them must be reduced in a controlled fashion. This is achieved by the osmotic stress method [124], which can be applied in different ways:

For rather mild dehydration of multilamellar liposomes or solid-supported membrane stacks in aqueous solution, polymers such as polyethylene glycol which are too bulky to enter the volume between adjacent bilayers are added [18, 125]. The gradient in polymer concentration leads to a removal of water from the interbilayer space and thus effectively reduces the water layer thickness d_w .

For considerably stronger dehydration as required in this thesis, solid-supported samples are placed in an atmosphere of controlled concentration of water molecules in the gas phase, *i.e.* partial pressure of water [124]. This has the great advantage that attenuation of the x-ray beam by bulk water is circumvented. Consider the situation sketched in Fig. 3.1 (*left*): A phospholipid bilayer stack is placed inside a closed cell. Saturation of the air with water vapour is assured by a reservoir of pure water. The vapour pressure p_1 inside the cell is the saturation vapour pressure p^* , whose variation with temperature is given by the Clausius-Clapeyron equation. The phospholipid system will take up as much water from the gas phase as required to minimize the repulsion between adjacent bilayers and swell up to the equilibrium distance d_w^* corresponding to excess water conditions (*cf.* Fig. 1.8).

By several methods, *e.g.* replacing the water reservoir by a saturated salt solution [126] or creation of temperature gradients, the amount of water molecules in the gas phase can be reduced, corresponding to a vapour pressure $p_2 < p^*$ (Fig. 3.1, *right*). The ratio p/p^* defines the relative humidity

$$RH = \frac{p}{p^*} \cdot 100\%, \quad (3.1)$$

which is used as the control parameter in our experiments. At $RH < 100\%$, one observes that the bilayer stack does not swell to d_w^* any longer. d_w typically decreases monotonously if RH is systematically reduced. This can be interpreted as an additional

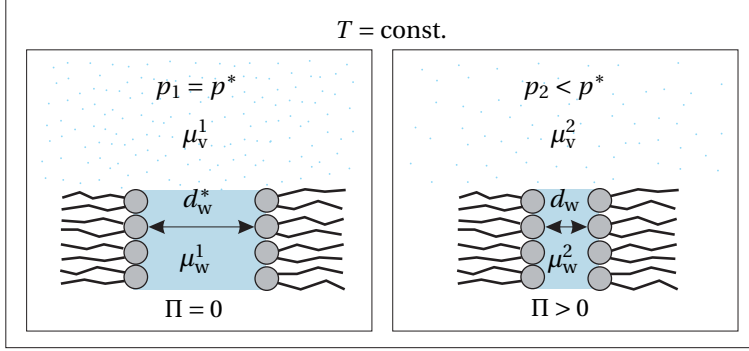


Figure 3.1: Sketch for derivation of the osmotic pressure Π corresponding to relative humidity $RH = p/p^*$. On the left, the vapour pressure p is the equilibrium vapour pressure p^* . The air is fully saturated with water, and the lipid bilayer stack can imbibe as much water as is required to minimize the interbilayer potential. On the right, the vapour pressure is reduced to $p < p^*$, the bilayer stack cannot swell to d_w^* anymore. This is interpreted as the osmotic pressure Π pushing lipid bilayers together.

attractive pressure, called the *osmotic pressure* Π , which pushes adjacent bilayers together. To quantify Π as a function of RH , one uses the condition that the chemical potential of water in both phases must be identical in thermal equilibrium, $\mu_v = \mu_w$ [127]. For the situation sketched in Fig. 3.1, this implies

$$\mu_v^2 - \mu_v^1 = \mu_w^2 - \mu_w^1. \quad (3.2)$$

From the Maxwell relations of thermodynamics, it follows that

$$\left(\frac{\partial \mu}{\partial p}\right)_T = v(p, T), \quad (3.3)$$

where v denotes the partial volume of water. If the vapour phase is treated as an ideal gas, one obtains

$$\mu_v^2 - \mu_v^1 = k_B T \int_{p^*}^p \frac{1}{p} dp = k_B T \ln\left(\frac{p}{p^*}\right). \quad (3.4)$$

In the aqueous phase, the partial volume of water is assumed to be constant. A mass density of $1 \text{ g} \cdot \text{cm}^{-3}$ yields $v_w = 29.97 \text{ \AA}^3$. The corresponding pressure difference obtained by integration $\int v_w dp$ is defined as the osmotic pressure Π :

$$\mu_v^2 - \mu_v^1 = \Pi \cdot v_w. \quad (3.5)$$

Combining the above equations, the osmotic pressure Π at relative humidity RH is

$$\Pi = -\frac{k_B T}{v_w} \ln\left(\frac{RH}{100\%}\right). \quad (3.6)$$

Following the conventions used in section 1.4, the minus sign indicates that Π reduces the interbilayer distance. For $RH = 100\%$, $\Pi = 0$. This situation is equivalent to a sample fully immersed in water, since, by definition, the chemical potential in the vapour phase at p^* is the same as in bulk water. Importantly, it should be pointed out that full hydration by water vapour is experimentally difficult to achieve due to long equilibration times and presence of temperature gradients [124], but can be achieved with specifically designed environmental chambers [128]. In addition, commercial RH sensors often fail to give reliable results at RH very close to 100%.

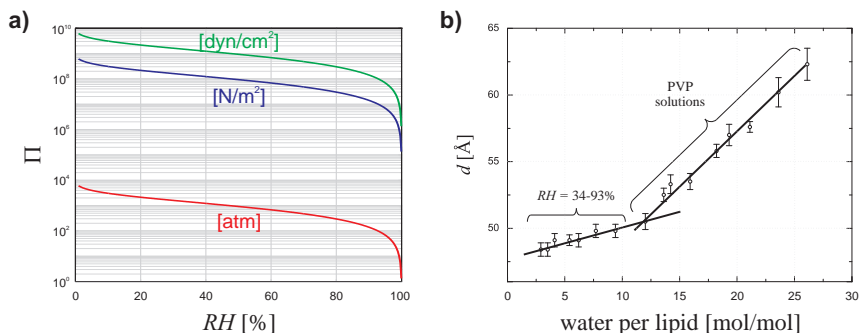


Figure 3.2: (a) Osmotic pressure Π calculated by Eq. (3.6) in different units. (b) Lattice constant d of a DOPC bilayer stack as a function of the number of water molecules per lipid molecule. Redrawn from data given by HRISTOVA *et al.* [121]. Solid black lines are shown as guides to the eye. The break in the curve at about 12 waters per lipid has been attributed to completion of the hydration shell of the PC headgroups ([121] and references therein).

The experiments in this work were carried out at $RH \leq 95\%$, which already corresponds to quite strong dehydration. Fig. 3.2(b) shows some literature data for dehydration of DOPC, the standard lipid used in this thesis. Importantly, the relation of RH and water molecules per lipid is highly nonlinear. As noted in [124], $RH = 99\%$ already leads to removal of almost half the water from a fully hydrated bilayer stack.

3.2 Experimental

3.2.1 Sample preparation

Solid-supported, oriented lipid bilayer stacks were prepared by deposition from organic solution based on the protocol introduced by Seul and Sammon [129] and used in all experiments described in this thesis. Polished silicon wafers cut to substrates of $15 \times 10 \text{ mm}^2$ and $25 \times 15 \text{ mm}^2$ were purchased from Silchem (Freiberg, Germany). The lipids in Tab. 3.1 were purchased as lyophilized powders from Avanti Polar Lipids (Alabaster, AL, USA) and used as delivered. The substrates were thoroughly cleaned by repeated washing cycles with methanol and deionized water in an ultrasonic bath, dried in a nitrogen stream, rendered hydrophilic in a plasma cleaner (Harrick PDC-002) and placed on a horizontally aligned table. Lipid stock solutions were prepared

in chloroform/(2,2,2)-trifluoroethanol (1:1 vol:vol) with a concentration of 10 mg/ml. DOPC/PIP₂ samples were prepared by S. K. GHOSH and a mixture of chloroform, methanol and water (20:9:1 vol:vol:vol) was used. For lipid mixtures with a molar fraction X of DOPE, Chol or PIP₂, a volume V was obtained by combination of two volumes

$$V_2 = V \left[1 + \frac{1-X}{X} \cdot \frac{c_2}{c_1} \right]^{-1} \quad \text{and} \quad V_1 = V - V_2, \quad (3.7)$$

where $c_{1,2}$ denote the molar concentrations of the stock solutions. The index 1 is used for DOPC and 2 for the other component, respectively. These two volumes were pipetted into one glass vial and thoroughly vortexed. 200 μ l solution per sample were pipetted uniformly onto the 25 \times 15 mm² substrates used for phase diagram determination and reflectivity scans. For synchrotron measurements and DOPC/PIP₂ phase diagram determination, 15 \times 10 mm² substrates and 80 μ l lipid solution per sample were used. After few hours, the bulk solvent had evaporated and the lipids formed a stable thin film. Residual solvent was extracted by storage in vacuum (< 1 mbar) for at least 12 h. For an area per lipid headgroup of about 70 \AA^2 [68], the number of bilayers in a stack is estimated to be about 1400 for both substrate sizes. Between sample preparation and experiments, samples were stored at 7 $^\circ$ C.

lipid	abbreviation	M [g \cdot mol ⁻¹]	T_m [$^\circ$ C]
di-14:1(Δ 9- <i>cis</i>)-phosphatidylcholine	–	673.5	–
di-16:1(Δ 9- <i>cis</i>)-phosphatidylcholine	–	729.5	–
di-18:1(Δ 9- <i>cis</i>)-phosphatidylcholine	DOPC	785.6	-18.3 ± 3.6
di-20:1(Δ 11- <i>cis</i>)-phosphatidylcholine	–	841.7	-4.3
di-22:1(Δ 13- <i>cis</i>)-phosphatidylcholine	–	897.7	$+12.1 \pm 1.6$
di-24:1(Δ 15- <i>cis</i>)-phosphatidylcholine	–	953.8	$+25.9 \pm 2.5$
di-16:0[CH ₃] ₄ -phosphatidylcholine	DPhPC	845.7	–
di-18:1(Δ 9- <i>cis</i>)-phosphatidylethanolamine	DOPE	743.5	-6.0
Phosphatidylinositol-4,5-bisphosphate	PIP ₂	1098.2	–
cholesterol	Chol	386.5	no bilayers

Table 3.1: Used lipids, common abbreviations and main transition temperatures T_m at full hydration available from the literature [130, 131].

3.2.2 Sample environment

Fig. 3.3(a) shows a schematic of the setup used for relative humidity control in all measurements reported in this thesis. The setup was constructed by T. REUSCH, a detailed description is given in his diploma thesis [132]. In addition, it has been described previously in [31]. In brief, a constant stream of dry nitrogen is divided into two fractions, whose flow rates are determined by two mass flow controllers (MKS Instruments, Munich, Germany). One fraction is hydrated with water vapour, while the other one remains dry. Recombining both fractions yields a stream of nitrogen with RH between ~ 10 and typically up to $\sim 98\%$. RH and T inside the sample chamber are measured by a combined relative humidity/temperature sensor (Driesen+Kern, Bad Bramstedt, Germany) in the vicinity (≈ 1 cm) of the sample. This sensor and the mass

flow controllers are interfaced *via* serial ports with the diffractometer control software SPEC. By PID (proportional-integral-derivative) control, *RH* setpoints in the interval of $\sim 10 - 98\%$ can be reached and remain stable to within $\pm 0.1\%$ (Fig. 3.3b). This enables to run long, fully automated scan macros with *RH* as a parameter.

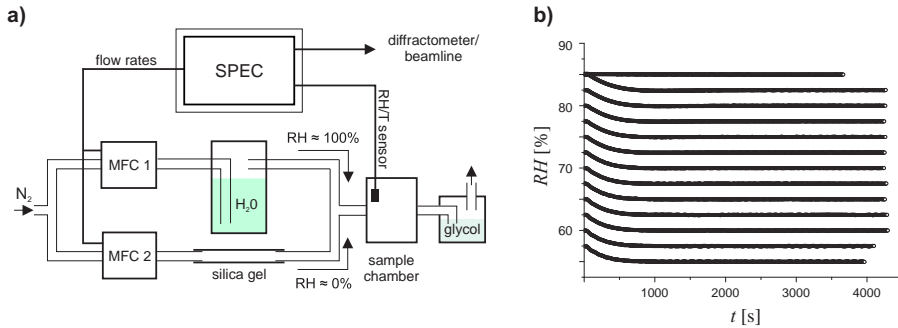


Figure 3.3: (a) Sketch of the setup used for relative humidity (*RH*) control. Figure taken from AEFNER *et al.* [31] and used with kind permission from Springer. (b) Plot of the *RH* logfile of a swelling experiment. Each requested setpoint in *RH* is reached after approximately 10 minutes and subsequently maintained constant to within $\approx 0.1\%$ for one hour. This stability was essential during all experiments.

Sample chamber and water reservoir for hydration of the nitrogen can be heated or cooled by flows of water/glycol mixtures from temperature-controlled reservoirs (Julabo, not shown in Fig. 3.3). All experiments presented in this thesis were performed at room temperature, $T \approx (22.5 \pm 1)^\circ\text{C}$. At fixed *RH*, a temperature change of 2°C results in a relative change $\Delta\Pi/\Pi$ below 1%. This is considerably smaller than a change resulting from varying *RH* about 1%. Based on this estimation, effects of small temperature changes were neglected [31]. Reaching high *RH* setpoints was sometimes facilitated by heating the water reservoir, heating the pipings conducting the water vapour to the sample chamber through a heating wire wrapped around them, and by gently cooling the sample chamber. The used humidity sensors were calibrated and controlled on a regular basis by saturated salt solutions using tabulated values [133, 134, 135] (Fig. 3.4).

3.2.3 In-house small-angle x-ray scattering setup

$2d$ diffraction patterns in GXD geometry were recorded by a home-built diffractometer described previously in [126, 132]. Cu- K_α radiation ($E = 8.048\text{keV}$, $\lambda = 1.54055\text{\AA}$) is generated by a sealed tube (Seifert FK61, $P = 35\text{kV} \times 50\text{mA}$) and parallelized and monochromatized by a Goebel mirror (Xenocs Fox 2D Cu 12INF). Two pinholes of 1 mm in diameter determine the primary beam profile. For different alignments, the obtained primary intensity was between $0.6 - 1.8 \cdot 10^8$ photons/s measured at the sample position by a PIN diode (Forvis Technologies). The sample can be translated and rotated by Huber stages. Diffraction patterns were recorded by a xenon-filled multiwire proportional counter (HiStar, Bruker) with an active area of 11.5 cm in diameter and an effective pixel size of $105 \times 105 \mu\text{m}^2$. The distance D between sample and detector

salt	RH [%]
LiCl	11.3
MgCl ₂	32.9
NaBr	57.7
NaCl	75.3
(NH ₄) ₂ SO ₄	80.3
KCl	84.4
BaCl ₂	90.2
K ₂ SO ₄	97.1

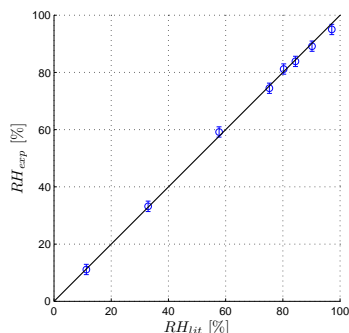


Figure 3.4: Literature values used for calibration of the RH sensors [133, 134, 135] (left) and example of a calibration curve (right). Errorbars of $\pm 1.8\%$ indicate the uncertainty in RH given by the manufacturer.

was determined using silver behenate powder as a calibration standard, which yielded D between 30 and 35 cm for different series of measurements. The primary beam is blocked by a beam stop mounted directly in front of the detector. The detector region around the first in-plane reflection and the primary beam was additionally covered by a strip of Al or Pb. Prior to each series of measurements, the detector bias voltage was checked and correction tables for detector sensitivity and spatial distortion were recorded as described in the detector manual. To this end, a weakly radioactive ^{55}Fe sample mimicking a point source was placed at the sample position. A cylinder with Kapton windows was mounted in front of the detector and evacuated to minimize scattering and absorption effects by air. Automatic attenuators were used to avoid damage to the detector. The instrument is controlled by the software SPEC (Certified Scientific Software). The beam of a weak He-Ne laser ($\lambda = 632.8\text{ nm}$) can be deflected into the path of the x-ray beam by a mirror such that both beams are collinear. This facilitates alignment of beamstop, pinholes and samples.

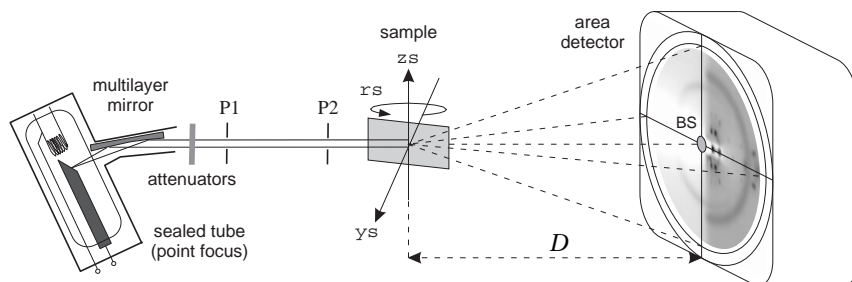


Figure 3.5: Sketch of the instrument used for phase diagram determination by grazing-incidence x-ray diffraction. The sample chamber and a vacuum cylinder placed between sample and detector are not shown for clarity.

3.2.4 Phase diagram determination

Samples were placed inside the sample chamber mounted on the goniometer. The sample chamber was connected to the setup for relative humidity control. The angle of incidence α_i was aligned by motor rs. During this step, careful use of attenuators is essential to avoid damage to the detector, which may occur if α_i accidentally fulfills the Bragg condition for the first Bragg peak. α_i was chosen such that the specular beam reflected from the substrate was located in between primary beam position and first Bragg sheet. If α_i is too large, reflections with small q_z component are absorbed by the substrate and phase identification is impeded. The counting time for images allowing proper phase identification was typically 10 to 20 minutes. Improving the signal-to-noise ratio by a factor of 2 requires a four-fold increase in counting time due to Poissonian statistics. After sample alignment, diffraction patterns in a chosen RH interval were recorded in a fully automatic fashion using the SPEC command `humidity_scan` developed by T. REUSCH [132].

In regard to possible effects of thermal history of the samples, two different protocols used for phase diagram determination must be distinguished: In the earliest experiments using DOPC/Chol and DPhPC/Chol mixtures published in [31], samples from the fridge were heated several times to 50°C for few hours in a saturated water vapour atmosphere and cooled down to room temperature again prior to the measurements. During phase diagram determination, RH was increased from low to high values (protocol 1). In later experiments, samples from the fridge were equilibrated in saturated water vapour at room temperature for few hours and subsequently in the sample chamber at high RH (e.g. $RH = 90\%$) for about one hour. Phase diagrams were recorded by successively lowering RH in steps of $\Delta RH = 2\%$ (protocol 2).

3.3 Results

In the following, the results of extended measurements at our in-house small-angle x-ray scattering instrument are presented. After a general description of the observed characteristic diffraction patterns, the results on lyotropic phospholipid phase behavior of single-component samples and binary lipid mixtures are summarized in several phase diagrams. Subsequently, indexing of the diffraction patterns, which is the first step towards electron density reconstruction, is described.

3.3.1 Characteristic diffraction patterns

Fig. 3.6 shows five distinct diffraction patterns observed during phase diagram determination. In the right column, closeups of the small-angle region are given. The broad ring is due to the Kapton windows of the sample chamber and flight tube. The specularly reflected beam (SB) and the first Bragg sheet were attenuated to avoid overexposure of the detector.

A lamellar phase L is indicated by a single series of equidistant diffuse Bragg sheets and absence of out-of-plane reflections. This phase was observed for most samples at the highest RH values used. Due to long-range order in only one dimension, a single

Miller index h is sufficient for indexing of the reflections. All form factors $\{F(\vec{q}_h)\}$ can be measured by X-ray reflectivity scans (*cf.* chapter 4).

At lower RH , several nonlamellar phases can be distinguished. Upon dehydration, a phase transition from the lamellar phase L to the rhombohedral phase R was observed in most samples reported here. In DOPC/Chol and DOPC/DOPE mixtures, the rhombohedral phase transformed to the distorted inverted hexagonal phase $H_{II\delta}$ upon further dehydration for a range of lipid compositions. At the first glance, the R and $H_{II\delta}$ phase patterns look quite similar and are sometimes difficult to distinguish, especially if only few strong peaks are visible. Moreover, in a certain RH range in the phase diagrams, these two phases were found in coexistence. For comparison, reciprocal space maps of both phases, *i.e.* transforms of the raw diffraction patterns to reciprocal space $(q_{||}, q_z)$, recorded at a synchrotron are shown in Fig. 3.7. Appearance of the $\{113\}$ peak indicated in Fig. 3.6 was used as a criterion for the R phase. In case of $H_{II\delta}$, peak positions in $q_{||}$ are equidistant, and the $\{113\}$ peak is absent. Finally, at low hydration, diffraction patterns characteristic for the inverted hexagonal phase sketched in Fig. 1.2 were observed.

The diffraction pattern C has, to our knowledge, not been reported before. It was observed in DOPC/Chol samples at $X_{\text{Chol}} > 0.3$ following the first protocol given in section 3.2.4. Indexing of the rhombohedral phase, the diffraction pattern C and an additional tetragonal phase only observed during a synchrotron measurement is described in section 3.3.3 in detail. For the H_{II} and $H_{II\delta}$ phases, we refer to *e.g.* [119, 136].

3.3.2 Phase diagrams

Fig. 3.9 to 3.13 show the obtained partial phase diagrams. Dashed lines are shown as guides to the eye. The figure captions contain further information on the number of measurements and the protocol used for thermal equilibration of the samples.

In case of DOPC and DPhPC, the existence of the rhombohedral phase was known from the literature [30, 51, 137]. We observed the R phase also in other di-monounsaturated lipids with different chain lengths structurally similar to DOPC (Fig. 3.9). Of these lipids, DOPC requires the least osmotic pressure to arrange into the R phase. Interestingly, this correlates very well with the areas per lipid headgroup (at full hydration) given by KUCERKA *et al.* [138]. We will expand on this point at the end of chapter 4. The lipid di24:1PC is in the gel phase at room temperature and full hydration (Tab. 3.1), which could explain the absence of the R phase. Since the main phase transition of several lipids is known to increase upon dehydration [130], the same could also apply to di22:1PC.

The phase behaviour of lipid mixtures is more complex. Focusing on stalk formation, the main effect upon addition of DOPE, Chol and PIP₂ is a shift of the L/R phase boundary to higher RH values. For DOPE, this has been reported before [137]. Following continuum theory, this could be due to either effects of bending and lipid packing, effects on bilayer interaction, or a combination of these. In the following chapters, both possibilities are further explored using structural data of the lamellar and rhombohedral phases. In addition, H_{II} and $H_{II\delta}$ phases appear at elevated Chol or DOPE

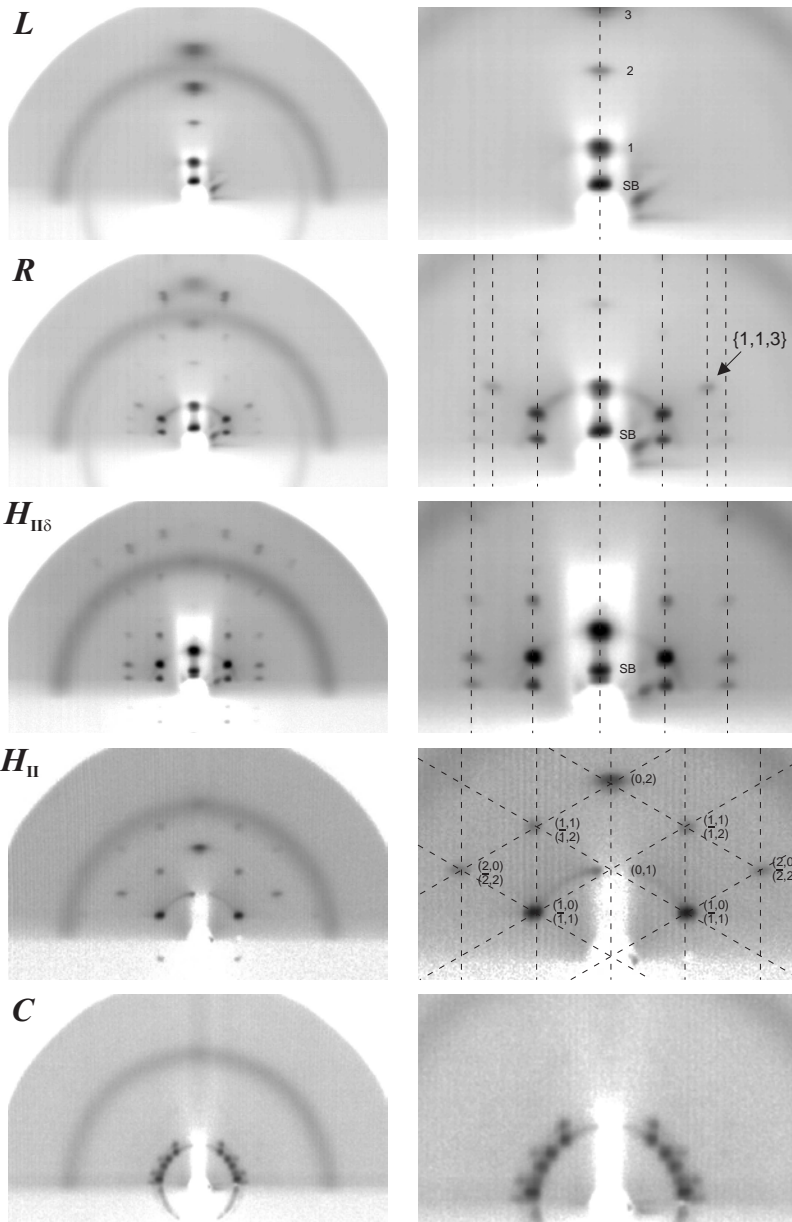


Figure 3.6: Characteristic diffraction patterns. Miller indices are shown for the lamellar (L) and inverted hexagonal (H_{II}) phases. Indexing of the rhombohedral phase (R) and the pattern termed C , which is most likely a cubic phase of symmetry $Ia\bar{3}d$, are described below. A semitransparent Al strip was used to attenuate the specular reflection and the first Bragg sheet in the three upper rows. In case of the two last rows, a Pb absorber was used.

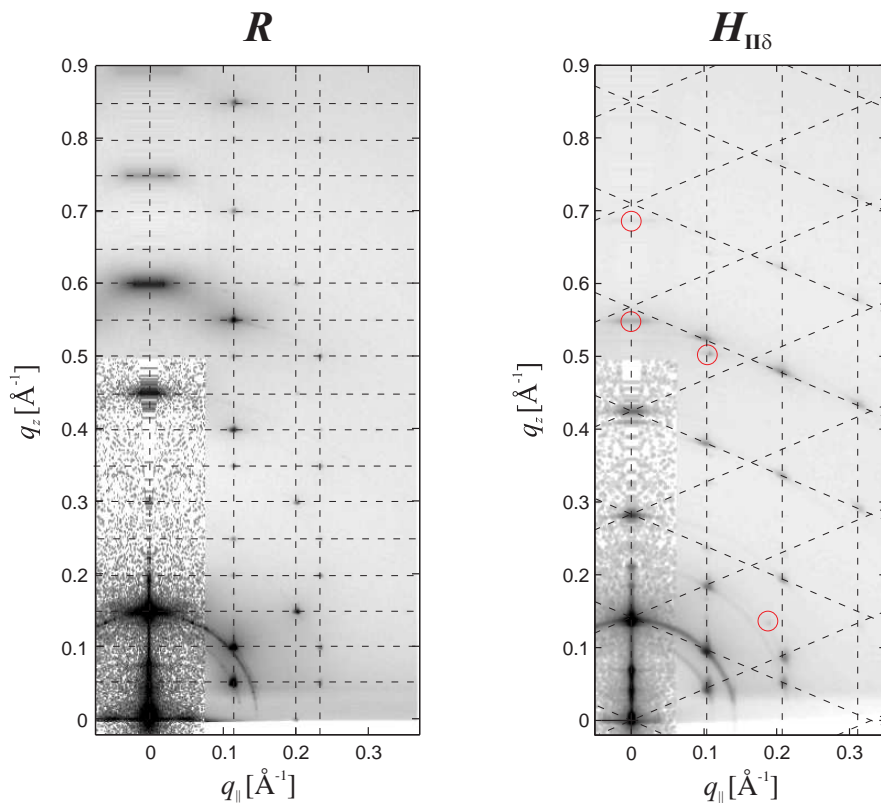


Figure 3.7: Comparison of the reciprocal lattices of the R phase (di16:1PC, $RH = 18\%$) and $H_{II\delta}$ phase (DOPC/Chol 7:3, $RH = 40\%$). Data were recorded at the Swiss Light Source and processed as described in chapter 5. Red circles in the $H_{II\delta}$ pattern indicate some residual R phase peaks.

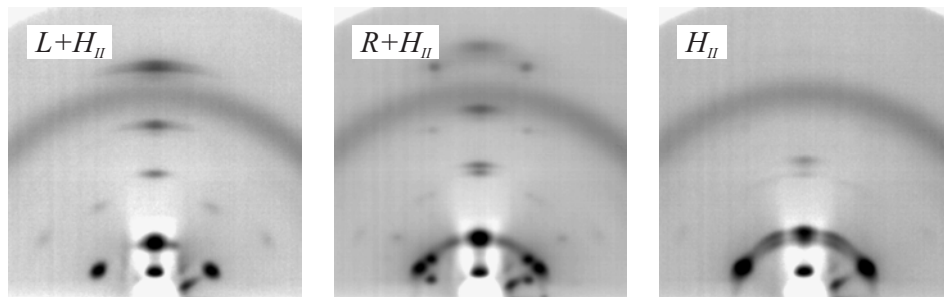


Figure 3.8: Diffraction patterns of DOPC/PIP₂ samples: $L + H_{II}$ phase coexistence (6 mol% PIP₂, $RH = 70\%$) R/H_{II} phase coexistence (4 mol% PIP₂, $RH = 40\%$) and H_{II} phase (10 mol% PIP₂, $RH = 10\%$).

content at low hydrations, while these phases are absent in pure DOPC in the applied RH range.

Given the rather low molar fractions of PIP₂, the effect of this lipid is particularly strong. Apart from a shift of the L/R phase boundary, the observation of additional peaks indicative of a H_{II} phase appearing at $X_{PIP_2} > 4\%$ is striking, since pure DOPC alone does not form the inverted hexagonal phase at all and considerable fractions of DOPE or Chol are required to induce a similar effect. Representative diffraction patterns of DOPC/PIP₂ mixtures are shown in Fig. 3.8. In case of R/H_{II} coexistence, the H_{II} reflections become more pronounced for low RH .

In this respect, DOPC/PIP₂ mixtures are similar to DPhPC/Chol mixtures at $X_{Chol} \geq 15\%$, which display the same phase sequence $H_{II} \rightarrow R \rightarrow H_{II}$ in the RH interval between 80 and 90%. A similar re-entrant phase behavior $H_{II} \rightarrow L \rightarrow H_{II}$ has been observed for DOPE and quantitatively explained by the balance of hydration and bending energies [139, 140].

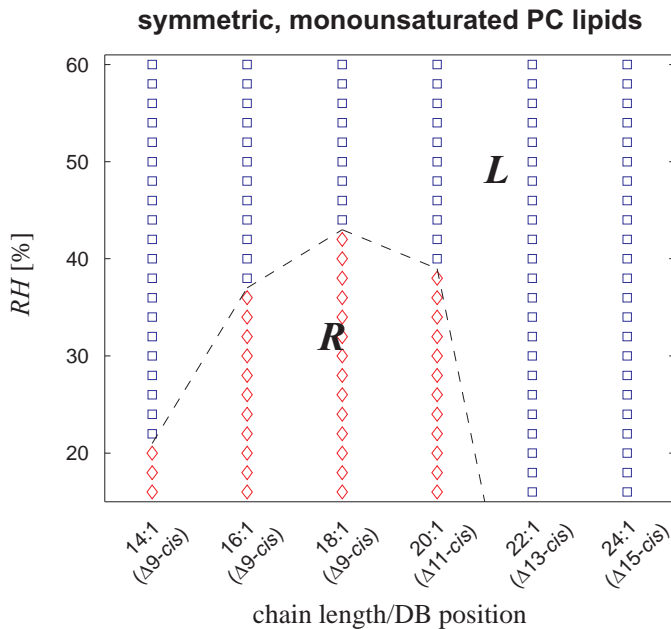


Figure 3.9: Lyotropic phase diagram of different monounsaturated lipids recorded at room temperature (protocol 2). Several lipids which are in the fluid L_{α} phase at room temperature and full hydration (Tab. 3.1) display the R phase upon dehydration. Least osmotic pressure is required to induce the R phase in DOPC.

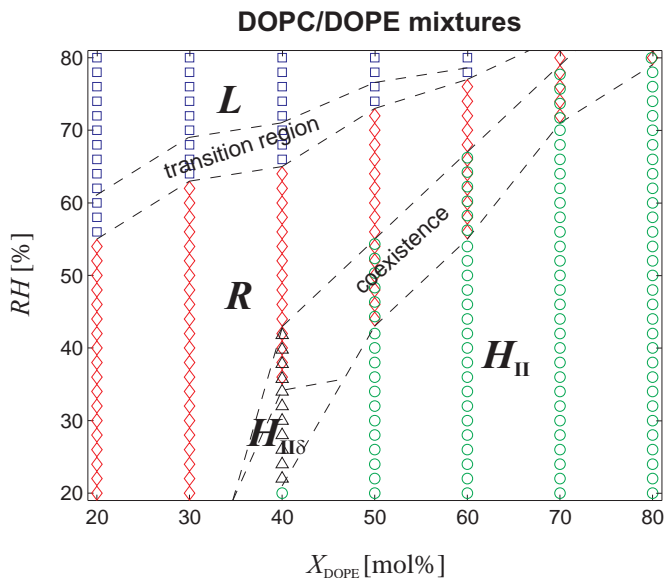


Figure 3.10: Lyotropic phase diagram of DOPC/DOPE mixtures at room temperature (protocol 2). This lipid mixture has been investigated previously [137], our results are in good agreement.

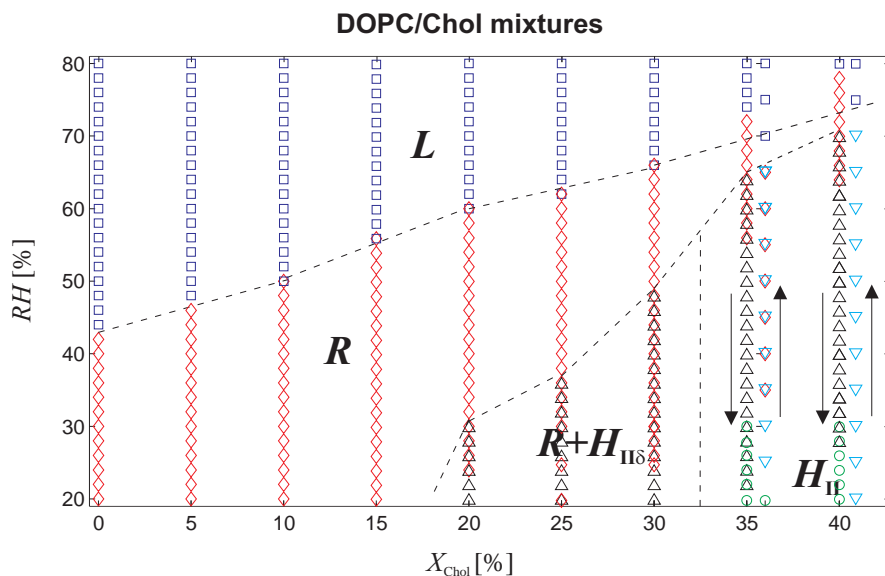


Figure 3.11: Lyotropic phase diagram of DOPC/Chol mixtures at room temperature based two series of measurements following protocols 1 and 2. In case of protocol 1, the pattern C (∇) was observed for high Chol content.

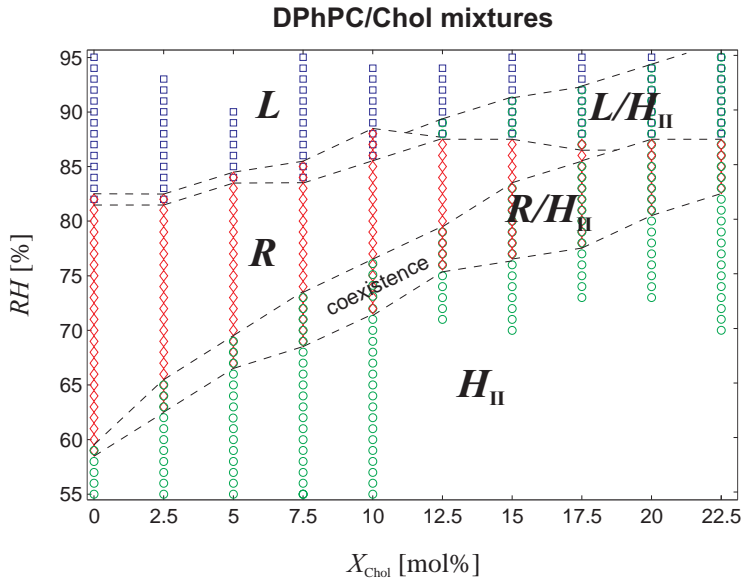


Figure 3.12: Lyotropic phase diagram of DPhPC/Chol mixtures at room temperature (protocol 1). At elevated Chol content, the R phase disappeared.

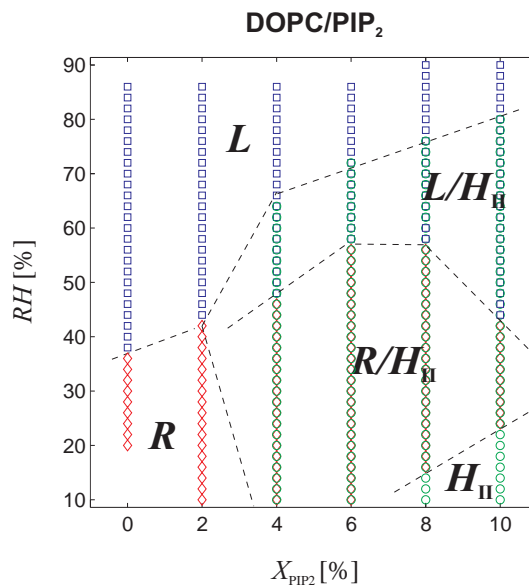


Figure 3.13: Lyotropic phase diagram of DOPC/PIP₂ mixtures at room temperature based two series of measurements following protocol 2. Data were recorded together with S. K. GHOSH [35].

3.3.3 Indexing of Diffraction patterns

All $3d$ crystalline structures can be classified into 7 crystal systems and 14 Bravais lattices shown in Fig. 3.14. The unit cell is spanned by three linearly independent vectors characterized by up to six lattice parameters a, b, c and α, β, γ . Corresponding reciprocal lattice vectors \vec{q}_{hkl} follow from Eq. (2.9). \vec{e}_z is perpendicular to the substrate surface. Due to the $2d$ powder character of the samples, the Bragg peak positions in the (q_{\parallel}, q_z) -plane are determined by

$$q_{\parallel} = \sqrt{(\vec{e}_x \cdot \vec{q}_{hkl})^2 + (\vec{e}_y \cdot \vec{q}_{hkl})^2}, \quad (3.8)$$

$$q_z = \vec{e}_z \cdot \vec{q}_{hkl}. \quad (3.9)$$

Rhombohedral phase

From the literature, it is known that the pattern R corresponds to the rhombohedral phase [30]. Here, it is briefly explained how this can be seen: The rhombohedral phase is observed upon dehydration of the lamellar phase, the series of equidistant Bragg sheets along the q_z axis is preserved. Therefore, one basis vector is chosen parallel to \vec{e}_z . Diffraction peaks are located in several columns of approximately constant q_{\parallel} with ratios of approximately $0:1:\sqrt{3}:2$. By calculating the diffraction patterns of $2d$ powders of the seven crystal systems with the unique axis perpendicular to the substrate, it turns out that a hexagonal lattice with basis vectors

$$\vec{a}_H = a(1, 0, 0)^T, \quad \vec{b}_H = a\left(-\frac{1}{2}, \frac{\sqrt{3}}{2}, 0\right)^T, \quad \vec{c}_H = c(0, 0, 1)^T. \quad (3.10)$$

and the resulting reciprocal lattice vectors

$$\Rightarrow \vec{a}_H^* = \frac{4\pi}{\sqrt{3}a} \left(\frac{\sqrt{3}}{2}, \frac{1}{2}, 0\right)^T, \quad \vec{b}_H^* = \frac{4\pi}{\sqrt{3}a} (0, 1, 0)^T, \quad \vec{c}_H^* = \frac{2\pi}{c} (0, 0, 1)^T \quad (3.11)$$

leads to the experimentally observed peak distribution (Fig. 3.15, *top*). The corresponding momentum transfer components parallel and perpendicular to the substrate are

$$q_{\parallel}^{(hk)} = \underbrace{\sqrt{h^2 + hk + k^2}}_{=0,1,\sqrt{3},2,\sqrt{7},3,\dots} \cdot \frac{4\pi}{\sqrt{3}a}, \quad q_z^{(\ell)} = \ell \cdot \frac{2\pi}{c}. \quad (3.12)$$

However, diffraction peaks which do not fulfil the reflection condition

$$-h + k + \ell = 3n, \quad n \in \mathbb{Z} \quad (3.13)$$

are systematically absent in this parameterization. This occurs if, in addition to the basis vectors, additional translational symmetries exist. Tables of reflection conditions and corresponding symmetry elements can be found in crystallography text-

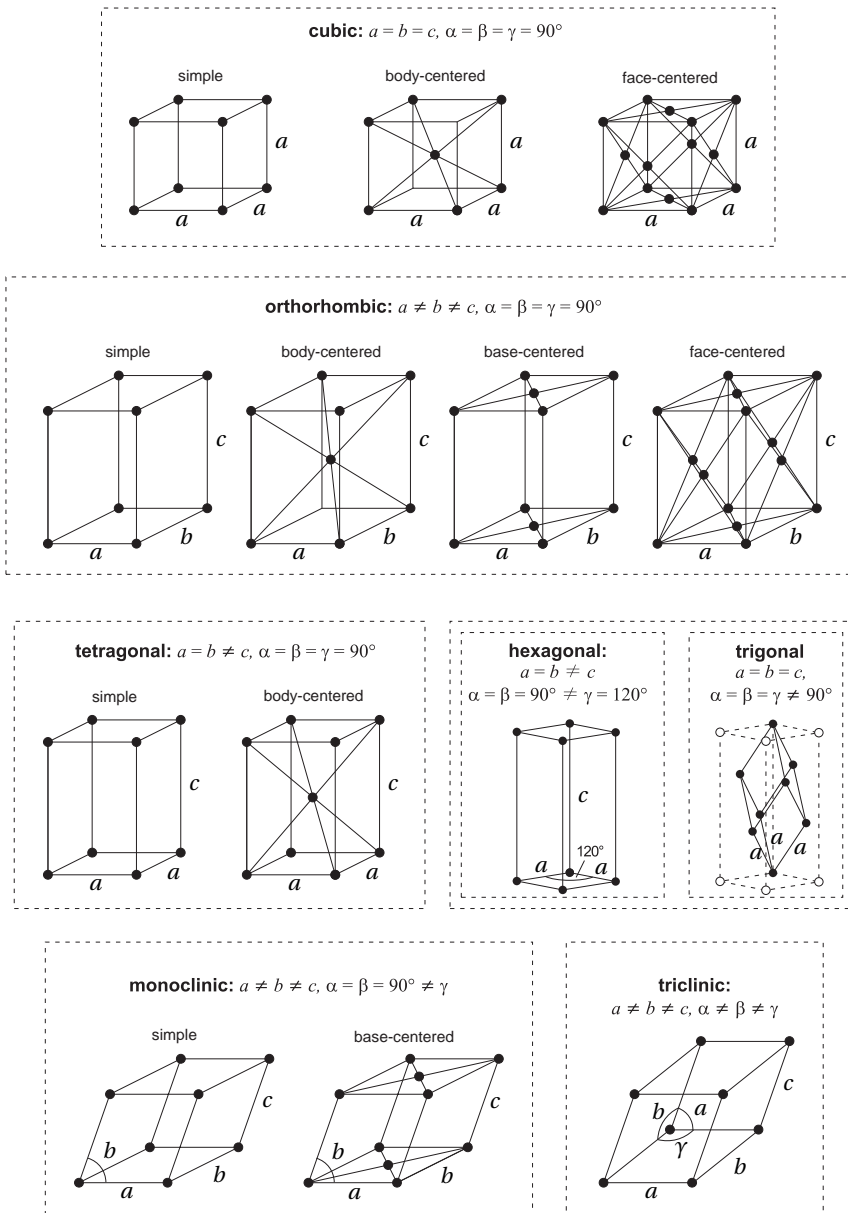


Figure 3.14: Seven crystal systems and corresponding fourteen Bravais lattices in 3d. The hexagonal and trigonal systems are sometimes combined, since also the trigonal system can be described by a non-primitive hexagonal unit cell [141].

books [141]. In the present case, Eq. (3.13) indicates rhombohedral symmetry. Alternatively, the rhombohedral unit cell of the trigonal crystal system can be used (Fig. 3.15, *center*):

$$\vec{a}_R = (b, 0, d)^T, \quad \vec{b}_R = \left(-\frac{b}{2}, \frac{\sqrt{3}b}{2}, d\right)^T, \quad \vec{c}_R = \left(-\frac{b}{2}, -\frac{\sqrt{3}b}{2}, d\right)^T, \quad (3.14)$$

where $b = a/\sqrt{3}$ and $d = c/3$. This parameterization yields only the observed peak positions. In some textbooks trigonal is treated as a subset of hexagonal [141]. The systematic absences can be understood as follows: Consider a crystal of identical atoms with form factor f arranged on a rhombohedral lattice. Translation of the crystal by one of the rhombohedral basis vectors is a symmetry operation. If one uses hexagonal coordinates instead, each unit cell contains three identical atoms placed at

$$\vec{r}_1 = (0, 0, 0)^T, \quad \vec{r}_2 = \left(0, \frac{a}{\sqrt{3}}, d\right)^T, \quad \vec{r}_3 = \left(\frac{a}{2}, \frac{a}{2\sqrt{3}}, 2d\right)^T. \quad (3.15)$$

The unit cell form factor is then given by the sum

$$F(\vec{q}) = \sum_{j=1}^3 f_j(\vec{q}) \exp(i\vec{q}_{hk\ell} \cdot \vec{r}_j) \quad (3.16)$$

$$= f \left[1 + \exp\left(\frac{2\pi}{3} [2h + k + \ell]\right) + \exp\left(\frac{2\pi}{3} [h + 2k + 2\ell]\right) \right], \quad (3.17)$$

which yields the above reflection condition [142]. The hexagonal unit cell as defined by Eq. (3.10) is a non-primitive one which contains 3 lattice points (full circles) and does not reflect the full symmetry of the lattice.

As a third alternative, by choosing a different parallelepiped with $\gamma = 120^\circ$ as the unit cell, hexagonal ABC stacking coordinates can be used [143] (Fig. 3.15, *bottom*):

$$\vec{a}_{ABC} = a(1, 0, 0)^T, \quad \vec{b}_{ABC} = a\left(-\frac{1}{2}, \frac{\sqrt{3}}{2}, 0\right)^T, \quad \vec{c}_{ABC} = \left(\frac{a}{2}, \frac{a}{2\sqrt{3}}, d\right)^T. \quad (3.18)$$

All three parameterizations are equivalent and lead, if applied consistently, to the same electron density distribution. Following [51], hexagonal indices are used for electron reconstruction in chapter 5. The corresponding basis vectors of the lattices in real and reciprocal space are pairwise orthogonal. The lateral momentum transfer component q_{\parallel} depends only on h, k and the normal component q_z only on ℓ . This is used further below for the swelling method for the R phase (*cf.* section 5.2).

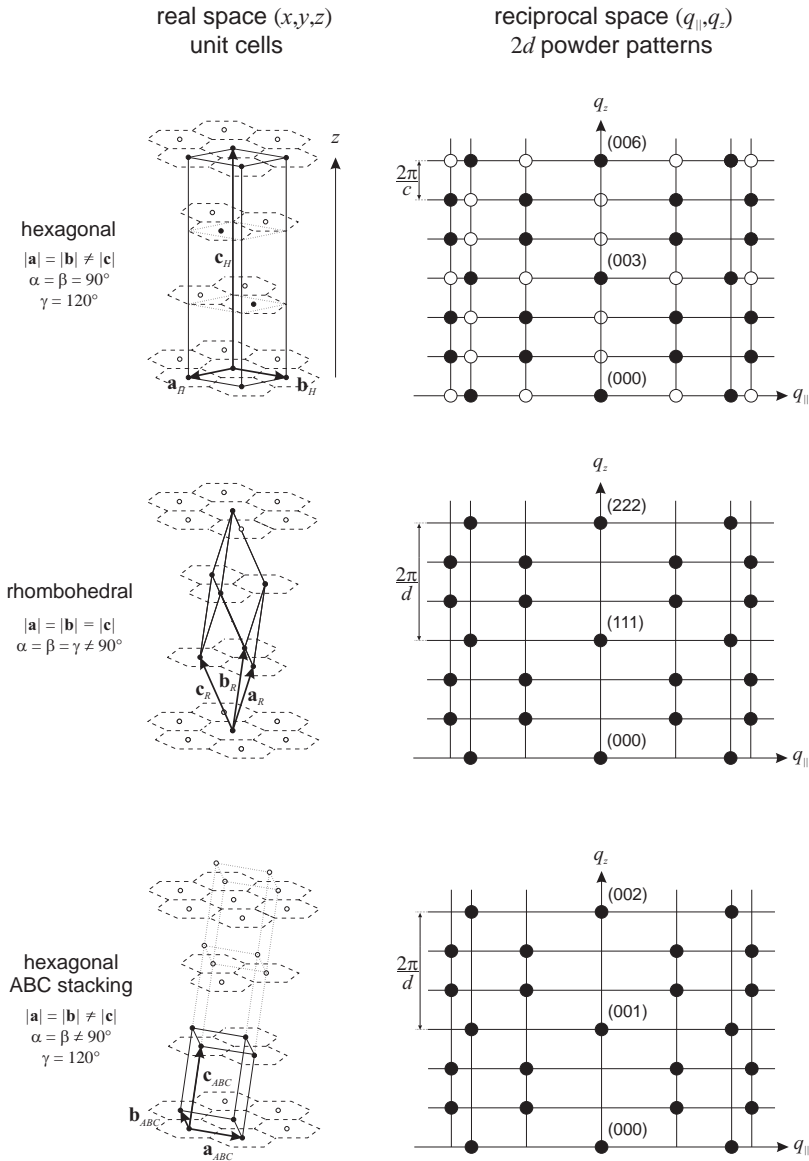


Figure 3.15: Different unit cells compatible with the diffraction pattern of the R phase (left) and corresponding $2d$ powder patterns (right). For the nonprimitive hexagonal unit cell, reflections which do not fulfil Eq. (3.13) are indicated by empty circles. Due to space limitations, Miller indices (hkl) are only shown for reflections where $q_{\parallel} = 0$. A fully indexed pattern of the R phase is shown in Fig. 3.16.

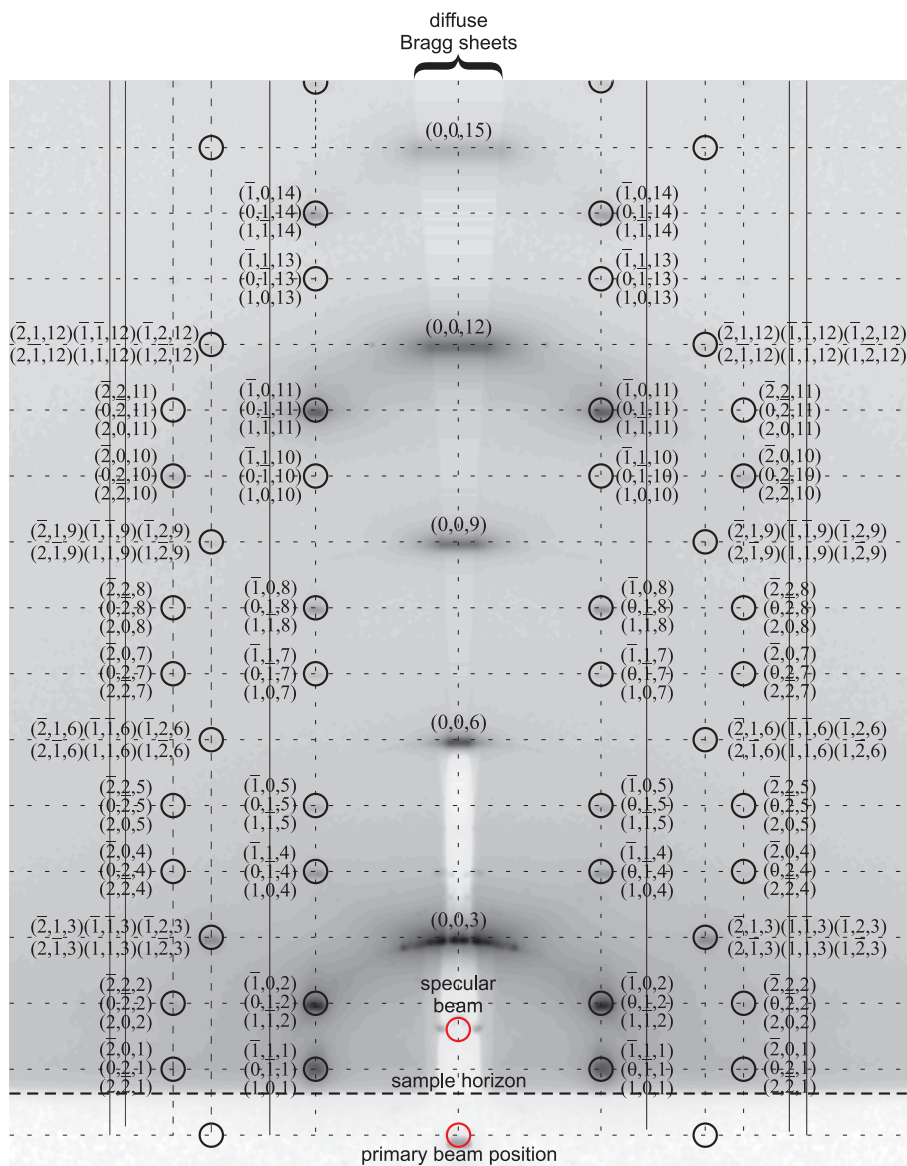


Figure 3.16: Superposition of the theoretical diffraction peak positions (empty black circles) and part of an actual diffraction pattern of the rhombohedral phase (DOPC/Chol 70:30, RH = 60%, ID01, after corrections). The angle of incidence α_i is chosen such that the specular beam is located approximately in the center of the primary beam and the first diffuse Bragg sheet (0,0,3).

Cubic phase

A diffraction pattern of the type *C* observed in DOPC/cholesterol samples of elevated cholesterol content has, to our knowledge, not been reported before. However, similar patterns with diffraction peaks located in concentric circles are known from studies on solid-supported diblock copolymer or silica thin films [103, 144], where they are attributed to cubic phases.

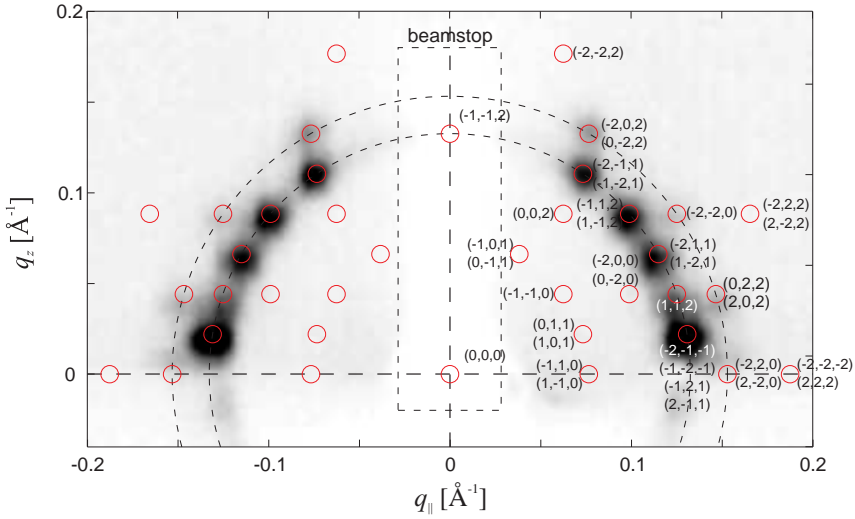


Figure 3.17: Diffraction pattern of a cubic phase observed in DOPC/Chol mixtures of high cholesterol content ($X_{\text{Chol}} = 0.4$, $RH = 50\%$) after several heating/cooling cycles and peak positions predicted by a body-centered cubic lattice with an orientation as described in the main text.

A cubic lattice with one basis vector perpendicular to the substrate is spanned by

$$\vec{a}_C = (a, 0, 0)^T, \quad \vec{b}_C = (0, a, 0)^T, \quad \vec{c}_C = (0, 0, a)^T. \quad (3.19)$$

The observed pattern is not compatible with Bragg peak positions predicted by this parameterization. GIBAUD *et al.* note that, if a sample can transform from a cubic to a $2d$ hexagonal phase and *vice versa*, the (111) direction in the cubic phase should point along the direction of cylindrical water tubes. A similar statement is made in [145]. Therefore, we consider a cubic phase with (111) parallel to the substrate. To rotate the vector $a(1, 1, 1)^T$ into the xy plane, the matrices

$$R_1 = \begin{pmatrix} \sqrt{\frac{1}{2}} & \sqrt{\frac{1}{2}} & 0 \\ -\sqrt{\frac{1}{2}} & \sqrt{\frac{1}{2}} & 0 \\ 0 & 0 & 1 \end{pmatrix} \quad \text{and} \quad R_2 = \begin{pmatrix} \sqrt{\frac{2}{3}} & 0 & \sqrt{\frac{1}{3}} \\ 0 & 1 & 0 \\ -\sqrt{\frac{1}{3}} & 0 & \sqrt{\frac{2}{3}} \end{pmatrix}, \quad (3.20)$$

are used. R_1 corresponds to a rotation by 45° about \vec{e}_z (*i.e.* into the xz plane) and R_2 to a rotation by $\arccos(\sqrt{2/3}) = 35.26^\circ$ about \vec{e}_y [144]. The theoretical diffraction

peak positions of a $2d$ powder of these crystallites were then calculated by the script `index_cubic.m` and found in good agreement with the observed peak positions (Fig. 3.17, lattice constant $a \approx 116\text{\AA}$). All observed peaks are accounted for if a body-centered cubic lattice (symmetry element I for *innenzentriert*, reflection condition $h+k+\ell = 2n$, $n \in \mathbb{Z}$) is assumed. TENCHOV *et al.* observed cubic phases in aqueous dispersions of DOPC/Chol mixtures which were subject to heating/cooling cycles by powder diffraction [146]. In their analysis, the strong $\{211\}$ and $\{220\}$ reflections corresponding to a ratio of spacings $\sqrt{6}:\sqrt{8}$ indicate space group $Ia\bar{3}d$ containing gyroid structures (Fig. 1.2). However, in our case, other space groups can not be ruled out with certainty since only few of the allowed reflections could be observed. Metastability and difficulties in reproducibility of bicontinuous phases, where kinetic factors seem to play an important role, have been frequently noted in the literature [88, 146, 147, 148]. This could explain why the appearance of pattern C depended on the protocol for thermal equilibration prior to the measurements.

Tetragonal phase

Fig. 3.18 shows a diffraction pattern observed during the experiment at the Swiss Light Source (*cf.* chapter 5) in DOPC/Chol 70:30 after RH was increased from 40 to 70%. All observed reflections can be indexed using a tetragonal lattice ($a = b \neq c$, $\alpha = \beta = \gamma = 90^\circ$) spanned by vectors

$$\vec{a}_T = (a, 0, 0)^T, \quad \vec{b}_T = (0, a, 0)^T, \quad \vec{c}_T = (0, 0, 4d)^T, \quad (3.21)$$

where $a = (78.0 \pm 0.5)\text{\AA}$ and $d = (49.1 \pm 0.2)\text{\AA}$. Peaks are found in columns with constant $q_{||}$ values in the ratio $0:\sqrt{1}:\sqrt{2}:\sqrt{4}:\sqrt{5}$. Reflections which do not fulfil the condition

$$h + k + \ell = 2n, \quad n \in \mathbb{Z} \quad (3.22)$$

are systematically absent, indicating a body-centered lattice [141]. In addition, the reflection condition $\ell = 4n$, $n \in \mathbb{Z}$ seems to hold for the reflections 00ℓ . A body-centered tetragonal phospholipid phase of this symmetry is briefly mentioned in [120], where it was observed in bromine-labeled DSPC in a narrow hydration interval between the lamellar and the rhombohedral phase. Also in samples composed of DOPC and the antimicrobial peptide alamethicin, a diffraction pattern compatible with a body-centered tetragonal lattice has been reported [149]. To our knowledge, the unit cell electron density distribution of a tetragonal phospholipid phase has not been determined so far.

During phase diagram determination at our in-house instrument, this phase could not be observed. Similar to the cubic phase, it seems not unlikely that this phase is metastable, at least in case of DOPC/Chol 70:30, and its appearance depends on kinetic factors and thermal history. Since it was observed in the transition region between the lamellar and rhombohedral phase, it is possibly the first nonlamellar phase to form upon dehydration of bilayer stacks of certain lipid compositions, and would certainly be worthwhile further investigation. To this end, lipid compositions and experimental parameters where this phase is reproducibly observed should be explored first.

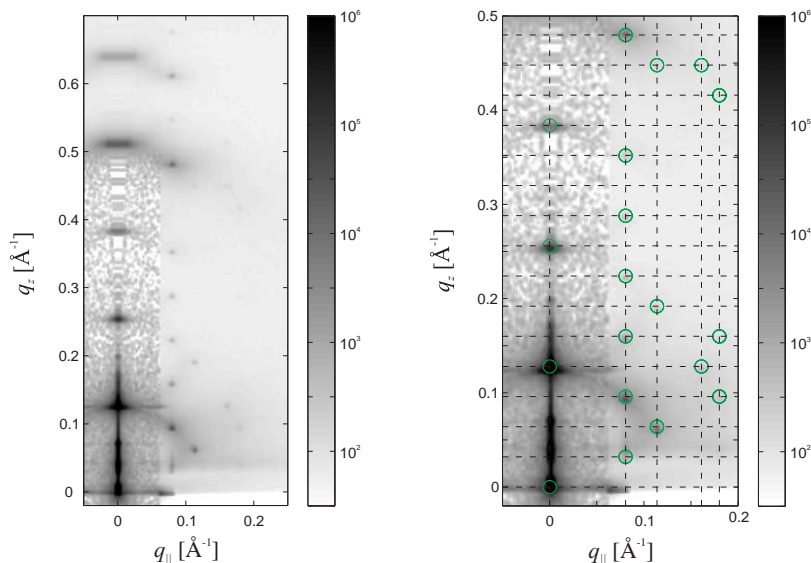


Figure 3.18: Diffraction pattern of a tetragonal phase observed in DOPC/Chol with $X_{\text{Chol}} = 0.3$ at $RH = 70\%$ (SLS experiment). The green circles on the right indicate observed reflections which coincide with the positions predicted by a $2d$ powder of crystallites of space group $I4_1$ with the unique axis perpendicular to the substrate.

3.4 Conclusions

The time available for synchrotron experiments is usually severely limited. Therefore, experiments must be planned with great care to allow for an efficient use of the granted beam time. This is difficult to reconcile with the determination of extended phase diagrams, which requires measurements of many samples over a wide range of control parameters. To this end, our in-house GIXD setup has proven to be an indispensable tool since it can be operated without temporal restrictions. Particularly interesting points in the phase diagrams of multicomponent model membrane systems can be identified. The limited synchrotron beamtime can be efficiently used to record data for electron density reconstruction.

The obtained phase diagrams indicate that formation of the rhombohedral phase is a common feature of symmetric, monounsaturated phosphatidylcholines with fluid chains. In addition, the physiologically relevant additives cholesterol, phosphatidylethanolamine and PIP₂ promote stalk phase formation, *i.e.* lower the osmotic pressure corresponding to the L/R phase boundary. Given the low molar concentrations of PIP₂, the effects are particularly strong for this lipid. Intuitively, due to its bulky and charged head group (Fig. 1.1), one would not expect this lipid to promote inverted phases.

In the subsequent chapters, it is investigated more closely to what extent changes in phase behaviour are associated with changes in bilayer interactions at small separation and effects on the equilibrium structure of stalks.

4 Bilayer structure and interactions

Prior to stalk formation, membranes must necessarily approach each other. However, lipid bilayers strongly repulse at small separation, even if they possess no net charges. Therefore, establishing local close contact of membranes is associated with a considerable energy barrier. In vivo, different classes of fusion proteins are regarded as the machinery performing the required work. In protein-free model membrane systems, repulsive forces between lipid bilayers can be studied in a systematic fashion as a function of bilayer composition. Complementary to the analysis of stalk structures in the rhombohedral phase, we studied lipid bilayer interactions prior to stalk phase formation, i.e. at hydration levels between full hydration and the phase boundary to the stalk phase obtained in the previous chapter. To this end, the osmotic stress method and electron density profile analysis were used. The swelling method to solve the crystallographic phase problem is considered for the one-dimensional case, before it is extended to the three-dimensional rhombohedral phase in the subsequent chapter.

4.1 Electron density profiles

Aligned lipid bilayer stacks are characterized by a single series of equidistant in-plane reflections. The structure of each bilayer is represented by the one-dimensional electron density profile (EDP) $\rho(z)$ (Fig. 4.1). This denotes the temporally averaged projection of the electron density of a single lipid bilayer onto the direction \vec{e}_z along the bilayer normal. A lipid bilayer stack is not a static structure, but displays protrusions of single lipid molecules and bilayer undulations out of the bilayer plane [75]. As explained in section 2.6, this limits the number of observable reflections and a smooth EDP as shown in Fig. 4.1 correctly represents the mean bilayer structure. Electron density maxima correspond to the phospholipid headgroup regions and minima to the methyl trough region in the bilayer center (Tab. 4.1). Similar EDPs are also observed in molecular dynamics simulations [150].

Different methods to obtain EDPs exist. In the classical approach derived from conventional crystallography (*cf.* section 2.1), EDPs are reconstructed by Fourier synthesis using the discrete form factor values obtained from integrated Bragg peak intensities as coefficients. A different method called full q -range fitting uses the discrete form factors and additional experimental parameters for least-squares fitting of the entire reflectivity curve and yields EDPs on an absolute scale [116]. In another recent technique, off-specular diffuse scattering at or close to full hydration is used to obtain the continuous form factor $|F(q_z)|$. Subsequently, EDP models consisting of several Gaussians and step functions are fitted to the form factor data [68, 151]. While this approach is certainly interesting, it seems less suited for the objectives in this thesis, since diffuse scattering is strongly suppressed in partially dehydrated conditions prior to stalk formation and the use of synchrotron radiation is mandatory. In this work, we follow the classical Fourier synthesis approach, which can conveniently be combined with the swelling method to solve the crystallographic phase problem.

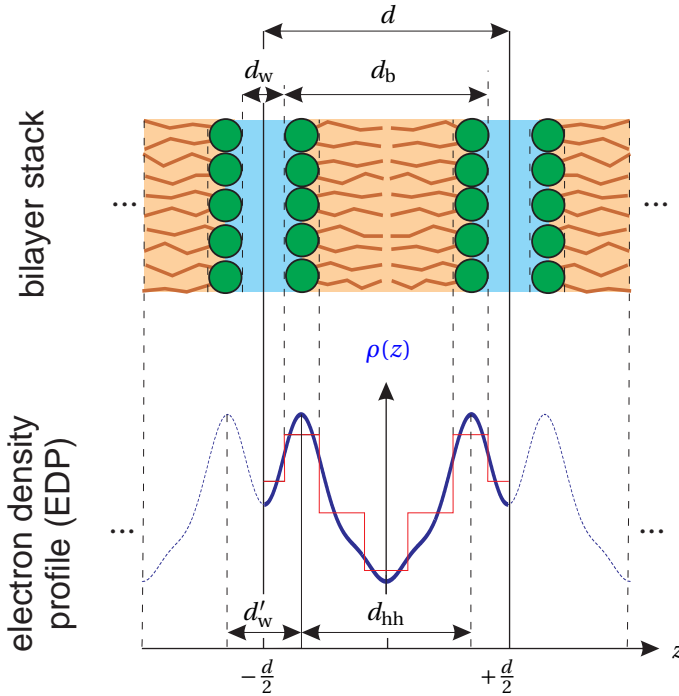


Figure 4.1: Sketch of a lipid bilayer, corresponding electron density profile (—) and definitions of structural parameters. Due to the soft-matter character of the bilayer stack, features such as headgroup peaks and methyl trough region are smeared out. In a coarse description using stepwise constant electron densities (---), one can distinguish water, lipid headgroup, hydrocarbon and methyl trough regions (cf. Tab. 4.1).

4.2 Osmotic stress method

The osmotic stress method described here has been reviewed in [47, 74, 75, 124, 152]. The equilibrium distance between two parallel uncharged lipid bilayers in water is determined by several interaction potentials introduced in section 1.4, where also difficulties in the mathematical description were addressed. Empirically, it is well established that a strong repulsion between lipid bilayers exists at short separation distances, which is well described by an exponentially decaying total repulsive pressure

$$P_{\text{r}}(d_{\text{w}}) = P_{\text{hyd}}(d_{\text{w}}) + P_{\text{und}}(d_{\text{w}}) + \dots = P_{\text{r},0} \exp\left(-\frac{d_{\text{w}}}{\lambda_{\text{r}}}\right). \quad (4.1)$$

The individual components can not directly be assessed. If the dominant repulsive pressure is the hydration repulsion $P_{\text{hyd}} = P_0 \exp(-d_{\text{w}}/\lambda_{\text{h}})$ (cf. Fig. 4.2), then $\lambda_{\text{r}} \approx \lambda_{\text{h}}$ and $P_{\text{r},0} \approx P_0$. This assumption is used in the following. The finite distance observed between uncharged lipid bilayers in excess water results from the equilibrium

region/electron density	ρ [$e^-/\text{\AA}^3$]	
	[153]	[154]
headgroup peak	0.450	0.540
hydrocarbon region	0.296	0.300
methyl trough region	0.165	0.160

Table 4.1: Electron densities for different regions of the unit cell in electron density strip models. The electron density of water, 0.334\AA^{-3} , can easily be determined using a mass density of $1\text{g}\cdot\text{cm}^{-3}$ for bulk water.

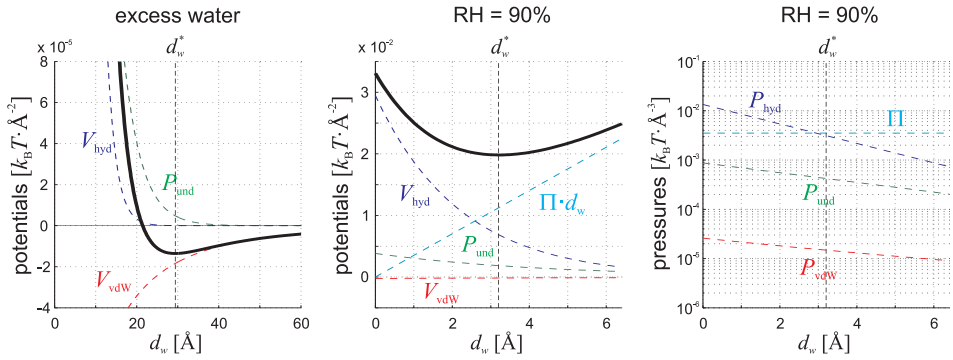


Figure 4.2: Interaction potentials of two DOPC bilayers in excess water (left) and at $RH = 90\%$ (center) calculated from the relations given in section 1.4. At $RH = 90\%$, the equilibrium distance d_w^* is determined by the pressures Π and P_{hyd} (right). The following constants are used: $P_0 = 0.55 \cdot 10^8 \text{Jm}^{-3}$, $\lambda_h = 2.2\text{\AA}$, $\kappa = 8.0 k_B T$, $d_{\text{CH}_2} = 26.8\text{\AA}$, $d_{\text{HG}} = 9.0\text{\AA}$ [68].

$$|P_{\text{vdW}}(d_w)| = |P_{\text{hyd}}(d_w)|. \quad (4.2)$$

The osmotic stress method employs osmotic pressure Π as an additional attractive potential:

$$|P_{\text{vdW}}(d_w)| + \Pi = |P_{\text{hyd}}(d_w)| \quad (4.3)$$

In case of hydration from water vapour as used in this work, Π is given by

$$\Pi = -\frac{k_B T}{v_w} \ln\left(\frac{RH}{100\%}\right). \quad (4.4)$$

For osmotic pressures leading to d_w several \AA below the equilibrium value in excess water, the total attractive pressure is dominated by Π , and the van der Waals pressure P_{vdW} can be neglected (Fig. 4.2, right) [75, 155]. Therefore, determination of Π directly yields the hydration pressure

$$\Pi = P_0 \exp\left(-\frac{d_w}{\lambda_h}\right). \quad (4.5)$$

Application of different osmotic pressures allows to record pressure-distance curves $\Pi(d_w)$, from which P_0 and λ_h are obtained as empirical fit parameters. This can be achieved in two different ways. Both rely on X-ray diffraction experiments, but use different assumptions and definitions of the water layer thickness (indicated in Fig. 4.1):

- **Gravimetric method:**

For this method, which has been applied in a long series of publications by RAND, PARSEGAN and coworkers, unoriented samples are prepared by combining weighted amounts of lipid and water. The lamellar repeat spacing d is measured by x-ray diffraction as a function of lipid weight fraction c . Further analysis relies on the assumption that water and lipids are localized in completely distinct layers of thickness d_b and d_w with molecular volumes identical to their bulk values. The volume fraction occupied by lipids then is

$$\phi = \left(1 + \frac{1-c}{c} \frac{\bar{v}_w}{\bar{v}_l}\right)^{-1}, \quad (4.6)$$

where \bar{v}_w and \bar{v}_l denote the partial specific volumes of water and lipid. Bilayer thickness d_b and water layer thickness d_w are obtained as

$$d_b = \phi d \quad \text{and} \quad d_w = (1 - \phi)d. \quad (4.7)$$

In a second series of measurements using samples at defined osmotic pressures Π , d is determined as a function of Π . Since the change of d is monotonous with Π , combination of the results from gravimetric and osmotically stressed samples yields the pressure-distance relation $\Pi(d_w)$ and thus P_0 and λ_h .

- **Electron density profile (EDP) method:**

This method was pioneered in another impressive series of papers by MCINTOSH, SIMON and coworkers. EDPs are constructed at different osmotic pressures. The distance between adjacent electron density maxima indicating the lipid headgroups are used to define the headgroup-headgroup distance d_{hh} and the water layer thickness d'_w , which includes also parts of the lipid headgroup region. The relation $\Pi(d'_w)$ then follows without the need for additional measurements or assumptions about the partitioning of water and lipid molecules.

Importantly, both methods use a different decomposition of the lamellar repeat spacing d into aqueous and lipidic regions (Fig. 4.1), which has to be taken into account if results for P_0 and λ_h are compared:

$$d = \begin{cases} d_b + d_w & \text{gravimetric method} \\ d_{hh} + d'_w & \text{EDP method} \end{cases} \quad (4.8)$$

In the gravimetric method, a possible intercalation of lipid headgroups and water is ignored. In addition, as pointed out in [47], water can not exclusively be localized between multilamellar regions with well-defined bilayer stacking, but also occupies defect regions which necessarily occur in case of unoriented samples. Therefore, the reliability of the gravimetric method has been questioned repeatedly ([47] and references therein) and, as noted by RAND himself [74], its results may differ substantially from the EDP method.

The EDP method, in contrast, does not require assumptions on the partitioning of lipid and water molecules. The rough and diffuse character of lipid bilayers and as well as their fluctuations are implicitly taken into account, since an EDP is a spatial and temporal average over the entire bilayer stack. Therefore, this method seems better suited to quantify the repulsive forces between bilayers prior to stalk phase formation and was put into practice as described below.

4.3 Motivation of our work

After this introduction to the osmotic stress method to study bilayer interactions, the motivation behind our efforts presented in this chapter should be clarified:

In addition to lipid monolayer deformations and transient contact of hydrophilic lipid tails and water, the energy required to overcome the hydration repulsion may constitute a decisive barrier to membrane fusion. Bilayer EDPs close to the L/R phase boundary can reveal the critical bilayer separation $d'_{w,crit}$ at which stalk phase formation becomes energetically favourable. This corresponds to the inter-bilayer distance which must be established locally by fusion proteins to initiate hemifusion *in vivo*. Knowledge of $d'_{w,crit}$ and the hydration force parameters P_0 and λ_h also allows to estimate the corresponding work

$$W_{hyd} = -A \int_{\infty}^{d'_{w,crit}} P_{hyd}(x) dx = A\lambda_h P_0 \exp\left(-\frac{d'_{w,crit}}{\lambda_h}\right), \quad (4.9)$$

where A denotes a typical contact area. For lipids displaying the stalk phase, literature values of P_0 and λ_h are only available for pure DOPC and a DOPC/DOPE mixture. In addition, these seem inadequate to study phenomena at small bilayer separation:

Values of P_0 and λ_h for DOPC and DOPC/DOPE with $X_{DOPE} = 0.75$ obtained by the gravimetric method exist [74, 156]. These are based on pressures up to $\Pi = 10^4$ atm [156], which corresponds to RH close to 0% (*cf.* Fig. 3.2*a*). Therefore, nonlamellar phase formation in DOPC and DOPC/DOPE mixtures over a considerable pressure interval was not taken into account. In addition to the general problems associated with the gravimetric method addressed above, this is another reason why these values P_0, λ_h should be used with caution.

Consideration of the measured interval of $\Pi(d_w)$ is also crucial in case of more recent values for DOPC obtained by the EDP method, $P_0 = 0.55 \cdot 10^8 \text{ Nm}^{-2}$ and $\lambda_h = 2.2 \text{ \AA}$ [68, 157]. Here, the maximum osmotic pressure was $\Pi = 56 \text{ atm}$, which corresponds to $RH \approx 96\%$ (*cf.* Fig. 3.2*a*). In this regime, the undulation pressure P_{und} still dominates bilayer repulsion (Fig. 4.2). Stalk phase formation in DOPC is observed at $RH \approx 43\%$,

which corresponds to values of Π more than one order of magnitude higher. This precludes a reliable extrapolation of P_0 and λ_h to pressures relevant for stalk formation.

In order to close this existing gap, quantify the repulsive interbilayer forces at bilayer separations relevant to stalk formation and elucidate the effect of changes in lipid composition, we performed the EDP method as described in the following.

4.4 Experimental

4.4.1 X-ray reflectivity Instrument

X-ray reflectivity experiments were performed at our institute using a home-built diffractometer sketched in Fig. 4.3. The x-ray beam was generated by a sealed tube with Cu anode and line focus (Seifert Dx-Cu12 \times 0.4-S long fine focus, 35 kV \times 40 mA). A multilayer mirror (Pantak Seifert) was used to parallelize the beam and select the Cu-K α line ($E = 8048$ eV, $\lambda = 1.54056$ Å). After collimation to a size of 0.5×6.5 mm² by a set of motorized slits (S1), the primary flux I_0 was 2.3×10^8 photons per second. Stability of I_0 was monitored by an additional detector not shown in Fig. 4.3, which measures the intensity of a small fraction of the primary beam scattered by a Kapton foil placed behind slit S1. The sample chamber was placed on a Huber stage with three translational and three rotational degrees of freedom (motors x_s , y_s , z_s and t_h , χ , ϕ , respectively). Samples were mounted inside the sample chamber with vertical sample surface orientation and fixed to the sample holder by double-sided tape. Behind the sample, the reflected beam was collimated in horizontal direction by two slits of 2 mm (S2) and 0.8 mm (S3) in width placed directly behind the environmental chamber and in front of the detector (Cyberstar fast scintillation counter, Oxford Danfysik), respectively. The distance between the center of rotation of the Huber stage and slit S3 is 400 mm. The instrument is controlled by the software SPEC (Certified Scientific Software).

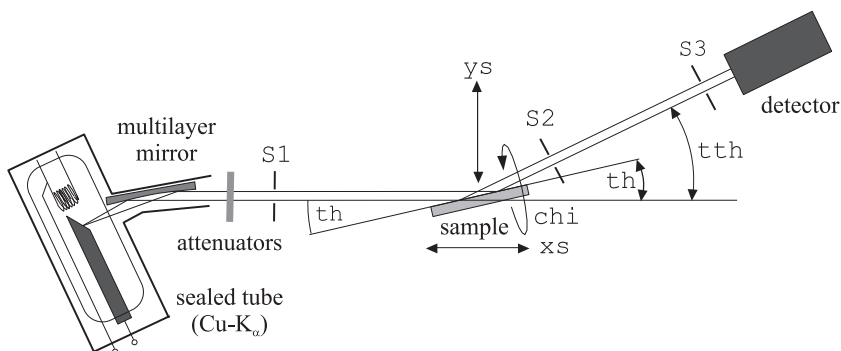


Figure 4.3: Sketch of the instrument used for reflectivity scans (top view).

4.4.2 Measurements

Samples were prepared on $25 \times 15 \text{ mm}^2$ substrates as described in section 3.2.1. Prior to a measurement, the sample was equilibrated inside the environmental chamber at the highest chosen *RH* level (typically between 90 and 95%) for several hours or over night. After sample alignment, the specularly reflected intensity was recorded as a function of the incident angle α_i using the SPEC command `a2scan` with a stepsize of $\Delta\alpha_i = 0.005^\circ$. In a diffraction experiment, the counting process of photons follows Poissonian statistics. The standard deviation corresponding to N counted photons is \sqrt{N} . To improve the signal-to-noise level $N/\sqrt{N} = \sqrt{N}$, one has to increase the number of observations, which can be achieved either by higher primary intensity I_0 or by choosing longer counting times. For the given value of I_0 , an exposure of 1 s per datapoint was regarded sufficient for the lower orders of diffraction. For higher order Bragg peaks, the counting time was increased to 5 or 10 s to improve the signal-to-noise ratio. Automatic attenuators were used to avoid detector saturation. For all lipids which also displayed the stalk phase, $n_{\text{max}} = 7 - 9$ Bragg peaks could be detected in the lamellar phase with a signal-to-noise level allowing for proper determination of integrated peak intensities. In case of gel-phase lipids, the number of peaks increases to $n_{\text{max}} = 14 - 15$ (cf. Fig. 2.8). To speed up the measurements and avoid deterioration of the samples, which was sometimes observed during preliminary runs after longer exposure, only intervals of about $\pm 0.3 \text{ \AA}^{-1}$ around each peak were recorded for most *RH* levels. The peak width was typically 0.07° (full width at half maximum). Scans were repeated for several hydration levels covering the desired *RH* range in descending order.

4.4.3 Data reduction

The recorded intensity curves $I(\alpha_i)$ were corrected for different counting times and absorption, polarization and illumination effects using the equations given in section 2.4. The corrected intensity was subsequently plotted as a function of momentum transfer $q_z = \frac{4\pi}{\lambda} \sin \alpha_i$ perpendicular to the bilayer plane (Fig. 4.5a). For each *RH* level, d and the corresponding error were determined as the mean and standard deviation of the values obtained from the positions of the Bragg peak maxima *via* $d = 2\pi/q$ for the diffraction orders two to seven. The first Bragg peak was not used because its position is systematically shifted towards slightly higher q_z due to superposition with the Fresnel reflectivity from the substrate and by refraction effects. For each peak, a linear background was determined using the mean value of the first five and last five datapoints in the measured interval (dark gray area in the inset of Fig. 4.5a). The corresponding area was subtracted from the total area below the measured curve, yielding the integrated peak intensity I_n (light gray area in Fig. 4.5a). Subsequently, the amplitude of the corresponding form factor was obtained using the Lorentz correction factor for oriented samples, $K \cdot |F_n| = \sqrt{n \cdot I_n}$. K denotes the unknown experimental constant. This procedure, which was performed by the MATLAB script `data_extraction_reflectivity.m`, yields the form factor amplitudes $\{K \cdot |F_n|\}$ on arbitrary scale and lattice constants d for all hydration levels.

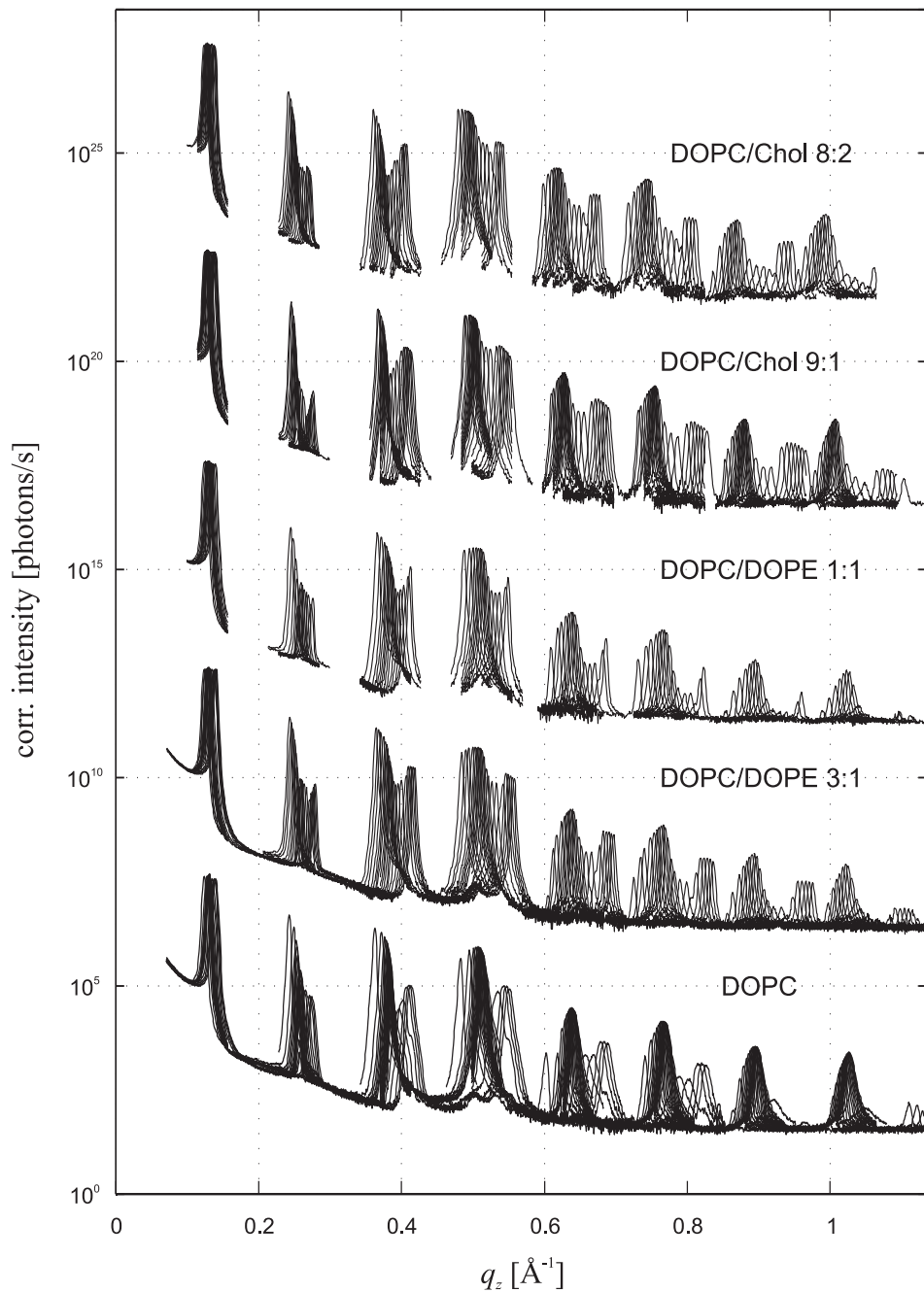


Figure 4.4: Typical reflectivity scans for several lipid mixtures from $RH \geq 90\%$ down to the stalk phase. The curves are shifted vertically for clarity.

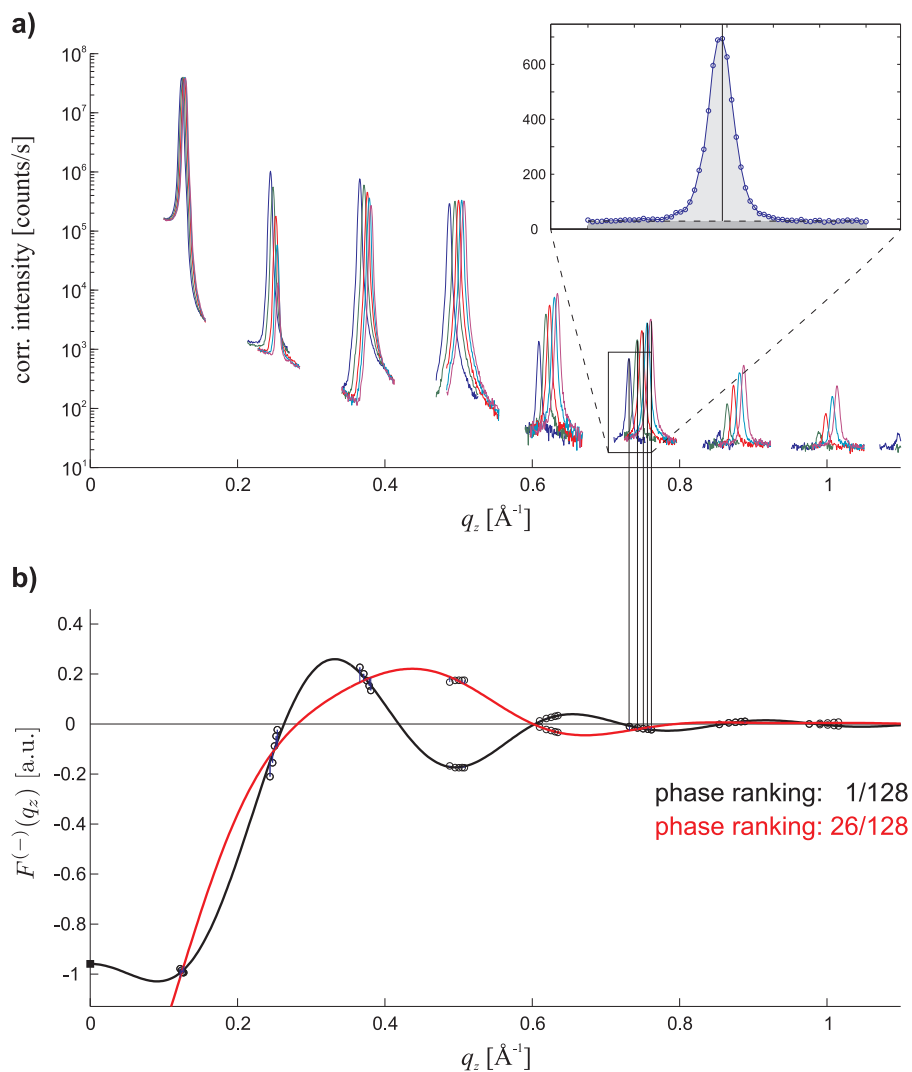


Figure 4.5: (a) Bragg peaks of DOPC/DOPE 50:50 recorded at five different RH levels between 96% (blue) and 91% (magenta). The inset shows the integrated intensity (light gray) and background (dark gray) for one peak. (b) Corresponding continuous form factors obtained by the swelling method for phase determination as described in section 4.4.5. In this case, best agreement of discrete form factor values (circles) and continuous form factor is obtained with the phase combination $- - + - + - + -$ (black solid line), whereas other phase combinations lead to obviously worse results (red solid line).

4.4.4 Fourier Synthesis of electron density profiles

In case of a lamellar phase, the form factor is obtained by integration of the one-dimensional EDP $\rho(z)$ over the width d of the unit cell (Fig. 4.1). If the center of the symmetric lipid bilayer is chosen as the origin, $\rho(z) = \rho(-z)$ is centrosymmetric and the resulting form factor

$$F(q_z) = \int_{-d/2}^{+d/2} \rho(z) \exp(iq_z z) dz = \int_{-d/2}^{+d/2} \rho(z) \cos(q_z \cdot z) dz \quad (4.10)$$

is real-valued and centrosymmetric as well. In addition, $\rho(z)$ can be written as a Fourier series [158]

$$\rho(z) = \frac{a_0}{2} + \sum_{n=1}^{\infty} \left[a_n \cos\left(n \frac{2\pi}{d} z\right) + b_n \sin\left(n \frac{2\pi}{d} z\right) \right] \quad (4.11)$$

with coefficients

$$a_n = \frac{2}{d} \int_{-d/2}^{+d/2} \rho(z) \cos\left(n \frac{2\pi}{d} z\right) dz \quad \text{and} \quad b_n = \frac{2}{d} \int_{-d/2}^{+d/2} \rho(z) \sin\left(n \frac{2\pi}{d} z\right) dz. \quad (4.12)$$

Due to centrosymmetry, $b_n = 0 \forall n$. By comparison of Eq. (4.10) and Eq. (4.12), one recognizes that the form factor values $F_n = F(q_n)$ corresponding to momentum transfer $q_n = n \cdot \frac{2\pi}{d}$ are the coefficients in the Fourier Cosine series of $\rho(z)$:

$$\rho(z) = \frac{2}{d} \sum_{n=-\infty}^{\infty} F_n \cos(q_n \cdot z) \quad (4.13)$$

In the following, the experimental constant K in the measured values $\{K \cdot |F_n|\}$ and the factor $\frac{2}{d}$ are ignored. The EDPs obtained in the end are on arbitrary scale. From the experiments, only the amplitudes of the form factors $F_n = \nu_n |F_n|$ are known, the corresponding phase factors $\nu_n = \pm 1$ are not directly accessible from the experimental data. This is the well-known phase problem of crystallography. To retrieve the phase information, additional efforts are required. Note that, due to centrosymmetry, the phase problem is already strongly simplified, since only a finite number of $2^{n_{\max}}$ solutions exist. In general, the number of possible phase combinations is infinite.

4.4.5 Phase retrieval: The swelling method

An established technique to recover phase information from scattering experiments on lipid bilayer stacks is the so-called *swelling method* (e.g. [159] and references therein). It is based on thickness changes of the water layer d_w separating adjacent bilayers. Therefore, precise and stable hydration control as provided by the setup explained in section 3.2.2 is a prerequisite. In the following, the equations needed for application and implementation of the swelling method are derived. In a later chapter, the formalism is extended to the rhombohedral phase.

We start with some introductory considerations: Inserting Eq. (4.13) into (4.10), using the trigonometric identity

$$\cos(x) \cos(y) = \frac{1}{2} [\cos(x - y) + \cos(x + y)] \quad (4.14)$$

and carrying out the integration yields the continuous form factor

$$F(q_z) = \sum_{n=-\infty}^{\infty} v_n |F_n| \operatorname{sinc} \left(\frac{d}{2} q_z - n\pi \right), \quad (4.15)$$

where $\operatorname{sinc}(x) = \sin(x)/x$. Since $\rho(z)$ is symmetric, $F(q_z)$ is also symmetric, *i.e.* $F_n = F_{-n}$. If the phase factors $v_n = \pm 1$ are known, Eq. (4.15) can be used to reconstruct the continuous form factor $F(q_z)$ from discrete values measured at positions $\{q_n\}$. This statement is related to the *sampling theorem* known from signal theory [160, 161]. The sum contains infinitely many orders of diffraction. In any real experiment, the number of observable reflections with sufficient signal-to-noise ratio is limited. All equations derived in this chapter are thus approximations when used to fit experimental data.

At this stage, Eq. (4.15) is of little use and changes with the hydration state of the bilayer stack. In addition, the form factor F_0 is not accessible by diffraction experiments, since it corresponds to forward scattering which coincides with the primary beam and can thus not be measured. On absolute scale, $F_0 = \bar{\rho}d$ is proportional to the mean electron density $\bar{\rho}$ in the unit cell, but the measured form factors $\{|F_n|\}$ are on a different arbitrary scale.

An important step to solve the phase problem is to introduce the *minus fluid model* [162, 163]: Assume that the unit cell can be divided into the bilayer structure confined to $z \in [-\frac{d_b}{2}, +\frac{d_b}{2}]$ and a bulk water layer of width d_w of constant electron density ρ_w (Fig. 4.6). If ρ_w is subtracted from $\rho(z)$, the minus-fluid EDP

$$\rho^{(-)}(z) = \rho(z) - \rho_w \quad (4.16)$$

is nonzero only for $z \in [-\frac{d_b}{2}, +\frac{d_b}{2}]$. In addition, we assume that changes in d_w do not affect the bilayer structure. Therefore, the corresponding continuous form factor

$$F^{(-)}(q_z) = \int_{-d_b/2}^{+d_b/2} \rho^{(-)}(z) \cos(q_z \cdot z) dz \quad (4.17)$$

is also constant for different d_w . In analogy to the derivation of Eq. (4.15), one obtains the modified interpolation formula

$$F^{(-)}(q_z) = \sum_{n=-\infty}^{\infty} v_n |F_n| \operatorname{sinc} \left(\frac{d}{2} q_z - n\pi \right) - \rho_w d \operatorname{sinc} \left(\frac{d}{2} q_z \right). \quad (4.18)$$

Apart from the additional sinc term centered around $q_z = 0$, this is identical to Eq. (4.15): The difference between $F(q_z)$ and $F^{(-)}(q_z)$ is solely encoded in the term corresponding to forward scattering. Since $\operatorname{sinc}(n\pi) = 0$ for $n \in \mathbb{Z} \setminus \{0\}$,

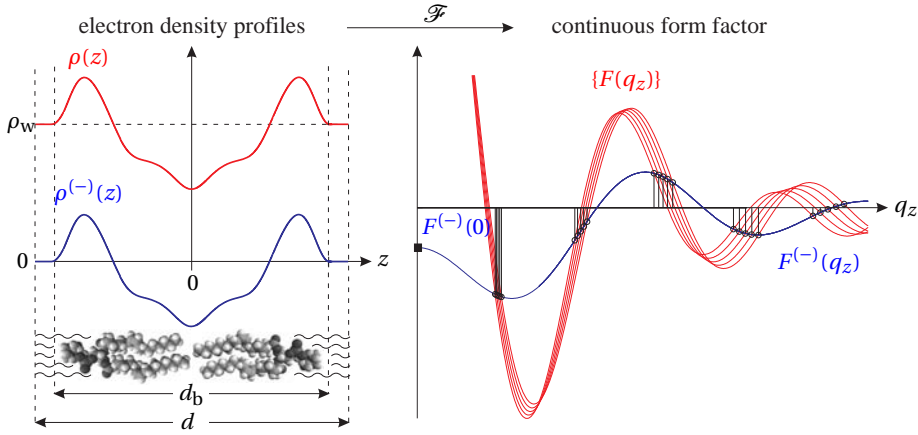


Figure 4.6: A simulation illustrating the minus-fluid model and the swelling method: For constant bilayer structure and water layers of varying thickness $d_w = d - d_b$, the continuous form factors $\{F(q_z)\}$ are determined by Fourier transform. The values $\{F_n\}$ corresponding to different d_w lie on the continuous form factor $F^{(-)}(q_z)$ of the minus-fluid model. By recording these in a diffraction experiment, the modulus of $F^{(-)}(q_z)$ is sampled at the positions indicated by vertical lines.

$$F_n^{(-)} = F^{(-)}(q_n) = \begin{cases} F_0 - \rho_w d & n = 0, \\ F_n & n \neq 0. \end{cases} \quad (4.19)$$

$F_0^{(-)}$ can be determined as follows: In the framework of the minus-fluid model, $\rho^{(-)}(z)$ must vanish at $z = \pm \frac{d}{2}$,

$$\rho^{(-)}\left(\frac{d}{2}\right) = \frac{1}{d} v_0 |F^{(-)}(0)| + \frac{2}{d} \sum_{n=1}^{\infty} v_n |F_n| \cos\left(n \frac{2\pi d}{2}\right) \stackrel{!}{=} 0. \quad (4.20)$$

For the correct phases $\{v_n\}$, $F_0^{(-)}$ follows from the remaining form factors *via* [164]

$$F_0^{(-)} = 2 \cdot \sum_{n=1}^{\infty} (-1)^{n+1} v_n |F_n|. \quad (4.21)$$

After these preparations, the *swelling method* can be used to solve the phase problem and determine the phase factors $\{v_n = \pm 1\}$. Consider the effect of increasing the water layer thickness d_w : In the minus-fluid model, the continuous form factor (4.17) is constant for different d spacings if the structure of the lipid bilayer is not affected by the swelling process. If the $\{|F_n|\}$ are measured at different values of d , the modulus of the continuous form factor $|F^{(-)}(q_z)|$ is sampled at slightly different positions (Fig. 4.6). Out of $2^{n_{\max}}$ possible choices, the most reasonable phase combination according to the swelling method is the one where the discrete datapoints $\{v_n |F_n|\}$ and the continuous form factor reconstructed by

$$F^{(-)}(q_z) = \sum_{n=-\infty}^{\infty} v_n |F_n^{(-)}| \operatorname{sinc}\left(\frac{d}{2}q_z - n\pi\right) \quad (4.22)$$

using Eq. (4.19) and (4.21) agree best. An example is shown in Fig. 4.5(b). During a long series of reflectivity scans for one sample, the sample quality and alignment may slightly deteriorate, thus reducing the diffracted intensity. Therefore, datasets recorded at different hydration levels should be properly normalized relative to each other prior to application of the swelling method. To this end, a condition introduced by BLAUROCK is used [165]: As noted above, a minus-fluid EDP $\rho^{(-)}(z)$ which does not change with hydration corresponds to a Fourier transform $F^{(-)}(q_z)$ which is also independent on RH . Consequently, also the integral

$$\int_{-\infty}^{\infty} |F^{(-)}(q_z)|^2 dq_z \quad (4.23)$$

is constant for different values of RH . This leads to the normalization condition

$$\int_{-\infty}^{\infty} |F^{(-)}(q_z)|^2 dq_z \stackrel{!}{=} \text{const.} \quad (4.24)$$

$$= \sum_n \sum_m F_n F_m \int_{-\infty}^{\infty} \operatorname{sinc}\left(\frac{d}{2}q_z - n\pi\right) \operatorname{sinc}\left(\frac{d}{2}q_z - m\pi\right) dq_z \quad (4.25)$$

$$= \frac{2}{d} \sum_n \sum_m F_n F_m \underbrace{\int_{-\infty}^{\infty} \operatorname{sinc}(x - n\pi) \operatorname{sinc}(x - m\pi) dx}_{= \begin{cases} \pi & n = m \\ 0 & \text{else} \end{cases}} \quad (4.26)$$

$$= \frac{2\pi}{d} \sum_{n=-\infty}^{\infty} |F_n|^2 \quad (4.27)$$

Importantly, this condition does not require knowledge of the phase factors $\{v_n\}$. Each dataset is normalized by making the sum of squared form factor amplitudes for one hydration level proportional to the corresponding d -spacing

$$\sum_n |F_{n,RH}|^2 \propto d(RH). \quad (4.28)$$

Implementation of the swelling method was carried out in MATLAB, the program code is provided in appendix A.4. The script `swelling_lamellar.m` reads the output file of `data_extraction_lamellar.m`, performs the normalization of datasets by condition (4.28) and finds the best phase combination according to the swelling method using the minimum residual sum of squares

$$\sum_{RH} \sum_{n=1}^{n_{\max}} |v_n |F_{n,RH}| - F^{(-)}(q_{n,RH})|^2 \stackrel{!}{=} \min \quad (4.29)$$

as a criterion. Here, phase combinations which differ only by a global factor -1 yield the same results. Only those where $v_1 = -1$ are used, since only these yield EDPs compatible with the typical bilayer structure (*cf.* Tab. 4.1). $F^{(-)}(q_z)$ is constructed by Eq.

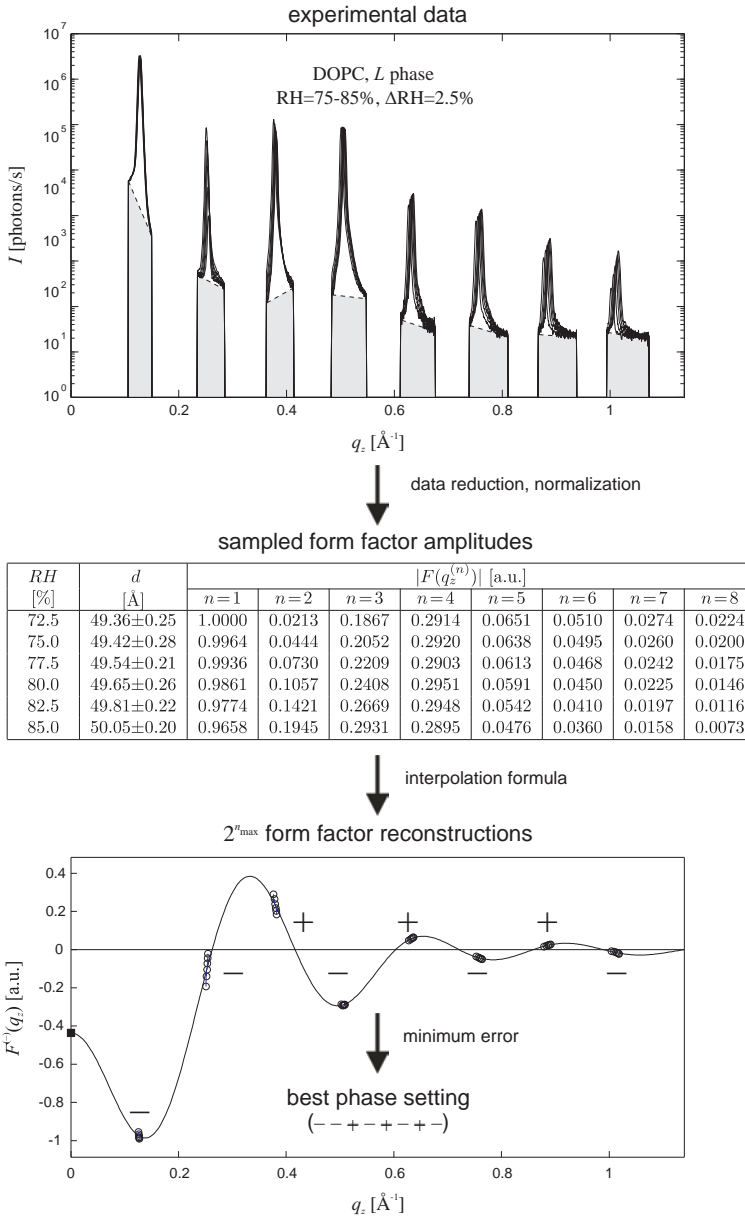


Figure 4.7: Scheme of the swelling method for the case of a lamellar stack of pure DOPC bilayers. The phase setting $\{v_n \pm 1\}$ for which the sampled form factors and the interpolated continuous form factor match best is considered the most reasonable one.

(4.22) using the average d spacing and the average value of each form factor $|F_n|$ for all values of RH . For the best phase combination, the corresponding EDPs $\Delta\rho(z)$ are displayed and the structural parameters d_{hh} and d'_w are determined (Fig. 4.8). Since the form factor F_0 is not accessible and the experimental constant K is not known, EDPs are shown as the electron density contrast $\Delta\rho(z)$ (*i.e.* the deviation from the mean electron density in the unit cell) and on arbitrary scale. All EDPs are normalized such that $\max[\Delta\rho(z)] = 1$.

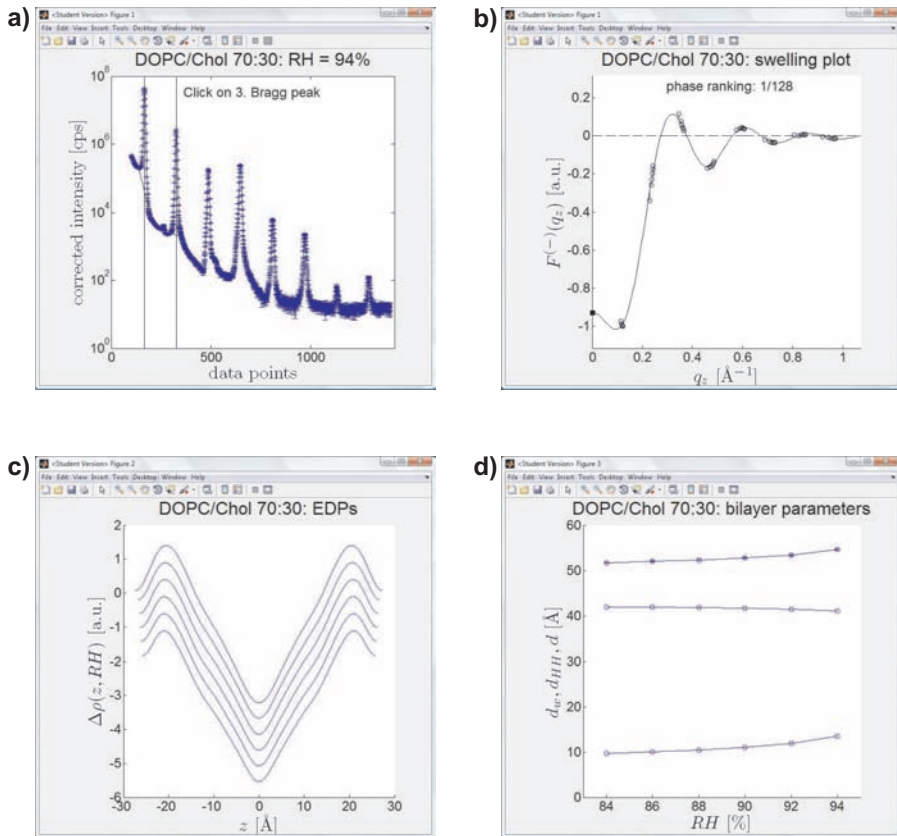


Figure 4.8: Output of `data_extraction_lamellar.m` and `swelling_reflectivity.m`: (a) Experimental data and integration of peak intensities, (b) application of the swelling method, (c) EDPs for several humidities (shifted vertically for clarity) and (d) structural parameters d , d_{hh} and d'_w .

4.5 Results and Discussion

Data were recorded for all pure lipids investigated in chapter 3 which were found to display the stalk phase, for DOPC/Chol mixtures with molar fractions $X_{\text{Chol}} = 0.1, 0.2, 0.3$ and for DOPC/DOPE mixtures with molar fractions $X_{\text{DOPE}} = 0.25$ and 0.5 and processed as explained above. The number of used reflections is $n_{\text{max}} = 7$ in case of DPhPC and $n_{\text{max}} = 8$ in case of all other samples.

4.5.1 Effects at close bilayer separation

For most samples, data were recorded over a RH interval covering both L and R phases (e.g. Fig. 4.4). The bilayer stacking distance d follows immediately from the Bragg peak positions. Upon dehydration, d decreases monotonously.

In the RH interval around the L/R phase boundaries obtained in chapter 3, two series of Bragg peaks indicating phase coexistence could be clearly resolved only in case of DPhPC (Fig. 4.9a, compare also [166]). For all other lipids, the phase transition was indicated by shoulders of the Bragg peaks similar to the example shown in Fig. 4.9b. The corresponding RH values agree with the L/R phase boundaries of the phase diagrams in section 3.3.2 to within $\pm 2\%$.

Distinct regimes can be recognized in the curves $d(RH)$ (Fig. 4.9c and 4.10). The rate $\left| \frac{\partial d}{\partial RH} \right|$ changes in a non-monotonous fashion, and $d(RH)$ is characterized by two inflection points. The one at lower RH is in very good agreement with the L/R phase boundary of the respective sample. In the RH interval between these two points, termed “transition region” in Fig. 4.9c, the following observations indicate changes in the bilayer stack:

As shown in Fig. 4.9d for pure DOPC, a drop of the form factor amplitudes $|F_{n,RH}|$ of the higher-order reflections is visible at $RH \leq 60\%$.⁹ Agreement of the sampled form factor amplitudes $|F_{n,RH}|$ and the reconstructed continuous form factor becomes significantly worse in the transition region. Except for DPhPC, a similar effect could be observed for all samples. Fig. 4.9e shows GIXD data on DOPC in the corresponding hydration interval. Upon lowering RH and prior to appearance of out-of-plane reflections indicating the R phase, the shape of the diffuse Bragg sheets begins to change and additional diffuse scattering components appear around the position of future out-of-plane reflections. This effect was observed in DOPC during both synchrotron beam-times (cf. chapter 5). A detailed analysis and explanation can not yet be provided. A feasible explanation could be that isolated and transient stalks or a “stalk fluid” without long-range correlations form at bilayer separations slightly above the L/R phase transition.

4.5.2 Bilayer structure

For further analysis, only data corresponding to RH above this transition region were used. The corresponding RH intervals are listed in Tab. 4.2. Fig. 4.10 summarizes the obtained results on lipid bilayer structure.

⁹ Note that the normalization by Eq. (4.28) is still valid since $|F_1|$ increases, which is not visible in Fig. 4.9d.

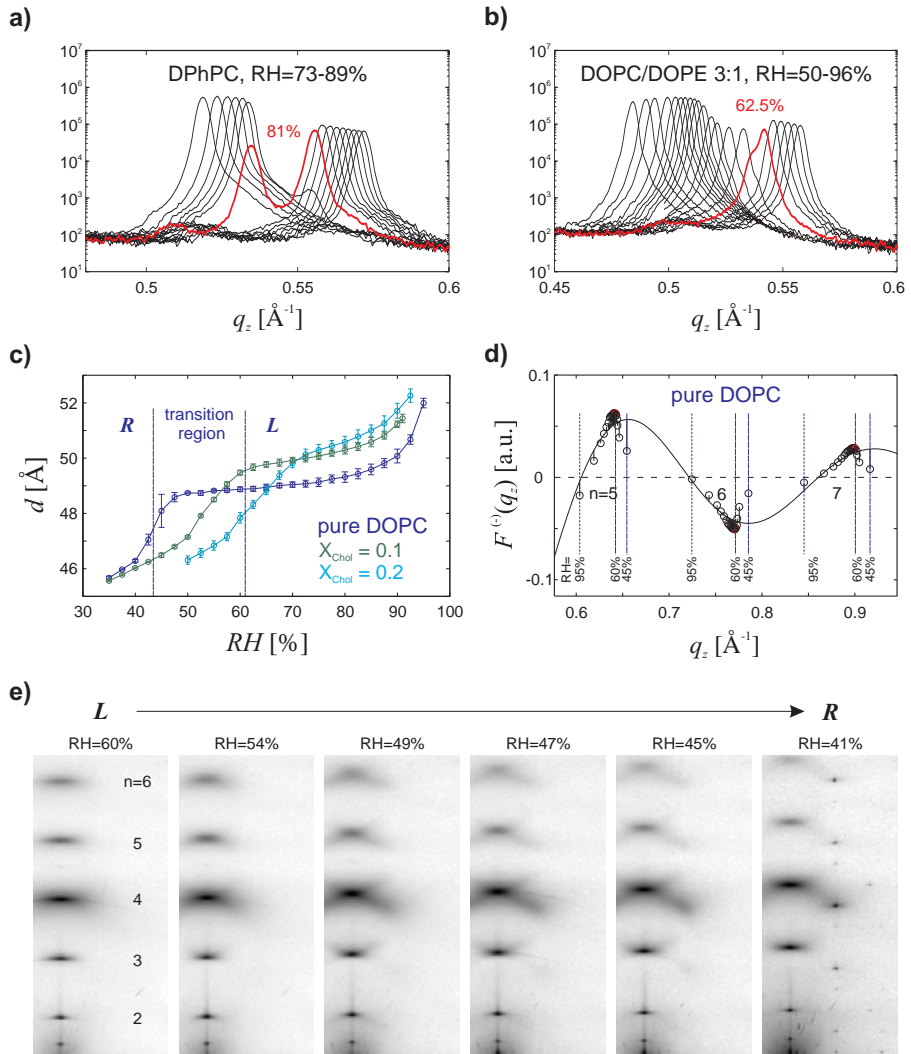


Figure 4.9: (a) 4th Bragg peaks of DPhPC and (b) DOPC/DOPE 3:1 over the entire applied RH intervals. Curves indicating the L/R phase transition are shown in red. (c) Lattice constant d in DOPC/Chol mixtures. Dashed vertical lines indicate inflection points of the curve $d(\text{RH})$ of DOPC. (d) In this transition region, agreement of the discrete samples $|F_{n,\text{RH}}|$ and the continuous form factor reconstructed from all datapoints in the L phase becomes worse. (e) Also GIXD patterns in this interval indicate structural changes (MS beamline, cf. section 5.1.1). The shape of the Bragg sheets changes and considerable diffuse scattering is visible at RH levels slightly above the appearance of sharp out-of-plane reflections.

For all investigated samples, sufficient osmotic pressure to reduce d'_w to about $9 \pm 0.5 \text{ \AA}$ has to be applied until the observed transition region begins. In case of lipid mixtures, both DOPE and Chol facilitate dehydration of lipid bilayers, indicated by a shift of the curve $d'_w(RH)$ to the right. It is well-known in the literature that PE lipids imbibe less water than PC lipids at full hydration. For the lipid mixtures eggPC and eggPE, the number of water molecules per lipid molecule at full hydration has been given as 23 and 12, respectively [74, 75, 167]. Interestingly, our data show that the difference in hydration between PC and PE is not associated with a corresponding change of the critical value of d'_w at which stalk formation occurs.

The headgroup-headgroup thickness d_{hh} increases upon dehydration for all samples. In the applied RH ranges, this effect is strongest for the case of DOPC where d_{hh} increases about $\approx 10\%$. If the molecular lipid volume remains approximately constant [125, 168], this indicates a simultaneous decrease of the cross-sectional area per lipid headgroup A_L in the bilayer plane about the same percentage, which also reduces the number of bound water molecules per lipid [47]. A part of the work performed by application of osmotic pressure goes into bilayer deformation. For the case of the lipid mixture eggPC and using the assumptions of the gravimetric method, this contribution has been estimated to constitute a fraction of about 10% [125].

The structure of DOPC bilayers between full hydration and the L/R phase boundary has recently been investigated by energy-dispersive x-ray diffraction [169]. In comparison to this study, we note that the number of reflections n_{\max} used by us is higher (8 *vs.* 5), our experimental error in d is considerably smaller and we incorporate a sign change of v_2 at $RH \approx 70\%$, while the authors in [169] use a fixed phase combination $- - + - +$. Contrary to our results, they do not report any observations that indicate structural changes in the bilayer stack between $RH \approx 45 - 60\%$.

In case of DOPC/Chol samples, the bilayer thickness quantified by d_{hh} increases with cholesterol content. This effect has been observed previously in our group by B. WEINHAUSEN [142] for $RH > 90\%$ and can be explained by the preference of cholesterol to reside primarily in the hydrocarbon region, where it increases the conformational order and thus extent of acyl chains [37, 170]. Our values d_{hh} closest to full hydration are in very good agreement with those in [41].

4.5.3 Hydration force parameters

Each reconstructed electron density profile yields the water layer thickness $d'_w = d - d_{hh}$. Combined with the applied osmotic pressure Π (Eq. 4.4), this yields samples of the pressure-distance relation $\Pi(d'_w)$. When plotted on semilogarithmic scale, the datapoints are approximately located on a straight line for each lipid composition (Fig. 4.11), thus confirming a total repulsive pressure that can be described empirically by an exponential decay. The hydration force parameters P_0 and λ_h and corresponding standard errors were therefore obtained by fitting the function $\Pi(d'_w) = P_0 \exp(-d'_w/\lambda_h)$ to the experimental data.

For several lipid compositions, more than one series of reflectivity scans were conducted. In this case, P_0 and λ_h are the weighted means of the individual results. All obtained results are summarized in Tab. 4.2. Importantly, these are valid only for the

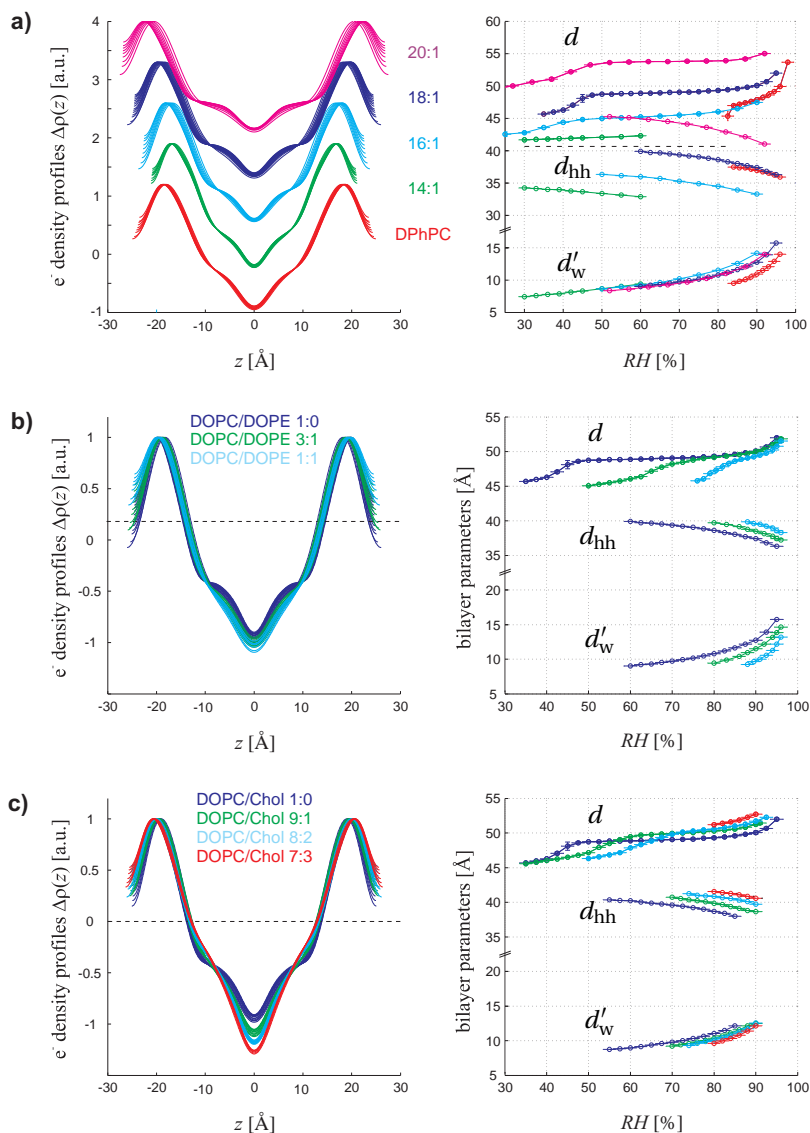


Figure 4.10: Electron density profiles and corresponding bilayer data d_{hh} and d'_w for (a) pure lipids which display the stalk phase, (b) DOPC/DOPE and (c) DOPC/Chol mixtures. Both DOPE and Chol facilitate dehydration of lipid bilayers, indicated by the shift of the curves $d'_w(RH)$ to the right. Cholesterol, in addition, leads to an increase in bilayer thickness and a more pronounced electron density minimum in the methyl trough region around $z = 0$.

chosen definition of d'_w , which has to be considered for future use. As visible in Fig. 4.11, the datapoints for the lowest values of Π tend towards larger values of d'_w . In addition to the hydration pressure, the undulation pressure may become relevant at these inter-bilayer distances.

In case of pure lipid bilayers, the role of DPhPC is striking. Despite an identical phosphatidylcholine headgroup, its hydration pressure amplitude P_0 is about one order of magnitude smaller than those of the di-monounsaturated lipids. The values for di14:1PC are based on a smaller interval in Π and should therefore be used with caution.

Literature values of the hydration force parameters P_0 and λ_h for lipids relevant to stalk phase formation used in this work could be found only for pure DOPC and DOPC/-DOPE where $X_{\text{DOPE}} = 0.75$ [74, 68, 156, 157]. Their limited applicability was discussed above. Due to different underlying assumptions and definitions of d'_w , the values of P_0 cannot directly be compared. However, we note that our value $\lambda_{h,\text{DOPC}}$ is closer to the 2.2\AA given in [68, 157] and 2.1\AA given in [74] than to that of 2.9\AA in [156].

Upon addition of Chol or DOPE, a reduction of the hydration pressure amplitude P_0 by about one order of magnitude is observed for the largest molar fractions. At the same time, λ_h increases about $\sim 50\%$. In case of cholesterol, these general trends agree with the observations made on eggPC/Chol samples by the EDP method [87]. Results for the system eggPC/Chol have also been reported by the gravimetric method [74], indicating an increase of P_0 by three orders of magnitude from pure eggPC to an equimolar eggPC/cholesterol mixture. This is in striking contrast to our observations and those in [87] and emphasizes once again that results obtained by the gravimetric method should be used with great care.

lipid or lipid mixture	P_0 [$10^9\text{J}\cdot\text{m}^{-3}$]	λ_h [\AA]	RH interval	samples
di14:1PC	4.13 ± 0.38	2.29 ± 0.06	50 – 70	1
di16:1PC	2.62 ± 0.45	2.56 ± 0.12	50 – 90	1
di18:1PC (DOPC)	3.35 ± 0.37	2.35 ± 0.06	60 – 95	2
di20:1PC	3.19 ± 0.77	2.34 ± 0.14	50 – 90	1
DPhPC	0.39 ± 0.04	3.50 ± 0.11	82 – 94	1
DOPC/Chol 90:10	1.57 ± 0.10	2.56 ± 0.04	67.5 – 95	3
DOPC/Chol 80:20	1.24 ± 0.09	2.66 ± 0.05	72.5 – 95	3
DOPC/Chol 70:30	0.43 ± 0.11	3.22 ± 0.24	84 – 95	2
DOPC/DOPE 75:25	0.62 ± 0.07	3.21 ± 0.12	76 – 94	1
DOPC/DOPE 50:50	0.24 ± 0.04	3.68 ± 0.23	85 – 94	1

Table 4.2: Hydration force parameters of the investigated lipids and lipid mixtures and corresponding RH interval of the pressure-distance relation (cf. Fig. 4.11). In several cases, the results are the weighted means of two or three independent measurements per lipid composition.

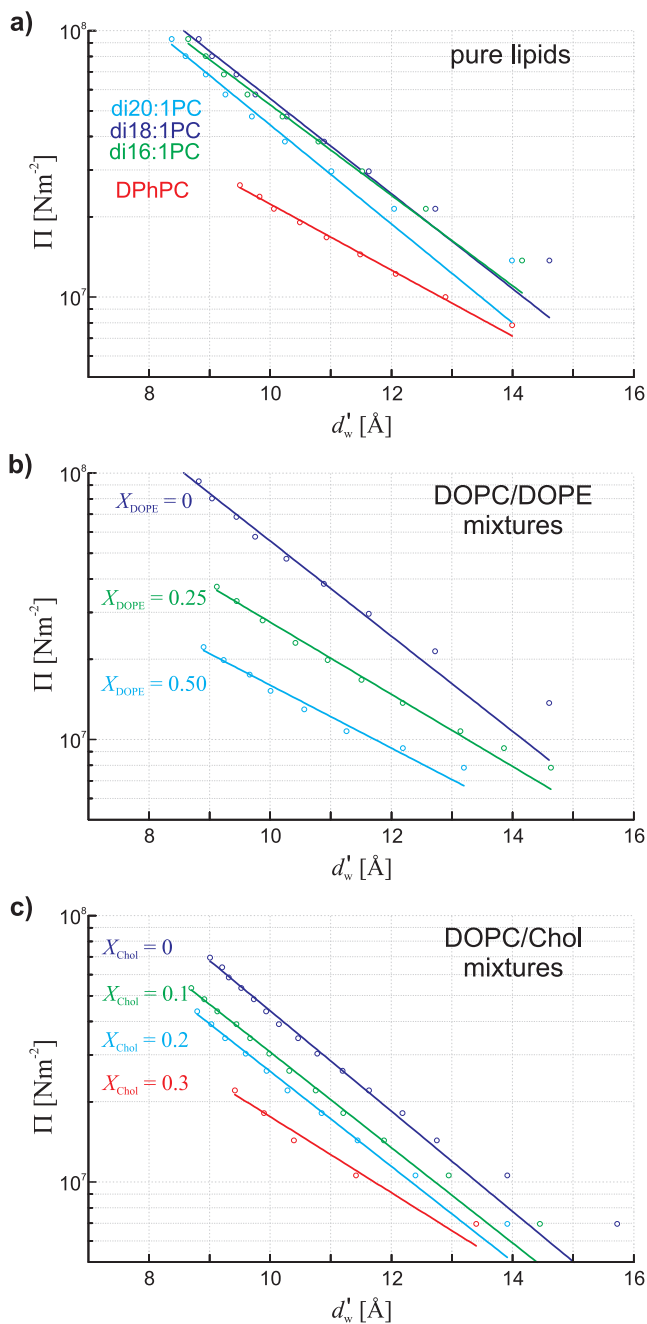


Figure 4.11: Pressure-distance curves Π vs. d'_w (circles) and exponential fits (solid lines) yielding the hydration force parameters P_0, λ_h . For pure DOPC, two different datasets are shown.

After presentation of our results and comparison to the literature, we discuss a feasible explanation of the observed changes in bilayer repulsion. GEVC and MARSH described the hydration pressure by an electrostatic model where the dipoles in the phospholipid headgroup region (*cf.* Fig. 1.1) lead to an orientation of water molecules [73]. This, in turn, gives rise to the repulsive hydration pressure when two bilayers are forced into close contact (*cf.* section 1.4). They obtained the expression

$$P_0 = \frac{2\epsilon_0(\epsilon - 1)}{\epsilon} \cdot \left(\frac{\Psi}{\lambda_h}\right)^2 \quad (4.30)$$

for the hydration pressure amplitude.¹⁰ Ψ denotes the dipole potential and Ψ/λ_h the polarizing electrical field of the lipid bilayer [75]. The quadratic dependence of P_0 on Ψ has been confirmed experimentally [172].

In single-component bilayers, an increase of the cross-sectional area A_L per lipid would lower the dipole density and thus reduce P_0 . Tab. 4.3 shows recent values of A_L for the phosphatidylcholines used in this work. These correlate very well with our data on the critical relative humidity RH^* of the L/R phase boundary, and also with the hydration pressure amplitude P_0 , taking into account the experimental errors. The larger A_L , the larger RH^* and the smaller P_0 . The strikingly different values of RH^* and P_0 for DPhPC compared to the di-monounsaturated lipids are well compatible with its large A_L . Within the four di-monounsaturated lipids, the order of A_L reflects the values of RH^* obtained by us. If the propensity for R phase formation was determined by bending energy, one would expect RH^* to decrease from 14:1PC to 20:1PC, since the bending modulus κ is expected to increase quadratically with hydrocarbon chain length [86]. Our results on RH^* , which were confirmed by repeated measurements, clearly indicate that this is not the case.

In this spirit, SIMON proposed that a common mechanism of membrane fusogens could be to increase the area per lipid and hence decrease the dipole density in the headgroup region [168]. The preferred location of Chol in a lipid bilayer has been described by the so-called *umbrella model* [173]. Due to its largely unipolar character,

lipid	A_L [\AA^2]	RH^* [%]	P_0 [10^9Nm^{-2}]
di14:1PC	64.2	21	4.13 ± 0.38
di16:1PC	65.8	37	2.62 ± 0.45
di20:1PC	66.6	39	3.19 ± 0.77
di18:1PC	66.9	43	3.35 ± 0.37
DPhPC	80.5	81	0.39 ± 0.04

Table 4.3: Pure lipids investigated in this thesis sorted according to the critical value RH^* of the L/R phase transition, which was confirmed by repeated measurements. The propensity for R phase formation correlates very well with recent values of the area per lipid headgroup at full hydration A_L taken from [138, 176].

¹⁰Note that, in our analysis, P_0 is an empirical fit parameter which applies only for the chosen definitions on bilayer structure. No assumptions about its physical origin are made.

Chol accumulates in the hydrocarbon region of the bilayer, its single OH group (*cf.* Fig. 1.1) constituting the polar part of the molecule is located at the hydrocarbon/lipid headgroup interface. The average area A_L per lipid molecule (PC and Chol) decreases upon addition of Chol, known as the *condensing effect* [170]. However, A_L per PC molecule increases [174], which in total may lead to a decrease of the dipole density and thus explain the observed decrease of P_0 .

Increasing A_L by membrane tension has been discussed as a possible mechanism by which proteins could facilitate membrane fusion [175]. Lateral tension is a key parameter in simulations of bilayer fusion [58]. Spreading lipid headgroups apart could also facilitate the formation of solvent-exposed lipid tails prior to stalk formation, which has recently been proposed as the rate-determining step in membrane fusion [53]. However, studying lateral tension is out of the scope of the methods used in this work.

4.5.4 Hydration barrier for membrane fusion

In chapter 6, values of 40–50 Å are obtained for the diameter d_s of the stalk neck region (*cf.* Fig. 6.1). The area $A_s = \frac{\pi}{4} d_s^2$ can be considered the minimum area on which two bilayer patches must be brought into close contact to induce hemifusion. The associated work given by Eq. 4.9,

$$W_{\text{hyd}}^{\text{min}} = A_s \lambda_h P_0 \exp\left(-\frac{d'_{\text{w,crit}}}{\lambda_h}\right), \quad (4.31)$$

is therefore a lower bound for the “hydration barrier” for membrane fusion. In Fig. 4.12a, $W_{\text{hyd}}^{\text{min}}$ is plotted for $A_s = 20 \text{ nm}^2$, $d'_{\text{w,crit}} = 9.0 \pm 0.5 \text{ Å}$ and the values P_0, λ_h from Table 4.2. The maximum molar fractions of Chol or DOPE reduce $W_{\text{hyd}}^{\text{min}}$ by more than 50%. *Vice versa*, if Chol or PE are removed from membranes, the energy to overcome the hydration barrier that needs to be provided by fusion proteins increases. This may *e.g.* explain why depletion of cholesterol prevents viral entry mediated by several viral fusion proteins [177]. For the area $\sqrt{3}a^2/2 \approx 40\text{--}50 \text{ nm}^2$ per stalk in the stalk phase, $W_{\text{hyd}}^{\text{min}}$ has to be multiplied by a factor of 2–2.5, yielding $\sim 80\text{--}200 k_B T$ per stalk for the used lipid compositions. Following KOZLOVSKY *et al.* [55], the energy $W_{\text{hyd}}^{\text{min}}$ may be released during stalk formation, since the hydration repulsion vanishes on the area A_s , and thus compensate for the energy required for lipid monolayer deformation.

In a similar fashion, one can estimate the hydration barrier to establish a minimum distance of $z_{\text{min}} = d'_{\text{w,crit}}$ for stalk formation between a spherical vesicle of radius R and a planar membrane (Fig. 4.12b): In cylindrical coordinates, the hydration energy for an infinitesimal area element is

$$dW_{\text{hyd}}^{\text{vesicle}} = \lambda_h P_0 \exp\left(-\frac{z(r)}{\lambda_h}\right) r dr d\phi. \quad (4.32)$$

With $z(r) = d'_{\text{w,crit}} + R - \sqrt{R^2 - r^2}$, integration over r and ϕ yields

$$W_{\text{hyd}}^{\text{vesicle}} = 2\pi\lambda_h P_0 \exp\left(-\frac{d'_{\text{w,crit}} + R}{\lambda_h}\right) \cdot \int_0^R r \exp\left(\frac{\sqrt{R^2 - r^2}}{\lambda_h}\right) dr \quad (4.33)$$

$$\approx 2\pi\lambda_h^2 R P_0 \exp\left(-\frac{d'_{\text{w,crit}}}{\lambda_h}\right), \quad R \gg \lambda_h. \quad (4.34)$$

These energies are plotted in Fig. 4.12a as well, using a typical radius of a synaptic vesicle of $R = 20$ nm [178, 179]. Remarkably, for each lipid composition, $W_{\text{hyd}}^{\text{vesicle}}$ exceeds $W_{\text{hyd}}^{\text{min}}$ merely by a factor of ~ 2 and corresponds to 3-4 times the energy of $35 \pm 7 k_B T$ released during formation of a single SNARE complex [180]. Since synaptic vesicle membranes contain about 40 mol% cholesterol and considerable amounts of PE lipids and PIP₂ [178], the value $W_{\text{hyd}}^{\text{vesicle}}$ for the physiologically relevant case is probably lower than those shown in Fig. 4.12. Therefore, our results are compatible with recent observations that SNARE-mediated membrane fusion requires only 1-3 SNARE complexes [181, 182, 183] and provide the dominating role of hydration energies as a possible explanation.

Due to the discussed shortcomings of previous data P_0, λ_h based on the gravimetric method, these can yield very different results. For example, using $P_0 = 10^{9.6} \text{ Nm}^{-2}$ and $\lambda_h = 2.1 \text{ \AA}$ obtained for DOPC [74] and adding 10 \AA to d_{hh} as indicated in [75] to account for the lipid headgroup thickness, one obtains $W_{\text{hyd}}^{\text{min}} > 6 \cdot 10^3 k_B T$, which severely overestimates the hydration barrier.

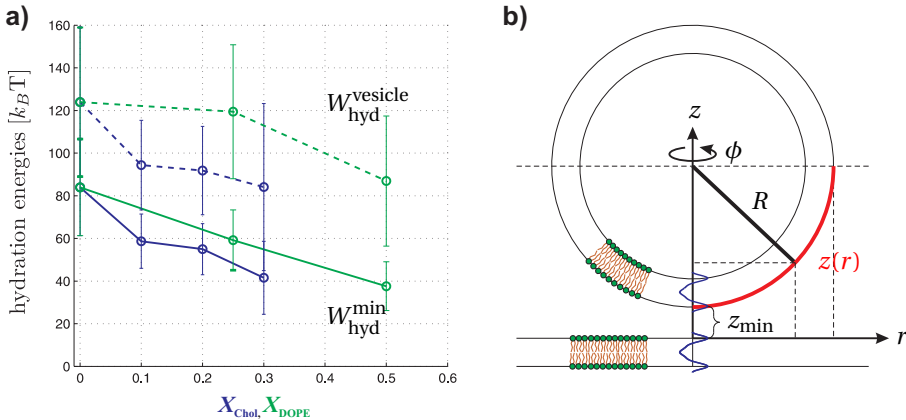


Figure 4.12: (a) Hydration barrier for establishing the distance $d'_{\text{w,crit}} = 9.0 \pm 0.5 \text{ \AA}$ between two parallel bilayer patches per cross-sectional area of a stalk ($W_{\text{hyd}}^{\text{min}}$) and between a spherical vesicle ($R = 20$ nm) and a planar bilayer ($W_{\text{hyd}}^{\text{vesicle}}$) as sketched in (b). Addition of 30 mol% Chol or 50 mol% DOPE reduces the hydration barrier by about 50%. All energies correspond to few times the energy $35 \pm 7 k_B T$ released during formation of a single SNARE complex.

4.6 Conclusions

This chapter described systematic studies of bilayer structure and interaction at close bilayer contact prior to stalk phase formation. To this end, the osmotic stress method and electron density profile analysis were used. Based on the obtained data, we conclude the following: The critical bilayer separation $d'_{w,crit}$ at which stalk phase formation is initiated is about 9Å for all investigated lipids and mixtures. Addition of cholesterol and DOPE shows no detectable effect on this value. These molecules rather facilitate dehydration and thereby shift the phase boundary between lamellar and rhombohedral phase towards lower osmotic pressure. The corresponding critical values RH^* of pure lipids correlate with the area per lipid headgroup at full hydration. The hydration force parameters obtained by us fill a gap in the literature and allow more reliable estimates *e.g.* of the work that fusion proteins must perform to bring bilayers into close contact. As a perspective for future work, the diffuse scattering observed close to the phase transition may contain additional information on stalk formation.

5 Structure determination of stalks

This chapter addresses the primary goal of this thesis: Studying stalk structures in the rhombohedral phase by x-ray diffraction. The required experimental methods have been introduced in chapter 2, regions in the phase diagram of several lipids and lipid mixtures where this phase exists have been identified in chapter 3. With this knowledge at hand, grazing-incidence x-ray diffraction data on the stalk phase of several phospholipids were recorded during two synchrotron beamtimes. In combination with additional in-house x-ray reflectivity and powder diffraction measurements, the crystallographic data for electron density reconstruction were obtained. The extended swelling method for the rhombohedral phase and additional criteria were then used for phase retrieval. All experimental aspects and data reduction are described here in detail. In the end, stalk structures in seven different lipid systems suitable for further quantitative analysis in the subsequent chapter are obtained.

5.1 Data collection and reduction

As demonstrated by our group, the electron density of stalks can be reconstructed using conventional sealed-tube laboratory diffractometers [31, 126, 132]. However, due to significantly higher beam quality in terms of brilliance [97], experiments at state-of-the-art synchrotron beamlines are required for optimum data quality and to push the obtainable resolution. Within the framework of this thesis, GIXD data were collected during two synchrotron beamtimes. The goal of these experiments was to obtain the maximum number of observable form factor amplitudes $\{|F_{hkl}|\}$ of out-of-plane reflections ($q_{\parallel} \neq 0$) as allowed by the inherent disorder of phospholipid samples (*cf.* section 2.6) of the stalk phases of several phospholipids. These data are combined with the form factor amplitudes $\{|F_{00\ell}|\}$ of in-plane reflections ($q_{\parallel} = 0$) obtained by reflectivity measurements performed in our laboratory as described for bilayer data in chapter 4.

A step of great practical importance is the subsequent relative normalization of these two sets of form factor amplitudes. From GIXD and reflectivity data alone, this is a highly nontrivial task. The form factor amplitudes recorded in each of these geometries result from a different number of crystallites due to the $2d$ powder character of the samples. In addition, effects such as mosaicity and crystallite size may affect the diffraction signal in both geometries in possibly different ways. In this thesis, additional powder measurements from true $3d$ powder samples are introduced to solve this issue.

5.1.1 Synchrotron GIXD experiments

Materials Science Beamline (Swiss Light Source)

Grazing-incidence x-ray diffraction data for the rhombohedral phases of the lipids di14:1-PC, di16:1-PC, di18:1-PC (DOPC), DPhPC and an equimolar lipid mixture of DOPC and DOPE were recorded at the Materials Science beamline (MS-X04SA) at the Swiss Light Source (SLS) at the Paul Scherrer Institute (PSI, Villigen, Switzerland). A

complete beamline layout and further background information is available *e.g.* from the web page of the beamline¹¹ and in [184]. The 2+3-circle surface diffractometer (Micro-Controle Newport) at the surface diffraction endstation (experimental hutch 2) was used with horizontal sample surface orientation. The sample stage is mounted on a hexapod. A double-crystal monochromator consisting of two Si(111) crystals was used to select the photon energy $E = 19.5 \text{ keV}$ corresponding to a wavelength of $\lambda = 0.6358 \text{ \AA}$ from the wiggler beam. The energy resolution has been determined previously as $\frac{\Delta E}{E} = 1.39 \cdot 10^{-4}$ [184]. The beam was collimated by a set of slits to a size of $200 \mu\text{m}$ in horizontal and $50 \mu\text{m}$ in vertical direction, yielding a primary intensity $I_0 = 2.4 \times 10^{10}$ photons per second. For some samples, the horizontal extent of the beam was reduced to $100 \mu\text{m}$. Diffraction patterns were recorded using a Pilatus II pixel detector (487×195 pixels with a size of $172 \times 172 \mu\text{m}^2$) mounted on the detector arm of the diffractometer at a fixed distance of $1140.8 \pm 0.25 \text{ mm}$ from the center of rotation. The path between sample and detector was evacuated by a flight tube. To correct for different detector pixel sensitivities, *flatfield* files were recorded using a piece of lead glass as a diffuse scatterer.

Aligned samples were prepared on $15 \times 10 \text{ mm}^2$ substrates few days before the trip to the synchrotron. During the beam time, they were stored in a fridge. Prior to a measurement, each sample was rehydrated in an atmosphere saturated with water vapour at room temperature for typically few hours. Samples were fixed by double-sided tape in a custom-built chamber shown in Fig. 5.1 optimized for application during the synchrotron beamtimes and connected to the setup for *RH* control described in section 3.2.2. The inner volume of the chamber of about 4 cm^3 allowed a fast response to changes in the *RH* setpoint. During sample alignment, *RH* was set to a value corresponding to the *L* phase of the used lipid. The windows of the chamber consisted of polypropylene foil with a thickness below $1 \mu\text{m}$ to minimize background scattering. No signals comparable to the Kapton ring visible in Fig. 3.6 for the other chambers could be detected. To suppress scattering from air, lead tape was used to cover the vast part of the entrance window and create a horizontal entrance slit just large enough for the primary beam.

During sample alignment, the beam intensity was attenuated by a factor of 10^6 . A user-defined region of interest on the detector around the primary beam position was used as a quasi-point detector. Translations and rotations of the sample were achieved by the hexapod, which allows to control all six degrees of freedom by pseudo-motors. The sample was first translated in vertical direction (motor hz) to move the lipid film into the beam center, indicated by a drop of intensity to 50%. At this position, the sample was rotated using motor oh to align the sample surface parallel to the beam (incident angle $\alpha_i = 0$) as indicated by an intensity maximum. Subsequently, the sample was translated in horizontal direction perpendicular to the beam (motor hx) to check if the substrate surface remained at the same position in the beam and thus the number of photons hitting the lipid film approximately constant for different regions of the sample. This was achieved by rotation about the axis parallel to the primary beam direction (motor hroy). This procedure was iterated several times until the obtained motor

¹¹<http://www.psi.ch/sls/ms/ms>

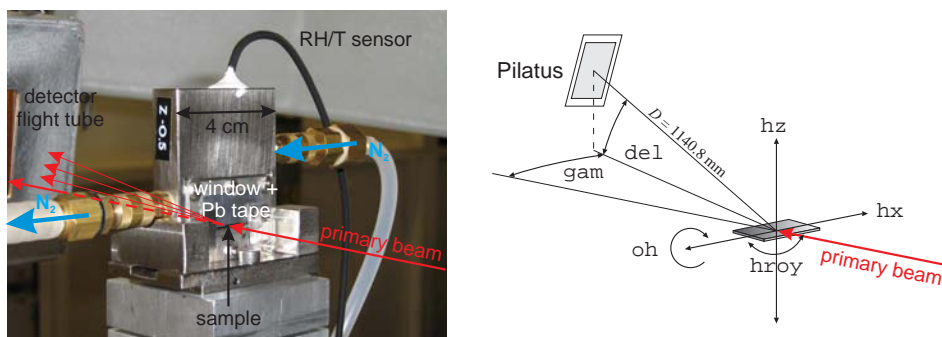


Figure 5.1: Sample chamber used during the synchrotron GIXD experiments and sketch of the setup and used motors at the MS beamline.

positions of hz , oh , $hroy$ remained approximately constant, indicating alignment of the substrate surface in the beam center and parallel to both the beam and the direction of translation (motor hx). The angle of incidence α_i was set to $\alpha_i \approx 0.15^\circ$ (motor oh), *i.e.* about 1.5 times the critical angle α_c of total external reflection from the silicon substrate for the used energy (Tab. 2.1). This angle was sufficiently small such that all reflections were located above the sample horizon. With a length of $l = 1$ cm of the sample in beam direction, the lipid film extends over $l \sin \alpha_i = 26 \mu\text{m}$ in z direction (*cf.* Fig. 2.7). Finally, the motor position hz was increased by $10 \mu\text{m}$ to reduce the fraction of the primary beam passing unhindered above the sample and thus reduce background scattering by air.

Since the active area of the detector did not subtend the entire region where diffraction peaks were visible, a complete diffraction pattern was obtained by combination of four slightly overlapping frames at different detector positions as sketched in Fig. 5.2. To this end, the motors del and gam moving the detector arm were used. At each position, a partial diffraction pattern was recorded with an exposure of 30 s. After each frame, the sample was translated along the beam (hx) to expose a fresh patch of the lipid film and prevent radiation damage. For the detector position recording the primary and specular beam ($del = gam = 0$), an attenuation factor of 10^3 was used. This cycle was repeated several (≥ 3) times for subsequent addition of corresponding frames and thus improvement of the signal-to-noise ratio. To allow for phase retrieval by the swelling method, data were recorded for at least 4 different RH levels with a typical stepsize of $\Delta RH = 2 - 3\%$ for each lipid.

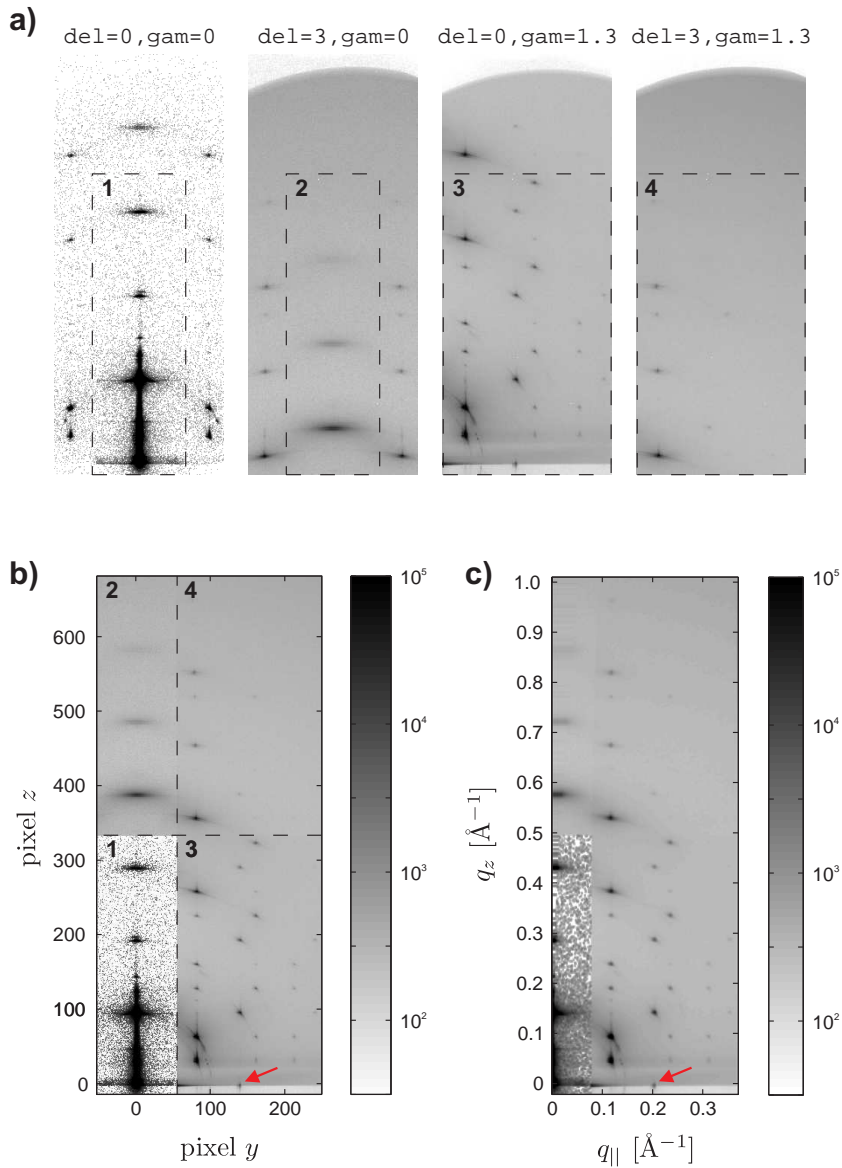


Figure 5.2: Conversion of grazing-incidence data recorded during the SLS beamtime to reciprocal space maps $I(q_{||}, q_z)$ (DPhPC, RH = 70%): **(a)** Pilatus frames, 487×195 pixel. In case of $\text{del}=\text{gam}=0$, an attenuator is used. **(b)** Composite diffraction pattern **(c)** Reciprocal space map obtained by transformation from pixel coordinates to the $(q_{||}, q_z)$ plane as explained in the main text. Arrows indicate the {110} reflection below the sample horizon which was obtained from powder diffraction data.

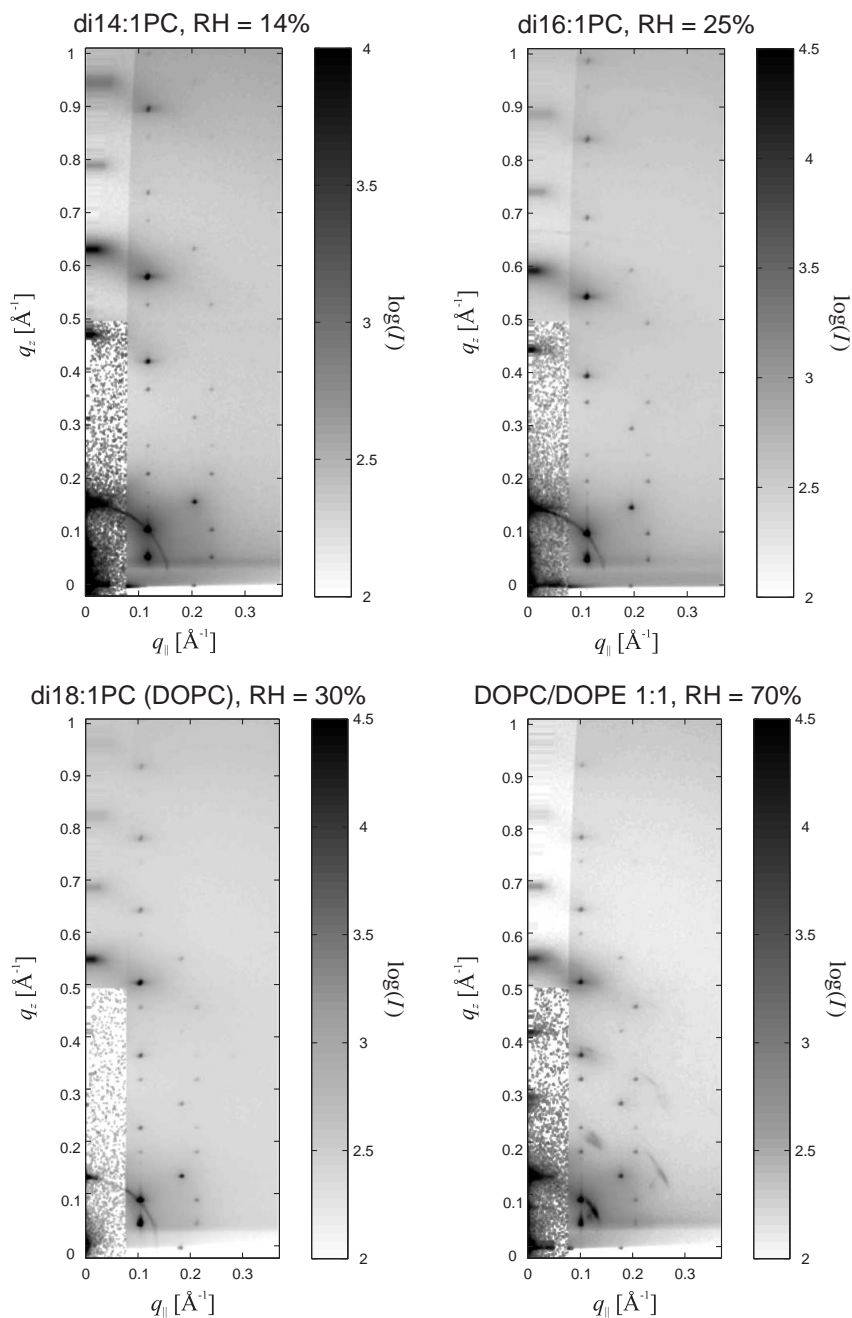


Figure 5.3: RSMs of further lipids recorded at the Materials Science beamline. The colormaps are adjusted to maximize the visibility of weaker diffraction peaks. In case of DOPC/DOPE 1:1, traces of a second phase, most likely H_{II} , are visible.

Beamline ID01 (European Synchrotron Radiation Facility)

GIXD data on DOPC/Chol samples were recorded in a different experiment at beamline ID01¹² at the European Synchrotron Radiation Facility (ESRF, Grenoble, France). A photon energy of 17 keV ($\lambda = 0.7293 \text{ \AA}$) was selected from the undulator beam by a double-crystal monochromator composed of two Si(111) crystals and collimated to a size of $500 \times 100 \mu\text{m}^2$. The resulting primary beam intensity was $1 - 2 \times 10^{10}$ photons per second, depending on the refill status of the storage ring. A Princeton CCD detector (1340×1300 pixels $48 \times 49 \mu\text{m}^2$ in size) mounted on the detector arm at distances of 495.1 ± 2.4 or 487.0 ± 1.8 mm to the sample was used to record diffraction patterns.¹³ The synchrotron sample chamber shown in Fig. 5.1 was mounted on the Huber tower of the ID01 diffractometer. A fast shutter was used to prevent exposition of the sample to the beam when no data were recorded.

Handling of the samples and sample environment were the same as described in the previous section. However, sample alignment was different, since no quasi-point detector was available. The sample height and angle of incidence were first varied in small steps (motors `hz`, `hai`) to find a position where the characteristic diffraction pattern of the rhombohedral phase was visible. This was achieved by direct visual inspection of diffraction patterns recorded with 1 s exposure. Sample alignment was then optimized such that no peaks were attenuated by the substrate, *i.e.* the (still unknown) angle of incidence α_i was sufficiently small, and the pattern was symmetric with respect to a line in z direction on the detector. Precaution was taken to assure that the fraction of the primary beam passing the chamber without hitting the sample was minimized in order to reduce scattering by air. At ID01 this issue was more severe than at the MS beamline, since no flight tube between sample and detector was available, and a strong background appeared if the sample position was too low.

Prior to data acquisition, several frames with different α_i were recorded to determine the distance between sample and detector from the positions of the specular reflections as described in [142]. The specular reflection and the first, very strong Bragg sheet were attenuated by an absorber strip mounted directly in front of the CCD. The size of the CCD allowed to record all visible diffraction peaks using a single detector position. The exposure for each frame was limited to 10 or 20 s before the CCD was read out. 30 to 50 equivalent frames were recorded for each RH level. Fig. 5.4 shows a typical diffraction pattern. The sample was translated along the beam to use the entire available sample area and prevent radiation damage. After a translation, the sample position in z sometimes had to be readjusted to keep the diffracted signal strong and at the same time background scattering weak. Note that changes in the illuminated sample volume are not a problem due to the normalization procedures applied later for the swelling method and for combination with reflectivity data as described below. Only the relative strength of reflections at one RH is required.

¹² *e.g.* <http://www.esrf.eu/UsersAndScience/Experiments/StructMaterials/ID01/>

¹³ Different values of D are due to the fact that the night shifts of the ESRF beamtime were dedicated to measurements of the chain correlation peak at $q \approx 1.4 \text{ \AA}^{-1}$, which required smaller D [142].

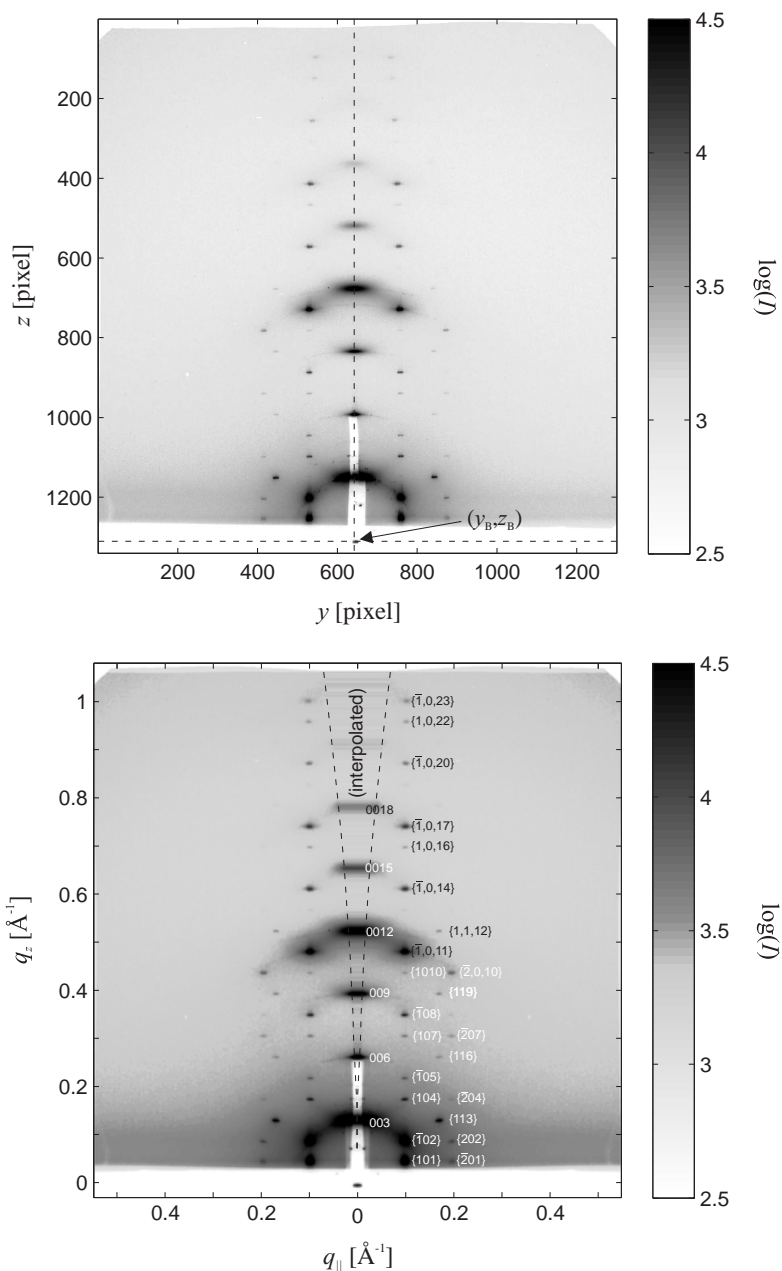


Figure 5.4: Raw diffraction pattern recorded at ID01 (DOPC/Chol, $X_{\text{Chol}} = 0.3$, $RH = 60\%$, sum of 50 frames of 10 s exposure) (top) and corresponding RSM obtained after polarization correction, left/right averaging, smoothing by a 3×3 box filter and transformation to (q_{\parallel}, q_z) coordinates (bottom).

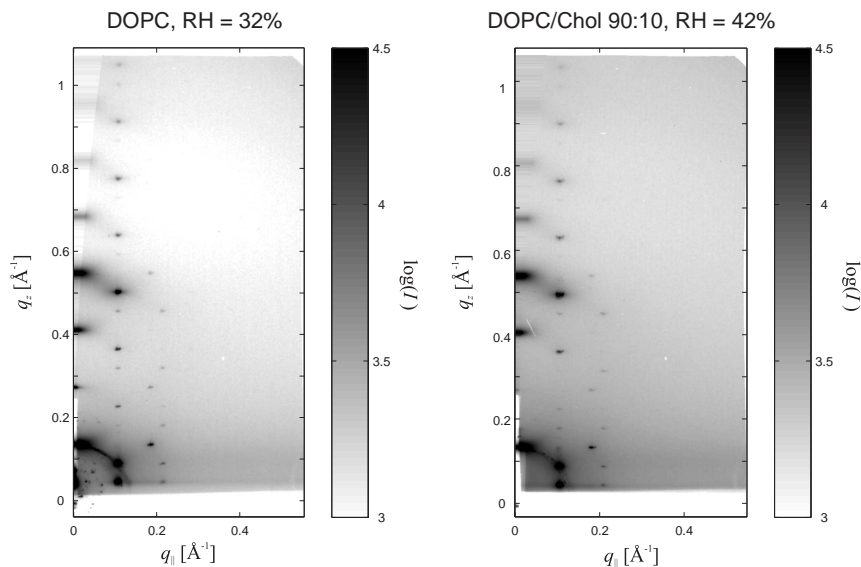


Figure 5.5: RSMs of pure DOPC and DOPC/Chol 90:10 recorded at ID01.

Data reduction

The MATLAB script `data_extraction_GISAXS.m` was written to process the data of both synchrotron experiments. The main steps are briefly explained in the following:

1. Data import

Prior to data analysis, ESRF data files in `.edf` format were opened in FIT2D and equivalent CCD frames were added. The resulting diffraction patterns with higher signal-to-noise ratio corresponding to an exposure of several minutes (Fig. 5.4) were saved in `.spr` format which can be opened by MATLAB. To import `.img` datafiles recorded at the MS beamline, the function `imagerread.m` written by R. HERGER and provided by the MS beamline was included.

2. Combination of frames to complete patterns (SLS data only)

After flatfield correction and elimination of dead pixels, frames recorded at four different detector positions were combined into a full diffraction pattern. This was achieved using the known steps in `del` and `gam` by which the detector was moved between the different positions and the angle of $0.00863^\circ \times 0.00863^\circ$ subtended by each detector pixel (Fig. 5.2).

3. Transformation to reciprocal space coordinates

For further analysis, it is convenient to convert diffraction patterns to reciprocal space coordinates (q_{\parallel}, q_z), *i.e.* scattering vector components parallel and perpendicular to the substrate surface. We call the obtained intensity distribution

$I(q_{\parallel}, q_z)$ a reciprocal space map (RSM). From Fig. 2.4, the angles α_f and ψ corresponding to each detector pixel are obtained as

$$\alpha_f = \arctan\left(\frac{\Delta z}{D}\right) - \alpha_i, \quad \text{and} \quad \psi = \arctan\left(\frac{\Delta y}{D}\right) \quad (5.1)$$

provided the active area of the detector is almost perpendicular to the primary beam. These angles are also used to perform the polarization correction. The subsequent transformation from (α_f, ψ) to (q_{\parallel}, q_z) based on Eq. (2.24) and (2.25) is then performed by a modified version of the function `scaling.m` written by B. WEINHAUSEN [142]. Again, recall that the lateral momentum transfer q_{\parallel} vanishes only at the positions of the primary beam and the specular reflection in a GIXD pattern (*cf.* section 2.2). After transformation to $I(q_{\parallel}, q_z)$, there is a wedge-shaped region along the q_z axis with no corresponding datapoints. These regions are filled by interpolation (Fig. 5.4, *bottom*). For ID01 data, the left and right half of a RSM were averaged.

4. Determination of lattice parameters

Since no additional information such as a powder pattern of a calibration standard was acquired for beam center determination, the following strategy was used to simultaneously determine beam center coordinates (y_B, z_B) and the lattice parameters a, d : Since sharp and distinct Bragg peaks are observed, we know that well-defined lattice constants a, d must exist. In a RSM, these follow from Bragg peak positions by Eq. (3.12). To assess errors in a and d , the mean and standard deviation of values obtained from different Bragg peaks are used. If the chosen (y_B, z_B) do not coincide with the actual beam center, the obtained lattice parameters are affected by a systematic error increasing their standard deviation. The correct choice of (y_B, z_B) therefore minimizes errors in a, d . To find these coordinates, we proceeded iteratively. First, approximate primary beam coordinates (y_B, z_B) were determined from the diffraction patterns. Using these, the transformation to (q_{\parallel}, q_z) was performed as described in the previous step. The lattice parameter d and its error $\sigma(d)$ were then determined as the mean and standard deviation of the values $d = 2\pi\ell/3q_{00\ell}$ obtained from the first five Bragg sheets (Fig. 5.6a). This was repeated for several values of z_B . Minimum error in d indicates a choice z_B closest to the actual beam center. Subsequently, the procedure was repeated with y_B and lattice parameter a . In this case, a was obtained from several pairs of peaks in the first and third off-axis column corresponding to $q_{\parallel} = 4\pi/\sqrt{3}a$ and $8\pi/\sqrt{3}a$ (Fig. 5.6b). The obtained lattice parameters are included in the formfactor tables in appendix A.2.

5. Indexing

Miller indices hkl were assigned to the reflections as described in section 3.3.3 using a nonprimitive hexagonal unit cell. In Fig. 5.4, the Miller indices corresponding to each peak are shown again. This time, the notation $\{hkl\}$ for a family of symmetry-related coinciding reflections is used. For example, $\{101\}$ denotes the $101, 0\bar{1}1$ and $\bar{1}11$ reflections (*cf.* Tab. A.1). Due to the assumption of a centrosymmetric unit cell and thus $F_{hkl} = F_{\bar{h}\bar{k}\bar{\ell}}$, diffraction peaks with $q_z < 0$

located below the sample horizon have a symmetry-related counterpart with $q_z > 0$. Therefore, it is sufficient to measure reflections in one quadrant in the upper half plane of $(q_{||}, q_z \geq 0)$ to obtain full information.

6. Peak integration and correction factors

The intensity $I(q_{||}, q_z)$ was first integrated in $q_{||}$ direction over several narrow intervals containing all diffraction spots of each peak series (Fig. 5.6c). The integrated peak intensities were then obtained from the one-dimensional profiles. For each peak, an interval of fixed width around the peak maximum was considered. The peak area equivalent to the integrated intensity $I_{hk\ell}$ was obtained by subtraction of linear background (Fig. 5.6d) and addition of the remaining intensity values. Up to a scaling factor K_{OPR} , the form factor amplitudes $\{|F_{hk\ell}|, |h| + |k| \neq 0\}$ of the out-of-plane peaks were obtained by

$$K_{\text{OPR}} \cdot |F_{hk\ell}| = \sqrt{q_{||} I_{hk\ell} / m_{hk\ell}} \quad (5.2)$$

using peak multiplicities $m_{hk\ell} = 3, 6, 3, 6, 6$ for the 1. to 5. off-axis column and $q_{||} \propto 1, \sqrt{3}, 2, \sqrt{7}, 3$ to take into account the Lorentz factor using the approximation $L \propto q_{||}^{-1}$ (cf. section 2.4).

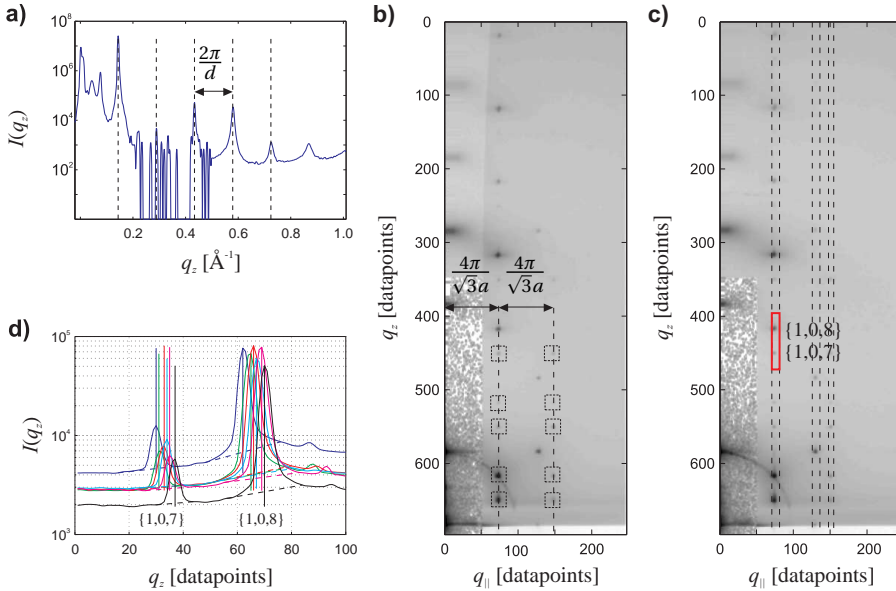


Figure 5.6: Determination of lattice parameters a, d and Bragg peak intensities $I_{hk\ell}$ from a RSM (di16:1PC): (a) d is determined from the Bragg sheet positions along q_z , (b) a from the positions of out-of-plane reflections in $q_{||}$. (c) Integration intervals in $q_{||}$ for each peak series. (d) The peak area in the resulting 1d profiles yields the integrated intensity $I_{hk\ell}$ corresponding to a family of reflections $\{F_{hk\ell}\}$.

5.1.2 X-ray reflectivity experiments

Additional x-ray reflectivity measurements were required to record the Bragg peaks along the q_z axis. Experiments were performed in the same way as for the bilayer data using our laboratory reflectometer described in section 4.4.1. For several hydration levels covering the RH range of the corresponding grazing-incidence dataset, the specularly reflected intensity was recorded using a stepsize of $\Delta\alpha_i = 0.005^\circ$, automatic attenuators and an exposure of 1 s per datapoint for reflections with $\ell \leq 15$ and 5 or 10 s for the weaker higher-order reflections. To speed up the measurements, only the intervals required for integration of the Bragg peaks were recorded. The time required for one RH level and 8 Bragg peaks was less than one hour.¹⁴ Reflectivity data obtained for pure DOPC and DOPC/Chol ($X_{\text{Chol}} = 0.3$) are shown in Fig. 5.7. No signs of sample deterioration or radiation damage such as changes in peak width or lineshape were observed. The raw data were processed and corrections applied as described in section 4.4.3, yielding 7 to 8 form factor amplitudes $\{K_{\text{IPR}} \cdot |F_{00\ell}|\}$ at several RH values covering the range in d of the corresponding synchrotron GIXD data. K_{IPR} denotes the experimental scaling factor.

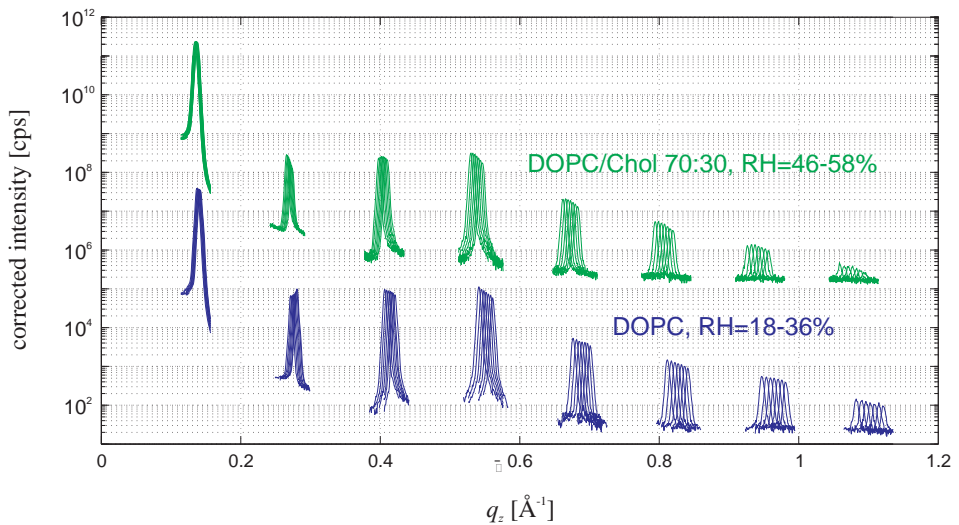


Figure 5.7: Reflectivity data of the rhombohedral phase of DOPC/Chol ($X_{\text{Chol}} = 0.3$, $\Delta RH = 2\%$) and pure DOPC ($\Delta RH = 3\%$). With lower RH , the peak positions moved to higher q_z , indicating a decrease in d .

¹⁴ In addition to the pure counting time, few seconds per datapoint are required for motor movements and finding the most appropriate attenuator.

5.1.3 Powder diffraction experiments

At this stage, the following problem due to the unusual $2d$ powder character of the samples occurs: For electron density reconstruction, two sets of form factor amplitudes

$$\{K_{\text{IPR}} \cdot |F_{00\ell}|\} \quad \text{and} \quad \{K_{\text{OPR}} \cdot |F_{hk\ell}|, |h| + |k| \neq 0\} \quad (5.3)$$

must be brought to a common scale. However, the two scaling factors K_{IPR} and K_{OPR} are unknown. To achieve relative normalization, the ratio $K_{\text{IPR}}/K_{\text{OPR}}$ is required. Obviously, this step is crucial to obtain correct structures $\Delta\rho(\vec{r})$ enabling a further analysis. The most straightforward way to achieve relative normalization is to measure form factor amplitudes corresponding to both groups in Eq. 5.3 on a common scale. To this end, the alignment of crystallites in the rhombohedral phase with respect to the substrate must be circumvented. This was achieved by preparing true $3d$ powder samples without preferred crystallite orientations.

Preparation of powder samples

For the powder measurements presented here, lipid solutions of concentrations of 0.5 or 1 g/ml were prepared. The considerably higher concentration compared to aligned samples was required to achieve sufficiently high scattering volumes. For each sample, $10 \mu\text{l}$ were pipetted onto an area of approximately $10 \times 2 \text{ mm}^2$ on a cellulose/polyester wiper (Durx 670, Berkshire) which served as a rough surface that does not, unlike the silicon substrates, induce a preferred crystallite orientation. Solvent extraction was achieved by evaporation in air and subsequent storage in vacuum in the same way as for the oriented samples. The sheet was then cut into several stripes about 2 mm in width. These were stacked on top of each other to increase the amount of lipid in the x-ray beam (Fig. 5.8a).

Instrumental setup and data collection

The basic powder diffraction geometry is shown in Fig. 2.5. We used the setup applied previously for phase diagram determination. The distance between sample and detector was increased to $D = 867.9 \pm 1.8 \text{ mm}$ as determined by silver behenate calibration standard. For this distance, no flight tube was available. A beamstop was placed directly behind the sample to remove the primary beam and thus reduce background scattering by air. For each lipid composition, powder diffraction patterns were recorded for several RH values covering the RH range of the corresponding grazing-incidence data. The exposure per frame was typically 3 or 4 hours. The observed L/R phase boundaries were in agreement with those found in chapter 3. A typical powder pattern of the rhombohedral phase is shown in Fig. 5.8(b).

Data reduction

For each sample, the beam center was determined by the “beam centre” function in FIT2D from about 20 manually selected points on the very strong ring corresponding to the 003 reflection. The script `data_extraction_powder.m` was then used for data

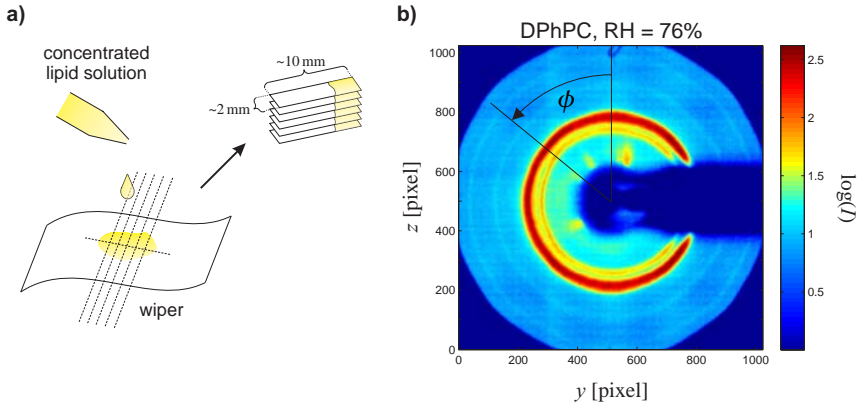


Figure 5.8: (a) Sketch of the preparation of powder samples and (b) powder diffraction pattern of the rhombohedral phase of DPhPC.

analysis. For each pixel, the corresponding modulus of the scattering vector was determined by (cf. Fig. 2.5)

$$q = \frac{4\pi}{\lambda} \sin \left[\frac{1}{2} \arctan \left(\frac{\sqrt{\Delta y^2 + \Delta z^2}}{D} \right) \right]. \quad (5.4)$$

The 2d array of intensity values was transformed to the 1d curve $I(q)$ by division of the measured q range into bins of $\Delta q = 0.0005 \text{ \AA}^{-1}$ and addition of the intensity values of all pixels falling into one bin, equivalent to integration over the azimuthal angle ϕ . A typical curve $I(q)$ is shown in Fig. 5.9. Values of ϕ corresponding to regions covered by the beamstop were excluded from the analysis.

The curves $I(q)$ show one strong double peak located in the q interval between 0.10 and 0.16 \AA^{-1} . The weaker peak of this pair corresponds to the $\{101\}$ reflections, whereas the stronger one contains contributions both from the overlapping $\{003\}$ and $\{102\}$ reflections due to the strongly broadened peaks as compared to GIXD and reflectivity data. Therefore, we denote the corresponding integrated intensity as I_{mix} . A further considerably weaker peak visible at higher q is compatible with Miller indices $\{110\}$. In reciprocal space maps obtained by GIXD, this peak is sometimes faintly visible along the q_{\parallel} axis (cf. Fig. 5.2), but attenuated by the substrate and therefore not suitable for further analysis. By powder diffraction, also the form factor amplitude $|F_{110}|$ becomes accessible.

To obtain lattice parameters and form factor amplitudes, the following empirical strategy was employed: For each peak, a Pseudo-Voigt (pV) profile, *i.e.* a linear combination of a Lorentzian (L) and a Gaussian (G) with the same center q_0 and full width at half maximum 2ω was assumed [185, 186, 187]:

$$pV(I, \eta, q, q_0, \omega) = I \cdot [\eta \cdot L(q, q_0, \omega) + (1 - \eta) \cdot G(q, q_0, \omega)] \quad 0 \leq \eta \leq 1 \quad (5.5)$$

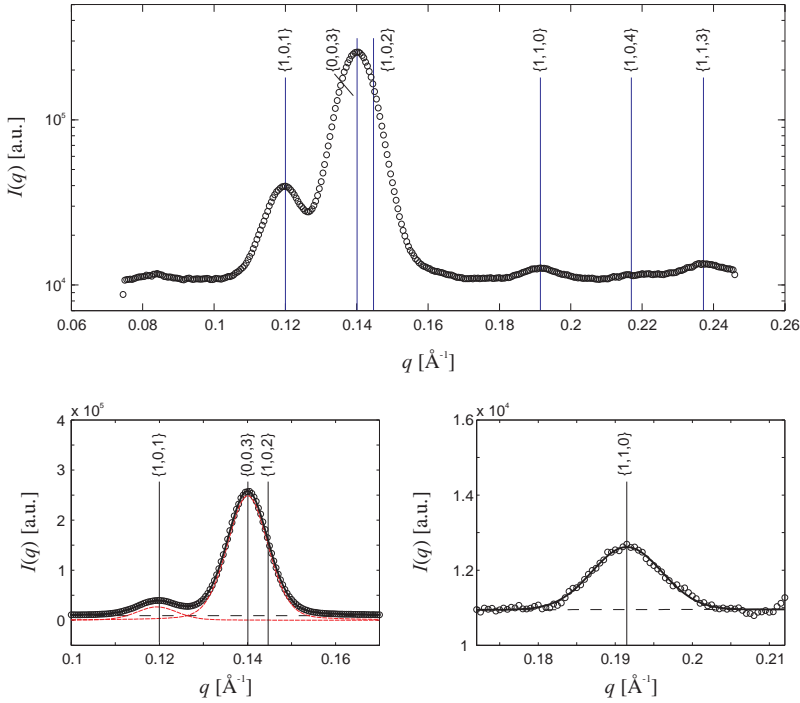


Figure 5.9: One-dimensional intensity profile $I(q)$ obtained from the diffraction pattern in Fig. 5.8 (top) and peak fitting (bottom). Vertical lines indicate the peak positions obtained after profile fitting. The $\{102\}$ and $\{003\}$ peaks strongly overlap and can not be separated. The integrated area of the resulting strong peak was decomposed into these two contributions as described in the text (DPhPC, $RH = 76\%$).

where

$$L(q, q_0, \omega) = \left[1 + \left(\frac{q - q_0}{\omega} \right)^2 \right]^{-1}, \quad G(q, q_0, \omega) = \exp \left[-\ln(2) \left(\frac{q - q_0}{\omega} \right)^2 \right]. \quad (5.6)$$

I denotes the peak amplitude and η the mixing parameter. The low-angle region of $I(q)$ containing the strong double peak was then fitted using a model composed of polynomial background up to quadratic order and two pseudo-Voigt peaks with the same ω and η . For the $\{110\}$ peak, a single pseudo-Voigt peak and an interval of $\pm 0.02 \text{ \AA}^{-1}$ around the approximate peak position was used. Peak fitting was performed by the MATLAB function `fminsearch`. Typical results are shown in Fig. 5.9. From the obtained fit parameters, integrated intensities I_{hkl} were obtained as the area

$$A_{pV} = \eta \cdot \pi \omega + (1 - \eta) \cdot \sqrt{\pi / \ln(2)} \omega \quad (5.7)$$

below a pseudo-Voigt peak. With the correction factors for the powder case provided in section 2.4, the corresponding form factors of the $\{101\}$ and $\{110\}$ reflections are

$$K_p \cdot |F_{hk\ell}| = \left[\frac{I_{hk\ell}}{m_{hk\ell} L_{hk\ell} P_{hk\ell}} \right]^{\frac{1}{2}}, \quad (5.8)$$

where K_p denotes the unknown scaling factor of a powder diffraction experiment. The mixed peak was assumed to contain both intensities I_{003} and I_{102} ,

$$I_{\text{mix}} = I_{003} + I_{102} \quad (5.9)$$

$$= K_p^2 \cdot [L_{003} P_{003} m_{003} |F_{003}|^2 + L_{102} P_{102} m_{102} |F_{102}|^2]. \quad (5.10)$$

This can be rearranged into

$$K_p \cdot |F_{003}| = \left[\frac{1}{L_{003} P_{003} m_{003}} (I_{\text{mix}} - L_{102} P_{102} m_{102} \cdot |F_{102}|^2) \right]^{\frac{1}{2}} \quad (5.11)$$

$$= \left[\frac{1}{L_{003} P_{003} m_{003}} \left(I_{\text{mix}} - L_{102} P_{102} m_{102} \cdot |F_{101}|^2 \cdot \left| \frac{F_{102}}{F_{101}} \right|^2 \right) \right]^{\frac{1}{2}} \quad (5.12)$$

$$= \left[\frac{1}{L_{003} P_{003} m_{003}} \left(I_{\text{mix}} - \frac{L_{102} P_{102} m_{102}}{L_{101} P_{101} m_{101}} \cdot I_{101} \cdot \left| \frac{F_{102}}{F_{101}} \right|^2 \right) \right]^{\frac{1}{2}} \quad (5.13)$$

The ratio $|F_{102}/F_{101}|$ is known from the grazing-incidence data and typically in the range of 1 to 1.5 for all samples investigated in this thesis (*cf.* appendix A.2). Since $I_{101}/I_{\text{mix}} \ll 1$, the second term in brackets in the above equation is only a small correction to $|F_{003}|$. The Lorentz and polarization factors follow from the lattice parameters a, d obtained from the fits and the peak multiplicities are $m_{003} = 1$, $m_{101} = m_{102} = 3$. Combination of Eq. (5.8) and (5.13) finally yields the form factor ratios

$$\left| \frac{F_{101}}{F_{003}} \right| =: c_{\text{norm}} \quad \text{and} \quad \left| \frac{F_{110}}{F_{003}} \right| \quad (5.14)$$

independent of an experimental scaling factor. c_{norm} is the ratio of the form factor amplitudes of the strongest in-plane and one very strong out-of-plane reflection. This allows to perform the relative normalization of GIXD and reflectivity data and put all formfactor amplitudes onto a common relative scale. In addition, powder measurements provide the form factor amplitude $|F_{110}|$ which is inaccessible by GIXD measurements.

A different method for relative normalization is described in [51, 101]. However, it can only be applied if in- and out-of-plane reflections are measured using the same instrument. In addition, to obtain exact values, the scattering volume must remain constant. This may be difficult to achieve in practice if translation of the sample along the beam is required to minimize radiation damage. For future experiments, one could place both oriented and powder samples in one sample chamber and record powder patterns of higher quality along with the synchrotron GIXD data. However, as will be demonstrated below, also the present strategy yields satisfactory results.

5.1.4 Combination of different X-ray geometries

Diffraction data in all three geometries, GIXD, reflectivity and powder, were recorded for several RH levels and thus values of d in the rhombohedral phase. For nominally identical RH , the d values were slightly different, which is due to limited precision of the used RH sensors, experimental errors in determination of d and possibly thermal history of the different samples. The lattice constant d is directly related to the hydration state of the samples and indicates the true hydration, rather than the measured RH value. We performed a linear interpolation of the reflectivity and powder data as a function of d as shown in Fig. 5.10 and 5.11. Each GIXD dataset at a given d was combined with the corresponding interpolated values of $\{K_{\text{IPR}} \cdot |F_{00\ell}|(d)\}$ from reflectivity data. Relative normalization was performed according to the condition

$$\frac{K_{\text{OPR}} |F_{101}(d)|}{K_{\text{IPR}} |F_{003}(d)|} \stackrel{!}{=} c_{\text{norm}}(d). \quad (5.15)$$

In addition, the form factor amplitude $|F_{110}|$ from powder data was added in a similar way. Finally, this yields complete datasets consisting of all measured form factor amplitudes $\{|F_{hkl}|\}$ on a common relative scale.

5.2 Solving the phase problem

The next step towards electron density reconstruction is to solve the phase problem. The swelling method as explained in section 4.4.5 can be extended the rhombohedral phase. The following derivation is based on YANG *et al.* [51]. The authors use a hexagonal prism of height d with the same volume $\frac{\sqrt{3}}{2} a^2 d$ as the primitive unit cell. The hexagonal footprint corresponds to the Wigner-Seitz cell of a $2d$ hexagonal lattice (*e.g.* Fig. 5.16). As will turn out later, this is the volume corresponding to one stalk between two planar bilayers. This choice is not a parallelepiped and thus no primitive unit cell in the conventional crystallographic sense. However, the rhombohedral phase can be obtained by combining these hexagonal prisms into layers and stacking the layers on top of each other in ABC fashion [51]. The center of the hexagonal prism is chosen as the origin and centrosymmetry $\rho(\vec{r}) = \rho(-\vec{r})$ is assumed. In analogy to the lamellar case, one starts from the form factor $F(\vec{q})$ (Eq. 2.37) and Fourier cosine series of $\rho(\vec{r})$ (Eq. 2.38) of a centrosymmetric unit cell:

$$F(\vec{q}) = \int_V \rho(\vec{r}) \cos(\vec{q} \cdot \vec{r}) dV \Leftrightarrow \rho(\vec{r}) = \frac{1}{V} \sum_{h,k,\ell} F_{hkl} \cos(\vec{q}_{hkl} \cdot \vec{r}) \quad (5.16)$$

Substitution of $\rho(\vec{r})$ by its Fourier series and use of the trigonometric identity $\cos \alpha \cdot \cos \beta = \frac{1}{2} [\cos(\alpha - \beta) + \cos(\alpha + \beta)]$ yields

$$F(\vec{q}) = \frac{1}{2V} \sum_{h,k,\ell} F_{hkl} \int_V \{\cos[(\vec{q} - \vec{q}_{hkl}) \cdot \vec{r}] + \cos[(\vec{q} + \vec{q}_{hkl}) \cdot \vec{r}]\} dV. \quad (5.17)$$

The vectors are split into components parallel and perpendicular to the substrate. If Miller indices corresponding to the nonprimitive hexagonal unit cell with $\alpha = \beta = 90^\circ$

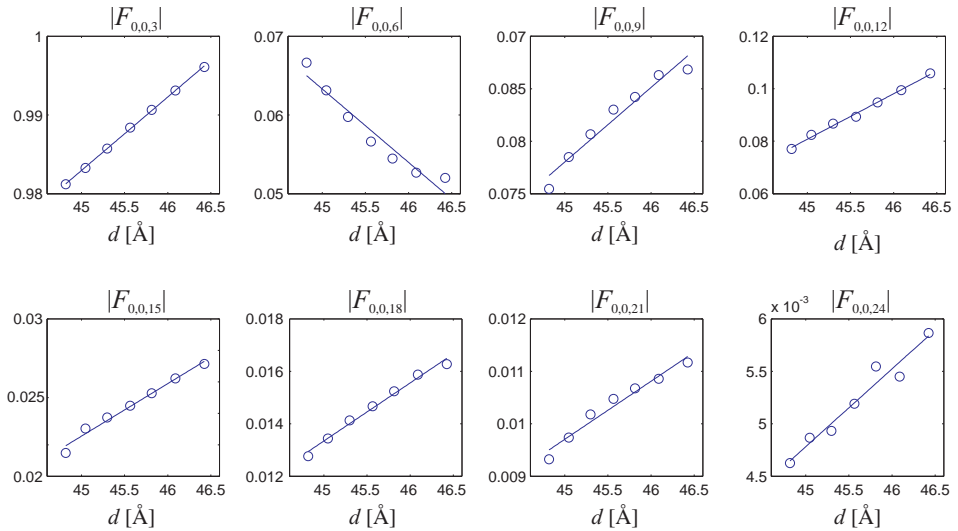


Figure 5.10: Linear interpolation of the form factor amplitudes $|F_{00\ell}|$ obtained by x-ray reflectivity measurements (DOPC, RH = 18 – 36%). The datasets of different RH levels were normalized according to Eq. (5.29).

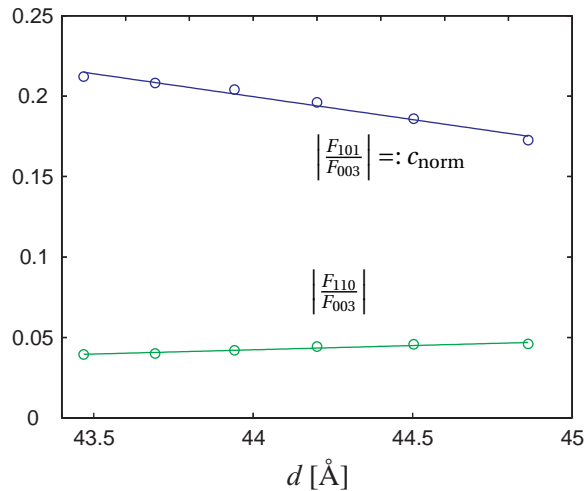


Figure 5.11: Form factor ratios $|F_{101}/F_{003}|$ and $|F_{110}/F_{003}|$ obtained by powder diffraction. Values corresponding to the d spacings of GIXD datasets are determined by linear interpolation (DPhPC, RH = 66 – 76%).

are used (Eq. 3.10), the parallel component of \vec{q}_{hkl} depends only on h, k and the perpendicular component only on ℓ :

$$\vec{q} = \underbrace{\begin{pmatrix} q_x \\ q_y \\ 0 \end{pmatrix}}_{\vec{q}_{\parallel}} + \underbrace{\begin{pmatrix} 0 \\ 0 \\ q_z \end{pmatrix}}_{\vec{q}_z} \quad \vec{q}_{hkl} = \underbrace{\begin{pmatrix} q_{hk,x} \\ q_{hk,y} \\ 0 \end{pmatrix}}_{\vec{q}_{hk}} + \underbrace{\begin{pmatrix} 0 \\ 0 \\ q_\ell \end{pmatrix}}_{\vec{q}_\ell} \quad \vec{r} = \underbrace{\begin{pmatrix} x \\ y \\ 0 \end{pmatrix}}_{\vec{r}_{\parallel}} + \underbrace{\begin{pmatrix} 0 \\ 0 \\ z \end{pmatrix}}_{\vec{r}_z} \quad (5.18)$$

With $\cos(\alpha + \beta) = \cos \alpha \cos \beta - \sin \alpha \sin \beta$, the integrands in Eq. (5.17) factorize into contributions parallel and perpendicular to the substrate depending only on h, k or only on ℓ , respectively:

$$\int_V \cos[(\vec{q} \pm \vec{q}_{hkl}) \cdot \vec{r}] dV = \underbrace{\iint_A \cos[(\vec{q}_{\parallel} \pm \vec{q}_{hk}) \cdot \vec{r}_{\parallel}] dx dy}_{=: C_{hk}^{\pm}(\vec{q}_{\parallel})} \cdot \int_{-\frac{d}{2}}^{+\frac{d}{2}} \cos[(q_z \pm q_\ell) \cdot z] dz \quad (5.19)$$

$$= C_{hk}^{\pm}(\vec{q}_{\parallel}) d \operatorname{sinc} \left[\frac{d}{2} (q_z - q_\ell) \right] \quad (5.20)$$

The continuous form factor then is

$$F(\vec{q}_{\parallel}, q_z) = \frac{d}{2V} \sum_{h,k,l} F_{hkl} \left\{ C_{hk}^+(\vec{q}_{\parallel}) \operatorname{sinc} \left[\frac{d}{2} (q_z + q_\ell) \right] + C_{hk}^-(\vec{q}_{\parallel}) \operatorname{sinc} \left[\frac{d}{2} (q_z - q_\ell) \right] \right\}. \quad (5.21)$$

In the swelling method for lamellar phases, the continuous form factor was considered as a function of q_z . In analogy, $F(\vec{q}_{\parallel}, q_z)$ is considered separately for each peak series in a diffraction pattern parallel to the q_z axis where $\vec{q}_{\parallel} = \vec{q}_{h',k'}$. In this case,

$$C_{hk}^{\pm}(\vec{q}_{h'k'}) = \iint_A \cos[\vec{q}_{h\pm h', k\pm k'} \cdot \vec{r}_{\parallel}] dx dy = \begin{cases} \frac{V}{d} & h = \mp h', k = \mp k', \\ 0 & \text{else.} \end{cases} \quad (5.22)$$

This result can either be obtained by explicit integration¹⁵ or inferred from the cosine waves sketched in Fig. 5.12. The case $\vec{q}_{h\pm h', k\pm k'} = 0$ is obvious. We obtain

$$F(\vec{q}_{hk}, q_z) = \frac{1}{2} \sum_{\ell} \left\{ F_{\bar{h}\bar{k}\ell} \operatorname{sinc} \left[\frac{d}{2} (q_z + q_\ell) \right] + F_{hk\ell} \operatorname{sinc} \left[\frac{d}{2} (q_z - q_\ell) \right] \right\}. \quad (5.23)$$

Due to centrosymmetry, $F_{\bar{h}\bar{k}\ell} = F_{hk\ell}$ and therefore [51]

$$F(\vec{q}_{hk}, q_z) = \sum_{\ell} \nu_{hk\ell} |F_{hk\ell}| \operatorname{sinc} \left[\frac{d}{2} q_z - \frac{\ell}{3} \pi \right], \quad h, k = \text{const.} \quad (5.24)$$

¹⁵ Consider the footprint of the unit cell sketched in Fig. 5.12. The sum of two reciprocal lattice vectors is another reciprocal lattice vector. Due to the symmetry of the cosine, consider only $x \geq 0$ and write the integration limits in y as $y = \pm(a-x)/\sqrt{3}$. Solving the double integral results in cosine terms that cancel each other.

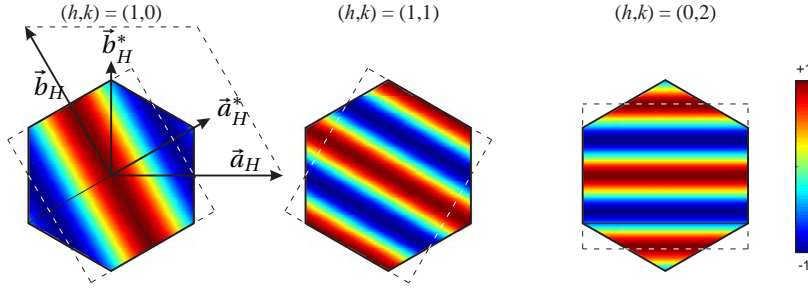


Figure 5.12: Sketch of partial waves $\cos(\vec{q}_{hk} \cdot \vec{r}_{\parallel})$. The sum of all contributions inside the hexagonal area is zero unless $\vec{q}_{hk} = 0$. For definitions of the lattice vectors see section 3.3.3.

This result is very similar to the lamellar case in section 4.4.5. Assuming that the underlying structure and thus $F(\vec{q}_{hk}, q_z)$ is approximately constant for different levels of hydration, Eq. (5.24) can be used in the same way as for the lamellar phases. After assigning correct phase factors $\{v_{hkl}\}$ to all reflections of a series with $h, k = \text{const.}$, the discrete datapoints $\{v_{hkl}|F_{hkl}\}$ corresponding to different hydration levels should approximately lie on a continuous form factor reconstruction obtained by Eq. (5.24). Form factor amplitudes $|F_{hkl}|$ corresponding to $\ell < 0$ are obtained because their symmetry-related counterparts with $|F_{\bar{h}\bar{k}\bar{\ell}}|$ are located in the upper half plane of reciprocal space (q_{\parallel}, q_z) .

To correct for changes in the scattering volume due to *e.g.* translation of the sample along the beam, datasets recorded at different hydration levels must be normalized with respect to each other. Similar to the case of lipid bilayers, this is achieved by requiring that $F(\vec{q}_{hk}, q_z)$ and hence $|F(\vec{q}_{hk}, q_z)|^2$ is approximately constant for slightly different hydration levels and thus [51] (*cf.* section 4.4.5)

$$\int_{-\infty}^{+\infty} |F(\vec{q}_{hk}, q_z)|^2 dq_z \stackrel{!}{=} \text{const.} \quad h, k = \text{const.} \quad (5.25)$$

$$= \sum_{\ell} \sum_{\ell'} F_{hkl} F_{hkl'} \int_{-\infty}^{\infty} \text{sinc}\left(\frac{d}{2}q_z - \frac{\ell}{3}\pi\right) \text{sinc}\left(\frac{d}{2}q_z - \frac{\ell'}{3}\pi\right) dq_z \quad (5.26)$$

$$= \sum_{\ell} \sum_{\ell'} F_{hkl} F_{hkl'} \underbrace{\frac{2}{d} \int_{-\infty}^{\infty} \frac{\sin(x)}{x} \cdot \frac{\sin[x + (\ell - \ell')\pi]}{x + (\ell - \ell')\pi} dx}_{= \begin{cases} \pi & \ell = \ell' \\ 0 & \text{else} \end{cases}} \quad (5.27)$$

$$= \frac{2\pi}{d} \sum_{\ell} |F_{hkl}|^2 \quad h, k = \text{const.} \quad (5.28)$$

For application of the swelling method to each peak series, the sets of form factor amplitudes at different hydration levels are normalized such that

$$\sum_{\ell} |F_{hk\ell}|^2 \propto d(RH), \quad h, k = \text{const.} \quad (5.29)$$

For lipid bilayers, our results in chapter 4 indicate an increase in bilayer thickness upon dehydration, thus rendering the assumption of constant lipid structure an approximation. However, the phase information obtained by the swelling method yield very reasonable bilayer electron density profiles. In the rhombohedral phase, the assumption of a constant lipidic structure has an even more approximative character, since there is no way to shrink a unit cell containing a continuous $3d$ lipid structure without changing the structure itself. The continuous form factor (5.24) must change slightly for different levels of hydration. Nevertheless, as shown below, the swelling method yields phase combinations that lead to reasonable electron density maps also for the case of rhombohedral phases, which justifies the approximations.

The data corresponding to in-plane reflections 00ℓ were treated using the script `swelling_reflectivity.m` already applied in the lamellar case. F_{000} was set to a fixed value of ± 0.8 , since no relation comparable to Eq. (4.21) is available for the rhombohedral phase. This choice improved the agreement of $F(\vec{q}_{hk}, q_z)$ and discrete datapoints for the case of most lipids.

For out-of-plane reflections obtained by GIXD, the script `swelling_GISAXS.m` was used. Its structure is very similar to `swelling_reflectivity.m`. Since the datapoints $\{|F_{hk\ell}|\}$ are subject to stronger experimental noise than the reflectivity data $\{F_{00\ell}\}$, one additional step was included: A straight-line fit was applied to each group of datapoints corresponding to fixed Miller indices $hk\ell$. The interpolated values were used for the swelling method (but not for electron density reconstruction) to suppress the effect of possible outliers. Continuous form factors $F(\vec{q}_{hk}, q_z)$ were reconstructed by Eq. (5.24) using the mean lattice constant d and the mean value of each form factor amplitude $|F_{hk\ell}|$.

Fig. 5.13 shows typical results of the swelling method. Swelling diagrams for all other datasets used in this thesis are provided in appendix A.2. For each peak series, the displayed curves correspond to the phase factor combination $\{v_{hk\ell} | h, k = \text{const.}\}$ out of 2^{N-1} possibilities (N denotes the number of reflections) minimizing the residual sum of squares

$$\sum_d \sum_{\ell} |v_{hk\ell} |F_{hk\ell, d}| - F(\vec{q}_{hk}, q_z)|^2 \stackrel{!}{=} \min. \quad (5.30)$$

Each combination is determined up to a total factor ± 1 , *i.e.* only the relative phase relations inside each peak series are obtained.

Considering the swelling diagrams, the following can be noted: In each series, the signs $\{v_{hk\ell}\}$ are typically alternating, *i.e.* signs of two adjacent reflections with $\Delta\ell = 3$ are different in most cases. This is related to the triplet relationship for centrosymmetric structures used in direct methods of crystallography: It can be shown that the signs corresponding to three reflections with

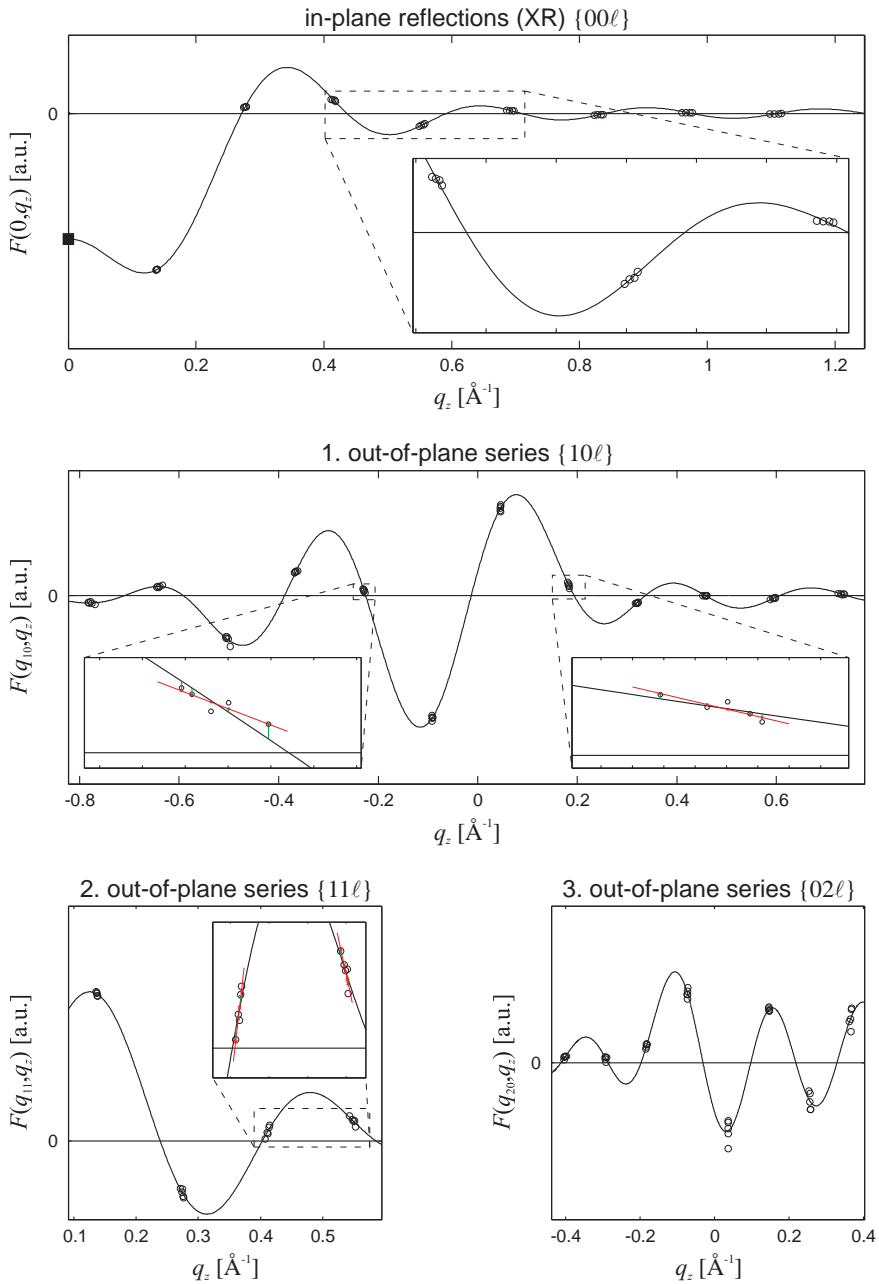


Figure 5.13: Swelling plots for the stalk phase of DOPC/DOPE 1:1 indicating the best phase combinations for each peak series. For $q_{||} \neq 0$, each group of datapoints (\circ) was fit by a straight line ($-$), the interpolated values (\times) were used to determine the residuals (\square).

$$\sum_{i=1}^3 \vec{q}_{h_i k_i \ell_i} = 0 \quad (5.31)$$

are likely to fulfil the condition

$$\prod_{i=1}^3 v_{h_i k_i \ell_i} = +1 \quad (5.32)$$

if the corresponding $|F_{h_i k_i \ell_i}|$ are all relatively strong [141, 188]. The underlying principle is sketched in appendix A.1. In all of our datasets, $|F_{003}|$ is by far the strongest form factor amplitude (*cf.* appendix A.2). Electron density maps which display one continuous region of elevated electron density separating two continuous regions of lower electron density are only obtained if $v_{003} = -1$. For triplets containing $\{003\}$, the triplet relationship makes

$$v_{hk\ell} \cdot v_{\bar{h}\bar{k}(\bar{\ell}-3)} \cdot v_{003} = +1 \quad (5.33)$$

likely. Due to centrosymmetry and for $v_{003} = -1$, this yields

$$v_{hk\ell} \cdot v_{hk(\ell+3)} = -1 \quad (5.34)$$

in agreement with the observed behaviour of $F(\vec{q}_{hk}, q_z)$. Importantly, this is a probabilistic statement for triplets of strong reflections. In the final version of the script `swelling_GISAXS.m`, only phase combinations with $v_{003} = -1$ and $v_{101} = -v_{102}$ were used, since these constitute the strongest triplet.

Subsequent to determination of the $\{v_{hk\ell}\}$ within each series by the swelling method, the relative phases between the four series were determined by considering all 8 possible electron density maps $\Delta\rho(0, y, z)$ and choosing the only one which leads to plausible electron density distributions (Fig. 5.14) [51].

For all lipids under investigation, the final phase combinations are very similar. Without exception, the phase factors $\{v_{11\ell}\}$ where $\ell = 3, 6, 9, 12$ were obtained as $+ - + +$ for all lipids. For the $\{110\}$ reflection determined from powder measurements, we used $v_{110} = -v_{113}$, in agreement with the triplet relationship. A slight ambiguity arises for the phase factors $\{v_{20\ell}\}$ where $\ell = -2, 1, 4, 7, 10$. For different datasets, both $+ - + - +$ and $- - + - +$ were obtained as the best combinations according to the swelling method. Based on the corresponding electron density maps in the x, y plane, we used the former choice because it leads to a more homogeneous and radially symmetric electron density in the lipid headgroup region (Fig. 5.15).

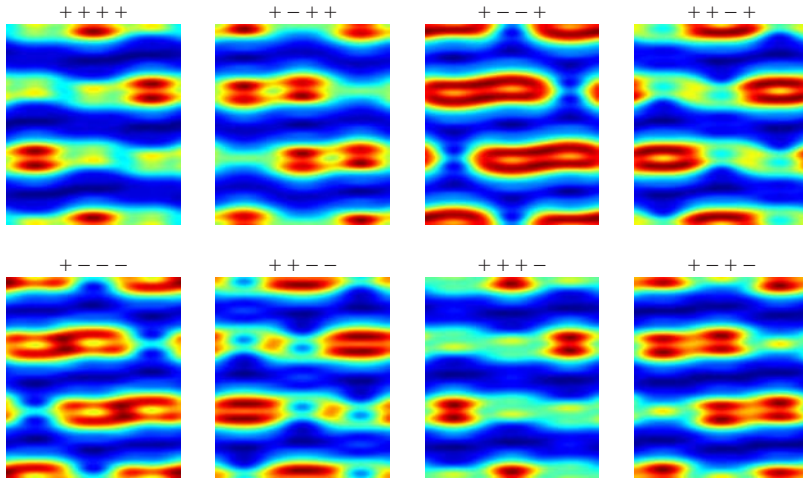


Figure 5.14: Electron density maps in the yz plane for eight possible combinations of the total phases of the four peak series $q_{\parallel} / \frac{4\pi}{\sqrt{3}a} = 0, 1, \sqrt{3}, 2$ after fixing the phase of the specular series to assure that $v_{003} = -1$ (DOPC/DOPE 1:1, RH = 68%). Only the phase combination $+ - - +$ is compatible with continuous lipid monolayers and typical molecular dimensions.

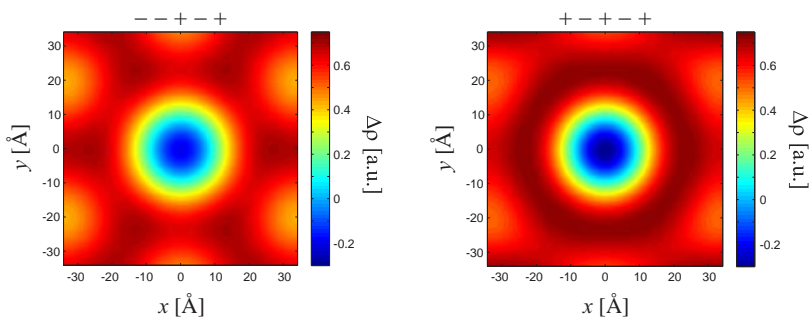


Figure 5.15: Electron density maps $\Delta\rho(x, y, 0)$ for two different phase combinations of the reflections $\{20\ell\}$. For some lipids, the signs $- - + - +$ were obtained by the swelling method. However, only the choice $+ - - - +$ leads to a smooth region of increased electron density with nearly circular symmetry and is therefore considered the correct one (DOPC, SLS, $d = 45.79 \text{ \AA}$).

5.3 Results

After data reduction and phase determination, the form factors $\{F_{hkl}\}$ of 26 to 37 independent (*i.e.* not symmetry-related) reflections are obtained for several hydration levels of 7 different lipids and lipid mixtures. All data used for electron density reconstruction are provided in appendix A.2. The electron density contrast $\Delta\rho(x, y, z)$, *i.e.* the deviation from the mean electron density in the unit cell, is constructed by

$$\Delta\rho(\vec{r}) = \sum_{h,k,l} v_{hkl} |F_{hkl}| \cos\left(2\pi\left[\frac{h}{a}x + \frac{2k+h}{\sqrt{3}a}y + \frac{\ell}{3d}z\right]\right) \quad (5.35)$$

and normalized such that $\max[\Delta\rho(\vec{r})] = 1$ for each RH level. Absolute scaling would require knowledge of the exact number of lipid and water molecules per unit cell and the form factor F_{000} encoding the mean electron density. The latter cannot be measured, since it corresponds to scattering in forward direction which coincides with the primary beam. For our purposes, absolute scaling is not required. In the electron density maps presented in this chapter, all diffraction peaks listed in the tables in the appendix were used. The phase relations within each peak series are those indicated as the best choices by the swelling method, with the exception of the third out-of-plane series $\{02\ell\}$ as explained above.

Fig. 5.16(a) shows slices of $\Delta\rho(\vec{r})$ for a region consisting of several nonprimitive hexagonal unit cells spanned by vectors $\vec{a}_H, \vec{b}_H, \vec{c}_H$ (*cf.* section 3.3.3). Regions of elevated electron density contrast (dark red) indicate continuous lipid headgroup regions. These separate two regions of lower or negative electron density contrast indicative of the hydrocarbon region (blue) or residual water. Within the xy plane, the hexagonal arrangement of stalks can readily be recognized. Lattice parameter a corresponds to the distance between the centers of adjacent stalks. From one layer to the next, the stalk centers are shifted with respect to each other. The hexagonal prism of height d corresponding to one stalk is indicated in all three slices. In Fig. 5.16(b), a perspective view of this volume is shown.

On the following pages, $\Delta\rho(\vec{r})$ is visualized for each lipid and one arbitrary RH value by slices through the hexagonal prism corresponding to one stalk, both in $3d$ representation (Fig. 5.17 and 5.18) as well as by $2d$ slices along the xy , xz and yz planes (Fig. 5.19 and 5.20). The maximum number N of obtained reflections indicated in each figure is used. In all cases, a strongly curved lipid monolayer reminiscent of the *cis* monolayer in stalk can clearly and unambiguously be recognized. Close to $z = 0$, the radius of curvature of the lipid headgroup region in the xz or yz plane can be estimated to be on the order of few Å.

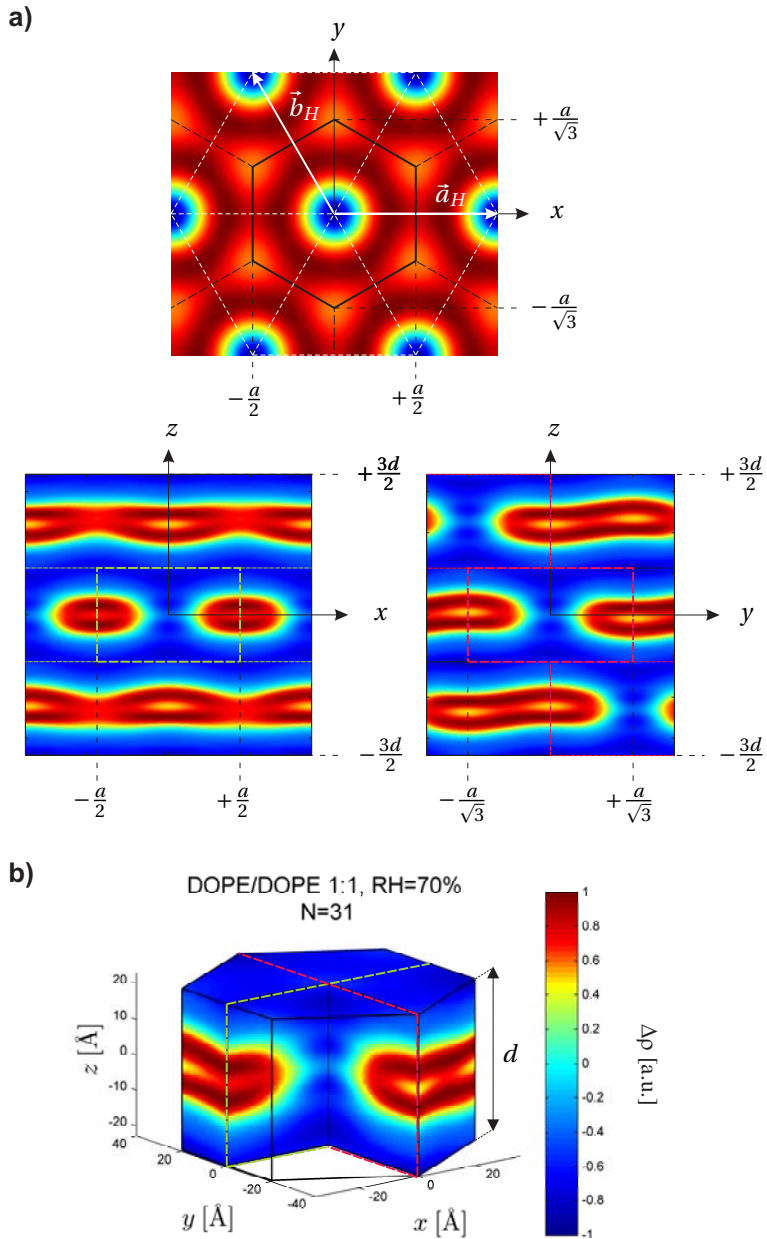


Figure 5.16: (a) Slices of $\Delta\rho(\vec{r})$ along the coordinate axes and (b) 3d representation of the hexagonal prism corresponding to one stalk (DOPC/DOPE 1:1, RH = 70%, N=31). The lattice constant a corresponds to the distance between adjacent stalks in one layer.

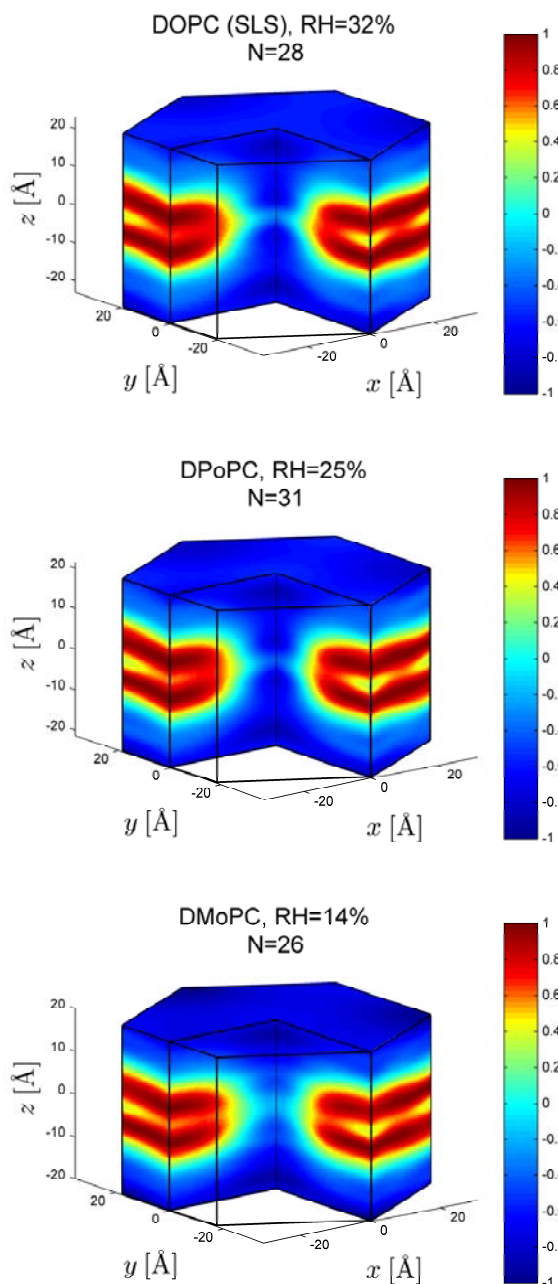


Figure 5.17: Representations of the hexagonal prism containing a single stalk for several lipids (DPOPC = dipalmitoleyl-PC = di16:1PC and DMOPC = dimyristoleyl-PC = di14:1PC).

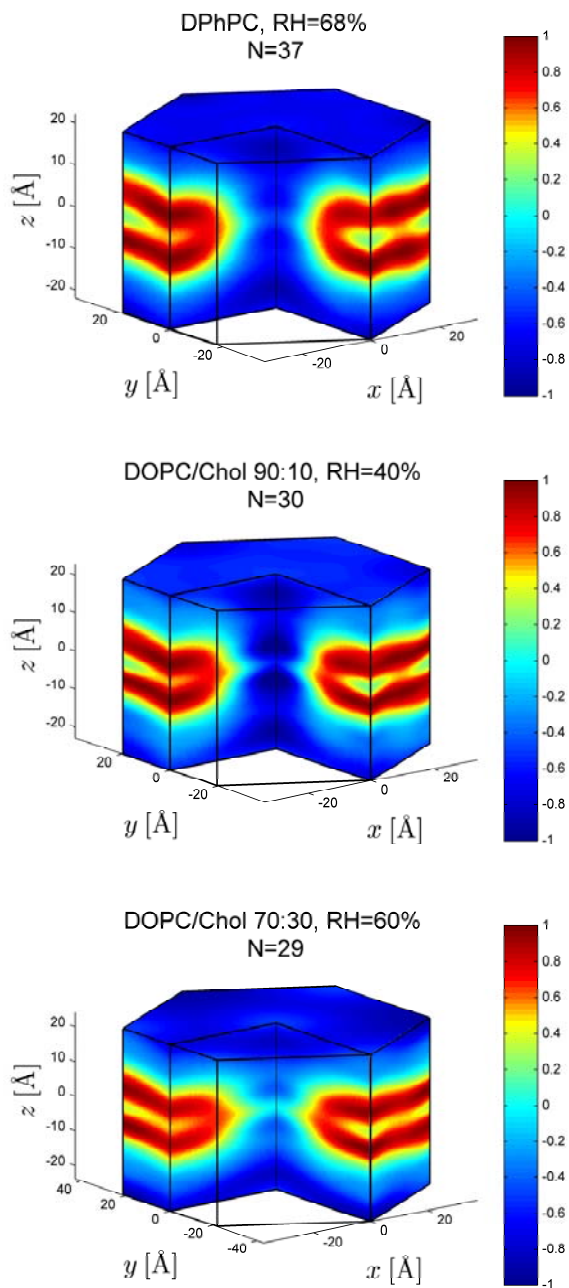


Figure 5.18: Representations of the hexagonal prism containing a single stalk for several lipids.

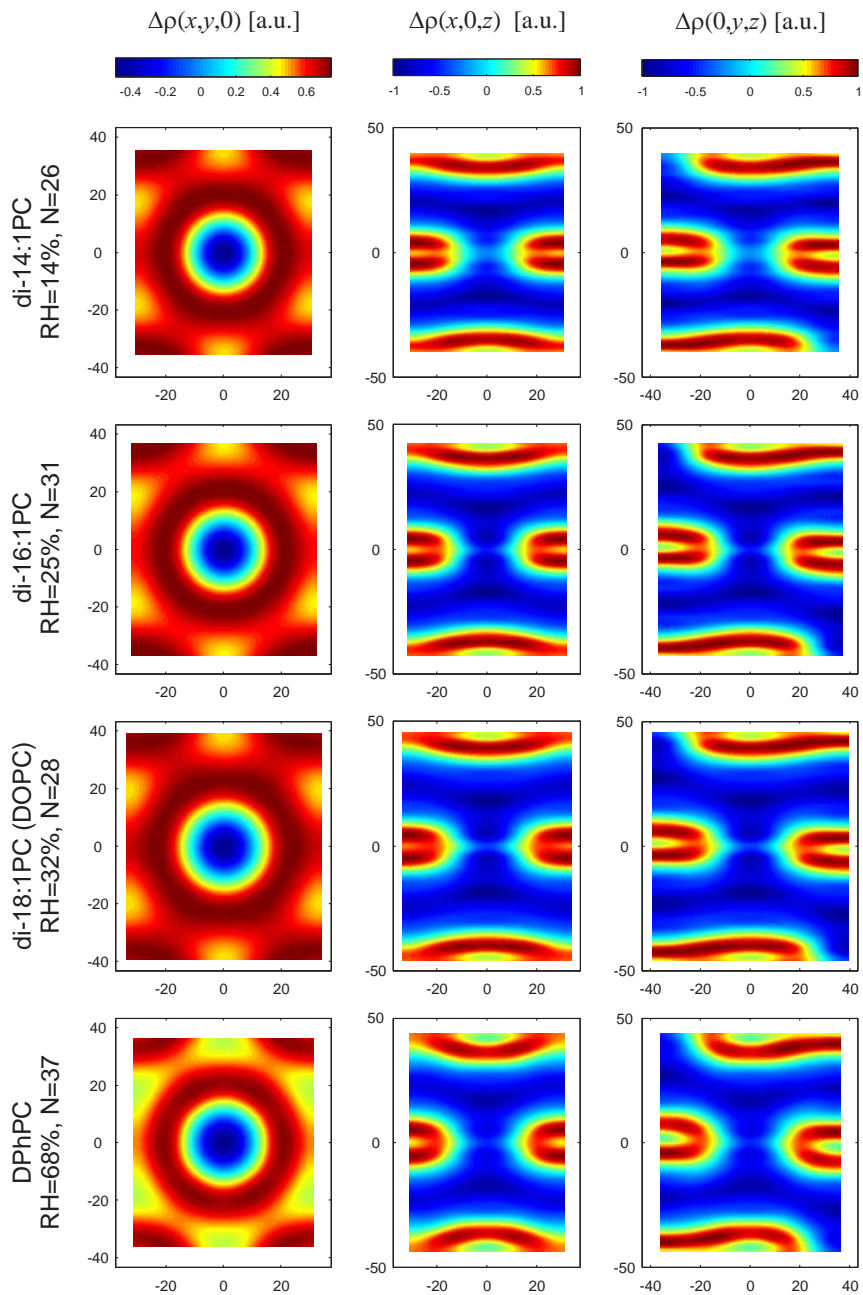


Figure 5.19: Electron density maps $\Delta\rho(\vec{r})$ reconstructed with the maximum number N of reflections. Colorbars apply to all figures in a column.

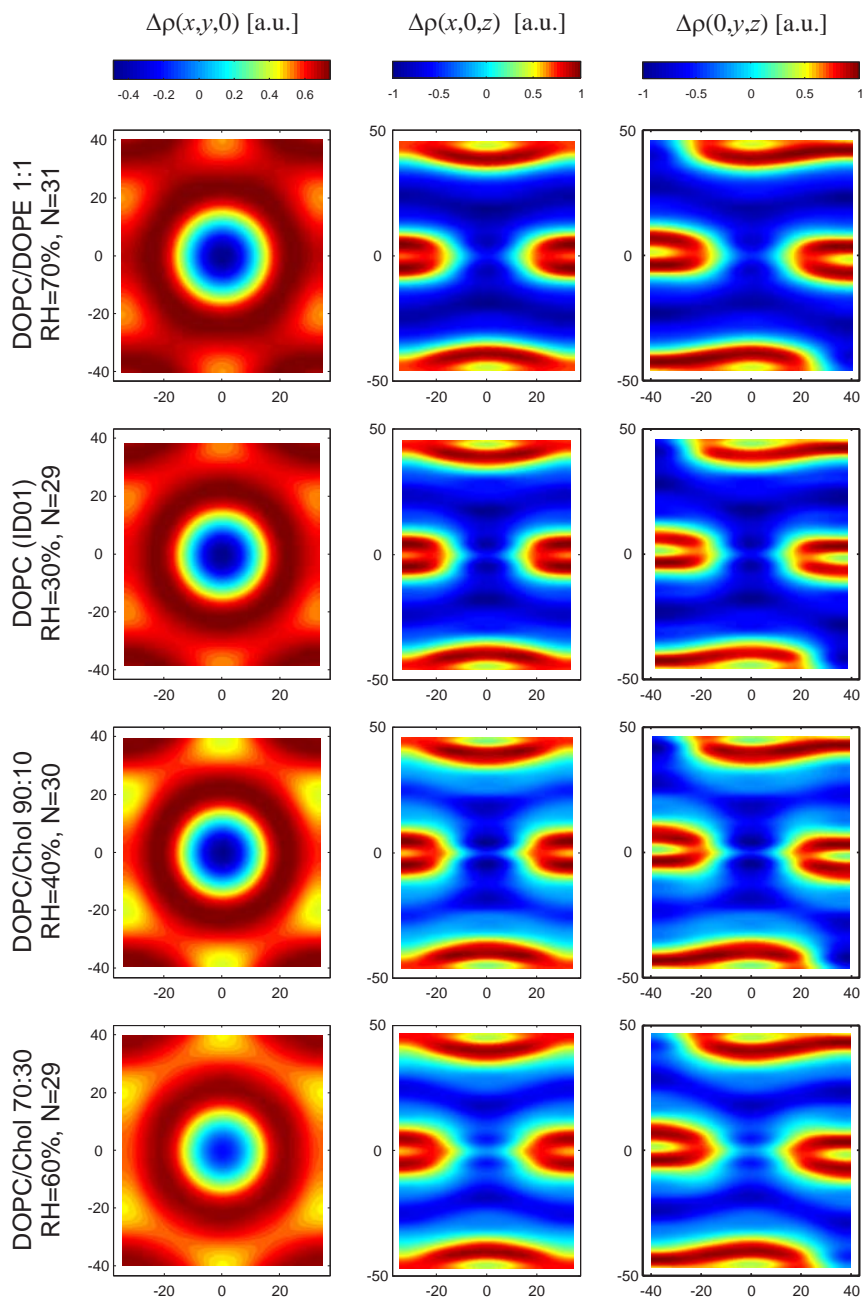


Figure 5.20: More electron density maps $\Delta\rho(\vec{r})$ reconstructed with the maximum number N of reflections. Colorbars apply to all figures in a column.

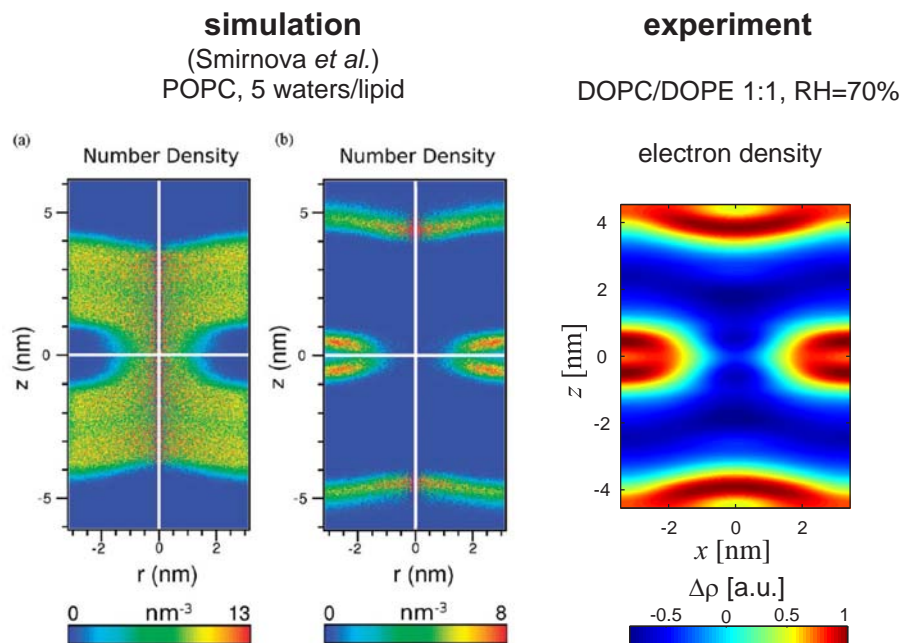


Figure 5.21: Comparison of a recent coarse-grained MD simulation by SMIRNOVA *et al.* (adapted with permission from [53], Copyright (2010) American Chemical Society) and our experimental data. Importantly, the lipid species are different and number densities are used instead of electron densities. However, the general stalk shape is strikingly similar.

5.4 Discussion

So far, to the very best of our knowledge, only data on stalks in pure DPhPC and DOPC are available in the literature. In the pioneering work of YANG *et al.* using DPhPC [51], the number of independent reflections used for electron density reconstruction is $N = 23$. Data on DOPC with $N = 20$ have been published by RAPPOLT *et al.* [52]. The number of independent reflections in our datasets is between 26 and 37. Therefore, our results increase both the number of datasets as well as the obtainable resolution in electron density maps and provide the first structural data on stalks in lipid mixtures.

To the naked eye, the reconstructed electron density maps are quite similar. Except for variations of the total dimensions in case of different chain lengths, only subtle variations can be distinguished. For example, the water region in case of DPhPC is slightly higher than in case of all other samples. The high degree of similarity is also reflected in the formfactor data provided in the appendix A.2: For all datasets, the relative amplitudes $|F_{hkl}|$ are typically very similar and the phase factors v_{hkl} are, with only few exceptions, the same.

Fig. 5.21 compares a recent simulation by SMIRNOVA *et al.* and one of the obtained electron density maps. Although the used lipids and displayed quantities are different

(number density *vs.* electron density), the general stalk shape is strikingly similar. For example, both the headgroup density in the simulation and the electron density in the lipid headgroup region in the experimental data decrease at the stalk neck close to $z = 0$, and the strength of the “dimples” of the *trans* monolayers are comparable.

5.5 Conclusions

In this chapter, the determination of stalk structures in terms of electron density contrast $\Delta\rho(\vec{r})$ by x-ray diffraction on the rhombohedral phase of several phospholipids and lipid mixtures has been described. To this end, we applied the methods pioneered by the group of HUANG [30, 51] with several modifications, *e.g.* the use of separate reflectivity scans and powder diffraction data, as well as a criterion derived from direct methods as an additional aid for phase determination.

Our results on seven different lipid systems, including the first data on lipid mixtures, considerably extend the available structural data on stalks and provide better resolution. The reconstructed electron density maps indicate a highly conserved structure of stalks in the rhombohedral phase with only subtle variations. These are investigated more closely in the following chapter.

6 Analysis of the 3d electron density of stalks

In the previous chapter, the structures of stalks in several lipids and lipid systems have been obtained by x-ray diffraction on the rhombohedral phospholipid phase. Based on these data, we study variations in stalk structure. After definition of structural parameters for stalk phase characterization, the major goal is to investigate the curvatures of the strongly bent *cis* monolayer. To this end, we propose the analysis of electron density isosurfaces. The required formalism derived from differential geometry of implicit surfaces is introduced and its application to reconstructed electron density data explained in detail. After presentation of our results, we compare these to existing continuum models.

6.1 Structural parameters of the stalk phase

6.1.1 Definitions

To characterize lipid bilayer structure, the headgroup-headgroup distance d_{hh} and the associated water layer thickness d'_{w} have been used in chapter 4. These parameters are obtained from the positions of electron density maxima indicative of phospholipid headgroup regions in one-dimensional bilayer electron density profiles. As a first step towards comparison of the structure of different stalks obtained in the previous chapter, we define similar structural parameters for the stalk phase.

The stalk diameter d_{s} along its “waist” is obtained from the electron density contrast $\Delta\rho$ in the xy plane (Fig. 6.1*a*). To this end, radial slices starting from the origin are extracted as a function of the angle ϕ . d_{s} is defined as twice the mean position of the electron density maximum for $\phi \in [0, 2\pi]$.

Bilayer thickness d_{b} and water layer thickness d_{w} in the stalk phase are defined as sketched in Fig. 6.1*b*). The one-dimensional electron density profile $\Delta\rho(0, 0, z)$ is reconstructed in the interval indicated by the vertical white line with a sampling of $\Delta z = 0.01 \text{ \AA}$. The line corresponds to the edges of two hexagonal prisms indicated by red dashed lines. This choice maximizes the distance to adjacent stalks, the original bilayer structure of the lamellar phase is expected to be least disturbed at this position. d_{b} and d_{w} are determined from the positions of electron density maxima. The relation $d = d_{\text{b}} + d_{\text{w}}$ (Eq. 4.8) used in case of the lamellar phase has to be replaced by

$$3d = d_{\text{b}} + 2d_{\text{w}} + d_{\text{t}}. \quad (6.1)$$

This also yields the parameter d_{t} indicating the minimum distance between the distal or *trans* monolayers corresponding to one stalk as shown in Fig. 6.1*c*).

An empirical measure for the volume fraction of water in the sample is obtained as sketched in Fig. 6.1*c*). Electron density maxima corresponding to the headgroup region of the strongly curved *cis* monolayer are approximated by semi-elliptical contours $z_{x,y}(r)$. The semimajor and semiminor axes are determined using the lattice parameter a , stalk neck diameter d_{s} and the positions $h_{x,y}$ of lipid headgroup peaks in $\Delta\rho$ along $(\frac{a}{2}, 0, z)^T$ and $(0, \frac{a}{\sqrt{3}}, z)^T$, respectively, yielding

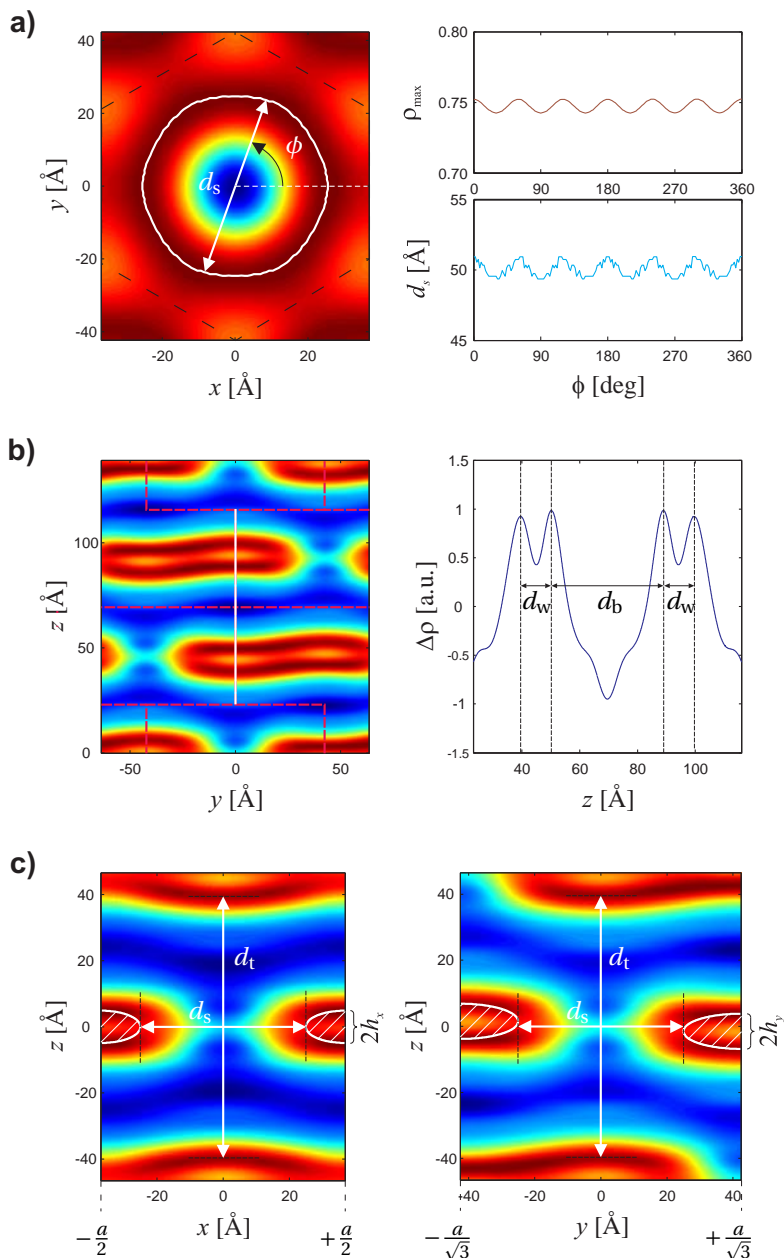


Figure 6.1: (a) Determination of the stalk diameter d_s in the xy plane as a function of polar angle ϕ and corresponding electron density ρ_{\max} . (b) Definitions of bilayer and water layer thickness d_b and d_w in the rhombohedral phase. (c) The hydrophilic volume is defined empirically by the solids of revolution obtained from the semi-elliptical areas shaded in white (DOPC/DOPE 1:1, RH = 74%).

$$z_x(r) = \pm \frac{h_x}{\frac{a}{2} - r_s} \sqrt{r_s^2 + a(r - r_s) - r^2}, \quad (6.2)$$

$$z_y(r) = \pm \frac{h_y}{\frac{a}{\sqrt{3}} - r_s} \sqrt{r_s^2 + \frac{2}{\sqrt{3}}a(r - r_s) - r^2} \quad (6.3)$$

The hydrophilic volume is approximated by solids of revolution obtained by rotation of the shaded areas about the z axis:

$$V_{\text{hyd}} = 4\pi \int r z_{x,y}(r) dr \quad (6.4)$$

The mean of the volumes obtained for $z_x(r)$ and $z_y(r)$ is used to take into account variations upon rotation.

The above steps have been carried out by the script `stalkanalysis.m` using the formfactor tables in the appendix. Some very weak reflections are subject to considerable experimental noise. This implies the danger of possibly incorrect phase assignments by the swelling method. Since the associated form factor amplitudes are very small, this hardly affects the visual appearance of the reconstructed electron density maps. However, effects on the results of a quantitative analysis can not be excluded. Therefore, we did not include a number of very weak reflections $\{hkl\}$ in electron density reconstruction in this chapter. These are the same for all datasets and are indicated in each formfactor table in appendix A.2. The data presented here are based on electron density maps reconstructed with a sampling of 0.1 \AA .

6.1.2 Results

Fig. 6.2 displays the obtained structural parameters along with the corresponding RH range of each dataset. To facilitate comparison of the results of different stalks, several dimensionless ratios are used. We summarize the significant observations:

The first plot displays the structural parameters d_b , d_s and d_t . In all cases, the stalk neck diameter d_s exceeds the corresponding bilayer thickness d_b . For the dimensionless ratio d_s/d_b , we find values of $1.13 < d_s/d_b < 1.33$. Upon addition of cholesterol, d_s/d_b decreases slightly, while addition of DOPE rather has the opposite effect. The ratio of transversal and lateral extent of the stalk quantified by d_t/d_s varies between $\approx 1.53 - 1.78$.

The water layer thickness d_w in most samples is above the critical value of $(9.0 \pm 0.5) \text{ \AA}$ where the onset of stalk phase formation has been observed in chapter 4 (Fig. 4.11). This effect is strongest in DPhPC and the three lipid mixtures. In addition to formation of stalks, the L/R phase transition also involves a spatial redistribution of the volumes occupied by lipid and water, which locally reduces the hydration repulsion.

In regard to hydration, DPhPC seems to differ from the remaining samples. According to our results, its stalk phase imbibes a significantly larger amount of water, since the values for d_w and V_{hyd}/V_s clearly exceed those of the remaining lipids.

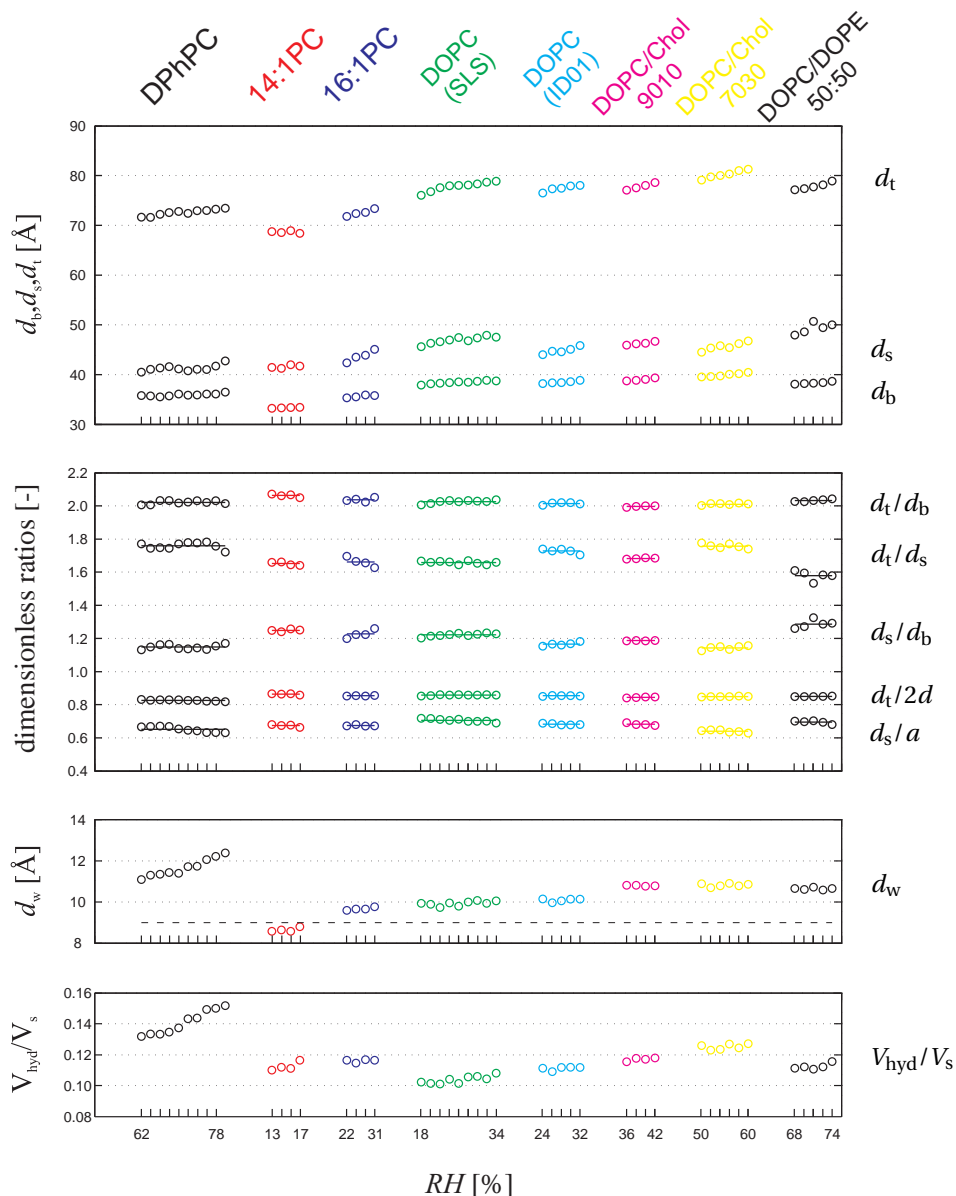


Figure 6.2: Structural parameters characterizing the stalk phase in eight different datasets. In the plot of d_w , the dashed horizontal line indicates the critical value for stalk phase formation of about 9 Å observed in lamellar phases.

6.2 Electron density isosurface analysis

6.2.1 Motivation

The continuum theory of membrane bending introduced in section 1.5 has been used and refined for almost 30 years to propose stalk geometries that minimize different energy functionals. As discussed below, it is disputed to what extent this formalism can yield reliable predictions of the free energy in case of strongly bent monolayers such as in membrane fusion intermediates of few nanometers in size. Nevertheless, analyzing our experimental data within this framework can certainly be helpful. Firstly, it may stimulate further refinements of the theory. Secondly, in addition to the structural parameters introduced in section 6.1, it provides additional criteria for an objective comparison of the obtained stalk structures in different lipids.

In case of the inverted hexagonal phase H_{II} , several authors have quantitatively analyzed electron density data to study elastic deformations of the water cylinders and chain packing [136, 189, 190]. To the very best of our knowledge, no comparable attempts exist in case of the stalk phase. While the latter is arguably more relevant with respect to membrane fusion, it also poses a higher degree of difficulty due to its three-dimensional structure. Here, we propose one possible strategy to analyze structural data of stalks in the framework of continuum theory.

Our goal is to minimize the amount of modelling and relate monolayer curvature as directly as possible to the measured crystallographic data. As the first step, in order to establish a connection between theory and our experimental results presented in the previous chapter, a reasonable criterion for possible neutral surfaces in electron density representation has to be found. In planar lipid bilayers, the neutral surface of each monolayer is assumed in the interfacial region between lipid headgroups and acyl chains. For DOPC, a fixed distance of 13Å from the bilayer midplane has been used [25, 88]. In a one-dimensional electron density profile representing a bilayer in the L phase, this corresponds to a constant value ρ_{iso} of electron density (Fig. 6.3).

If the electron density contrast $\Delta\rho(\vec{r})$ was free of truncation errors due to the limited number of measurable reflections, it would provide a perfect representation of the average stalk in the R phase. Also in this case, the neutral surfaces of the curved lipid monolayers of a stalk should, at least approximately, correspond to $2d$ surfaces of constant electron density embedded in $3d$ space. Therefore, we consider electron density isosurfaces

$$S_{\text{iso}} := \{\vec{r} \mid f(\vec{r}, \rho_{\text{iso}}) = 0\} \quad \text{where} \quad f(\vec{r}, \rho_{\text{iso}}) := \Delta\rho(\vec{r}) - \rho_{\text{iso}} \quad (6.5)$$

as approximations to possible neutral surfaces. Since $\Delta\rho(\vec{r})$ given by Eq. (5.35) is a sum of typically 80 to 100 cosine terms, the implicit function $f(\vec{r}, \rho_{\text{iso}}) = 0$ cannot be converted to parametric form such as the Monge representation $f : (x, y) \mapsto (x, y, h(x, y))$. Some concepts from differential geometry of implicit surfaces are required.

The basis for current energy functionals incorporating lipid tilt [25] or higher-order terms in curvature [85] is still the well-known Helfrich Hamiltonian

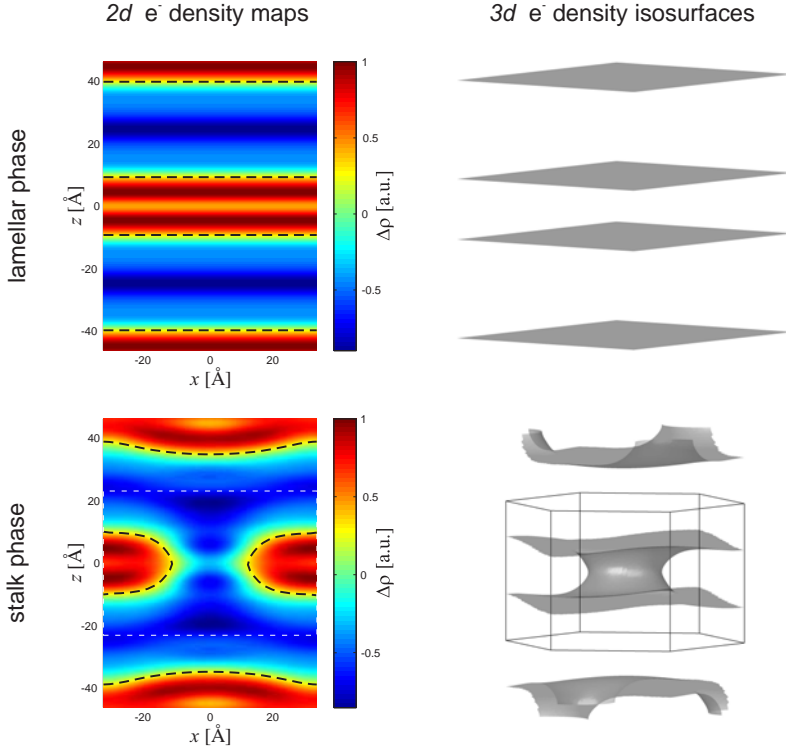


Figure 6.3: Bilayer and stalk represented by surfaces of constant electron density. Black dashed lines in the electron density maps correspond to the isosurface contours in the xz plane. As motivated in the main text, we analyze electron density isosurfaces as possible neutral surfaces with respect to bending (DOPC, $RH = 60\%$ (lamellar phase), $RH = 34\%$ (stalk phase, SLS dataset), $\rho_{iso} = 0.3$).

$$F_{\text{bend}} = \frac{\kappa}{2} \int_A (2H - c_0)^2 dA + \kappa_G \int_A K dA \quad (6.6)$$

describing the free energy with respect to bending deformations in terms of the mean and Gaussian curvature H and K of the neutral surface. For our purposes, we rewrite it into the more convenient form

$$\Delta F_{\text{bend}} = \Delta F_H + \Delta F_K \quad (6.7)$$

$$= \kappa (\Sigma_1 + c_0 \Sigma_2) + (-4\pi\kappa_G). \quad (6.8)$$

The terms ΔF_H and ΔF_K denote the energy difference due to mean and Gaussian curvature with respect to a flat monolayer of the same area, $F_{\text{bend}} = \frac{\kappa}{2} c_0^2 A$. The quantities

$$\Sigma_1 = 2 \int_A H^2 dA \quad \text{and} \quad \Sigma_2 = -2 \int_A H dA. \quad (6.9)$$

depend only on H and thus only on stalk geometry and can be used to compare stalks in different lipids irrespective of their elastic constants κ and c_0 , whose values are, at best, only approximately known. As noted above, the integrated Gaussian curvature of a smooth surface representing a stalk $\int K dA = -4\pi$ is constant due to the Gauss-Bonnet theorem.

In the following, we describe how to find an electron density isosurface for a given isodensity value ρ_{iso} , determine its principal, mean and Gaussian curvatures at any point and carry out surface integrals yielding Σ_1, Σ_2 , the monolayer area A and $\int K dA$.

6.2.2 Differential geometry of implicit surfaces

Due to crystal symmetry, it is sufficient to consider a single stalk in a hexagonal prism indicated in Fig. 6.3. Surfaces of constant $\Delta\rho(\vec{r})$ are given implicitly by Eq. (6.5), ρ_{iso} denotes the chosen density value. Expressions for the mean and Gaussian curvature of implicit surfaces are given in some differential geometry textbooks [191, 192]. The following considerations are based on GOLDMAN, where also rigorous proofs are provided [193]. For an implicit surface defined by $f(\vec{r}, \rho_{\text{iso}}) = 0$, the mean and Gaussian curvature at any point \vec{r} of the surface are

$$H = \frac{\nabla f^T \cdot \text{Hess}(f) \cdot \nabla f - |\nabla f|^2 \cdot \text{Tr}(\text{Hess}(f))}{2|\nabla f|^3} \quad \text{and} \quad (6.10)$$

$$K = \frac{\nabla f^T \cdot \text{Hess}^*(f) \cdot \nabla f}{|\nabla f|^4}, \quad (6.11)$$

where

$$\nabla f = (f_x, f_y, f_z)^T \quad (6.12)$$

denotes the gradient,

$$\text{Hess}(f) = \begin{pmatrix} f_{xx} & f_{xy} & f_{xz} \\ f_{yx} & f_{yy} & f_{yz} \\ f_{zx} & f_{zy} & f_{zz} \end{pmatrix} \quad (6.13)$$

the Hessian and

$$\text{Hess}^*(f) = \begin{pmatrix} \text{cofactor}(f_{xx}) & \text{cofactor}(f_{xy}) & \text{cofactor}(f_{xz}) \\ \text{cofactor}(f_{yx}) & \text{cofactor}(f_{yy}) & \text{cofactor}(f_{yz}) \\ \text{cofactor}(f_{zx}) & \text{cofactor}(f_{zy}) & \text{cofactor}(f_{zz}) \end{pmatrix} \quad (6.14)$$

$$= \begin{pmatrix} f_{yy}f_{zz} - f_{yz}f_{zy} & f_{yz}f_{zx} - f_{yx}f_{zz} & f_{yx}f_{zy} - f_{yy}f_{zx} \\ f_{xz}f_{zy} - f_{xy}f_{zz} & f_{xx}f_{zz} - f_{xz}f_{zx} & f_{xy}f_{zx} - f_{xx}f_{zy} \\ f_{xy}f_{yz} - f_{xz}f_{yy} & f_{yx}f_{xz} - f_{xx}f_{yz} & f_{xx}f_{yy} - f_{xy}f_{yx} \end{pmatrix} \quad (6.15)$$

the adjugate of the Hessian of $f(\vec{r})$. Therefore, H and K are fully determined by the first and second derivatives f_i and f_{ij} with respect to Cartesian coordinates $i, j = x, y, z$.¹⁶ In our analysis, the electron density contrast $\Delta\rho(\vec{r})$ and thus f is only known up to a scale factor. If f is replaced by $\lambda \cdot f$, $\lambda \in \mathbb{R}$, factors of λ^3 or λ^4 are introduced in both the numerator and the denominator of Eq. (6.10) and (6.11), respectively. Therefore, H is invariant under rescaling, while K changes its sign for $\lambda < 0$ [193]. Due to Schwarz's theorem, $\text{Hess}(f)$ and $\text{Hess}^*(f)$ are symmetric. Once H and K are known, the principal curvatures follow from [191]

$$c_{1,2} = H \pm \sqrt{H^2 - K}. \quad (6.16)$$

For a sphere of radius R given by $f(x, y, z) = x^2 + y^2 + z^2 - R^2 = 0$, one can easily verify that the above formulas lead to the expected results $H = R^{-1}$, $K = R^{-2}$, $c_{1,2} = R^{-1}$ [193].

6.2.3 Implementation

In the present case where $f(\vec{r}, \rho_{\text{iso}})$ contains the Fourier cosine series of $\Delta\rho(\vec{r})$ (Eq. 5.35), gradient and Hessian obtained from Eq. (6.5) are

$$\nabla f = - \sum_{h,k,\ell} v_{hk\ell} |F_{hk\ell}| \sin(\vec{q}_{hk\ell} \cdot \vec{r}) \cdot \vec{q}_{hk\ell}, \quad (6.17)$$

$$\text{Hess}(f) = -4\pi^2 \sum_{h,k,\ell} v_{hk\ell} |F_{hk\ell}| \cos(\vec{q}_{hk\ell} \cdot \vec{r}) \cdot \begin{pmatrix} \frac{h^2}{a^2} & \frac{h(2k+h)}{\sqrt{3}a^2} & \frac{h\ell}{3ad} \\ \frac{h(2k+h)}{\sqrt{3}a^2} & \frac{(2k+h)^2}{3a^2} & \frac{(2k+h)\ell}{3\sqrt{3}ad} \\ \frac{h\ell}{3ad} & \frac{(2k+h)\ell}{3\sqrt{3}ad} & \frac{\ell^2}{9d^2} \end{pmatrix}. \quad (6.18)$$

The adjugate of the Hessian can be determined using the cofactor relation

$$\text{cofactor}(f_{ij}) = (-1)^{i+j} M_{ij}, \quad (6.19)$$

where the minor M_{ij} denotes the determinant of the 2×2 matrix obtained by cancelling row i and column j of $\text{Hess}(f)$. These equations allow to determine H, K, c_1 and c_2 in an arbitrary point \vec{r} in a fully analytic way using exclusively the experimentally determined form factors and lattice parameters provided in the appendix.

In order to obtain the integrals Σ_1 and Σ_2 for a certain isosurface ρ_{iso} , only points $\{\vec{r} \mid f(\vec{r}, \rho_{\text{iso}}) = 0\}$ defining this surface must be considered. Due to the implicit surface definition, we use the following algorithm:

- As noted above, considering the hexagonal prism containing a single stalk is sufficient. In addition, due to centrosymmetry, the region $z \leq 0$ contains all relevant information.¹⁷ The coordinates (x, y) within the hexagonal base are discretized on a grid with $\Delta x = \Delta y = 0.25 \text{ \AA}$ (Fig. 6.4, *left*).

¹⁶ Alternatively, H is related to the divergence of the surface normal $\vec{n} = \frac{\nabla f}{|\nabla f|}$ by $2H = -\text{div}(\vec{n})$.

¹⁷ In fact, due to centrosymmetry and three-fold rotational symmetry about the z axis, one sixth of the hexagonal prism constituting the asymmetric unit would be sufficient.

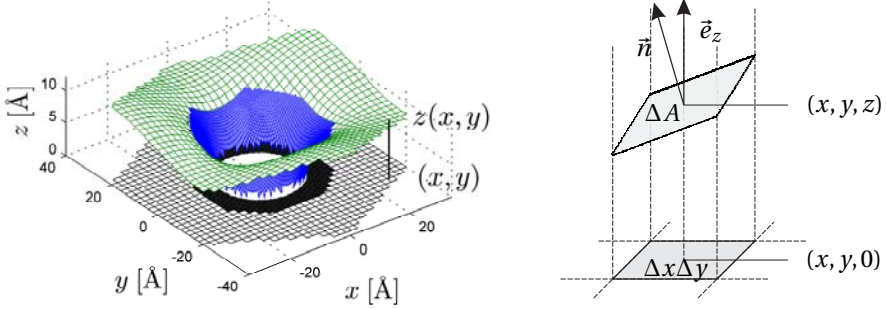


Figure 6.4: (left) Isosurface determination: The hexagonal base corresponding to one stalk is discretized. For each point (x, y) of the grid, the height $z(x, y)$ such that $f(x, y, z(x, y), \rho_{\text{iso}}) = 0$ is determined numerically (green). For higher accuracy, the strongly curved region was subsequently resampled using a finer grid (blue). For the final results presented in this work, the sampling was considerably finer than shown in the figure. (right) Sketch of an area element in the xy plane and corresponding isosurface patch of area ΔA .

- For each pair of coordinates (x, y) and a chosen isodensity ρ_{iso} , values $z \in [-20 \text{ \AA}, 0]$ solving $f(x, y, z, \rho_{\text{iso}}) = 0$ are computed numerically by the MATLAB function `fzero`. Depending on ρ_{iso} , either one, two, or no solutions are obtained. The latter applies to the waist region of the stalk where $\sqrt{x^2 + y^2}$ is close to or smaller than d_s . With an initial value $z_0 = -10 \text{ \AA}$, isosurfaces such as shown in Fig. 6.4 displaying no unphysical discontinuities are obtained. To improve the accuracy of the final results, the waist region of the stalk where the strongest curvatures were found to occur is resampled using a finer grid of $\Delta x = \Delta y = 0.05 \text{ \AA}$ and $z_0 = -1$.
- The area element ΔA corresponding to each pair (x, y) is required for numerical surface integration (Fig. 6.4, right). Projection of ΔA onto the xy plane yields the area $\Delta x \Delta y = |\vec{n} \cdot \vec{e}_z| \Delta A$ [194, 195]. With the surface normal $\vec{n} = \frac{\nabla f}{|\nabla f|}$, we obtain

$$\Delta A = \frac{|\nabla f|}{|\partial_z f|} \Delta x \Delta y = \frac{|\sum_{h,k,\ell} v_{hkl} |F_{hkl}| \cdot \sin(\vec{q}_{hkl} \cdot \vec{r}) \cdot \vec{q}_{hkl}|}{|\sum_{h,k,\ell} v_{hkl} |F_{hkl}| \cdot \sin(\vec{q}_{hkl} \cdot \vec{r}) \cdot \frac{2\pi}{3d} \ell|} \Delta x \Delta y. \quad (6.20)$$
- For all obtained points $\{\vec{r} = (x, y, z) | f(\vec{r}) = 0\}$, H and K are calculated by Eq. (6.10) and (6.11). The principal curvatures c_1, c_2 follow from Eq. (6.16).
- Integrations yielding Σ_1, Σ_2 , the isosurface area A and $\int_A K dA$ are performed by summation over all area elements. Finally, to take into account the entire *cis* monolayer corresponding to one stalk, the results are multiplied by 2.

This algorithm is implemented in the MATLAB script `isocurv.m` (appendix A.4). The only approximation is the use of non-infinitesimal area elements.

6.2.4 Results

Fig. 6.5 shows typical results of the electron density isosurface analysis. Electron density isosurfaces (*top*) and corresponding distributions of c_1, c_2, H and K (*bottom*) have been computed for $\rho_{\text{iso}} \in [-0.2, +0.8]$ with a stepsize of 0.02.¹⁸ The following general observations are common to all datasets:

At most positions, the two principal curvatures c_1, c_2 are different in sign and adopt large absolute values in a narrow region close to the stalk neck at $z = 0$. The latter applies also to the mean and Gaussian curvatures H and K . In a narrow region very close to $z = 0$, a small ring-like portion of the isosurface is missing due to discretization of the xy plane.

Fig. 6.6 shows the corresponding integrals Σ_1, Σ_2, A and $\int K dA$ as a function of ρ_{iso} . For $\rho_{\text{iso}} \leq 0.5$, the numerical results for $\int_A K dA$ are close to the theoretical value -4π .¹⁹ We use this as a control that the algorithm works correctly and attribute deviations from -4π to the missing area elements close to $z = 0$ where K assumes its most extreme values (*cf.* Fig. 6.5, *top*).

In this range of ρ_{iso} , all electron density isosurfaces possess a stalk-like topology. Σ_1 varies nonmonotonously and displays a minimum between 0.1 and 0.4 in ρ_{iso} , while Σ_2 increases monotonously in this interval. The monolayer area A decreases monotonously with ρ_{iso} , since the isosurface moves from the hydrophobic stalk interior towards the strongly curved lipid headgroup region with increasing ρ_{iso} .

For the different levels of hydration in each dataset indicated by different line colors in Fig. 6.6, the monolayer area A increases systematically with RH , compatible with the increasing lattice parameters. However, considering all datasets, no systematic changes in Σ_1 and Σ_2 with hydration could be inferred. At given ρ_{iso} , these vary rather randomly with RH , indicating that the experimental uncertainties preclude to study hydration effects. Therefore, in the subsequent figures, the mean and standard deviation of Σ_1 and Σ_2 obtained from the different hydration levels in each dataset are used to indicate the typical experimental errors.

¹⁸ One exception had to be made: In case of DOPC/Chol 70:30, values $\rho_{\text{iso}} < 0$ did not yield continuous isosurfaces describing the curved *cis* monolayer of a stalk. In this case, $\rho_{\text{iso}} = 0$ was used as a minimum.

¹⁹ In the stalk model including lipid tilt, KOZLOVSKY *et al.* obtain a slightly larger value of -11.8 since their neutral surface is nonsmooth and includes a discontinuity at $z = 0$ [55, 88].

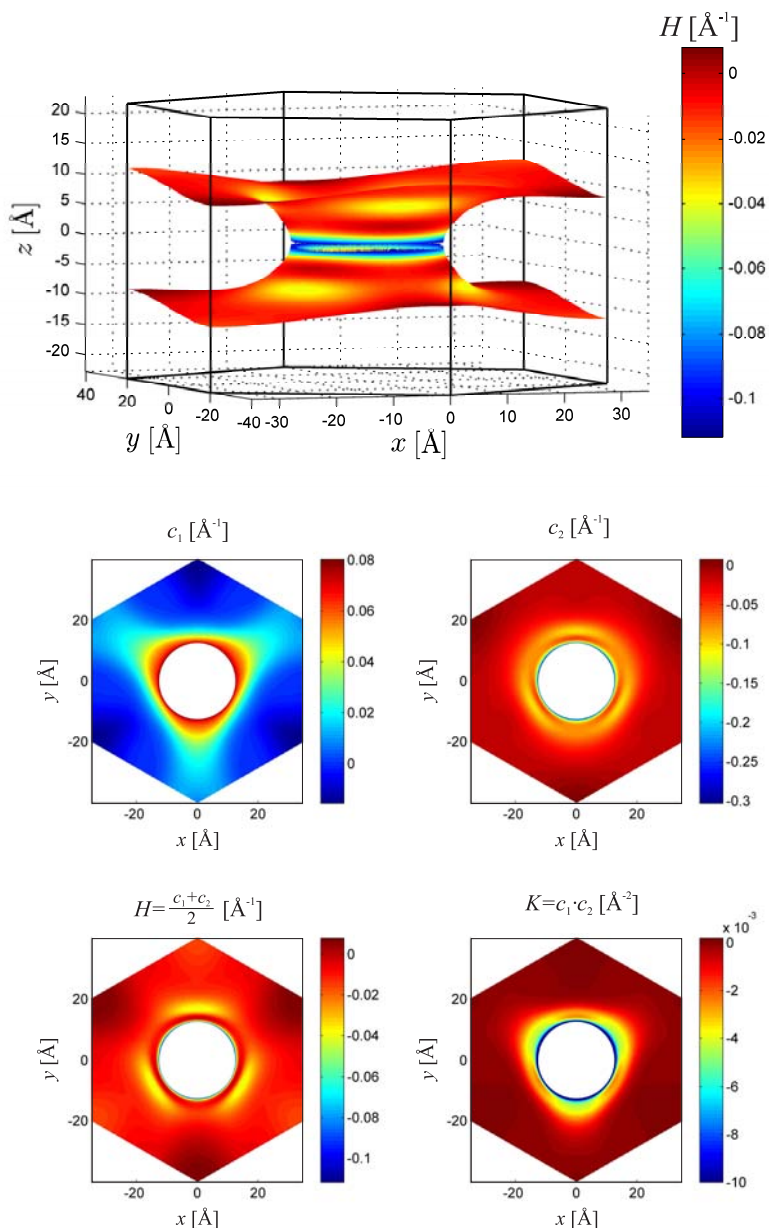


Figure 6.5: (top) Electron density isosurface $\Delta\rho = 0.3$ and (bottom) corresponding spatial distribution of curvatures c_1, c_2, H and K in the lower half of the isosurface viewed from the top. Extremal values of H and K are concentrated in a narrow region around the stalk neck close to $z = 0$. All images reflect the three-fold rotational symmetry of the rhombohedral phase about the z axis (DOPC/DOPE 1:1, $RH = 70\%$).

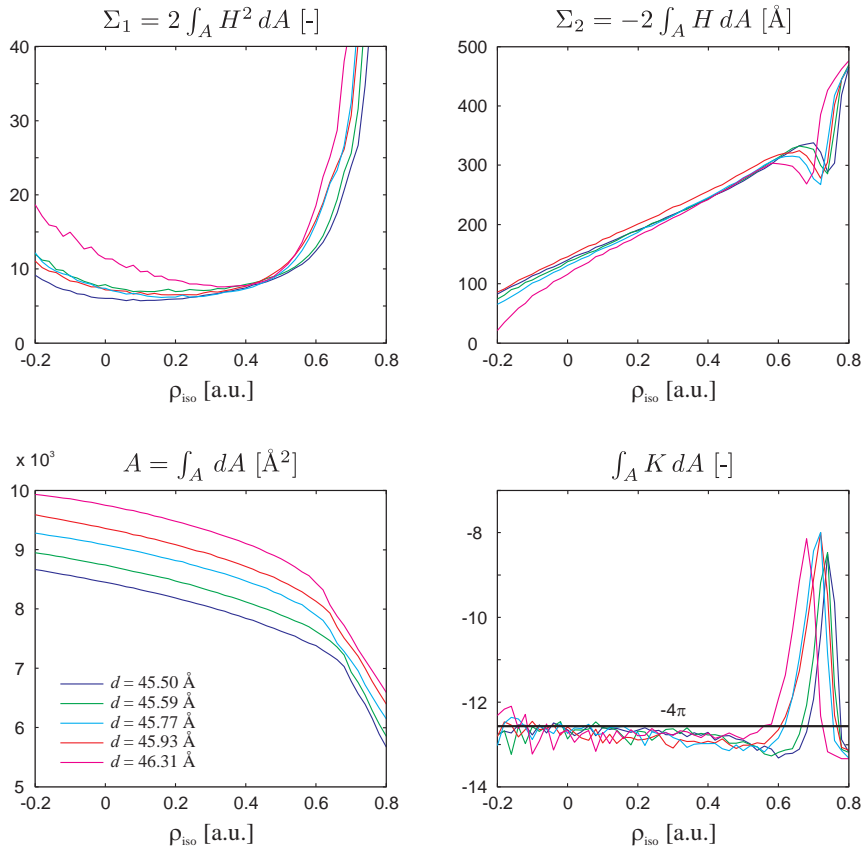


Figure 6.6: Typical results of electron density isosurface analysis (DOPC/DOPE 1:1, $RH = 68 - 74\%$). The monolayer area A at given ρ_{iso} increases with the lattice parameter d or degree of hydration. A value of $\int_A K dA = -4\pi$ is expected due to the Gauss-Bonnet theorem (cf. appendix A.3). Up to $\rho_{\text{iso}} \approx 0.5$, this value is approximately obtained in all datasets. The two quantities Σ_1, Σ_2 describe the mean curvature properties of the surface. Σ_1 typically displays minima at $\rho_{\text{iso}} = 0.3 \pm 0.2$, while Σ_2 increases monotonously in the interval where $\int_A K dA \approx -4\pi$.

Pure DOPC at different synchrotrons

For a start, it is desirable to check if the datasets including GIXD data recorded at different synchrotron beamlines yield comparable results. To this end, we compare the two DOPC datasets including data recorded at the Materials Science and ID01 beamlines, respectively. However, note that the reflectivity data to determine $\{F_{00\ell}\}$ and powder data for relative normalization are the same. Contour plots of constant electron density levels $\Delta\rho = 0.1, 0.3, 0.5$ in the xz and yz plane are shown in Fig. 6.7 (top). These indicate that the structure of stalks in the R phase of DOPC constructed from different GIXD datasets recorded at two different synchrotrons is very similar. Corresponding results of the electron density isosurface analysis are plotted Fig. in 6.7 (bottom). The results of both datasets agree within experimental uncertainty.

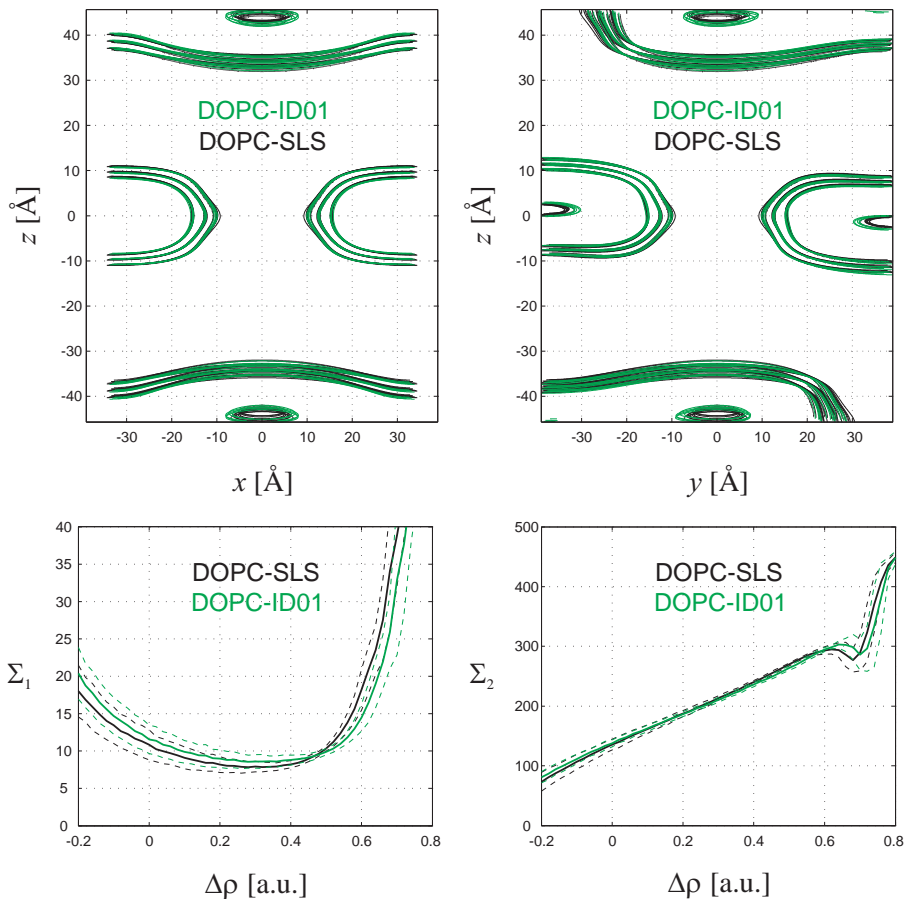


Figure 6.7: Comparison of two DOPC datasets recorded at different synchrotrons: (top) Lines of constant $\Delta\rho = 0.1, 0.3, 0.5$ in the xz and yz planes are in good agreement. For both datasets, isolines are shown for all hydration levels. (bottom) Also the isosurface analysis yields very similar results.

Effects of chain length and structure

In addition to DOPC (di18:1PC), data on the the structurally similar lipids di14:1PC and di16:1PC as well as DPhPC have been recorded and analyzed. Results are shown in Fig. 6.8. The minimum of Σ_1 increases with chain length and moves towards higher ρ_{iso} . The structure of stalks in DPhPC is different from the other lipids: The *trans* monolayers form more pronounced “dimples”, while the strongly curved *cis* monolayer surrounds a slightly larger aqueous region. Since its branched and bulky hydrocarbon chains are the characteristic feature of DPhPC, it is likely that these cause differences in stalk structure.

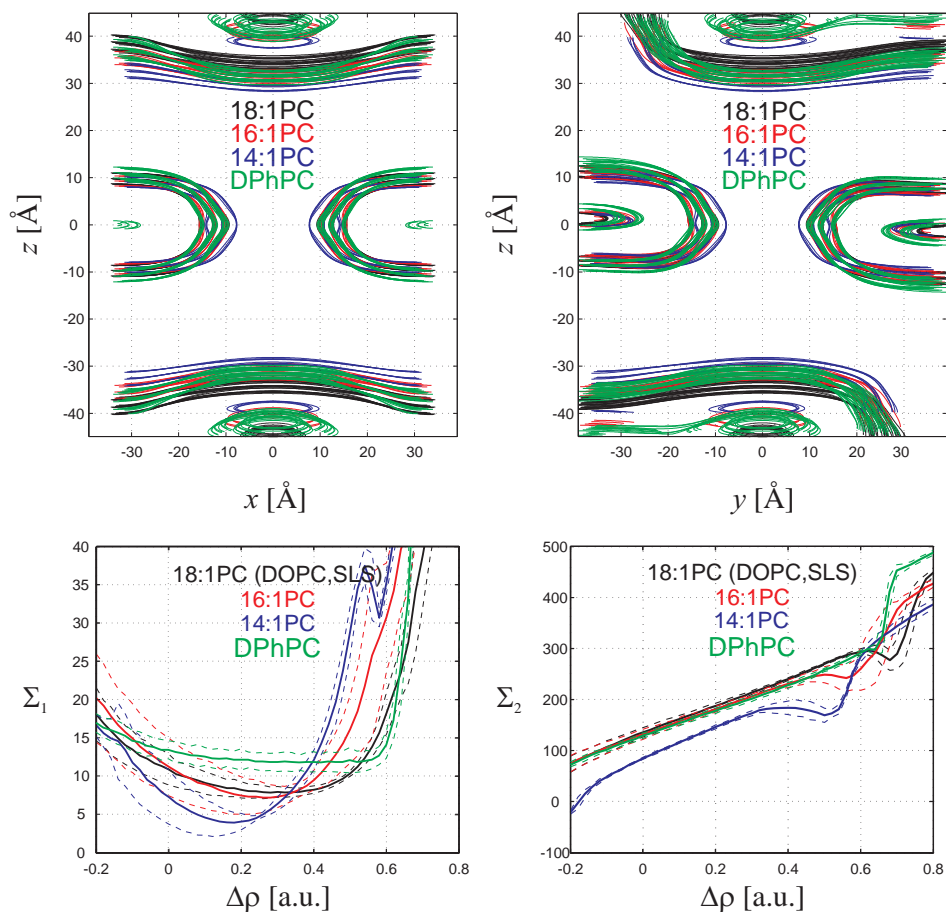


Figure 6.8: Comparison of lipids with different chain length and structure: (top) Lines of constant $\Delta\rho = 0.1, 0.3, 0.5$ in the xz and yz planes. Especially in the xz plane, the more pronounced dimples in the *trans* monolayers of DPhPC are visible. (bottom) Values of Σ_1 increase with chain length. The minimum of Σ_1 is less pronounced in case of DPhPC.

Effects of DOPE

The dataset of the equimolar mixture of DOPC and DOPE is the one with the highest molar ratio of a fusogenic additive used in this thesis. Electron density isocontours of stalks in pure DOPC and DOPC/DOPE 1:1 in the xy and xz plane are superimposed in Fig. 6.9(*top*). These almost coincide, no systematic differences can be observed by the naked eye. This indicates that addition of DOPE, despite its smaller headgroup and therefore different molecular shape, hardly affects the equilibrium structure of stalks. Also the isosurface results are very similar.

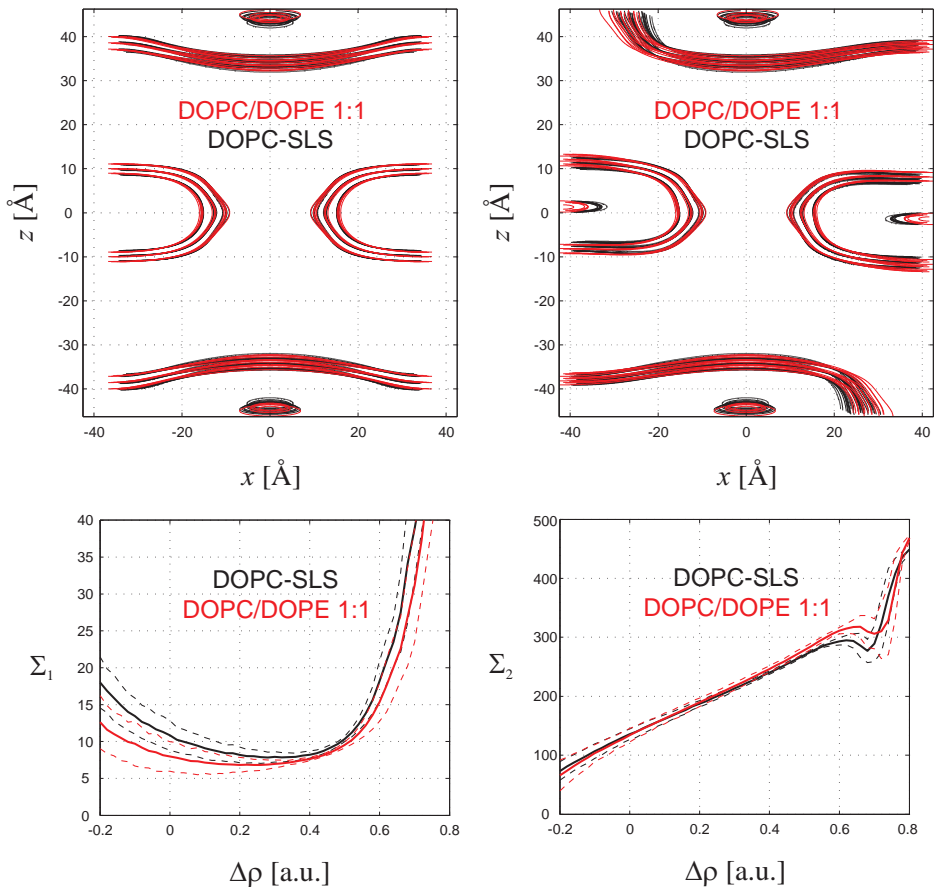


Figure 6.9: Comparison of DOPC and an equimolar mixture of DOPC and DOPE: (*top*) Lines of constant $\Delta\rho = 0.1, 0.3, 0.5$ in the xz and yz planes are in very good agreement. For both datasets, isolines are shown for all hydration levels. (*bottom*) Results of the isosurface analysis of both datasets are very similar. Although DOPE differs considerably in spontaneous curvature c_0 and hydration properties from DOPC, addition of an equimolar amount DOPE to DOPC has only a very subtle effect on stalk structure.

Effects of cholesterol

To study the effect of cholesterol on stalk structure, data on DOPC/Chol samples with molar ratios of 90:10, 80:20 and 70:30 have been recorded during the ID01 beamtime. During the analysis, it turned out that data on the 80:20 mixture were not suitable for further analysis, since the angle of incidence α_i was too high and the out-of-plane reflections with $\ell = 1$ were attenuated by the substrate. The results of electron density isosurface analysis of the remaining samples are plotted in Fig. 6.10. The minimum of Σ_1 increases with Chol content, whereas no clear trend is observable for Σ_2 . At the same time, upon addition of 30 mol% cholesterol, the stalk waist region becomes more narrow and the isocontours adopt a more pointed shape. This is also reflected in the increase of d_t/d_s in Fig. 6.2.

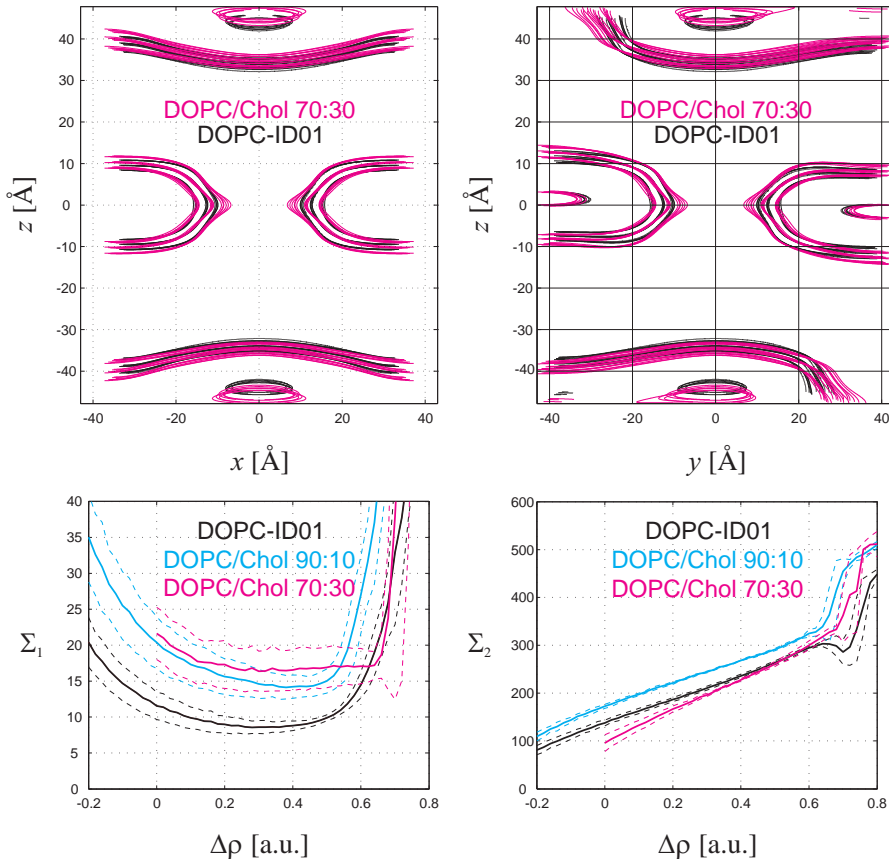


Figure 6.10: Comparison of DOPC and DOPC/Chol mixtures: Lines of constant $\Delta\rho = 0.1, 0.3, 0.5$ in the xz and yz planes indicate that the stalk waist becomes more narrow upon addition of cholesterol and the *cis* monolayer adopts a more pointed shape than in pure lipids. As discussed in the main text, this could be due to partial lipid demixing.

6.3 Discussion and comparison to continuum theory

6.3.1 General remarks

To the very best of our knowledge, the analysis of stalk structure in different lipids based on experimental data has not been attempted before. By the naked eye, electron density maps of stalks obtained in the previous chapter are very similar. As a first step, we have defined structural parameters like the diameter of the stalk waist to carry out a simple characterization of the typical length scales. Changes in the dimensionless ratios of these values are very moderate, even upon addition of 50 mol% DOPE or 30 mol% cholesterol. This indicates that, similar to the observation of an approximately constant critical bilayer separation for stalk phase formation in chapter 4, also the structure of stalks in the *R* phase is largely universal with only weak variations upon changes in lipid composition. Obviously, these findings must be considered in view of the rather low resolution resulting from the disorder inherent to lipid mesophases.

For further analysis, we have introduced a method to analyze stalk structures in terms of the curvature of electron density isosurfaces. The results obtained for DOPC at two different synchrotrons agree within errorbars. In addition, upon variation of the chain length or cholesterol content, we observe systematic variations. We consider this as an indication that the results correctly reflect small, but systematic changes in stalk structure.

Our results allow, for the first time, a comparison of experimentally obtained stalk structures to results and predictions of continuum theory. In principle, one can use the Helfrich Hamiltonian to estimate the bending energy of the strongly curved *cis* monolayer of stalks in the rhombohedral phase using the obtained values Σ_1, Σ_2 . We do this below, however, possible limitations of this approach should be addressed first.

As an alternative to electron density isosurfaces, one could also extract the surface corresponding to the electron density maximum of the lipid headgroup region and shift this to the expected neutral surface position at the interface of lipid headgroup and hydrocarbon region using parallel surface theory [191, 196, 197].

6.3.2 Possible limitations of continuum theory

Eq. (6.6) has been derived to describe *e.g.* vesicle shapes [198], where typical radii of curvature are large compared to molecular dimensions. In case of strongly bent monolayers expected in membrane fusion intermediates and visible in our electron density maps, radii of curvature are on the order of lipid monolayer thickness or even below.

With a typical area per lipid headgroup of 60 to 70 Å² (*cf.* Tab. 4.3), the obtained values of the isosurface area A indicate that the described *cis* monolayer of a stalk contains about 100 to 150 lipids. In addition, the strongly curved waist of the stalk, which gives the major contributions to Σ_1 and Σ_2 , contains only a minor fraction of these. For example, if the area per lipid headgroup A_L is modeled as a circle, the circumference πd_s of the waist of the stalk corresponds to only approximately 10 lipid headgroups.

For these reasons, it is debated to what extent the expansion of bending energy up to quadratic order in c_1, c_2 in the Helfrich Hamiltonian is still sufficient and the treatment of a lipid monolayer as an elastic continuum characterized by few global elastic con-

stants is justified in the case of membrane fusion intermediates [24, 25, 42, 53, 58, 88, 90].

Nevertheless, as noted in [25], continuum theory has been able *e.g.* to provide a quantitative explanation for the experimentally observed relative stability of lamellar and inverted hexagonal phases. Therefore, while aware of its possible limitations and thus rather semiquantitative character, we compare results of our analysis to predictions of continuum theory based on Eq. (6.6). Importantly, our method using electron density isosurfaces can be extended to any other functional of the principal curvatures c_1, c_2 .

lipid	$\kappa [k_B T]$	$c_0 [\text{\AA}^{-1}]$	$\kappa_G [k_B T]$
DOPC	9	-0.0115	-7.6 ± 1.5
DOPE	9	-0.0365	-8.3 ± 1.0
DOPC/Chol 1:1	11	-0.0250	-8.4 ± 1.1

Table 6.1: Literature values for curvature elastic constants relevant to our data. Taken from [88].

6.3.3 Comparison to continuum models

First, we consider general features of stalk shape. MARKIN *et al.* determined the structure of a stress-free stalk based on the Helfrich Hamiltonian (Eq. 6.6) by requiring that $2H - c_0 = 0$ in any point of the neutral surface [24]. KOZLOVSKY *et al.* included lipid tilt as an additional degree of freedom. In their stalk, this introduces a kink in the neutral surface at $z = 0$ [25, 55]. Our results derived from experimental data are located in between these two cases. This is not surprising: Obviously, isosurfaces of a Fourier series representation of $\Delta\rho(\vec{r})$ with a limited number of terms can neither possess a constant mean curvature, nor any discontinuities. However, we observe that the modulus of the mean curvature $|H|$ adopts large values in a concentrated region around the stalk waist. Therefore, our data rather support the Kozlovsky/Kozlov structure. In addition, as mentioned in the previous chapter, we do not observe pronounced hydrophobic voids. Absence of voids is another feature of the Kozlovsky/Kozlov stalk and also in agreement with a molecular dynamics simulation [54]. It should be noted that studies by continuum theory consider single, isolated stalks (*e.g.* [24, 25]) or neglect possible effects of packing stalks into a dense array [55].

In their paper on stalk phase formation, KOZLOVSKY *et al.* investigated the interplay of curvature and hydration energies. They report that the stalk shape obtained by minimization of the sum of these two energies was practically independent of the elastic moduli c_0 and κ_G (κ is similar for DOPC and DOPE, *cf.* Tab. 6.1) [55]. This is in very good agreement with the striking similarity of stalks in DOPC and DOPC/DOPE observed by us (*cf.* Fig. 6.9). However, as indicated in section 4.5.3, it could be that the parameters P_0 and λ used in [55] lead to an overestimation of the hydration force.

To examine the bending energies predicted by the Helfrich Hamiltonian for our electron density isosurfaces, numerical values of the curvature elastic constants κ , c_0 and κ_G are required. Values used in recent continuum models which are relevant for our

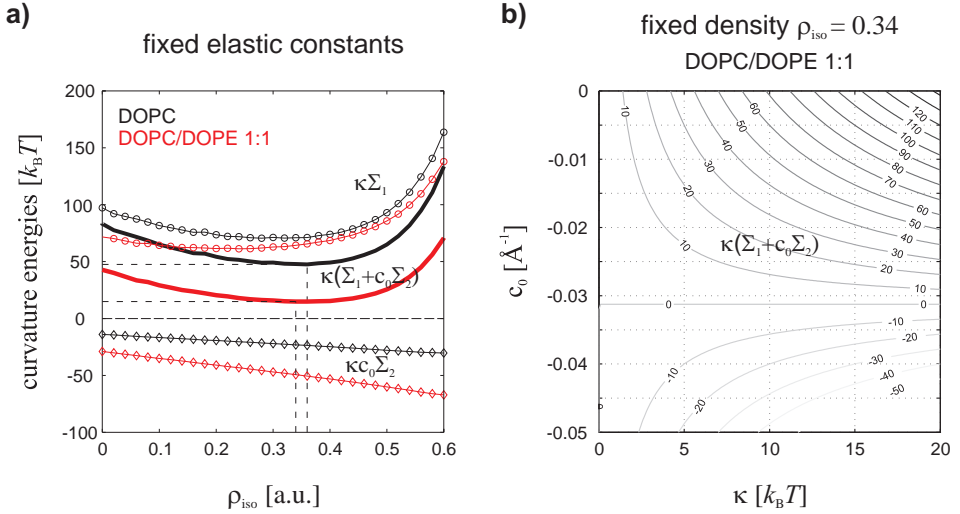


Figure 6.11: (a) Free energy term due to mean curvature $\Delta F_H = \kappa(\Sigma_1 + c_0 \Sigma_2)$ and its components for DOPC ($\kappa = 9 k_B T$, $c_0 = -0.0115 \text{\AA}^{-1}$) and an equimolar DOPC/DOPE mixture ($\kappa = 9 k_B T$, $c_0 = -0.024 \text{\AA}^{-1}$) as a function of ρ_{iso} . (b) ΔF_H for one isosurface as a function of c_0 and κ .

datasets are summarized in Tab. 6.1. Following [55], we estimate values for lipid mixtures by the molecular fraction-weighted mean of the parameters for the individual components. The results for the mean curvature contribution ΔF_H of DOPC and DOPC/DOPE 1:1 are plotted in Fig. 6.11. Since Σ_1 can only be positive and Σ_2 is also positive in all of our datasets, both terms in ΔF_H are different in sign for negative spontaneous curvature c_0 . Using our values of Σ_1 and Σ_2 , we obtain a minimum of $\Delta F_H \approx 15 k_B T$ for the DOPC/DOPE mixture and about $\Delta F_H \approx 50 k_B T$ for pure DOPC. Importantly, this is only the energy due to deviations from the spontaneous curvature. No additional contributions due to *e.g.* effects of lipid tilt or stretched chains are included.

The energy term $\Delta F_K = -4\pi\kappa_G$ due to Gaussian curvature has been neglected in many older papers. More recently, it has been realized that it may dominate the bending rigidity, which has stimulated new efforts to determine its value *e.g.* by experiments on bicontinuous cubic phases. It has been indicated that its modulus κ_G is negative and related to κ by [55, 88, 89, 199]

$$-1 \leq \frac{\kappa_G}{\kappa} \leq -\frac{1}{2}. \quad (6.21)$$

Tab. 6.1 provides recent values on some lipids used by us. With these, $\Delta F_K \approx 100 k_B T$ dominates the mean curvature term ΔF_H in case of DOPC and DOPC/DOPE 1:1. This agrees with results from continuum theory [55, 88] which point out a possibly crucial role of Gaussian curvature in stalk formation. Importantly, since the stalk phases we investigate are thermodynamically stable, there must be additional contributions to the

free energy which compensate the curvature energy and make the stalk phase stable with respect to the lamellar phase. We note that the work of hydration W_{hyd} corresponding to the cross section of the stalk waist estimated on the basis of our results of chapter 4 (*cf.* Fig. 4.12) is on the same order of magnitude as the total curvature energy. This makes the idea that stalk phase formation is driven by the interplay of hydration effects and Gaussian curvature energy put forward in [55] seem feasible.

In case of the two lipids with shorter chains, 14:1PC and 16:1PC, the minimum of Σ_1 is lower than in case of DOPC. In addition, due to the smaller monolayer thickness, κ is expected to be smaller as well. With an approximately constant spontaneous curvature, this predicts a decrease of ΔF_H for shorter chains. However, in the phase diagram (Fig. 3.9) we observe the reverse sequence, *i.e.* the stalk phase is formed most readily in DOPC. This example may serve to illustrate that mean and spontaneous curvature alone do not rationalize phospholipid phase behaviour.

Importantly, the available curvature elastic coefficients have been obtained in excess water conditions. It is not clear how and to what extent they vary upon dehydration. c_0 is expected to become more negative due to an decrease of the effective headgroup size by removal of water, κ_G is expected to become less negative. Both effects would lower ΔF_{bend} [55, 88]. In contrary, due to the observed thickening of lipid bilayers upon dehydration (*cf.* section 4.5.2), κ is expected to increase. Assuming a quadratic dependence of κ on the monolayer thickness [86] and a maximum increase of d_{hh} by about 10% (*cf.* Fig. 4.10) predicts a modest increase by a factor of ~ 1.2 .

While the observed structures of stalks in DOPC and the equimolar DOPC/DOPE mixture are very similar, changes are observed upon addition of cholesterol. On length scales relevant to stalk formation, the possibility of lipid demixing has been demonstrated for the distorted hexagonal phase [119]. Since we also observe this phase in DOPC/Chol mixtures (*cf.* section 3.3.1), the possibility of demixing should also be considered in case of the stalk phase in these lipid mixtures.

6.4 Conclusions

To the very best of our knowledge, the work presented in this chapter is the first attempt toward a structural characterization of stalks in different lipid systems based on experimental data. While some moderate changes are visible, our results indicate that the general features of stalks in the rhombohedral phospholipid phase are very similar for different lipid compositions. To analyze the curvature of the strongly bent lipid monolayer in a stalk, we have introduced an approach based on differential geometry of implicit surfaces. The obtained results indicate systematic changes in monolayer curvature with acyl chain length or cholesterol content. Being aware of the possible shortcomings of continuum theory on the length scales of membrane fusion intermediates, we note that our results are compatible with some of its recent predictions.

7 Summary

The aim of the present thesis was to use the stalk phase in phospholipids as a model system and study the initial steps in lipid bilayer fusion. Aligned lipid multibilayer stacks were used as samples throughout all experiments. *In vivo*, stalk formation and subsequent membrane fusion are most likely initiated by close bilayer contact mediated by proteins. To mimic this situation, the well-established osmotic stress method by relative humidity control was applied to vary the degree of hydration and thus the inter-bilayer distance in a controlled fashion. X-ray diffraction was then used to study lyotropic lipid polymorphism and identify conditions under which the stalk phase is stable (*chapter 3*), to quantify the repulsive forces opposing bilayer approach prior to stalk formation (*chapter 4*) and to obtain the structure of stalks in different lipids and lipid mixtures (*chapter 5*). Finally, concepts for the further analysis of stalk structures were presented (*chapter 6*).

The lyotropic phase behaviour of different lipids and several lipid mixtures was studied using a dedicated in-house diffractometer. The stalk phase was observed in several monounsaturated lipids structurally similar to dioleoylphosphatidylcholine (DOPC), where its existence was known before. Using DOPC as the host lipid, the effects of addition of cholesterol, dioleoylphosphatidylethanolamine (DOPE) and Phosphatidylinositol(4,5)-bisphosphate (PIP₂) were studied. These lipids promote stalk formation, *i.e.* lower the osmotic pressure required to induce the stalk phase or, equivalently, shift the phase boundary towards higher relative humidity. In addition, at lower hydration and higher molar ratio of cholesterol, DOPE or PIP₂, further nonlamellar phases were observed. In case of PIP₂, this effect was particularly strong. At a PIP₂ concentration of only 4 mol%, diffraction peaks characteristic for the inverted hexagonal phase appeared upon dehydration. This could have important implications for the role of PIP₂ in membrane fusion. The results of these experiments were summarized in several partial phase diagrams.

The repulsive forces between adjacent bilayers prior to stalk phase formation were studied for several pure phosphatidylcholines as well as DOPC/cholesterol and DOPC/DOPE mixtures. The parameters of the exponentially decaying repulsive pressure between bilayers in close contact, *i.e.* at low hydration, were determined by the osmotic stress method in conjunction with electron density profile analysis. To this end, the swelling method was implemented and successfully applied to solve the phase problem and obtain bilayer electron density profiles. For the investigated samples, our results indicate that stalk phase formation becomes feasible at an interbilayer distance below $9.0 \pm 0.5 \text{ \AA}$, measured as the distance between the electron density maxima of adjacent lipid bilayers. Addition of cholesterol or DOPE does not change this value, but rather promotes dehydration and thereby shifts the phase boundaries. The obtained hydration force parameters allow to calculate the work required to bring lipid bilayers into close contact, *i.e.* determine the “hydration barrier” opposing membrane fusion. The foremost goal was to characterize stalks in different lipid systems. Due to the unusual $2d$ powder character of aligned samples, measurements in different scattering geometries were required. Grazing-incidence x-ray diffraction data on the stalk phases of a variety of lipids were recorded during two synchrotron beam times. Combined

with additional reflectivity scans as well as powder diffraction data, the form factor amplitudes were obtained. Subsequently, by application of the swelling method for the rhombohedral phase and additional criteria, the phase problem was solved and electron density maps could be reconstructed for seven different lipid systems, including the first data on stalks in lipid mixtures. The observed number of reflections are clearly higher than in previous studies and thus yield better resolved electron density maps.

Finally, the obtained structures were investigated more closely. By direct visual inspection, stalks in the investigated lipid systems are very similar. This is confirmed by the dimensionless ratios of structural parameters defined in analogy to the lamellar phase. To assess the curvatures of lipid monolayers, a method based on electron density iso-surfaces is proposed. Only the experimentally determined form factors and lattice parameters are required as an input. To this end, concepts from differential geometry of implicit surfaces were applied. For monounsaturated phosphatidylcholines as well as for DOPC/cholesterol mixtures, systematic changes are observed. According to our results, addition of an equimolar amount of DOPE to DOPC has only a very subtle effect on stalk structure. In contrast, upon addition of 30 mol% cholesterol, changes can be observed in the strongly curved stalk waist region. Our results are discussed in the framework of the continuum theory of membrane bending. For the first time, they enable an evaluation of the bending and hydration energies involved in stalk formation on the basis of experimental data.

A Appendix

A.1 Triplet relationship

Consider a centrosymmetric crystal, *i.e.* $F_{hkl} = v_{hkl}|F_{hkl}|$ where $v_{hkl} = \pm 1$. For three reflections which are all strong and whose scattering vectors sum to zero,

$$\sum_{i=1}^3 \vec{q}_{h_i k_i \ell_i} = 0, \quad (\text{A.1})$$

it is likely that

$$\prod_{i=1}^3 v_{h_i k_i \ell_i} = +1. \quad (\text{A.2})$$

This is a special case of the triplet relationship known from direct methods of crystallography [141, 188]. To understand its origin, one has to ask under which circumstances a particular reflection is strong, *i.e.* the form factor amplitude $|F_{hkl}|$ is large. The electron density is always positive, $\rho(\vec{r}) \geq 0$. From the definition of the form factor in case of centrosymmetry,

$$F_{hkl} = \int_V \rho(\vec{r}) \cos(\vec{q}_{hkl} \cdot \vec{r}) dV, \quad (\text{A.3})$$

where V denotes the unit cell volume, it follows that F_{hkl} tends to adopt large positive values if the electron density is concentrated at positions \vec{r} where the cosine is close to its maximum value, *i.e.* $\vec{q}_{hkl} \cdot \vec{r} = 2\pi \cdot n$, $n \in \mathbb{Z}$. This is the definition of a family of lattice planes (hkl) . In contrast, if $\rho(\vec{r})$ is concentrated in regions between the lattice planes where the cosine is close to its minimum, the form factor will adopt large negative values.

In Fig. A.1, this principle is illustrated for two arbitrary reflections 200 and 010. For all four possible phase combinations $\{v_{200} = \pm 1, v_{010} = \pm 1\}$, an electron density distribution leading to large $|F_{200}|$ and $|F_{010}|$ exists. Now assume that the reflection $\bar{2}\bar{1}0$ which completes the triplet is strong as well. The corresponding family of planes $(\bar{2}\bar{1}0)$ is shown by solid blue lines in the right column. For each of the four electron density distributions leading to strong 200 and 010 reflections, the electron density is concentrated either close to or in between the planes $(\bar{2}\bar{1}0)$, thus making either $v_{\bar{2}\bar{1}0} = +1$ or $v_{\bar{2}\bar{1}0} = -1$ more likely. For each row, one recognizes that Eq. (A.2) is always fulfilled. Importantly, for realistic electron density distributions $\rho(\vec{r})$, triplet relationships have probabilistic character.

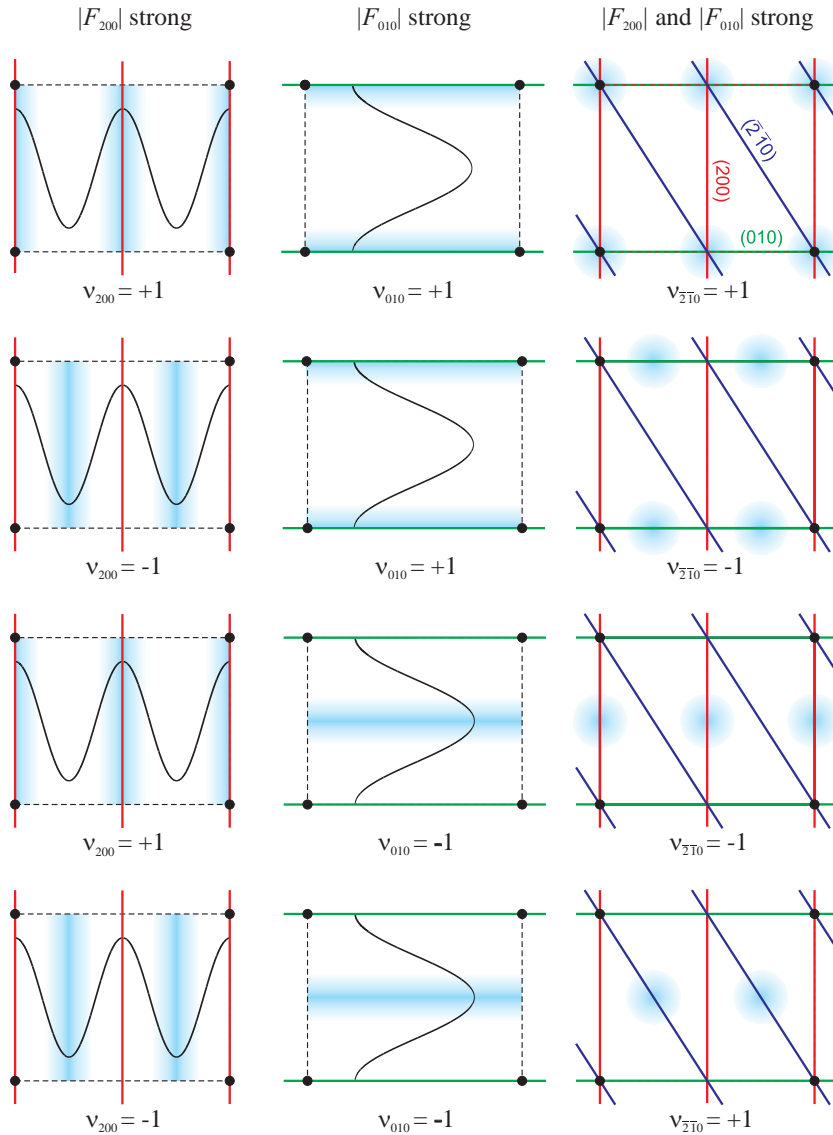


Figure A.1: Illustration of a triplet relationship. Blue regions indicate electron density maxima. The unit cell is centrosymmetric and the three form factor amplitudes $|F_{200}|, |F_{010}|, |F_{\bar{2}\bar{1}0}|$ are all assumed to be strong. Lattice planes (200) are shown in red, (010) in green and $(\bar{2}\bar{1}0)$ in blue. In the right column, electron density distributions leading to the four possible sign combinations $\{v_{200} = \pm 1, v_{010} = \pm 1\}$ are indicated. If v_{200} and v_{010} are fixed and provided that all three reflections are strong, then $v_{\bar{2}\bar{1}0} = \pm 1$ is likely to have a value such that Eq. A.2 is fulfilled.

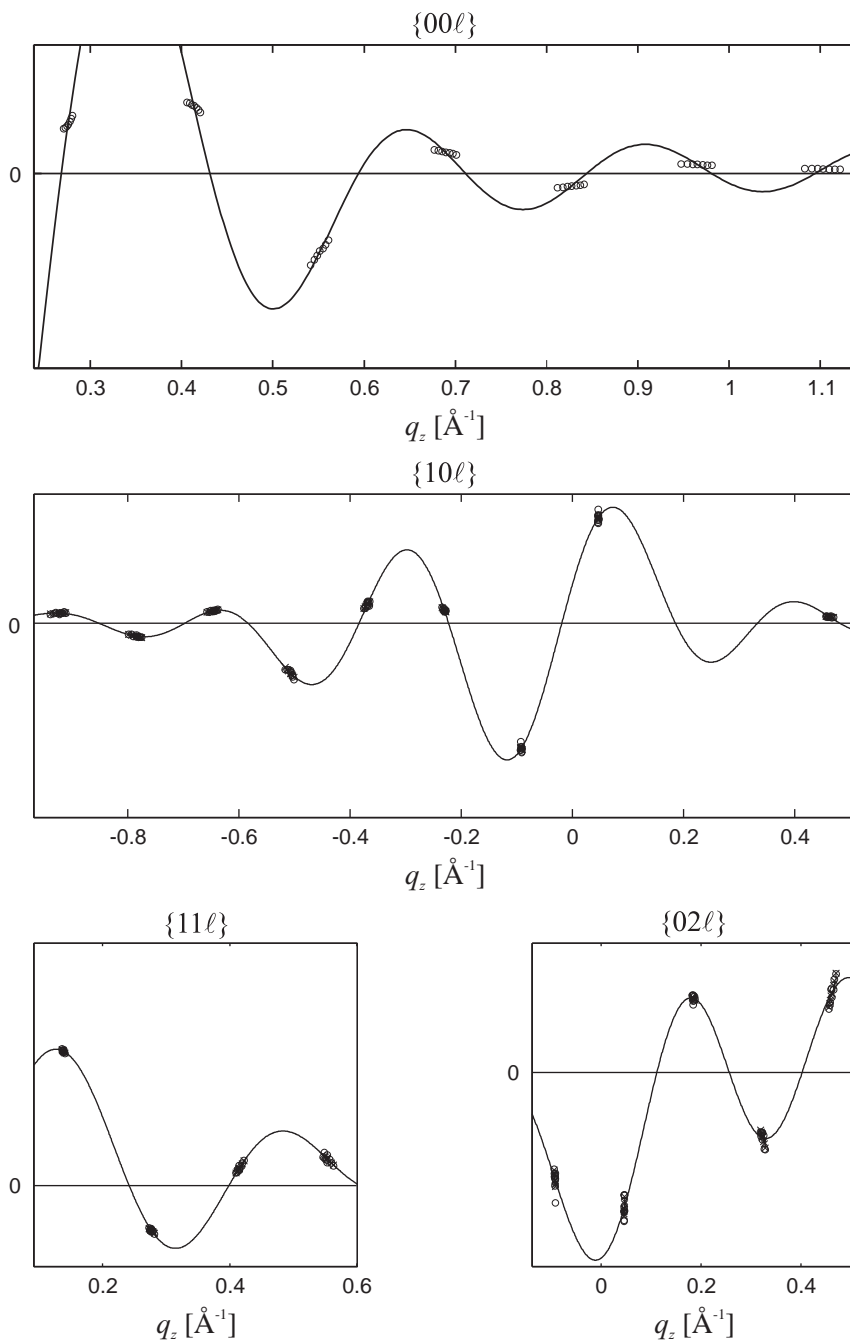
A.2 Crystallographic data and swelling diagrams

Below, the swelling diagrams used for phase determination are provided for all stalk phase datasets. The data correspond to the most likely phase factor combinations $\{v_{hkl} = \pm 1 | h, k = \text{const.}\}$ of each peak series as determined by the swelling method. After a swelling diagram, a table with the corresponding form factors (including phase information) and lattice parameters used for electron density reconstruction by Eq. (5.35) is given. The notation $\{hkl\}$ for a family of equivalent reflections summarized in Tab. A.1 is used. Lattice parameters were obtained from the GIXD data. Form factors in each column are normalized such that $\max[\Delta\rho] = 1$. Reflections which were not used for further analysis in chapter 6 are indicated by an asterisk *. When comparing the swelling diagrams and formfactor tables, the following points should be noted:

- Deviations between swelling plots and tables occur for some lipids in case of the $\{02\ell\}$ reflections, since the “best” phases according to the swelling method did not always yield the most reasonable $\Delta\rho(\vec{r})$ (cf. Fig. 5.15).
- Datapoints corresponding to the strong $|F_{003}|$ reflection with $v_{hkl} = -1$ are not shown in order to increase the visibility of the higher orders $\{00\ell\}$.
- The number of hydration levels used in reflectivity and GIXD data was different in most cases. Therefore, the number of datapoints in the swelling diagrams of in-plane and out-of-plane reflections may be different.
- SLS datasets for DOPC, DPhPC and DOPC/DOPE 1:1 are each composed of data from two samples. Therefore, some RH values may occur twice and, in case of DOPC, even in non-monotonous order. Here, the limitations in RH measurements become apparent once again.
- For the two DOPC datasets (SLS/ESRF) from two synchrotron beamlines, the same reflectivity (and powder) data were used. Therefore, the swelling plots for the $\{00\ell\}$ series are the same in both figures.

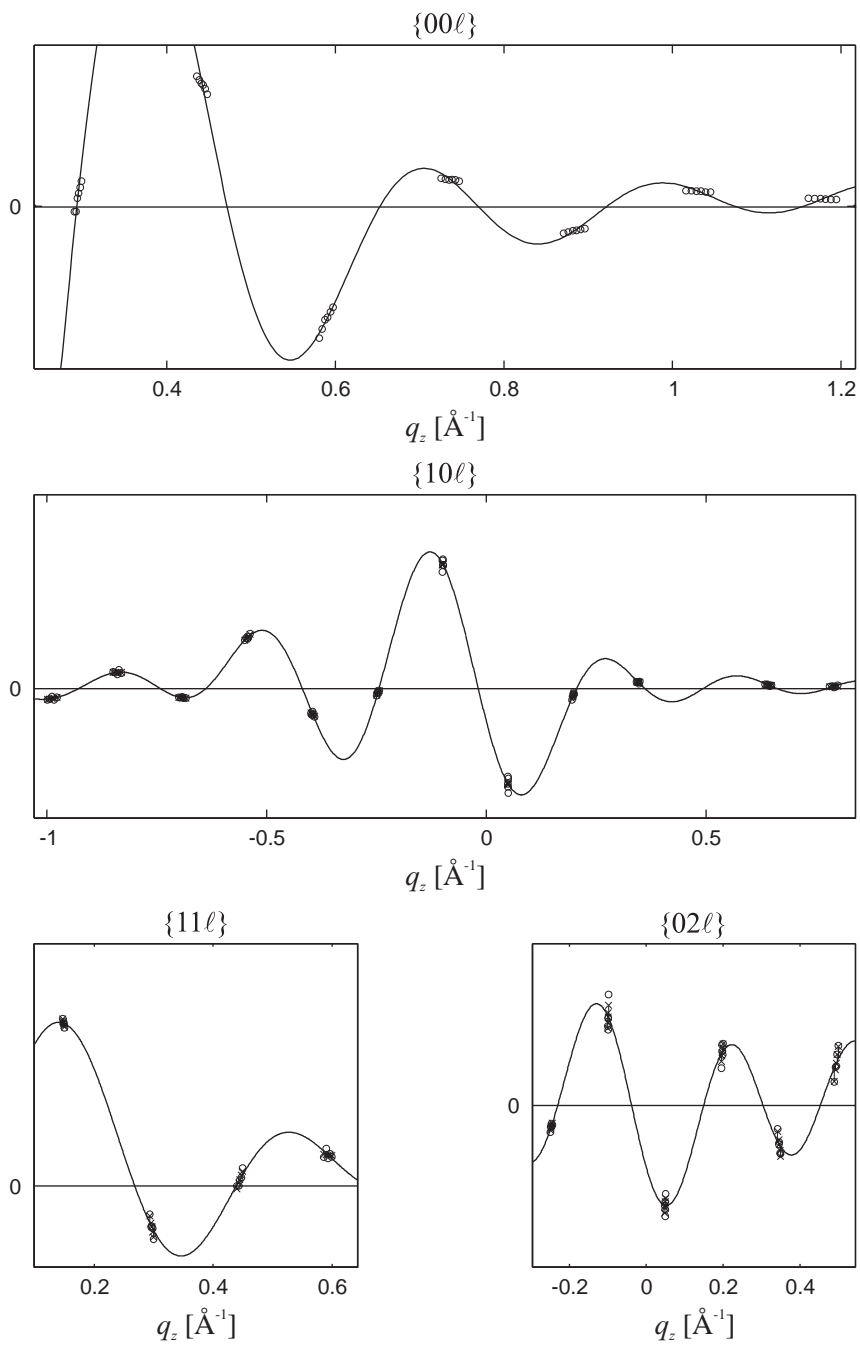
family	reflections	$q_{ } / \frac{4\pi}{\sqrt{3}a}$
$\{00\ell\}$	(00ℓ)	0
$\{10\ell\}$	$(10\ell), (0\bar{1}\ell), (\bar{1}1\ell)$	1
$\{11\ell\}$	$(11\ell), (\bar{1}\bar{1}\ell), (2\bar{1}\ell), (\bar{2}1\ell), (1\bar{2}\ell), (\bar{1}2\ell)$	$\sqrt{3}$
$\{02\ell\}$	$(02\ell), (\bar{2}0\ell), (2\bar{2}\ell)$	2
$\{21\ell\}$	$(21\ell), (3\bar{1}\ell), (1\bar{3}\ell), (\bar{1}\bar{2}\ell), (\bar{2}3\ell), (\bar{3}2\ell)$	$\sqrt{7}$
$\{30\ell\}$	$(30\ell), (\bar{3}0\ell), (03\ell), (0\bar{3}\ell), (3\bar{3}\ell), (\bar{3}3\ell)$	3

Table A.1: Families of reflections $\{hkl\}$ and their members (hkl) (R phase).

DOPC (SLS), $RH = 18 - 34\%$ 

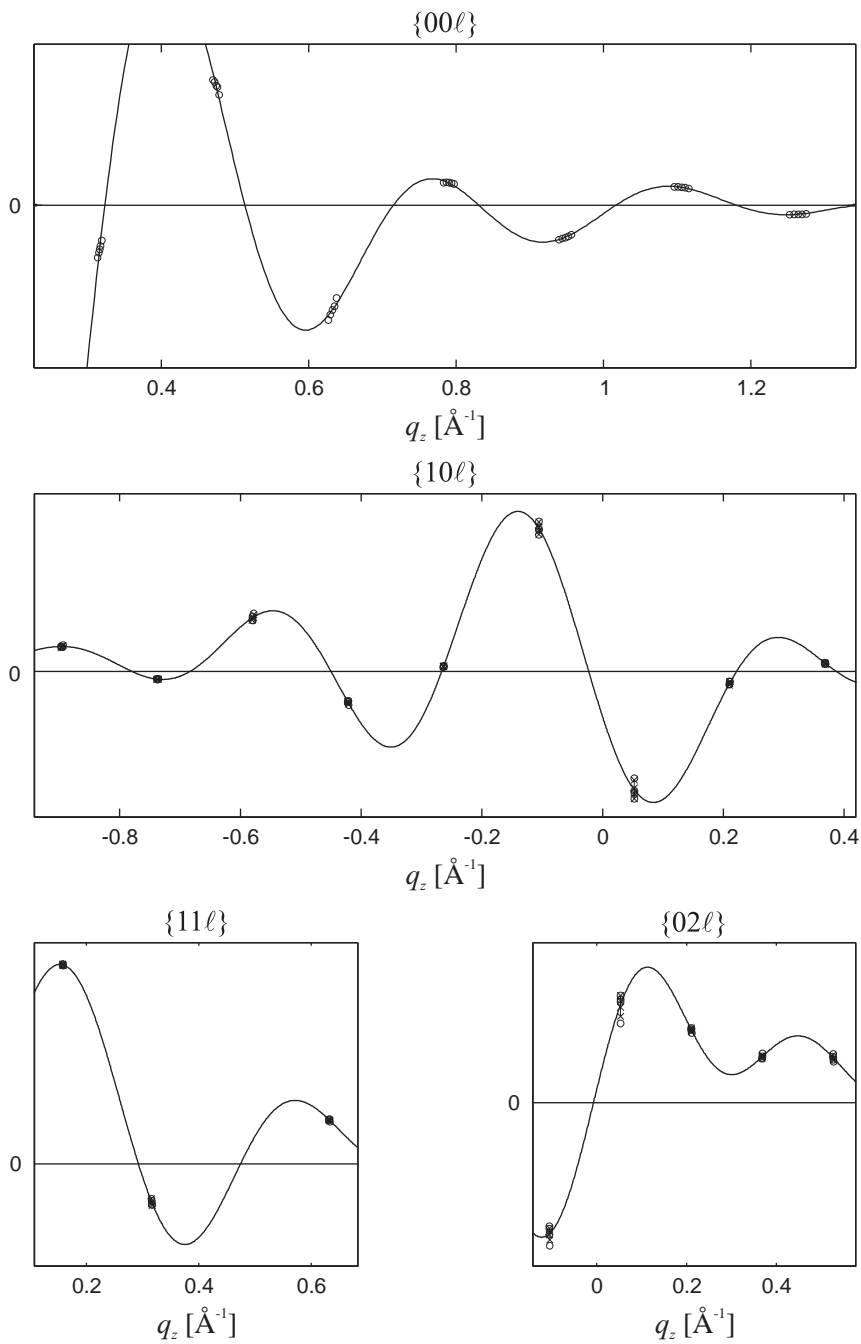
DOPC (SLS), $RH = 18 - 34\%$

<i>RH</i>	18	21	24	28	27	30	32	30	34	
<i>d</i>	44.59	44.89	45.07	45.40	45.41	45.49	45.66	45.79	45.95	
$\sigma(d)$	0.07	0.22	0.07	0.15	0.20	0.16	0.16	0.30	0.13	
<i>a</i>	63.47	64.53	65.49	66.49	66.66	66.90	67.74	68.21	68.89	
$\sigma(a)$	0.19	0.14	0.01	0.01	0.14	0.08	0.22	0.08	0.08	
{0, 0, 3}	-0.6295	-0.6468	-0.6717	-0.6790	-0.6759	-0.6803	-0.6760	-0.6785	-0.6930	
{0, 0, 6}	0.0431	0.0423	0.0428	0.0410	0.0408	0.0405	0.0391	0.0383	0.0381	
{0, 0, 9}	0.0451	0.0476	0.0502	0.0522	0.0520	0.0527	0.0531	0.0539	0.0557	
{0, 0, 12}	-0.0474	-0.0520	-0.0560	-0.0603	-0.0601	-0.0615	-0.0630	-0.0647	-0.0679	
{0, 0, 15}	0.0136	0.0146	0.0156	0.0164	0.0164	0.0167	0.0169	0.0173	0.0180	
{0, 0, 18}	-0.0080	-0.0086	-0.0092	-0.0098	-0.0098	-0.0099	-0.0101	-0.0103	-0.0108	
{0, 0, 21}	0.0060	0.0063	0.0067	0.0070	0.0070	0.0071	0.0071	0.0072	0.0075	
{0, 0, 24}* {1, 0, 20}* {1, 0, 17}	0.0029 0.0114 -0.0141	0.0031 0.0121 -0.0137	0.0033 0.0119 -0.0146	0.0035 0.0100 -0.0132	0.0035 0.0100 -0.0152	0.0035 0.0111 -0.0144	0.0036 0.0111 -0.0151	0.0037 0.0125 -0.0153	0.0038 0.0125 -0.0153	0.0038 0.0106 -0.0145
{1, 0, 14}	0.0144	0.0131	0.0142	0.0132	0.0134	0.0137	0.0139	0.0141	0.0145	
{1, 0, 11}	-0.0593	-0.0567	-0.0523	-0.0522	-0.0543	-0.0541	-0.0578	-0.0577	-0.0588	
{1, 0, 8}	0.0189	0.0183	0.0188	0.0231	0.0189	0.0237	0.0235	0.0186	0.0225	
{1, 0, 5}	0.0204	0.0174	0.0165	0.0139	0.0134	0.0139	0.0128	0.0135	0.0126	
{1, 0, 2}	-0.1619	-0.1549	-0.1331	-0.1366	-0.1393	-0.1347	-0.1445	-0.1386	-0.1301	
{1, 0, 1}	0.1319	0.1275	0.1275	0.1197	0.1190	0.1174	0.1120	0.1088	0.1067	
{1, 0, 7}	-0.0042	-0.0040	-0.0051	-0.0071	-0.0047	-0.0078	-0.0077	-0.0068	-0.0086	
{1, 0, 10}* {1, 1, 0}	0.0075 -0.0300	0.0069 -0.0296	0.0079 -0.0300	0.0070 -0.0289	0.0066 -0.0288	0.0070 -0.0286	0.0069 -0.0277	0.0076 -0.0273	0.0072 -0.0272	
{1, 1, 3}	0.0269	0.0260	0.0240	0.0239	0.0240	0.0234	0.0242	0.0232	0.0227	
{1, 1, 6}	-0.0099	-0.0089	-0.0083	-0.0079	-0.0077	-0.0080	-0.0079	-0.0077	-0.0071	
{1, 1, 9}	0.0051	0.0043	0.0034	0.0029	0.0028	0.0034	0.0028	0.0023	0.0021	
{1, 1, 12}	0.0040	0.0044	0.0046	0.0041	0.0054	0.0044	0.0047	0.0057	0.0047	
{0, 2, 2}	-0.0124	-0.0124	-0.0117	-0.0118	-0.0126	-0.0113	-0.0113	-0.0141	-0.0111	
{0, 2, 1}	0.0156	0.0150	0.0155	0.0149	0.0156	0.0151	0.0166	0.0132	0.0154	
{0, 2, 4}	-0.0093	-0.0092	-0.0080	-0.0079	-0.0075	-0.0084	-0.0084	-0.0083	-0.0080	
{0, 2, 7}	0.0098	0.0094	0.0071	0.0074	0.0067	0.0066	0.0067	0.0069	0.0062	
{0, 2, 10}	-0.0125	-0.0113	-0.0093	-0.0093	-0.0084	-0.0091	-0.0078	-0.0072	-0.0066	

di16:1PC (SLS), $RH = 18 - 31\%$ 

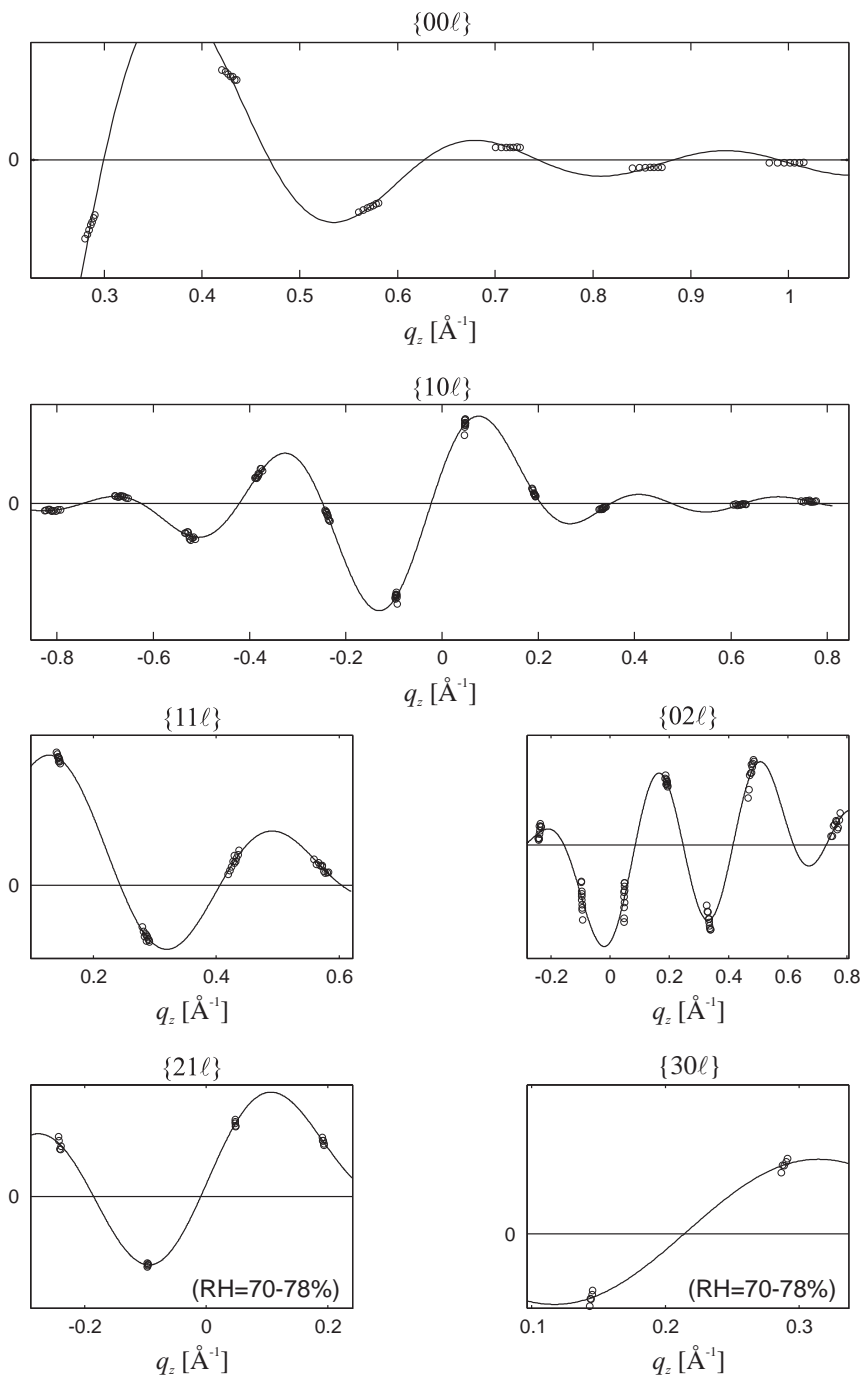
di16:1PC (SLS), $RH = 18 - 31\%$

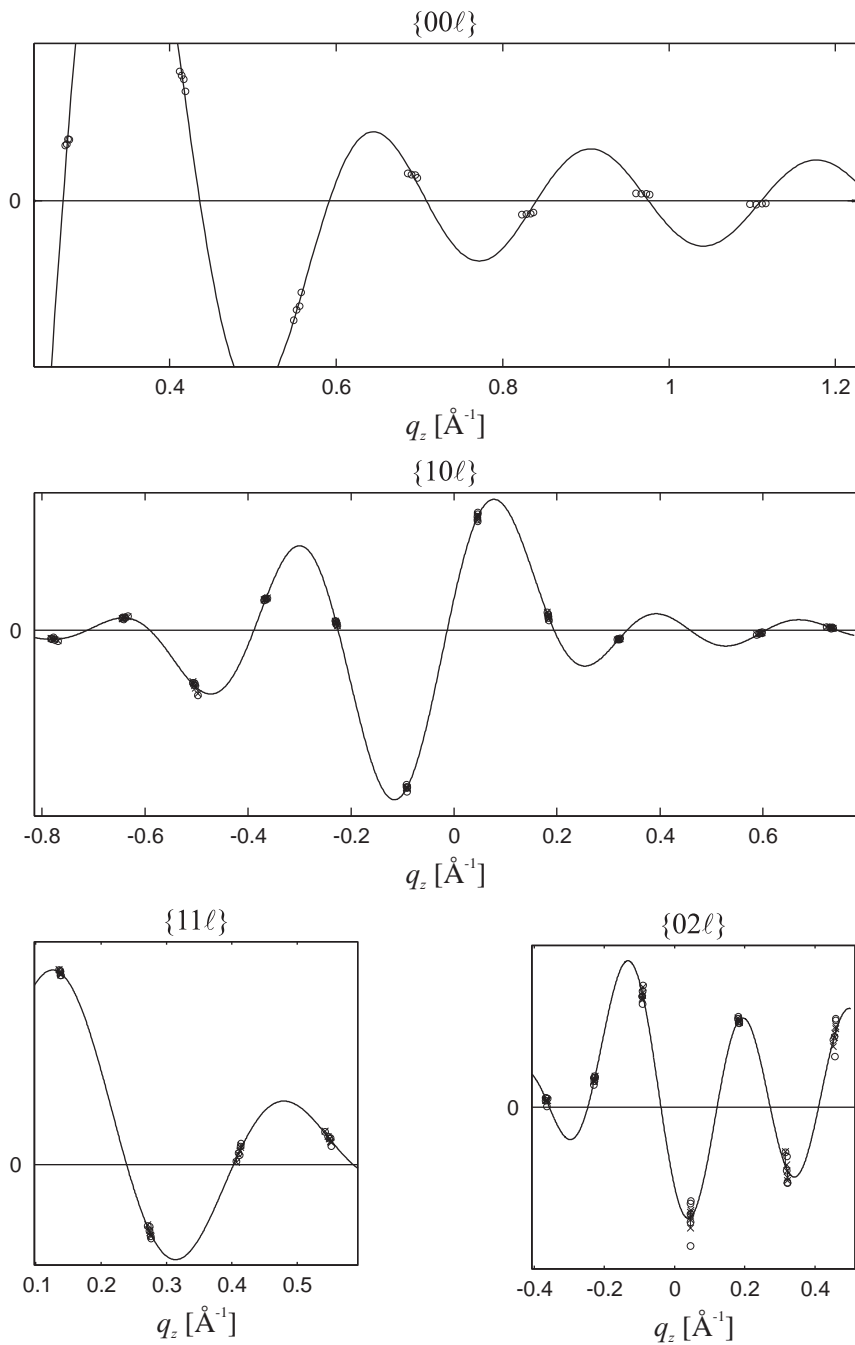
RH	18	22	25	28	31
d	41.93	42.14	42.38	42.56	42.88
$\sigma(d)$	0.07	0.10	0.06	0.10	0.05
a	61.85	62.93	63.86	65.37	67.10
$\sigma(a)$	0.20	0.01	0.16	0.17	0.07
{0,0,3}	-0.6302	-0.6791	-0.6943	-0.6662	-0.7171
{0,0,6}	0.0172	0.0149	0.0108	0.0073	0.0021
{0,0,9}	0.0665	0.0734	0.0771	0.0754	0.0839
{0,0,12}	-0.0573	-0.0650	-0.0703	-0.0702	-0.0806
{0,0,15}	0.0149	0.0163	0.0170	0.0165	0.0182
{0,0,18}	-0.0130	-0.0145	-0.0154	-0.0152	-0.0171
{0,0,21}	0.0084	0.0092	0.0095	0.0093	0.0102
{0,0,24}* {1,0,20}* {1,0,17}	0.0039 0.0152 -0.0217	0.0043 0.0125 -0.0185	0.0046 0.0094 -0.0167	0.0045 0.0135 -0.0228	0.0050 0.0096 -0.0168
{1,0,14}	0.0120	0.0110	0.0102	0.0118	0.0108
{1,0,11}	-0.0639	-0.0587	-0.0591	-0.0626	-0.0598
{1,0,8}	0.0326	0.0309	0.0274	0.0322	0.0313
{1,0,5}	0.0097	0.0056	0.0047	0.0048	0.0025
{1,0,2}	-0.1696	-0.1354	-0.1465	-0.1571	-0.1352
{1,0,1}	0.1193	0.1220	0.1169	0.1068	0.1045
{1,0,4}* {1,0,7}	0.0073 -0.0090	0.0055 -0.0057	0.0077 -0.0076	0.0097 -0.0076	0.0126 -0.0071
{1,0,13}* {1,0,16}* {1,1,0}	-0.0042 -0.0043 -0.0278	-0.0030 -0.0019 -0.0286	-0.0032 -0.0014 -0.0277	-0.0050 -0.0029 -0.0255	-0.0045 -0.0022 -0.0253
{1,1,3}	0.0335	0.0302	0.0312	0.0316	0.0293
{1,1,6}	-0.0113	-0.0079	-0.0076	-0.0079	-0.0050
{1,1,9}	0.0038	0.0016	0.0011	0.0000	0.0000
{1,1,12}	0.0062	0.0060	0.0052	0.0073	0.0051
{0,2,5}* {0,2,2}	0.0057 -0.0168	0.0041 -0.0162	0.0040 -0.0166	0.0036 -0.0146	0.0035 -0.0194
{0,2,1}	0.0188	0.0180	0.0198	0.0216	0.0176
{0,2,4}	-0.0130	-0.0094	-0.0103	-0.0117	-0.0065
{0,2,7}	0.0103	0.0089	0.0070	0.0076	0.0041
{0,2,10}	-0.0126	-0.0094	-0.0074	-0.0074	-0.0041

di14:1PC (SLS), $RH = 13.6 - 17\%$ 

di14:1PC (SLS), $RH = 13.6 - 17\%$

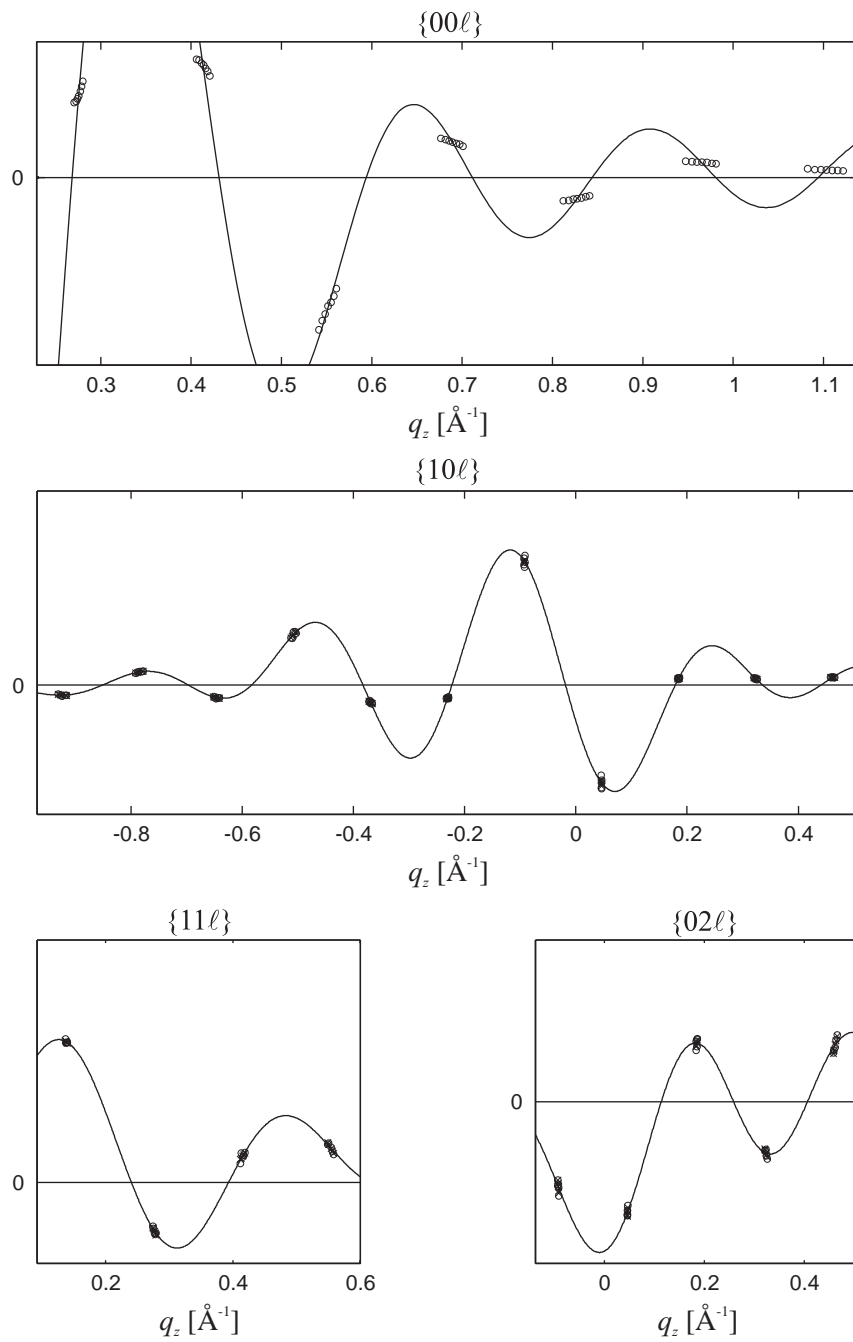
RH	13.6	14	15.6	17
d	39.68	39.72	39.77	39.85
$\sigma(d)$	0.07	0.06	0.11	0.17
a	60.87	61.14	61.96	62.93
$\sigma(a)$	0.01	0.29	0.24	0.01
$\{0, 0, 3\}$	-0.7611	-0.7523	-0.7644	-0.7466
$\{0, 0, 6\}$	-0.0301	-0.0304	-0.0317	-0.0321
$\{0, 0, 9\}$	0.0838	0.0834	0.0854	0.0844
$\{0, 0, 12\}$	-0.0729	-0.0729	-0.0751	-0.0748
$\{0, 0, 15\}$	0.0157	0.0156	0.0158	0.0155
$\{0, 0, 18\}$	-0.0226	-0.0225	-0.0231	-0.0229
$\{0, 0, 21\}$	0.0125	0.0124	0.0127	0.0125
$\{0, 0, 24\}^*$	-0.0065	-0.0064	-0.0066	-0.0065
$\{1, 0, \bar{1}7\}$	-0.0197	-0.0210	-0.0204	-0.0232
$\{1, 0, \bar{1}4\}$	0.0062	0.0065	0.0070	0.0066
$\{1, 0, \bar{1}1\}$	-0.0422	-0.0465	-0.0420	-0.0511
$\{1, 0, 8\}$	0.0251	0.0258	0.0243	0.0298
$\{1, 0, \bar{5}\}$	-0.0036	-0.0041	-0.0046	-0.0045
$\{1, 0, \bar{2}\}$	-0.1119	-0.1207	-0.1173	-0.1322
$\{1, 0, 1\}$	0.1045	0.1011	0.1001	0.0941
$\{1, 0, 4\}$	0.0084	0.0083	0.0106	0.0118
$\{1, 0, 7\}$	-0.0060	-0.0065	-0.0071	-0.0079
$\{1, 1, 0\}$	-0.0254	-0.0249	-0.0250	-0.0240
$\{1, 1, 3\}$	0.0213	0.0220	0.0215	0.0230
$\{1, 1, 6\}$	-0.0044	-0.0045	-0.0040	-0.0040
$\{1, 1, 12\}$	0.0045	0.0049	0.0047	0.0051
$\{0, 2, \bar{2}\}$	-0.0143	-0.0141	-0.0135	-0.0167
$\{0, 2, 1\}$	0.0109	0.0116	0.0116	0.0092
$\{0, 2, 4\}$	-0.0075	-0.0082	-0.0079	-0.0087
$\{0, 2, 7\}$	0.0050	0.0055	0.0048	0.0052
$\{0, 2, 10\}$	-0.0044	-0.0048	-0.0053	-0.0053

DPhPC (SLS), $RH = 62 - 78\%$ 

DOPC/DOPE 1:1(SLS), $RH = 68 - 74\%$ 

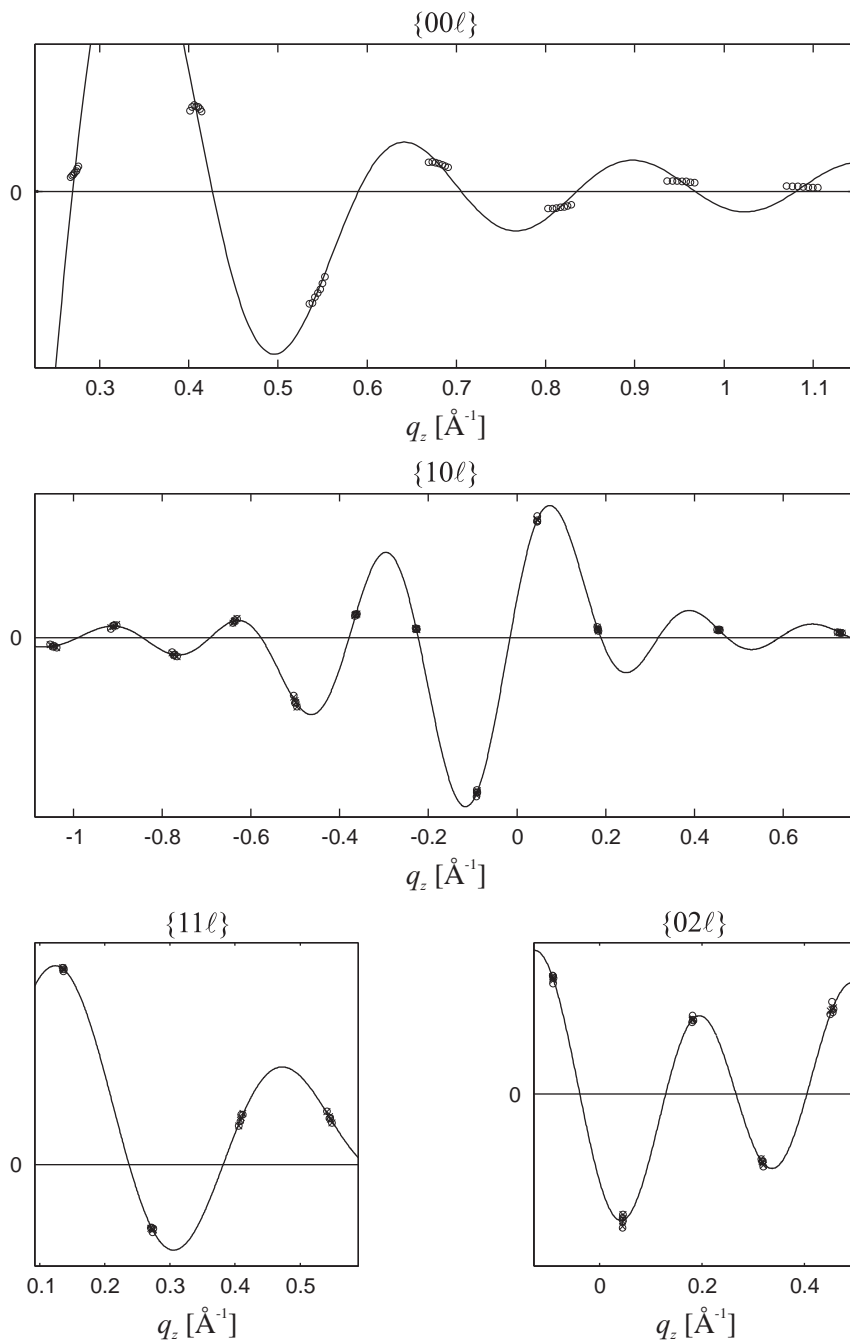
DOPC/DOPE 1:1 (SLS), $RH = 68 - 74\%$

RH	68	70	72	72	74
d	45.50	45.59	45.77	45.93	46.31
$\sigma(d)$	0.08	0.01	0.32	0.12	0.20
a	68.43	69.65	72.11	71.19	73.56
$\sigma(a)$	0.08	0.16	0.39	0.31	0.02
{0,0,3}	-0.7114	-0.7135	-0.7239	-0.7259	-0.7339
{0,0,6}	0.0289	0.0285	0.0281	0.0274	0.0259
{0,0,9}	0.0620	0.0632	0.0661	0.0682	0.0732
{0,0,12}	-0.0549	-0.0565	-0.0602	-0.0630	-0.0698
{0,0,15}	0.0131	0.0134	0.0140	0.0144	0.0155
{0,0,18}	-0.0066	-0.0067	-0.0071	-0.0073	-0.0079
{0,0,21}	0.0036	0.0037	0.0038	0.0040	0.0043
{0,0,24}*}	-0.0016	-0.0017	-0.0018	-0.0019	-0.0022
{1,0, $\bar{1}$ 7}	-0.0086	-0.0089	-0.0076	-0.0090	-0.0095
{1,0, $\bar{1}$ 4}	0.0109	0.0117	0.0104	0.0113	0.0117
{1,0, $\bar{1}$ 1}	-0.0520	-0.0522	-0.0528	-0.0509	-0.0559
{1,0, $\bar{8}$ }	0.0291	0.0284	0.0312	0.0286	0.0271
{1,0, $\bar{5}$ }	0.0089	0.0077	0.0057	0.0064	0.0034
{1,0, $\bar{2}$ }	-0.1542	-0.1467	-0.1609	-0.1445	-0.1340
{1,0,1}	0.1134	0.1111	0.1078	0.1034	0.0939
{1,0,4}*}	0.0095	0.0113	0.0154	0.0127	0.0149
{1,0,7}	-0.0081	-0.0087	-0.0096	-0.0087	-0.0084
{1,0,13}*}	-0.0022	-0.0033	-0.0029	-0.0033	-0.0042
{1,0,16}*}	0.0015	0.0023	0.0013	0.0022	0.0024
{1,1,0}	-0.0210	-0.0212	-0.0219	-0.0223	-0.0233
{1,1,3}	0.0294	0.0284	0.0305	0.0279	0.0263
{1,1,6}	-0.0115	-0.0108	-0.0098	-0.0097	-0.0083
{1,1,9}	0.0032	0.0027	0.0015	0.0016	0.0004
{1,1,12}	0.0029	0.0040	0.0041	0.0041	0.0044
{0,2, $\bar{8}$ }*}	-0.0008	-0.0011	-0.0011	-0.0001	-0.0009
{0,2, $\bar{5}$ }*}	-0.0028	-0.0035	-0.0033	-0.0036	-0.0032
{0,2, $\bar{2}$ }	-0.0139	-0.0133	-0.0131	-0.0135	-0.0132
{0,2,1}	0.0118	0.0117	0.0176	0.0125	0.0125
{0,2,4}	-0.0107	-0.0101	-0.0107	-0.0105	-0.0096
{0,2,7}	0.0095	0.0091	0.0063	0.0074	0.0050
{0,2,10}	-0.0111	-0.0105	-0.0064	-0.0082	-0.0073

DOPC (ESRF), $RH = 24 - 32\%$ 

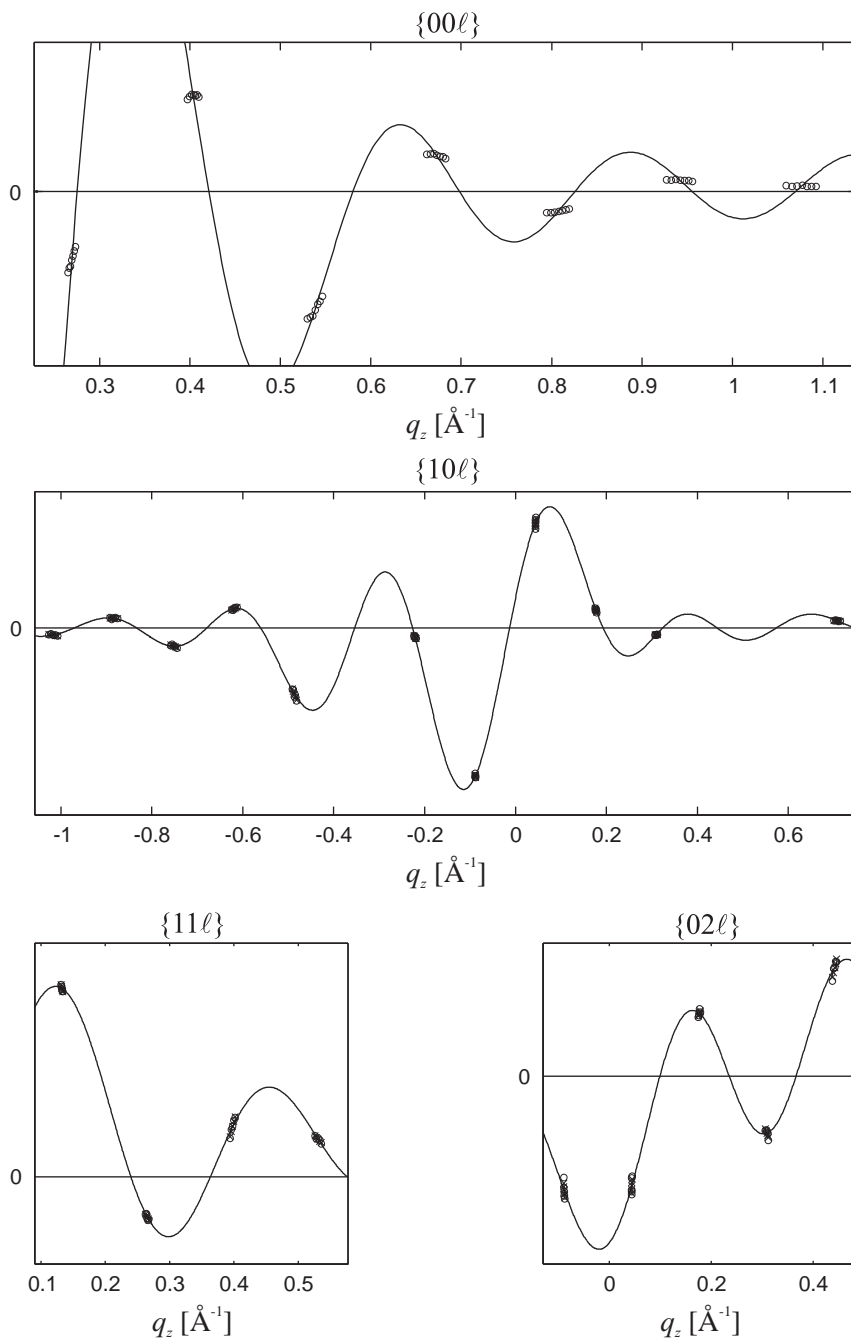
DOPC (ESRF), $RH = 24 - 32\%$

RH	24	26	28	30	32
D	44.99	45.18	45.34	45.62	45.75
$\sigma(d)$	0.22	0.23	0.25	0.27	0.25
a	64.01	65.13	65.69	66.50	67.41
$\sigma(a)$	0.41	0.46	0.68	0.36	0.44
$\{0, 0, 3\}$	-0.6014	-0.6376	-0.6298	-0.6352	-0.6292
$\{0, 0, 6\}$	0.0388	0.0399	0.0384	0.0369	0.0358
$\{0, 0, 9\}$	0.0446	0.0481	0.0482	0.0498	0.0498
$\{0, 0, 12\}$	-0.0493	-0.0543	-0.0554	-0.0588	-0.0595
$\{0, 0, 15\}$	0.0138	0.0150	0.0151	0.0158	0.0159
$\{0, 0, 18\}$	-0.0082	-0.0089	-0.0090	-0.0095	-0.0095
$\{0, 0, 21\}$	0.0059	0.0064	0.0064	0.0067	0.0067
$\{0, 0, 24\}^*$	0.0029	0.0032	0.0032	0.0034	0.0034
$\{1, 0, \bar{2}0\}^*$	0.0115	0.0114	0.0124	0.0116	0.0117
$\{1, 0, \bar{1}7\}$	-0.0142	-0.0139	-0.0145	-0.0141	-0.0154
$\{1, 0, \bar{1}4\}$	0.0142	0.0145	0.0151	0.0144	0.0146
$\{1, 0, \bar{1}1\}$	-0.0569	-0.0527	-0.0576	-0.0578	-0.0579
$\{1, 0, 8\}$	0.0205	0.0182	0.0195	0.0197	0.0219
$\{1, 0, \bar{5}\}$	0.0170	0.0154	0.0153	0.0146	0.0139
$\{1, 0, \bar{2}\}$	-0.1538	-0.1367	-0.1286	-0.1331	-0.1457
$\{1, 0, 1\}$	0.1162	0.1181	0.1125	0.1062	0.1020
$\{1, 0, 4\}^*$	-0.0086	-0.0073	-0.0059	-0.0073	-0.0064
$\{1, 0, 7\}$	-0.0066	-0.0062	-0.0065	-0.0072	-0.0076
$\{1, 0, 10\}^*$	-0.0091	-0.0080	-0.0083	-0.0078	-0.0083
$\{1, 1, 0\}$	-0.0280	-0.0288	-0.0277	-0.0266	-0.0258
$\{1, 1, 3\}$	0.0273	0.0254	0.0244	0.0243	0.0258
$\{1, 1, 6\}$	-0.0099	-0.0094	-0.0089	-0.0080	-0.0079
$\{1, 1, 9\}$	0.0057	0.0049	0.0044	0.0051	0.0034
$\{1, 1, 12\}$	0.0054	0.0057	0.0061	0.0068	0.0068
$\{0, 2, \bar{2}\}$	-0.0153	-0.0154	-0.0144	-0.0149	-0.0171
$\{0, 2, 1\}$	0.0203	0.0198	0.0199	0.0197	0.0203
$\{0, 2, 4\}$	-0.0122	-0.0100	-0.0108	-0.0105	-0.0092
$\{0, 2, 7\}$	0.0112	0.0099	0.0083	0.0085	0.0088
$\{0, 2, 10\}$	-0.0129	-0.0112	-0.0095	-0.0089	-0.0088

DOPC/Chol 90:10 (ESRF), $RH = 36 - 42\%$ 

DOPC/Chol 90:10 (ESRF), $RH = 36 - 42\%$

RH	36	38	40	42
d	45.79	46.01	46.15	46.45
$\sigma(d)$	0.29	0.28	0.36	0.30
a	66.38	67.81	68.02	69.10
$\sigma(a)$	0.51	0.44	0.75	0.73
{0, 0, 3}	-0.5790	-0.5863	-0.5970	-0.5983
{0, 0, 6}	0.0119	0.0112	0.0108	0.0096
{0, 0, 9}	0.0447	0.0453	0.0462	0.0463
{0, 0, 12}	-0.0504	-0.0531	-0.0554	-0.0584
{0, 0, 15}	0.0141	0.0147	0.0152	0.0157
{0, 0, 18}	-0.0079	-0.0083	-0.0086	-0.0090
{0, 0, 21}	0.0051	0.0053	0.0055	0.0057
{0, 0, 24}*}	0.0023	0.0024	0.0026	0.0027
{1, 0, $\bar{2}3$ }*}	-0.0081	-0.0107	-0.0092	-0.0106
{1, 0, $\bar{2}0$ }*}	0.0111	0.0145	0.0144	0.0139
{1, 0, $\bar{1}7$ }	-0.0180	-0.0205	-0.0192	-0.0206
{1, 0, $\bar{1}4$ }	0.0185	0.0190	0.0198	0.0210
{1, 0, $\bar{1}1$ }	-0.0715	-0.0769	-0.0725	-0.0758
{1, 0, 8}	0.0271	0.0276	0.0263	0.0263
{1, 0, $\bar{5}$ }	0.0120	0.0106	0.0096	0.0093
{1, 0, $\bar{2}$ }	-0.1964	-0.1821	-0.1717	-0.1705
{1, 0, 1}	0.1438	0.1388	0.1371	0.1281
{1, 0, 4}	0.0085	0.0097	0.0094	0.0119
{1, 0, 10}*}	0.0095	0.0099	0.0084	0.0089
{1, 0, 16}*}	0.0061	0.0059	0.0059	0.0062
{1, 1, 0}	-0.0383	-0.0371	-0.0368	-0.0345
{1, 1, 3}	0.0311	0.0293	0.0286	0.0279
{1, 1, 6}	-0.0102	-0.0103	-0.0091	-0.0090
{1, 1, 9}	0.0079	0.0075	0.0062	0.0054
{1, 1, 12}	0.0066	0.0071	0.0067	0.0075
{0, 2, $\bar{2}$ }	-0.0211	-0.0200	-0.0179	-0.0184
{0, 2, 1}	0.0216	0.0217	0.0203	0.0214
{0, 2, 4}	-0.0131	-0.0126	-0.0127	-0.0114
{0, 2, 7}	0.0130	0.0115	0.0111	0.0105
{0, 2, 10}	-0.0151	-0.0138	-0.0150	-0.0126

DOPC/Chol 70:30 (ESRF), $RH = 50 - 60\%$ 

DOPC/Chol 70:30 (ESRF), $RH = 50 - 60\%$

RH	50	52	54	56	58	60
d	46.75	46.94	47.14	47.36	47.60	47.82
$\sigma(d)$	0.32	0.32	0.29	0.28	0.32	0.33
a	69.06	70.06	70.76	71.62	72.54	74.44
$\sigma(a)$	0.45	0.42	0.76	0.82	0.57	0.41
{0,0,3}	-0.6933	-0.7197	-0.7219	-0.6968	-0.7065	-0.6924
{0,0,6}	-0.0271	-0.0295	-0.0310	-0.0314	-0.0335	-0.0343
{0,0,9}	0.0369	0.0381	0.0380	0.0365	0.0368	0.0358
{0,0,12}	-0.0461	-0.0490	-0.0504	-0.0499	-0.0520	-0.0523
{0,0,15}	0.0139	0.0147	0.0150	0.0147	0.0152	0.0151
{0,0,18}	-0.0078	-0.0083	-0.0085	-0.0084	-0.0088	-0.0089
{0,0,21}	0.0043	0.0045	0.0046	0.0045	0.0047	0.0047
{0,0,24} [*]	0.0020	0.0021	0.0022	0.0021	0.0022	0.0022
{1,0,20} [*]	0.0095	0.0090	0.0076	0.0084	0.0081	0.0074
{1,0,17}	-0.0162	-0.0162	-0.0150	-0.0162	-0.0159	-0.0168
{1,0,14}	0.0178	0.0162	0.0156	0.0171	0.0163	0.0166
{1,0,11}	-0.0622	-0.0558	-0.0554	-0.0608	-0.0555	-0.0601
{1,0,8}	0.0165	0.0153	0.0155	0.0162	0.0143	0.0152
{1,0,5}	-0.0072	-0.0072	-0.0077	-0.0082	-0.0089	-0.0088
{1,0,2}	-0.1454	-0.1320	-0.1327	-0.1315	-0.1225	-0.1232
{1,0,1}	0.0991	0.0996	0.0964	0.0893	0.0865	0.0810
{1,0,4}	0.0127	0.0136	0.0149	0.0162	0.0146	0.0159
{1,0,7}	-0.0073	-0.0064	-0.0059	-0.0065	-0.0057	-0.0062
{1,1,0}	-0.0244	-0.0231	-0.0207	-0.0173	-0.0146	-0.0116
{1,1,3}	0.0248	0.0235	0.0233	0.0232	0.0220	0.0221
{1,1,6}	-0.0065	-0.0054	-0.0055	-0.0051	-0.0043	-0.0044
{1,1,9}	0.0082	0.0075	0.0070	0.0062	0.0054	0.0044
{1,1,12}	0.0047	0.0042	0.0046	0.0048	0.0044	0.0047
{0,2,2}	-0.0156	-0.0163	-0.0147	-0.0171	-0.0154	-0.0164
{0,2,1}	0.0165	0.0147	0.0167	0.0146	0.0152	0.0158
{0,2,4}	-0.0096	-0.0093	-0.0090	-0.0095	-0.0080	-0.0078
{0,2,7}	0.0100	0.0095	0.0084	0.0079	0.0073	0.0073
{0,2,10}	-0.0190	-0.0167	-0.0165	-0.0155	-0.0143	-0.0126

A.3 Gauss-Bonnet theorem applied to stalks

For two exemplary surfaces which have been used to describe the neutral surface of fusion pores or stalks in the literature, we briefly show that the surface integral of the Gaussian curvature, $\int_A K dA$, actually yields -4π . We consider surfaces of revolution obtained by rotation of a contour $z(r)$ around the z axis:

$$\vec{R}(r, \phi) = \begin{pmatrix} r \cos \phi \\ r \sin \phi \\ z(r) \end{pmatrix}, \quad r \in [0, \infty), \phi \in [0, 2\pi). \quad (\text{A.4})$$

It can be shown that the principal curvatures c_1, c_2 are

$$c_1(r) = \frac{z''(r)}{\sqrt{1+z'^2(r)}^3} \quad \text{and} \quad c_2(r) = \frac{z'(r)}{r\sqrt{1+z'^2(r)}}. \quad (\text{A.5})$$

With the area element $dA = r\sqrt{1+z'^2(r)} dr d\phi$, the integral of the Gaussian curvature becomes

$$\int_A K dA = 2 \int_0^{2\pi} d\phi \int_{r_{\min}}^{r_{\max}} K(r) r \sqrt{1+z'^2(r)} dr \quad (\text{A.6})$$

$$= 4\pi \int_{r_{\min}}^{r_{\max}} c_1(r) c_2(r) r \sqrt{1+z'^2(r)} dr \quad (\text{A.7})$$

$$= 4\pi \int_{r_{\min}}^{r_{\max}} \frac{z''(r) z'(r)}{\sqrt{1+z'^2(r)}^3} dr. \quad (\text{A.8})$$

The factor 2 in the first line is used to take into account the lower half of the surfaces. As a first example, consider the catenoid defined by the contour

$$z(r) = \pm a \cdot \cosh^{-1}\left(\frac{r}{a}\right), \quad r \in [a, \infty]. \quad (\text{A.9})$$

Using Eq. (A.5) and $\frac{d}{dx} \cosh^{-1}(x) = (x^2 - 1)^{-1/2}$, we obtain

$$c_{1,2} = \mp \frac{a}{r^2} \quad \Rightarrow \quad H = 0, \quad K = -\frac{a^2}{r^4}. \quad (\text{A.10})$$

At each point of a catenoid, the mean curvature vanishes. The catenoid is thus a minimal surface. It can be shown that the catenoid is the only surface of revolution (except for a plane) which has this property [200]. Using these results, the surface integral over K yields ($x = \frac{r}{a}$)

$$\int_A K dA = -4\pi \underbrace{\int_1^\infty \frac{1}{x^2 \sqrt{x^2 - 1}} dx}_{=1} = -4\pi. \quad (\text{A.11})$$

As a second example, consider the semitoroidal surface obtained by rotation of a half circle of radius R centered at $r = a$ around \vec{e}_z . The first stalk models used this parameterization [21]. As can be inferred from Fig. A.2, the contour is

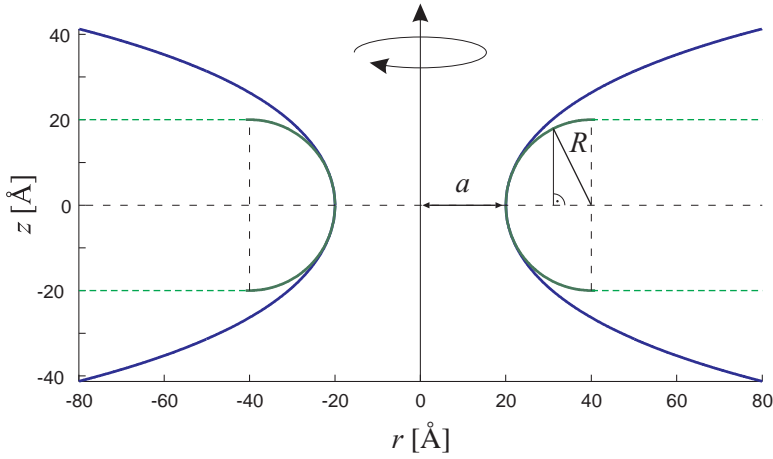


Figure A.2: Sketch of the contours of a catenoid (blue) and a semitoroidal connection (green, solid) connecting two planes (green, dashed) for the parameters $a = R = 20 \text{ \AA}$. The 2d surfaces of revolution embedded in 3d space are obtained by rotation of the contours around the z axis.

$$z(r) = \sqrt{R^2 - (R + a - r)^2}, \quad r \in [a, a + R]. \quad (\text{A.12})$$

After a somewhat lengthy calculation starting from Eq. (A.5), one obtains

$$c_1(r) = -\frac{1}{R} \quad \text{and} \quad c_2(r) = \frac{(R + a - r)}{rR}. \quad (\text{A.13})$$

As required, one curvature is given by the inverse radius of the circle describing the contour, $c_1 = R^{-1}$, whereas the other one fulfils $c_2(a) = \frac{1}{a}$ and $c_2(a + R) = 0$. The integral of the Gaussian curvature over the surface of revolution of $\pm z(r)$ yields

$$\int_A K dA = -\frac{4\pi}{R} \int_a^{a+R} \frac{R + a - r}{\sqrt{R^2 - (R + a - r)^2}} dr \quad (\text{A.14})$$

$$= -\frac{4\pi}{R} \int_0^R \frac{x}{\sqrt{R^2 - x^2}} dx \quad (x = R + a - r) \quad (\text{A.15})$$

$$= -\frac{4\pi}{R} \left[\sqrt{R^2 - x^2} \right]_0^R \quad (\text{A.16})$$

$$= -4\pi. \quad (\text{A.17})$$

A.4 MATLAB code: Examples

The data extraction and analysis tools written during this thesis comprise about 4000 lines of code and are available upon request. In the following, a limited selection of some very relevant scripts is provided.

Swelling method (lamellar phase)

swelling_lamellar.m

```

1 %%%%%%%%%%%%%%%%%%%%%%%%%%%%%%%%%%%%%%%%%%%%%%%%%%%%%%%%%%%%%%%%%%%%%%%%%
2 %           swelling_lamellar.m           %
3 %           Sebastian Aeffner, April 28, 2010           %
4 %           %           %           %           %           %           %
5 %           tool to obtain a reasonable phase setting           %
6 %           on the basis of the swelling method           %
7 %%%%%%%%%%%%%%%%%%%%%%%%%%%%%%%%%%%%%%%%%%%%%%%%%%%%%%%%%%%%%%%%%%%%%%%%%
8
9 clear;
10 close all;
11
12 % data input (all required corrections must have been completed!)
13 samplename = 'DOPC';
14 file_input = '23-Jul-2010_DOPC.mat';
15 file_output = strcat([date, '_', samplename, '_swellingdata']);
16 eval(['load ' file_input]);
17 disp(['Reading dataset ' file_input ' ... done']);
18
19 % display RH values corresponding to the available form factor sets and
20 % define which ones will be used to apply the swelling method
21 disp('Available d-spacings in the dataset:');
22 disp(' ');
23 strarray = cell(1,4);
24 strarray{1} = 'index';
25 strarray{2} = 'RH';
26 strarray{3} = 'd';
27 strarray{4} = 'std(d)';
28 disp(strarray);
29 disp([linspace(1,length(d_obs(:,1)),length(d_obs(:,1)))',RH, d_obs]);
30 firstindex = input('Enter index of first form factor set: ');
31 lastindex = input('Enter index of last form factor set: ');
32
33 % use only the data we have just defined
34 F_obs = F_obs(firstindex:1:lastindex,:);
35 d_errors = d_obs(firstindex:1:lastindex,2);
36 d_obs = d_obs(firstindex:1:lastindex,1);
37 RH = RH(firstindex:1:lastindex);
38
39 n_max = length(F_obs(1,:)); % number of recorded diffraction orders
40 n_obs = 1:1:n_max; % observed Bragg orders
41 num_RH = length(F_obs(:,1)); % number of RH values
42 d_mean = mean(d_obs); % mean d-spacing of the dataset
43 F_mean = sum(F_obs)/num_RH; % mean form factors for each order n
44
45 % generate all 2^{n_max} possible phase combinations
46 % (the phase for F(-)(0) will be determined from the other phases!)
47 nu = [1, -1]';
48 for i = 1:n_max-1;
49     nu = [ nu ones(length(nu(:,1)),1) ] ; -[nu ones(length(nu(:,1)),1) ] ;
50 end;
51 num_phases = length(nu(:,1));
52
53 % check if no phase combination occurs twice
54 for i = 1:num_phases;
55     for j = (i+1):num_phases;
56         if nu(i,:) == nu(j,:);
57             disp('Error: ');
58         end;
59     end;
60 end;
61
62 % generate all 2^{n_max} phased form factors including F(-)(0)
63 % (use formula of Nagle, F(-)(0) = 2*sum_n (-1)^{n+1}*...
64 F_mean_phased = zeros(num_phases, n_max+1);
65 for i = 1:num_phases;
66     F_mean_phased(i,1) = 2*sum( cos(pi*(1:1:n_max)))*(-1).^nu(i,:).*F_mean;
67     F_mean_phased(i,2:1:n_max+1) = nu(i,:).*F_mean;
68 end;
69
70 % due to centrosymmetry: incorporate "negative" orders of diffraction
71 n_obs = [-fliplr(n_obs) 0 n_obs];
72 F_mean_phased = [fliplr(F_mean_phased(:,2:1:(n_max+1))) F_mean_phased];

```



```

73 F_obs = [fliplr(F_obs) zeros(num_RH,1) F_obs];
74 q_z_obs = (1./d_obs)*2*pi*n_obs;
75
76
77 % data required for interpolation of continuous form factor
78
79 % generate q_z axis for form factor plot
80 delta_q_z = 50;
81 n_q = 2*(n_max+1)*delta_q_z;
82 q_z = linspace(-(n_max+1)*2*pi/d_mean,+(n_max+1)*2*pi/d_mean,n_q);
83
84 % sinc functions centered around q_z = n*2*pi/d_mean, n=-n_max...n_max
85 sinc_mean = zeros((2*n_max)+1,n_q);
86 for i = 1:length(n_obs);
87     argument = d_mean/2*q_z - n_obs(i)*pi;
88     sinc_mean(i,:) = sin(argument)./(argument);
89 end;
90
91 % generate all possible mean continuous form factors for d_mean, use en-
92 % tries in F_mean as coefficients.
93 F_mean_cont = F_mean_phased * sinc_mean;
94
95 % determine sum of squared errors
96 % vector containing sum of squared residuals for each phase setting
97
98 errors = zeros(num_phases,1);
99
100 for i = 1:num_phases; % for all possible phase combinations
101     sum_squares = 0;
102     F_obs_phased = (ones(num_RH,1)*[fliplr(nu(i,:)) 0 nu(i,:)])*F_obs;
103
104     for j = 1:num_RH; % for all RH_num humidity value
105         for k = 2:n_max+1; % for all n_max measured datapoints
106             % calculate function value of the mean, continuous form
107             % factor at the observed q_z value and subtract the
108             % observed F(q_z) value (-> NO F(-)(0))
109             argument = 0.5*d_mean*q_z_obs(j,n_max+k)-n_obs*pi;
110             delta = F_mean_phased(i,:)*(sin(argument)./(argument))' ...
111                 - F_obs_phased(j,n_max+k);
112             sum_squares = sum_squares + delta^2;
113         end;
114     end;
115     errors(i) = sum_squares;
116 end;
117
118 % sort phase combinations based on their fit quality
119 [errors_sorted, ind] = sort(errors,1);
120 nu_sorted = [];
121 for i = 1:length(nu(:,1));
122     nu_sorted = [nu_sorted; nu(ind(i,:),:)];
123 end;
124
125 % indices, phases and phased observed form factors for the two best phase
126 % combinations releted by total phase factor (-1)
127 i_opt = find(errors==min(errors));
128 nu_opt = nu(i_opt,:);
129 if nu_opt(1,1) == -1;
130     i_opt = i_opt(1);
131     nu_opt = nu_opt(i,:);
132 else i_opt = i_opt(2);
133     nu_opt = nu_opt(2,:);
134 end;
135 F_phased_opt = (ones(num_RH,1)*[fliplr(nu_opt) 1 nu_opt])*F_obs;
136
137 % Plot swelling graph for the num_plots best independent phase combinations
138 num_plots = input('How many swelling plots would you like to see? ');
139
140 for h = 1:(2*num_plots+1);
141
142     % out of 2 equivalent phase settings differing by global factor (-1),
143     % use the one which leads to EDP with bilayer interior centered around
144     % origin
145     if nu_sorted(h,1) ~= -1;
146         h = h + 1;
147     end;
148     F_obs_phased = ...
149         (ones(num_RH,1)*[fliplr(nu_sorted(h,:)) 1 nu_sorted(h,:)])*F_obs;
150
151     % create 'linear' versions of observed data required for plot
152     q_z_obs_lin = [];
153     F_obs_phased_lin = [];
154     for i = 1:num_RH;
155         q_z_obs_lin = [q_z_obs_lin q_z_obs(i,:)];
156         F_obs_phased_lin = [F_obs_phased_lin F_obs_phased(i,:)];
157     end;
158
159     % plot swelling graph
160     F_continuous = F_mean_cont(ind(h,:),:);
161     figure;

```



```

21 dataset = 'DOPC-SLS_formfactor_data_comparison';
22
23 eval(['load ' dataset]);
24
25 d_all = round(100*d)/100;
26 a_all = round(100*a)/100;
27
28 disp(' ');
29 disp(['Used data set: ' dataset '.mat']);
30 disp(' ');
31 disp(['d-spacings in dataset ' sample ':']);
32 disp(' ');
33 disp('# RH d a');
34 disp(' ');
35 for i = 1:length(RH);
36 disp([num2str(i) ' ' num2str(RH(i)) ' ' ...
37 num2str(d_all(i,1), '%10.2f') '+-' num2str(d_all(i,2), '%10.2f') ' ' ...
38 num2str(a_all(i,1), '%10.2f') '+-' num2str(a_all(i,2), '%10.2f') '']);
39 end;
40 disp(' ');
41
42 spacings = input(['Enter number of d-spacing for further analysis: ']);
43 cont = 1;
44 while cont ~= 0;
45 disp('d-spacings of datasets to be analyzed:');
46 disp(d_all(spacings,1));
47 cont = input('Add another spacing? Enter number (#) if yes,(0) if no: ');
48 if cont ~= 0;
49 spacings = [spacings cont];
50 end;
51 end;
52
53 % length of area element in xy plane
54 disp(' ');
55 delta = input('Enter length of area element dx*dy: ');
56
57 % parameters for electron density isosurface search
58 z_min_coarse = -20;
59 z_0_coarse = -10;
60 z_min_fine = -8;
61 z_0_fine = -1;
62
63 disp('Initial values for isosurface search:');
64 disp(['z_0_coarse = ' num2str(z_0_coarse)]);
65 disp(['z_0_fine = ' num2str(z_0_fine) ']);
66 dummy = input('Press return to continue ...');
67 disp(' ');
68
69 % minimum and maximum electron density considered
70 min_rho_iso = input('Enter minimum e- density for isosurfaces: ');
71 max_rho_iso = input('Enter maximum e- density for isosurfaces: ');
72 del_rho_iso = input('Enter e- density stepsize for isosurfaces: ');
73
74 rho_iso = min_rho_iso:del_rho_iso:max_rho_iso;
75
76 disp(['The following isosurfaces will be considered:']);
77 disp(num2str(rho_iso));
78 dummy = input('Is this correct? Press return to continue. ');
79 choice_isosurf = input(['Also show isosurface plots by MATLAB '...
80 'commands for comparison? Enter (Y)es/(N)o: '],'s');
81
82
83 %%%%%%%%%%%%%%%%%%%%%%%%%%%%%%%%%%%%%%%%%%%%%%%%%%%%%%%%%%%%%%%%%%%%%%%%%%%%%%%
84 % Numerical analysis of stalk electron densities for specified d-spacings %
85 %%%%%%%%%%%%%%%%%%%%%%%%%%%%%%%%%%%%%%%%%%%%%%%%%%%%%%%%%%%%%%%%%%%%%%%%%%%%%%%
86
87 disp(' ');
88 disp('=====');
89 disp(['Starting analysis of ' sample ' dataset.']);
90 disp(['Used d-spacings: [ ' num2str(d_all(spacings,1)) ' ' ]']);
91 disp('=====');
92 disp(' ');
93
94 for s = 1:length(spacings);
95
96 disp('=====');
97 disp(['sample ' , d = ' num2str(d_all(spacings(s),1))]');
98 disp('=====');
99
100 % Miller indices and form factors from reconstruction.m
101 h = table_hkl{spacings(s)}(:,1);
102 k = table_hkl{spacings(s)}(:,2);
103 l = table_hkl{spacings(s)}(:,3);
104 F = table_hkl{spacings(s)}(:,4);
105 num_terms = length(F);
106
107 % lattice parameters
108 a = a_all(spacings(s),1);
109 d = d_all(spacings(s),1);

```



```

377
378
379 % set entries in Z (coarse coordinates) to zero if they are in
380 % stalk-neck region -> avoid double integration
381 Z(ind_coarse) = 0;
382
383 % coarse sampling
384 mask_int = mask; % mask for integration (entries 1,0)
385 mask_int(find(Z==0)) = 0; % set values within stalk neck to 0
386 mask_plot = mask_int./mask_int;% mask for plots (entries 1,0,NaN)
387 %mask_plot_curv = mask_plot./mask_plot;
388
389 mask_norm = zeros(size(X)); % mask for surface normals
390 for m = 1:length(X(:,1));
391     for n = 1:length(X(1,:));
392         if mod(X(m,n),5) == 0 && mod(Y(m,n),5) == 0;
393             mask_norm(m,n) = 1;% show surf. normals on 5x5 AA grid
394         end;
395     end;
396 mask_norm = mask_norm .* mask_int;
397
398 % fine sampling
399 mask_int_fine = zeros(size(Z_fine));
400 mask_int_fine(ind_fine) = 1;
401 mask_int_fine(find(Z_fine == 0)) = 0;
402 mask_plot_fine = mask_int_fine./mask_int_fine;
403
404 mask_norm_fine = zeros(size(X_fine)); % mask for surface normals
405 for m = 1:length(X_fine(:,1));
406     for n = 1:length(X_fine(1,:));
407         if mod(X_fine(m,n),5) == 0 && mod(Y_fine(m,n),5) == 0;
408             mask_norm_fine(m,n) = 1; % normals on 5x5 AA grid
409         end;
410     end;
411 end;
412 mask_norm_fine = mask_norm_fine .* mask_int_fine;
413
414 % curvature analysis of isosurface in coarse sampling
415 [k1,k2,H,K,dA,n_x,n_y,n_z] = ...
416 curvanalysis(X,Y,Z,delta,h,k1,F,a,d,mask_int,mask_norm);
417 S_1_coarse(r) = 4*sum(sum( (H.^2) .*dA ));
418 S_2_coarse(r) = -4*sum(sum( H .*dA ));
419 area_coarse(r) = 2*sum(sum( dA ));
420 int_K_coarse(r) = 2*sum(sum( K .*dA ));
421
422 % plot and save isosurface figures
423 % (to save time, only for SOME datasets)
424 if mod(rho_C,0.1) == 0 || rho_C == 0.1;
425
426 % plot isosurface (coarse sampling)
427 disp('Plotting isosurface... ');
428 figure(1);
429 hold on;
430 surf(+X,+Y,+mask_plot.*Z,H);
431 surf(-X,-Y,-mask_plot.*Z,flipr(H));
432 quiver3(X,Y,Z,n_x,n_y,n_z,2/delta,'k'); % add surface normals
433 quiver3(-X,-Y,-Z,-n_x,-n_y,-n_z,2/delta,'k');
434 shading interp; % for 'flat' or 'faceted', H values will not be
435 % displayed correctly (see also help on 'surf')
436 xlabel('$x$ [AA]','interpreter','latex','fontsize',12);
437 ylabel('$y$ [AA]','interpreter','latex','fontsize',12);
438 zlabel('$z$ [AA]','interpreter','latex','fontsize',12);
439 headline{1} = [sample ', d=' num2str(d,'%02f') 'Å'];
440 headline{2} = ['\Delta\rho=' num2str(rho_C)];
441 title(headline,'fontsize',14);
442 colorbar;
443
444 % add lines indicating volume corresponding to cis monolayer
445 x_hex = 0.5*a*[1 1 0 -1 -1 0 1];
446 y_hex = 1/(2*sqrt(3))*a*[1 -1 -2 -1 1 2 1];
447 z_hex = 0.5*d*ones(1,7);
448 line(x_hex,y_hex,-z_hex,'color','black'); % lower hexagon
449 line(x_hex,y_hex,+z_hex,'color','black'); % upper hexagon
450 for i = 1:6;
451     line([x_hex(i) x_hex(i)], [y_hex(i) y_hex(i)],...
452         [-0.5*d 0.5*d],'color','black');
453 end;
454 axis equal tight;
455 view(3);
456
457 % plot c1,c2,H,K projected onto xy-plane (coarse sampling)
458
459 % use the same colormap for k1,k2 and H = 0.5*(k1+k2):
460 % -> Determine minimum and maximum curvature values in k1 & k2
461 % and set a pair of pixels in k1,k2,H to these values
462
463 extr = [min(min(mask_plot.*k1)) max(max(mask_plot.*k1)) ...
464         min(min(mask_plot.*k2)) max(max(mask_plot.*k2))];
465 curv_min_coarse = min(extr);

```

```

466     curv_max_coarse = max(extr);
467
468     figure(2);
469     plotdata = [{k1} {k2} {H} {K}];
470     titles = [{'$c_1$'} {'$c_2$'} {'$H$'} {'$K$'}];
471     for i = 1:4;
472         subplot(2,2,i);
473         hold on;
474         pcolor(x,y,real(mask_plot.*plotdata{i}));
475         %(if imagesc is used, NaN entries are also shown in color)
476         daspect([1 1 1]);
477         axis tight;
478         shading flat;
479         xlabel('$x$ \[AA]', 'interpreter', 'latex', 'fontsize', 12);
480         ylabel('$y$ \[AA]', 'interpreter', 'latex', 'fontsize', 12);
481         set(gca, 'xtick', [-20 0 20]);
482         set(gca, 'ytick', [-20 0 20]);
483         title(titles(i), 'interpreter', 'latex', 'fontsize', 16);
484         colorbar;
485     end;
486
487 end;
488
489 % curvature analysis of isosurface in fine sampling
490 [k1_fine, k2_fine, H_fine, K_fine, dA_fine, n_x, n_y, n_z] = ...
491     curvanalysis(X_fine, Y_fine, Z_fine, delta_fine, h, k, l, F, a, d, ...
492         mask_int_fine, mask_norm_fine);
493 S_1_fine(r) = 4*sum(sum( (H_fine.^2).*dA_fine ));
494 S_2_fine(r) = -4*sum(sum( H_fine.*dA_fine ));
495 area_fine(r) = 2*sum(sum( dA_fine ));
496 int_K_fine(r) = 2*sum(sum( K_fine.*dA_fine ));
497
498
499 if mod(rho_C, 0.1) == 0 || rho_C == 0.1;
500
501     % add isosurface (fine sampling) to isosurface (coarse sampling)
502     figure(1);
503     surf(+X_fine, +Y_fine, +mask_plot_fine.*Z_fine, H_fine);
504     surf(-X_fine, -Y_fine, -mask_plot_fine.*Z_fine, fliplr(H_fine));
505     quiver3(+X_fine, +Y_fine, +Z_fine, n_x, n_y, n_z, 2/delta_fine, 'k');
506     quiver3(-X_fine, -Y_fine, -Z_fine, -n_x, -n_y, -n_z, 2/delta_fine, 'k');
507     shading interp;
508
509     % add c1, c2, H, K projected onto xy-plane (fine sampling)
510
511     % use the same colormap for k1, k2 and H = 0.5(k1+k2):
512     % -> Determine minimum and maximum curvature values in k1 and k2
513     % and set a pair of pixels in k1, k2, H to these values
514
515     extr = [min(min(mask_plot_fine.*k1_fine)) ...
516         max(max(mask_plot_fine.*k1_fine)) ...
517         min(min(mask_plot_fine.*k2_fine)) ...
518         max(max(mask_plot_fine.*k2_fine))];
519     curv_min_fine = min(extr);
520     curv_max_fine = max(extr);
521     curv_min = min([curv_min_coarse curv_min_fine]);
522     curv_max = max([curv_max_coarse curv_max_fine]);
523
524     k1_fine(find(k1_fine==min(min(mask_plot_fine.*k1_fine)))) = curv_min;
525     k1_fine(find(k1_fine==max(max(mask_plot_fine.*k1_fine)))) = curv_max;
526     k2_fine(find(k2_fine==min(min(mask_plot_fine.*k2_fine)))) = curv_min;
527     k2_fine(find(k2_fine==max(max(mask_plot_fine.*k2_fine)))) = curv_max;
528     H_fine(find(H_fine==min(min(mask_plot_fine.*H_fine)))) = curv_min;
529     H_fine(find(H_fine==max(max(mask_plot_fine.*H_fine)))) = curv_max;
530
531     figure(2);
532     plotdata = [{k1_fine} {k2_fine} {H_fine} {K_fine}];
533     titles = [{'$c_1$'} {'$c_2$'} {'$H$'} {'$K$'}];
534
535     for i = 1:4;
536         subplot(2,2,i);
537         hold on;
538         pcolor(x_fine, y_fine, real(mask_plot_fine.*plotdata{i}));
539         %(if imagesc is used here, NaN entries are also shown in color)
540         daspect([1 1 1]);
541         axis tight;
542         shading flat;
543         xlabel('$x$ \[AA]', 'interpreter', 'latex', 'fontsize', 12);
544         ylabel('$y$ \[AA]', 'interpreter', 'latex', 'fontsize', 12);
545         set(gca, 'xtick', [-20 0 20]);
546         set(gca, 'ytick', [-20 0 20]);
547         title(titles(i), 'interpreter', 'latex', 'fontsize', 16);
548         colorbar;
549     end;
550     disp('Plotting curvatures ... ');
551
552     rho_string = [num2str(0) 'p' num2str(round(100*abs(rho_C)), '%02d')];
553     if sign(rho_C) == -1;
554         rho_string = ['- ' rho_string];

```


curvanalysis.m

```

1 function [k1,k2,H,K,dA,n_x,n_y,n_z] ...
2     = curvanalysis(X,Y,Z,delta,h,k,l,F,a,d,mask_int,mask_norm)
3
4 %%%%%%%%%%%%%%%%%%%%%%%%%%%%%%%%%%%%%%%%%%%%%%%%%%%%%%%%%%%%%%%%%%%%%%%%%
5 %           determine first and second partial derivatives           %
6 %%%%%%%%%%%%%%%%%%%%%%%%%%%%%%%%%%%%%%%%%%%%%%%%%%%%%%%%%%%%%%%%%%%%%%%%%
7
8 % first partial derivatives of surface rho = rho_C
9 f_x = zeros(size(X));
10 f_y = zeros(size(X));
11 f_z = zeros(size(X));
12
13 % second partial derivatives of surface rho = rho_C
14 f_xx = zeros(size(X));
15 f_xy = zeros(size(X));
16 f_xz = zeros(size(X));
17 f_yy = zeros(size(X));
18 f_yz = zeros(size(X));
19 f_zz = zeros(size(X));
20
21 for i = 1:length(F);
22
23     arg = 2*pi*( (h(i)/a)*X + (2*k(i)+h(i))/(sqrt(3)*a)*Y + ...
24               1(i)/(3*d)*(Z+1.5*d) );
25
26     C_1 = -2*pi *F(i)*sin(arg);
27     C_2 = -4*pi^2*F(i)*cos(arg);
28
29     % first partial derivatives
30     f_x = f_x + ( C_1 * (h(i)/a) );
31     f_y = f_y + ( C_1 * (2*k(i)+h(i))/(sqrt(3)*a) );
32     f_z = f_z + ( C_1 * 1(i)/(3*d) );
33
34     % second partial derivatives
35     f_xx = f_xx + ( C_2 * (h(i)/a)^2 );
36     f_xy = f_xy + ( C_2 * (h(i)*(2*k(i)+h(i)))/(sqrt(3)*a^2) );
37     f_xz = f_xz + ( C_2 * (h(i)*1(i)/(3*a*d)) );
38     f_yy = f_yy + ( C_2 * ((2*k(i)+h(i))/(sqrt(3)*a))^2 );
39     f_yz = f_yz + ( C_2 * (2*k(i)+h(i))*1(i)/(3*sqrt(3)*a*d) );
40     f_zz = f_zz + ( C_2 * (1(i)/(3*d))^2 );
41
42 end;
43
44 %%%%%%%%%%%%%%%%%%%%%%%%%%%%%%%%%%%%%%%%%%%%%%%%%%%%%%%%%%%%%%%%%%%%%%%%%
45 %           surface normals                                           %
46 %%%%%%%%%%%%%%%%%%%%%%%%%%%%%%%%%%%%%%%%%%%%%%%%%%%%%%%%%%%%%%%%%%%%%%%%%
47
48 % components of surface normals (pointing towards HG/H2O region)
49 n_x = mask_norm .* ( f_x ./ sqrt(f_x.^2 + f_y.^2 + f_z.^2) );
50 n_y = mask_norm .* ( f_y ./ sqrt(f_x.^2 + f_y.^2 + f_z.^2) );
51 n_z = mask_norm .* ( f_z ./ sqrt(f_x.^2 + f_y.^2 + f_z.^2) );
52
53
54 %%%%%%%%%%%%%%%%%%%%%%%%%%%%%%%%%%%%%%%%%%%%%%%%%%%%%%%%%%%%%%%%%%%%%%%%%
55 %           area elements                                             %
56 %%%%%%%%%%%%%%%%%%%%%%%%%%%%%%%%%%%%%%%%%%%%%%%%%%%%%%%%%%%%%%%%%%%%%%%%%
57
58 dA = mask_int .* abs( sqrt(f_x.^2 + f_y.^2 + f_z.^2) ./ f_z ) * delta^2;
59
60 %%%%%%%%%%%%%%%%%%%%%%%%%%%%%%%%%%%%%%%%%%%%%%%%%%%%%%%%%%%%%%%%%%%%%%%%%
61 %           mean, Gaussian and principle curvature                   %
62 %%%%%%%%%%%%%%%%%%%%%%%%%%%%%%%%%%%%%%%%%%%%%%%%%%%%%%%%%%%%%%%%%%%%%%%%%
63
64 H = zeros(size(X)); % array for mean curvature H
65 K = zeros(size(X)); % array for Gaussian curvature K
66
67 % Loops are not nice, I know, but it works
68 for m = 1:length(X(:,1));
69     for n = 1:length(X(1,:));
70
71         % gradient
72         grad = [ f_x(m,n) f_y(m,n) f_z(m,n) ]';
73
74         % Hessian
75         Hess = [ f_xx(m,n) f_xy(m,n) f_xz(m,n);
76                f_xy(m,n) f_yy(m,n) f_yz(m,n);
77                f_xz(m,n) f_yz(m,n) f_zz(m,n) ];
78
79         % mean curvature
80         H(m,n) = -(grad'*(Hess*grad) - norm(grad).^2*trace(Hess))./...
81                 (2*(norm(grad)).^3);
82
83         % adjoint of Hessian
84         Hess_ad = [...
85                 +det(Hess([2 3],[2 3])) -det(Hess([2 3],[1 3])) +det(Hess([2 3],[1 2]));...
86
87

```

```

88     -det(Hess([1 3],[2 3])) +det(Hess([1 3],[1 3])) -det(Hess([1 3],[1 2]));...
89     +det(Hess([1 2],[2 3])) -det(Hess([1 2],[1 3])) +det(Hess([1 2],[1 2]));
90
91     % %another possibility:
92     Hess_ad(1,1) = f_yy(m,n)*f_zz(m,n) - (f_yz(m,n))^2;
93     Hess_ad(1,2) = f_yz(m,n)*f_xz(m,n) - (f_xy(m,n)*f_zz(m,n));
94     Hess_ad(1,3) = f_xy(m,n)*f_yz(m,n) - (f_yy(m,n)*f_xz(m,n));
95     Hess_ad(2,1) = Hess_ad(1,2);
96     Hess_ad(2,2) = f_xx(m,n)*f_zz(m,n) - (f_xz(m,n))^2;
97     Hess_ad(2,3) = f_xy(m,n)*f_xz(m,n) - (f_xx(m,n)*f_yz(m,n));
98     Hess_ad(3,1) = Hess_ad(1,3);
99     Hess_ad(3,2) = Hess_ad(2,3);
100    % Hess_ad(3,3) = f_xx(m,n)*f_yy(m,n) - (f_xy(m,n))^2;
101
102    % Gaussian curvature
103    K(m,n) = (grad*(Hess_ad*grad))./((norm(grad)).^4);
104
105    end;
106 end;
107
108 k1 = real(H + sqrt(H.^2 - K));
109 k2 = real(H - sqrt(H.^2 - K));
110
111 %%%%%%%%%%%%%%%%%%%%%%%%%%%%%%%%%%%%%%%%%%%%%%%%%%%%%%%%%%%%%%%%%%%%%%%%%%%%%%%
112 % set entries outside stalk area to zero, get rid of "NaN" entries %
113 %%%%%%%%%%%%%%%%%%%%%%%%%%%%%%%%%%%%%%%%%%%%%%%%%%%%%%%%%%%%%%%%%%%%%%%%%%%%%%%
114
115 dA = mask_int .* dA;
116 H = mask_int .* H;
117 K = mask_int .* K;
118 k1 = mask_int .* k1;
119 k2 = mask_int .* k2;
120
121 dA(find(isnan(dA) == 1)) = 0;
122 H(find(isnan(H) == 1)) = 0;
123 K(find(isnan(K) == 1)) = 0;
124 k1(find(isnan(k1) == 1)) = 0;
125 k2(find(isnan(k2) == 1)) = 0;
126
127 end

```


References

- [1] G. L. Zubay: *Biochemistry*. 4th edition, McGraw-Hill (1998).
- [2] C. Tanford: The hydrophobic effect and the organization of living matter. *Science* **200** 1012-1018 (1978).
- [3] P. L. Yeagle: *The Structure of Biological Membranes*. CRC Press LLC (2004).
- [4] S. J. Singer and G. L. Nicolson: The Fluid Mosaic Model of the Structure of Cell Membranes. *Science* **175** 720-731 (1972).
- [5] D. M. Engelman: Membranes are more mosaic than fluid. *Nature* **438** 578-580 (2005).
- [6] D. Lingwood and K. Simons: Lipid Rafts as a Membrane-Organizing Principle. *Science* **327** 46-50 (2010).
- [7] R. Jahn and H. Grubmüller: Membrane fusion. *Curr. Opin. Cell Biol.* **14** 488-495 (2002).
- [8] R. Jahn, T. Lang and T. C. Südhof: Membrane Fusion. *Cell* **112** 519-533 (2003).
- [9] R. Blumenthal, M. J. Clague, S. R. Durell and R. M. Epand: Membrane Fusion. *Chem. Rev.* **103** 53-70 (2003).
- [10] L. K. Tamm, J. Crane and V. Kiessling: Membrane fusion: a structural perspective on the interplay of lipids and proteins. *Curr. Opin. Struct. Biol.* **13** 453-466 (2003).
- [11] M. B. Jackson and E. R. Chapman: The fusion pores of Ca^{2+} -triggered exocytosis. *Nature Struct. Mol. Biol.* **15** 684-689 (2008).
- [12] S. C. Harrison: Viral membrane fusion. *Nature Struct. Mol. Biol.* **15** 690-698 (2008).
- [13] R. Jahn: Some classic papers in the field of membrane fusion - a personal view. *Nature Struct. Mol. Biol.* **15** 655-657 (2008).
- [14] http://commons.wikimedia.org/wiki/File:Cell_membrane_detailed_diagram_en.svg, downloaded on May 17, 2011.
- [15] Y. A. Chen and R. H. Scheller: *Nature Rev. Mol. Cell Biol.* **2** 98-106 (2001).
- [16] L. V. Chernomordik and M. M. Kozlov: Protein-Lipid Interplay in Fusion and Fission Of Biological Membranes. *Annu. Rev. Biochem.* **72** 175-207 (2003).
- [17] L. V. Chernomordik and M. M. Kozlov: Membrane Hemifusion: Crossing a Chasm in Two Leaps. *Cell* **123** 375-382 (2005).
- [18] B. R. Lentz: PEG as a tool to gain insight into membrane fusion. *Eur. Biophys. J.* **36** 315-326 (2007).
- [19] S. Martens and H. T. McMahon: Mechanisms of membrane fusion: disparate players and common principles. *Nature Rev. Mol. Cell. Biol.* **9** 543-556 (2008).

- [20] L. V. Chernomordik and M. M. Kozlov: Mechanics of membrane fusion. *Nature Struct. Mol. Biol.* **15** 675-683 (2008).
- [21] M. M. Kozlov and V. S. Markin: Possible mechanism of membrane fusion (in Russian). *Biofizika* **28** 242-247 (1983).
- [22] D. P. Siegel: Energetics of intermediates in membrane fusion: comparison of stalk and inverted micellar intermediate mechanisms. *Biophys. J.* **65** 2124-2140 (1993).
- [23] D. P. Siegel: The Modified Stalk Mechanism of Lamellar/Inverted Phase Transitions and Its Implications for Membrane Fusion. *Biophys. J.* **76** 291-313 (1999).
- [24] V. S. Markin and J. P. Albanesi: Membrane Fusion: Stalk Model Revisited. *Biophys. J.* **82** 693-712 (2002).
- [25] Y. Kozlovsky and M. M. Kozlov: Stalk Model of Membrane Fusion: Solution of Energy Crisis. *Biophys. J.* **82** 882-895 (2002).
- [26] S. J. Marrink, A. H. de Vries and D. P. Tieleman: Lipids on the move: Simulations of membrane pores, domains, stalks and curves. *Biochim. Biophys. Acta* **1788** 149-168 (2009).
- [27] M. Schick: Membrane Fusion: The Emergence of a New Paradigm. *J. Stat. Phys.* **142** 1317-1323 (2011).
- [28] J. M. Seddon and R. H. Templer: Polymorphism of Lipid-Water Systems. in: *Handbook of Biological Physics*, Elsevier (1995)
- [29] R. M. Epan: Lipid polymorphism and protein-lipid interactions. *Biochim. Biophys. Acta* **1376** 353-368 (1998).
- [30] L. Yang and H. W. Huang: Observation of a Membrane Fusion Intermediate Structure. *Science* **297** 1877-1879 (2002).
- [31] S. Aeffner, T. Reusch, B. Weinhausen and T. Salditt: Membrane fusion intermediates and the effect of cholesterol: An in-house x-ray scattering study. *Eur. Phys. J. E* **30** 205-214 (2009).
- [32] R. Philipps, J. Kondev and J. Theriot: *Physical Biology of the Cell*. Garland Science (2009).
- [33] G. van Meer: Cellular lipidomics. *EMBO J.* **24** 3159-3165 (2005).
- [34] E. Sackmann and R. Merkel: *Lehrbuch der Biophysik*. Wiley-VCH (2010).
- [35] S. K. Ghosh, S. Aeffner, T. Salditt: Effect of PIP₂ on DOPC bilayer structure and phase behaviour studied by x-ray scattering. *Chem. Phys. Chem.* **12** 2633-2640 (2011).
- [36] W. F. D. Bennett, J. L. MacCallum, M. J. Hinner, S. J. Marrink and D. P. Tieleman: Molecular View of Cholesterol Flip-Flop and Chemical Potential in Different Membrane Environments. *J. Am. Chem. Soc.* **131** 12714-12720 (2009).
- [37] O. G. Mouritsen and M. J. Zuckermann: What's So Special About Cholesterol? *Lipids* **39** 1101-1113 (2004).
- [38] J. R. Silvius: Role of cholesterol in lipid raft formation: Lessons from lipid model systems. *Biochim. Biophys. Acta* **1610** 174-183 (2003).

- [39] Z. Chen and R. P. Rand: The Influence of Cholesterol on Phospholipid Membrane Curvature and Bending Elasticity. *Biophys. J.* **73** 267-276 (1997).
- [40] R. S. Gracia, N. Bezlyepkina, R. L. Knorr, R. Lipowsky and R. Dimova: Effect of cholesterol on the rigidity of saturated and unsaturated membranes: fluctuation and electrodeformation analysis of giant vesicles. *Soft Matter* **6** 1472-1482 (2010).
- [41] J. Pan, T. T. Mills, S. Tristram-Nagle and J. F. Nagle: Cholesterol Perturbs Lipid Bilayers Nonuniversally. *Phys. Rev. Lett.* **100** 198103 (2008).
- [42] T. Heimburg: *Thermal Biophysics of Membranes*. Wiley-VCH (2007).
- [43] V. Luzzati, T. Gulik-Krzywicki and A. Tardieu: Polymorphism of Lecithins. *Nature* **218** 1031-1034 (1968).
- [44] P. E. Harper, S. M. Gruner, R. N. A. H. Lewis and R. N. McElhaney: Electron density modeling and reconstruction of infinite periodic minimal surfaces (IPMS) based phases in lipid-water systems. II. Reconstruction of D surface based phases. *Eur. Phys. J. E* **2** 229-245 (2000).
- [45] J. N. Israelachvili: *Intermolecular & Surface Forces*. 2nd edition, Academic Press (1992).
- [46] T. Salditt: Lipid-peptide interaction in oriented bilayers probed by interface-sensitive scattering methods. *Curr. Opin. Struct. Biol.* **13** 467-478 (2003).
- [47] J. F. Nagle and S. Tristram-Nagle: Structure of lipid bilayers. *Biochim. Biophys. Acta* **1469** 159-195 (2000).
- [48] S. Tristram-Nagle and J. F. Nagle: Lipid bilayers: thermodynamics, structure, fluctuations, and interactions. *Chem. Phys. Lipids* **127** 3-14 (2004).
- [49] M. Rappolt: The Biologically Relevant Lipid Mesophases as "Seen" by X-rays. *Advances in Planar Lipid Bilayers and Liposomes* **5** 253-283 (2006).
- [50] Md. E. Haque, T. J. McIntosh and B. R. Lentz: Influence of Lipid Composition on Physical Properties and PEG-Mediated Fusion of Curved and Uncurved Model Membrane Vesicles: "Nature's Own" Fusogenic Lipid Bilayer. *Biochemistry* **40** 4340-4348 (2001).
- [51] L. Yang and H. W. Huang: A Rhombohedral Phase of Lipid Containing a Membrane Fusion Intermediate Structure. *Biophys. J.* **84** 1808-1817 (2003).
- [52] M. Rappolt, H. Amenitsch, J. Strancar, C. V. Teixeira, M. Kriechbaum, G. Pabst, M. Majerowicz, and P. Laggnner: Phospholipid mesophases at solid interfaces: in-situ X-ray diffraction and spin-label studies. *Adv. Coll. Int. Sci.* **111** 63-77 (2004).
- [53] Y. G. Smirnova, S.-J. Marrink, R. Lipowsky and V. Knecht: Solvent-Exposed Tails as Prestalk Transition States for Membrane Fusion at Low Hydration. *J. Am. Chem. Soc.* **132** 6710-6718 (2010).
- [54] S.-J. Marrink and A. E. Mark: Molecular View of Hexagonal Phase Formation in Phospholipid Membranes. *Biophys. J.* **87** 3894-3900 (2004).
- [55] Y. Kozlovsky, A. E. Efrat, D. P. Siegel and M. M. Kozlov: Stalk Phase Formation: Effects of Dehydration and Saddle Splay Modulus. *Biophys. J.* **87** 2508-2521 (2004).

- [56] H. Noguchi and M. Takasu: Fusion pathways of vesicles: A Brownian dynamics simulation. *J. Chem. Phys.* **115** 9547 (2001).
- [57] M. Müller, K. Katsov and M. Schick: New mechanism of membrane fusion. *J. Chem. Phys.* **116** 2342-2345 (2002).
- [58] M. Müller, K. Katsov and M. Schick: A New Mechanism of Model Membrane Fusion Determined from Monte Carlo Simulation. *Biophys. J.* **85** 1611-1623 (2003).
- [59] Y. Norizoe, K. Ch. Daoulas and M. Müller: Measuring excess free energies of self-assembled membrane structures. *Faraday Discuss.* **144** 369-391 (2010).
- [60] H. J. Risselada, C. Kutzner and H. Grubmüller: Caught in the Act: Visualization of SNARE-Mediated Fusion Events in Molecular Detail. *Chem. Bio. Chem.* **12** 1049-1055 (2011).
- [61] A. N. Gentilcore, N. Michaud-Agrawal, P. S. Crozier, M. J. Stevens and T. B. Woolf: Examining the Origins of the Hydration Force Between Lipid Bilayers Using All-Atom Simulations. *J. Membr. Biol.* **235** 1-15 (2010).
- [62] V. A. Parsegian and B. W. Ninham: Application of the Lifshitz Theory to the Calculation of Van der Waals Forces across Thin Lipid Films. *Nature* **224** 1197-1198 (1969).
- [63] V. A. Parsegian: *Van der Waals forces. A Handbook for Biologists, Chemists, Engineers and Physicists.* Cambridge University Press (2006).
- [64] R. Lipowsky and S. Leibler: Unbinding Transitions of Interacting Membranes. *Phys. Rev. Lett.* **56** 2541-2544 (1986).
- [65] M. Manciu and E. Ruckenstein: Free Energy and Thermal Fluctuations of Neutral Lipid Bilayers. *Langmuir* **17** 2455-2463 (2001).
- [66] U. Mennicke, D. Constantin and T. Salditt: Structure and interaction potentials in solid-supported lipid membranes studied by X-ray reflectivity at varied osmotic pressure. *Eur. Phys. J. E* **20** 221-230 (2006).
- [67] W. Fenzl: Van der Waals interaction of membranes. *Z. Phys. B* **97** 333-336 (1995).
- [68] J. J. Pan, S. Tristram-Nagle, N. Kucerka and J. F. Nagle: Temperature Dependence of Structure, Bending Rigidity, and Bilayer Interactions of Dioleoylphosphatidylcholine Bilayers. *Biophys. J.* **94** 117-124 (2008).
- [69] H. Wennerström and E. Sparr: Thermodynamics of membrane lipid hydration. *Pure Appl. Chem.* **75** 905-912 (2003).
- [70] J. N. Israelachvili and H. Wennerström: Role of hydration and water structure in biological and colloidal interactions. *Nature* **379** 219-225 (1996).
- [71] S. Marcelja and N. Radic: Repulsion of interfaces due to boundary water. *Chem. Phys. Lett.* **42** 129-130 (1976).
- [72] J. N. Israelachvili and H. Wennerström: Entropic forces between amphiphilic surfaces in liquids. *J. Phys. Chem.* **96** 520-531 (1992).

- [73] G. Cevc and D. Marsh: Hydration of noncharged lipid bilayer membranes. Theory and experiments with phosphatidylethanolamines. *Biophys. J.* **47** 21-31 (1985).
- [74] R. P. Rand and V. A. Parsegian: Hydration forces between phospholipid bilayers. *Biochim. Biophys. Acta* **988** 351-376 (1989).
- [75] T. J. McIntosh and S. A. Simon: Hydration and steric pressures between phospholipid bilayers. *Annu. Rev. Biophys. Biomol. Struct.* **23** 27-51 (1994).
- [76] J. N. Israelachvili and H. Wennerström: Hydration or steric forces between amphiphilic surfaces? *Langmuir* **6** 873-876 (1990).
- [77] V. A. Parsegian and R. P. Rand: Comment on "Molecular Protrusion as the Source of Hydration Forces". *Langmuir* **7** 1299-1301 (1991).
- [78] G. A. Zampighi, L. M. Zampighi, N. Fain, S. Lanzavecchia, S. A. Simon and E. M. Wright: Conical Electron Tomography of a Chemical Synapse: Vesicles Docked to the Active Zone are Hemi-Fused. *Biophys. J.* **91** 2910-2918 (2006).
- [79] W. Helfrich: Elastic properties of lipid bilayers: theory and possible experiments. *Z. Naturforsch.* **28** 693-703 (1973).
- [80] P. B. Canham: The minimum energy of bending as a possible explanation of the biconcave shape of the human red blood cell. *J. Theor. Biol.* **26** 61-81 (1970).
- [81] E. A. Evans: Bending Resistance and Chemically Induced Moments in Membrane Bilayers. *Biophys. J.* **14** 923-931 (1974).
- [82] P. I. Kuzmin, J. Zimmerberg, Y. A. Chizmadzhev and F. S. Cohen. A quantitative model for membrane fusion based on low-energy intermediates. *Proc. Natl. Acad. Sci. USA* **98** 7235-7240 (2001).
- [83] M. Hamm and M. M. Kozlov: Elastic energy of tilt and bending of fluid membranes. *Eur. Phys. J. E* **3** 323-335 (2000).
- [84] D. Marsh: Lateral Pressure Profile, Spontaneous Curvature Frustration, and the Incorporation and Conformation of Proteins in Membranes. *Biophys. J.* **93** 3884-3899 (2007).
- [85] D. P. Siegel: Fourth-order curvature energy model for the stability of bicontinuous inverted cubic phases in amphiphile-water systems. *Langmuir* **26** 8673-8683 (2010).
- [86] D. Marsh: Elastic curvature constants of lipid monolayers and bilayers. *Chem. Phys. Lipids* **144** 146-159 (2006).
- [87] T. J. McIntosh, A. D. Magid and S. A. Simon: Cholesterol modifies the short-range repulsive interactions between phosphatidylcholine membranes. *Biochemistry* **28** 17-25 (1989).
- [88] D. P. Siegel: The Gaussian Curvature Elastic Energy of Intermediates in Membrane Fusion. *Biophys. J.* **95** 5200-5215 (2008).
- [89] D. P. Siegel and M. M. Kozlov: The Gaussian Curvature Elastic Modulus of N-Monomethylated Dioleoylphosphatidylethanolamine: Relevance to Membrane Fusion and Lipid Phase Behavior. *Biophys. J.* **87** 366-374 (2004).

- [90] K. Katsov, M. Müller and M. Schick: Field Theoretic Study of Bilayer Membrane Fusion. I. Hemifusion Mechanism. *Biophys. J.* **87** 3277-3290 (2004).
- [91] Z. Liao, L. M. Cimakasky, R. Hampton, D. H. Nguyen, J. E. K. Hildreth: Lipid Rafts and HIV Pathogenesis: Host Membrane Cholesterol Is Required for Infection by HIV Type 1. *Aids Res. Human Retrov.* **17** 1009-1019 (2001).
- [92] T. Phalen and M. Kielian: Cholesterol is required for infection by Semliki Forest virus. *J. Cell Biol.* **112** 615-623 (1991).
- [93] L. V. Chernomordik: Non-bilayer lipids and biological fusion intermediates. *Chem. Phys. Lipids* **81** 203-213 (1996).
- [94] N. Fuller and R. P. Rand: The influence of lysolipids on the spontaneous curvature and bending elasticity of phospholipid membranes. *Biophys. J.* **81** 243-254 (2001).
- [95] J. Zimmerberg and K. Gawrisch: The physical chemistry of biological membranes. *Nature Chem. Biol.* **2** 564-567 (2006).
- [96] S. M. Gruner: Intrinsic curvature hypothesis for biomembrane lipid composition: A role for nonbilayer lipids. *Proc. Natl. Acad. Sci. USA* **82** 3665-3669 (1985).
- [97] J. Als-Nielsen and D. McMorrow: *Elements of Modern X-ray Physics*. Wiley (2001).
- [98] M. Tolan: *X-Ray Scattering from Soft-Matter Thin Films*. Springer (1999).
- [99] J. Drenth: Introduction to basic crystallography. in: *International Tables for Crystallography, Vol. F* pp. 45-63. Springer (2001).
- [100] M. C. Wiener and S. H. White: Fluid bilayer structure determination by the combined use of x-ray and neutron diffraction. I. Fluid bilayer models and the limits of resolution. *Biophys. J.* **59** 162-173 (1991).
- [101] L. Ding, W. Liu, W. Wang, C. H. Glinka, D. L. Worchester, L. Yang and H. W. Huang: Diffraction Techniques for Nonlamellar Phases of Phospholipids. *Langmuir* **20** 9262-9269 (2004).
- [102] T. Salditt: Thermal fluctuations and stability of solid-supported lipid membranes. *J. Phys. Condens. Matter* **17** R287-R314 (2005).
- [103] S. Jin, J. Yoon, K. Heo, H.-W. Park, J. Kim, K.-W. Kim, T. J. Shin, T. Chang and M. Ree: Detailed analysis of gyroid structures in diblock copolymer thin films with synchrotron grazing-incidence X-ray scattering. *J. Appl. Cryst.* **40** 950-958 (2007).
- [104] http://henke.lbl.gov/optical_constants/atten2.html, version of April 29, 2010.
- [105] M. C. Wiener and S. H. White: Structure of a fluid dioleoylphosphatidylcholine bilayer determined by joint refinement of x-ray and neutron diffraction data. II. Distribution and packing of terminal methyl groups. *Biophys. J.* **61** 428-433 (1992).
- [106] M. C. Wiener and S. H. White: Transbilayer distribution of bromine in fluid bilayers containing a specifically brominated analog of dioleoylphosphatidylcholine. *Biochemistry* **30** 6997-7008 (1991).

- [107] D.-M. Smilgies: Geometry-independent intensity correction factors for grazing-incidence diffraction. *Rev. Sci. Instrum.* **73** 1706-1710 (2002).
- [108] B. D. Cullity and S. R. Stock: *Elements of X-ray Diffraction*. 3. edition, Prentice Hall (2001).
- [109] M. J. Buerger: The correction of x-ray diffraction intensities for Lorentz and polarization factors. *Proc. Nat. Acad. Sci.* **26** 637-642 (1940).
- [110] A. E. Blaurock and C. R. Worthington: Treatment of Low-Angle X-ray Data from Planar and Concentric Multilayered Structures. *Biophys. J.* **6** 305-312 (1966).
- [111] D. C. Turner and S. M. Gruner: X-ray diffraction reconstruction of the inverted hexagonal (H_{II}) phase in lipid-water systems. *Biochemistry* **31** 1340-1355 (1992).
- [112] W. J. Sun, S. Tristram-Nagle, R. M. Suter and J. F. Nagle: Structure of the ripple phase in lecithin bilayers. *Proc. Natl. Acad. Sci. USA* **93** 7008-7012 (1996).
- [113] V. Luzzati and A. Tardieu: A pattern-recognition approach to the phase problem: Application to the X-ray diffraction study of biological membranes and model systems. *J. Mol. Biol.* **64** 269-286 (1972).
- [114] S. Qian, W. Wang, L. Yang and H. W. Huang: Structure of transmembrane pore induced by Bax-derived peptide: Evidence for lipidic pores. *Proc. Nat. Acad. Sci. USA* **105** 17379-17383 (2008).
- [115] A. Tardieu, V. Luzzati, F. C. Reman: Structure and polymorphism of the hydrocarbon chains of lipids: A study of lecithin-water phases. *J. Mol. Biol.* **75** 711-733 (1973).
- [116] T. Salditt, C. Li, A. Spaar and U. Mennicke: X-ray reflectivity of solid-supported, multilamellar membranes. *Eur. Phys. J. E* **7** 105-116 (2002).
- [117] C. R. Worthington: The Interpretation of Low-Angle X-Ray Data from Planar and Concentric Multilayered Structures: The Use of One-Dimensional Electron Density Strip Models. *Biophys. J.* **9** 222-234 (1969).
- [118] P. Mariani, V. Luzzati and H. Delacroix: Cubic phases of lipid-containing systems: Structure analysis and biological implications. *J. Mol. Biol.* **204** 165-189 (1988).
- [119] W. Wang, L. Yang and H. W. Huang: Evidence of Cholesterol Accumulated in High Curvature Regions: Implication to the Curvature Elastic Energy for Lipid Mixtures. *Biophys. J.* **92** 2819-2830 (2007).
- [120] S. Qian, W. Wang, L. Yang and H. W. Huang: Structure of the Alamethicin Pore Reconstructed by X-Ray Diffraction Analysis. *Biophys. J.* **94** 3512-3522 (2008).
- [121] K. Hristova and S. H. White: Determination of the Hydrocarbon Core Structure of Fluid Dioleoylphosphocholine (DOPC) Bilayers by X-Ray Diffraction Using Specific Bromination of the Double-Bonds: Effect of Hydration. *Biophys. J.* **74** 2419-2433 (1998).
- [122] S. Tristram-Nagle, Y. Liu, J. Legleiter and J. F. Nagle: Structure of Gel Phase DMPC Determined by X-Ray Diffraction. *Biophys. J.* **83** 3324-3335 (2002).

- [123] K. Tu, D. J. Tobias, J. K. Blasie and M. L. Klein: Molecular Dynamics Investigation of the Structure of a Fully Hydrated Gel-Phase Dipalmitoylphosphatidylcholine Bilayer. *Biophys. J.* **70** 595-608 (1996).
- [124] V. A. Parsegian, R. P. Rand, N. L. Fuller and D. C. Rau: Osmotic stress for the direct measurement of intermolecular forces. *Methods Enzymol.* **127** 400-416 (1986).
- [125] V. A. Parsegian, N. Fuller and R. P. Rand: Measured work of deformation and repulsion of lecithin bilayers. *Proc. Natl. Acad. Sci. USA* **76** 2750-2754 (1979).
- [126] S. Aeffner: *X-Ray Structural Analysis of Phospholipid Membrane Systems: Chain Correlations and Fusion Intermediates*. Diplomarbeit, Universität Göttingen (2007).
- [127] P. W. Atkins: *Physikalische Chemie*, 2nd edition. Wiley-VCH (1996).
- [128] J. Katsaras, S. Tristram-Nagle, Y. Liu, R. L. Headrick, E. Fontes, P. C. Mason and J. F. Nagle: Clarification of the ripple phase of lecithin bilayers using fully hydrated, aligned samples. *Phys. Rev. E* **61** 5668-5677 (2000).
- [129] M. Seul and M. J. Sammon: Preparation of Surfactant Multilayer Films on Solid Substrates by Deposition from Organic Solution. *Thin Solid Films* **185** 287-305 (1990).
- [130] R. Koynova and M. Caffrey: Phases and phase transitions of the phosphatidylcholines. *Biochim. Biophys. Acta* **1376** 91-145 (1998).
- [131] J. Erbes, C. Czeslik, W. Hahn, R. Winter, M. Rappolt and G. Rapp: On the existence of bicontinuous cubic phases in dioleoylphosphatidylethanolamine. *Ber. Bunsenges. Phys. Chem.* **98** 1287-1293 (1994).
- [132] T. Reusch: *Nichtlamellare Strukturen in Lipidmembranstapeln in Abhängigkeit der Hydratisierung: Probenumgebung, Phasendiagramme und Bestimmung der Elektronendichte*. Diplomarbeit, Universität Göttingen (2009).
- [133] S. L. Resnik, G. Favetto, J. Chirife and C. F. Fontan: A World Survey of Water Activity of Selected Saturated Salt Solutions used as Standards at 25°C. *Journal of Food Science* **49** 510-513 (1984).
- [134] P. W. Winston and D. H. Bates: Saturated Solutions For the Control of Humidity in Biological Research. *Ecology* **41** 232-237 (1960).
- [135] L. Greenspan: Humidity fixed points of binary saturated aqueous solutions. *J. Nat. Res. Bur. Stand. (A Phys. Chem.)* **81A** 89-96 (1977).
- [136] D. Pan, W. Wang, W. Liu, L. Yang and H. W. Huang: Chain Packing in the Inverted Hexagonal Phase of Phospholipids: A Study by X-ray Anomalous Diffraction on Bromine-labeled Chains. *J. Am. Chem. Soc.* **128** 3800-3807 (2006).
- [137] L. Yang, L. Ding and H. W. Huang: New Phases of Phospholipids and Implications to the Membrane Fusion Problem. *Biochemistry* **42** 6631-6635 (2003).
- [138] N. Kucerka, J. Gallova, D. Uhríkova, P. Balgavy, M. Bulacu, S.-J. Marrink and J. Katsaras: Areas of Monounsaturated Diacylphosphatidylcholines. *Biophys. J.* **97** 1926-1932 (2009).

- [139] K. Gawrisch, V. A. Parsegian, D. A. Hajduk, M. W. Tate, S. M. Gruner, N. L. Fuller and R. P. Rand: Energetics of a hexagonal-lamellar-hexagonal-phase transition sequence in dioleoylphosphatidylethanolamine membranes. *Biochemistry* **31** 2856-2864 (1992).
- [140] M. M. Kozlov, S. Leikin and R. P. Rand: Bending, hydration and interstitial energies quantitatively account for the hexagonal-lamellar-hexagonal reentrant phase transition in dioleoylphosphatidylethanolamine. *Biophys. J.* **67** 1603-1611 (1994).
- [141] W. Massa: *Crystal Structure Determination*. Springer (2000).
- [142] B. Weinhausen: *Strukturanalyse von Phospholipidmembranen in Anhängigkeit von der Hydratisierung und dem Cholesteringehalt: Elektronendichteprofile und Ordnung der Acylketten*. Diplomarbeit, Universität Göttingen (2010).
- [143] L. Yang, T. M. Weiss, R. I. Lehrer and H. W. Huang: Crystallization of Antimicrobial Pores in Membranes: Magainin and Protegrin. *Biophys. J.* **79** 2002-2009 (2000).
- [144] A. Gibaud, D. Grosso, B. Smarsly, A. Baptiste, J. F. Bardeau, F. Babonneau, D. A. Doshi, Z. Chen, C. J. Brinker, and C. Sanchez: Evaporation-Controlled Self-Assembly of Silica Surfactant Mesophases. *J. Phys. Chem. B* **107** 6114-6118 (2003).
- [145] S. Che, S. Kamiya, O. Terasaki and T. Tatsumi: The Formation of Cubic $Pm\bar{3}n$ Mesosstructure by an Epitaxial Phase Transformation from Hexagonal $p6mm$ Mesophase. *J. Am. Chem. Soc.* **123** 12089-12090 (2001).
- [146] B. G. Tenchov, R. C. MacDonald and D. P. Siegel: Cubic phases in phosphatidylcholine-cholesterol mixtures: Cholesterol as membrane "fusogen". *Biophys. J.* **91** 2508-2516 (2006).
- [147] C. E. Conn, O. Ces, X. Mulet, S. Finet, R. Winter, J. M. Seddon and R. H. Templer: Dynamics of Structural Transformations between Lamellar and Inverse Bicontinuous Cubic Lyotropic Phases. *Phys. Rev. Lett.* **96** 108102 (2006).
- [148] V. Cherezov, D. P. Siegel, W. Shaw, S. W. Burgess and M. Caffrey: The kinetics of non-lamellar phase formation in DOPE-Me: relevance to biomembrane fusion. *J. Membr. Biol.* **195** 165-182 (2003).
- [149] J. Pan, S. Tristram-Nagle and J. F. Nagle: Alamethicin Aggregation in Lipid Membranes. *J. Membrane Biol.* **231** 11-27 (2009).
- [150] J. S. Hub, T. Salditt, M. C. Rheinstädter and B. L. de Groot: Short-Range Order and Collective Dynamics of DMPC Bilayers: A Comparison between Molecular Dynamics Simulations, X-Ray, and Neutron Scattering Experiments. *Biophys. J.* **93** 3156-3168 (2007).
- [151] Y. Liu and J. F. Nagle: Diffuse scattering provides material parameters and electron density profiles of biomembranes. *Phys. Rev. E* **69** 040901 (2004).
- [152] H. I. Petrache, D. Harries and V. A. Parsegian: Measurement of Lipid Forces by X-Ray Diffraction and Osmotic Stress *Methods in Molecular Biology* **400** 405-419 (2007).
- [153] Y. K. Levine: Physical Studies of Membrane Structure. *Prog. Biophys. Mol. Biol.* **24** 1-74 (1972).

- [154] P. E. Harper, D. A. Mannock, R. N. A. H. Lewis, R. N. McElhaney and S. M. Gruner: X-Ray Diffraction Structures of Some Phosphatidylethanolamine Lamellar and Inverted Phases. *Biophys. J.* **81** 2693-2706 (2001).
- [155] D. M. LeNeveu, R. P. Rand, V. A. Parsegian and D. Gingell: Measurement and modification of forces between lecithin bilayers. *Biophys. J.* **18** 209-230 (1977).
- [156] L. J. Lis, M. McAllister, N. Fuller and R. P. Rand: Interactions between neutral phospholipid bilayer membranes. *Biophys. J.* **37** 657-666 (1982).
- [157] S. Tristram-Nagle, H. I. Petrache and J. F. Nagle: Structure and Interactions of Fully Hydrated Dioleoylphosphatidylcholine Bilayers. *Biophys. J.* **75** 917-925 (1998).
- [158] I. N. Bronstein, K. A. Semendjajew, G. Musiol and H. Mühlig: *Taschenbuch der Mathematik*, 5th edition. Verlag Harri Deutsch (2001).
- [159] C. R. Worthington: Sampling-Theorem Expressions in Membrane Diffraction. *J. Appl. Cryst.* **21** 322-325 (1988).
- [160] C. E. Shannon: Communication in the Presence of Noise. *Proceedings of the IRE* **37** 10-21 (1949).
- [161] D. Sayre: Some implications of a theorem due to Shannon. *Acta Cryst.* **5** 843 (1952).
- [162] C. R. Worthington, G. I. King and T. J. McIntosh: Direct Structure Determination of Multilayered Membrane-Type Systems Which Contain Fluid Layers. *Biophys. J.* **13** 480-494 (1973).
- [163] C. R. Worthington: The determination of the first-order phase in membrane diffraction using electron density strip models. *J. Appl. Cryst.* **14** 387-391 (1981).
- [164] J. F. Nagle and M. C. Wiener: Relations for lipid bilayers. Connection of electron density profiles to other structural quantities. *Biophys. J.* **55** 309-313 (1989).
- [165] A. E. Blaurock and W. Stoeckenius: Structure of the Purple Membrane. *Nature New Biol.* **233** 152-155 (1971).
- [166] W. C. Hung, F. Y. Chen and H. W. Huang: Order-disorder transition in bilayers of diphytanoyl phosphatidylcholine. *Biochim. Biophys. Acta* **1467** 198-206 (2000).
- [167] T. J. McIntosh: Hydration properties of lamellar and nonlamellar phases of phosphatidylcholine and phosphatidylethanolamine. *Chem. Phys. Lipids* **81** 117-131 (1996).
- [168] S. A. Simon, T. J. McIntosh and A. D. Magid: Magnitude and range of the hydration pressure between lecithin bilayers as a function of headgroup density. *J. Colloid Int. Sci.* **126** 74-83 (1988).
- [169] G. Caracciolo, D. Pozzi and R. Caminiti: Hydration effect on the structure of dioleoylphosphatidylcholine bilayers. *Appl. Phys. Lett.* **90** 183901 (2007).
- [170] T. Rog, M. Pasenkiewicz-Gierula, I. Vattulainen and M. Karttunen: Ordering effects of cholesterol and its analogues. *Biochim. Biophys. Acta* **1788** 97-121 (2009).

- [171] E. W. Weisstein: "Least Squares Fitting." From MathWorld - A Wolfram Web Resource. <http://mathworld.wolfram.com/LeastSquaresFitting.html>
- [172] S. A. Simon and T. J. McIntosh: Magnitude of the solvation pressure depends on hydration potential. *Proc. Natl. Acad. Sci. USA* **86** 9263-9267 (1989)
- [173] J. Huang and G. W. Feigenson: A Microscopic Interaction Model of Maximum Solubility of Cholesterol in Lipid Bilayers. *Biophys. J.* **76** 2142-2157 (1999).
- [174] N. Kucerka, J. D. Perlmutter, J. Pan, S. Tristram-Nagle, J. Katsaras and J. N. Sachs: The Effect of Cholesterol on Short- and Long-Chain Monounsaturated Lipid Bilayers as Determined by Molecular Dynamics Simulations and X-Ray Scattering. *Biophys. J.* **95** 2792-2805 (2008).
- [175] J. Zimmerberg and L. V. Chernomordik: Membrane fusion. *Advanced Drug Delivery Reviews* **38** 197-205 (1999).
- [176] S. Tristram-Nagle, D. J. Kim, N. Akhuzada, N. Kucerka, J. C. Mathai, J. Katsaras, M. Zeidel and J. F. Nagle: Structure and water permeability of fully hydrated diphytanoylPC. *Chem. Phys. Lipids* **163** 630-637 (2010).
- [177] M. Kielian and F. A. Rey: Virus membrane-fusion proteins: More than one way to make a hairpin. *Nature Rev. Microbiol.* **4** 67-76 (2006).
- [178] S. Takamori, M. Holt, K. Stenius, E. A. Lemke, M. Grønborg, D. Riedel, H. Urlaub, S. Schenck, I. B. Brügger, P. Ringler, S. A. Müller, B. Rammner, F. Gräter, J. S. Hub, B. L. De Groot, G. Mieskes, Y. Moriyama, J. Klingauf, H. Grubmüller, J. Heuser, F. Wieland, and R. Jahn: Molecular Anatomy of a Trafficking Organelle. *Cell* **127** 831-846 (2006).
- [179] S. Castorph, D. Riedel, L. Arleth, M. Sztucki, R. Jahn, M. Holt and T. Salditt: Structure Parameters of Synaptic Vesicles Quantified by Small-Angle X-Ray Scattering. *Biophys. J.* **98** 1200-1208 (2010).
- [180] F. Li, F. Pincet, E. Perez, W. S. Eng, T. J. Melia, J. E. Rothman and D. Tareste: Energetics and dynamics of SNAREpin folding across lipid bilayers. *Nat. Struct. Mol. Biol.* **14** 890-896 (2007).
- [181] G. v. d. Bogaart, M. G. Holt, G. Bunt, D. Riedel, F. S. Wouters and R. Jahn: One SNARE complex is sufficient for membrane fusion. *Nat. Struct. Mol. Biol.* **17** 358-364 (2010).
- [182] R. Mohrmann, H. de Wit, M. Verhage, E. Neher and J. B. Sørensen: Fast Vesicle Fusion in Living Cells Requires at Least Three SNARE Complexes. *Science* **330** 502-505 (2010).
- [183] G. v. d. Bogaart and R. Jahn: Counting the SNAREs needed for membrane fusion. *J. Mol. Cell Biol.* **3** 204-205 (2011).
- [184] B. D. Patterson, C. Brönnimann, D. Maden, F. Gozzo, A. Groso, B. Schmitt, M. Stampanoni and P. R. Willmott: The materials science beamline at the Swiss Light Source. *Nucl. Instrum. Methods Phys. Res. Sect. B* **238** 224-228 (2005).
- [185] V. K. Pecharsky and P. Y. Zavalij: *Fundamentals of Powder Diffraction and Structural characterization of Materials*. Springer (2005).

- [186] W. I. E. David: Powder diffraction peak shapes. Parameterization of the pseudo-Voigt as a Voigt function. *J. Appl. Cryst.* **19** 63-64 (1986).
- [187] <http://de.wikipedia.org/wiki/Pseudo-Voigt-Profil>.
- [188] H. Schenk: An Introduction to Direct Methods. The Most Important Phase Relationships and their Application in Solving the Phase Problem. International Union of Crystallography, Commission on Crystallographic Teaching, Teaching Pamphlet 17. University College Cardiff Press (1984). <http://www.iucr.org/education/pamphlets/17>.
- [189] S. Perutkova, M. Daniel, G. Dolinar, M. Rappolt, V. Kralj-Iglic and A. Iglic: Chapter 9 - Stability of the Inverted Hexagonal Phase. *Advances in Planar Lipid Bilayers and Liposomes* **9** 237-287 (2009).
- [190] S. Perutkova, M. Daniel, M. Rappolt, G. Pabst, G. Dolinar, V. Kralj-Iglic and and A. Iglic: Elastic deformations in hexagonal phases studied by small-angle X-ray diffraction and simulations. *Phys. Chem. Chem. Phys.* **13** 3100-3107 (2011).
- [191] A. Gray: *Modern Differential Geometry of Curves and Surfaces with MATHEMATICA*. 2nd edition, CRC Press (1998).
- [192] M. Spivak: *A Comprehensive Introduction to Differential Geometry, Vol. 3*. Publish or Perish (1975).
- [193] R. Goldman: Curvature formulas for implicit curves and surfaces. *Computer Aided Geometric design* **22** 632-658 (2005).
- [194] K. F. Riley, M. P. Hobson and S. J. Bence. *Mathematical methods for physics and engineering*. Cambridge University Press (1997).
- [195] W. I. Smirnow: *Lehrgang der höheren Mathematik, Teil 2*. VEB Deutscher Verlag der Wissenschaften (1986).
- [196] G. C. Shearman, O. Ces, R. H. Templer and J. M. Seddon: Inverse lyotropic phases of lipids and membrane curvature. *J. Phys. Condens. Matter* **18** S1105-S1124 (2006).
- [197] M. M. Kozlov: Membrane shape equations. *J. Phys. Condens. Matter* **18** S1177-S1190 (2006).
- [198] U. Seifert: Configurations of fluid membranes and vesicles. *Adv. Phys.* **46** 13-137 (1997).
- [199] D. P. Siegel: Determining the Ratio of the Gaussian Curvature and Bending Elastic Moduli of Phospholipids from Q_{II} Phase Unit Cell Dimensions. *Biophys. J.* **91** 608-618 (2006).
- [200] E. W. Weisstein: "Catenoid". From MathWorld - A Wolfram Web Resource. <http://mathworld.wolfram.com/Catenoid.html>.

List of publications

- S. Aeffner, T. Reusch, B. Weinhausen and T. Salditt: Membrane fusion intermediates and the effect of cholesterol: An in-house x-ray scattering study. *Eur. Phys. J. E* **30** 205-214 (2009).
- B. Brüning, M. C. Rheinstädter, A. Hiess, B. Weinhausen, T. Reusch, S. Aeffner and T. Salditt: Influence of cholesterol on the collective dynamics of the phospholipid acyl chains in model membranes. *Eur. Phys. J. E* **30** 419-428 (2010).
- S. K. Ghosh, S. Aeffner, T. Salditt: Effect of PIP₂ on DOPC bilayer structure and phase behaviour studied by x-ray scattering. *Chem. Phys. Chem.* **12** 2633-2640 (2011)
- S. Aeffner, T. Reusch, B. Weinhausen and T. Salditt: The energetics of stalk intermediates in membrane fusion are controlled by lipid composition. *Submitted*.

Danksagung

Die vorliegende Arbeit wurde ermöglicht durch die Unterstützung von Seiten vieler Personen, denen ich an dieser Stelle meinen Dank aussprechen möchte.

Professor Dr. Tim Salditt danke ich für die Möglichkeit zur Anfertigung dieser Arbeit unter seiner Anleitung sowie für die Stellung des sehr vielseitigen und interessanten Themas. Sein Enthusiasmus und großer Einsatz für dieses und andere Projekte, sowie seine zahlreichen motivierenden Hinweise und Vorschläge haben mich schon während der Diplomarbeit sehr beeindruckt. Dies hat sich in der anschließenden Promotion nahtlos fortgesetzt und vertieft, und ich weiß sein mir entgegengebrachtes Vertrauen sehr zu schätzen.

Ich bedanke mich herzlich bei Professor Dr. Marcus Müller für seine Bereitschaft, das Amt des Koreferenten für diese Dissertation zu übernehmen, sowie für die Begleitung dieser Arbeit durch die Mitgliedschaft *thesis committee*.

Professor Dr. Claudia Steinem danke ich ebenfalls ganz herzlich für die Begleitung dieser Arbeit durch ihre Mitgliedschaft im *thesis committee*.

Außerdem bedanke ich mich bei Dr. Simone Techert, Professor Dr. Sarah Köster, Professor Dr. Reinhard Jahn und Professor Dr. Bert de Groot für das Interesse an meiner Arbeit und ihre Bereitschaft, die Prüfungskommission für meine Disputation zu stellen.

Professor Dr. Max Wardetzky danke ich für die Anregungen zur Differentialgeometrie impliziter Flächen.

Es ist eine besondere Freude, dem Team um Dr. Dina Carbone, Dr. Peter Boesecke und Dr. Till-Hartmut Metzger von der Beamline ID01 der European Synchrotron Radiation Facility zu danken. Ihre Unterstützung während der Experimente dort, notfalls auch zu weit fortgeschrittener Stunde, war essentiell für den Erfolg dieser Messzeit. Gleiches gilt auch für Roberto Homs, der uns durch das Einbinden unserer SPEC-Makros zur Steuerung der Probenumgebung an ID01 die Arbeit erheblich erleichtert hat.

In gleichem Maße möchte ich dem Team um Professor Dr. Phil Wilmott und Dr. Stephan Pauli von der MS-Beamline an der Swiss Light Source meinen Dank aussprechen. Die Meßbedingungen waren perfekt auf unsere Anforderungen zugeschnitten, so dass wir ebenfalls Daten in hervorragender Qualität gewinnen konnten, deren weitere Auswertung eine große Freude war.

Tobias Reusch danke ich mich für seine exzellente Arbeit bei der Konstruktion der Probenumgebung sowie der damit verbundenen Aufrüstung der Diffraktometer durch die vielen hilfreichen SPEC-Makros. Erst durch die so geschaffenen Bedingungen sind die hier vorgestellten Ergebnisse möglich geworden. Darüberhinaus auch noch einmal vielen Dank für die Unterstützung bei der SLS-Messzeit und das fachkundige Korrekturlesen der Arbeit.

Ein herzliches Dankeschön geht an Britta Weinhausen, Dr. André Beerlink und Dr. Philipp Schneggenburger für die Unterstützung bei den Synchrotron-Messzeiten. Außerdem danke ich diesen dreien sowie Dr. Sajal Ghosh und Dr. Simon Castorph für zahlreiche hilfreiche Gespräche zur Membranbiophysik und Strukturuntersuchung von Membranen mit Röntgenstreuung.

Marius Priebe, Jan-David Nicolas, Dr. Klaus Giewekemeyer, Dr. Christian Olendrowitz, Dr. Dong-Du Mai und Dr. Jörg Hallmann danke ich sehr für die große Hilfe beim Korrekturlesen der Arbeit. Außerdem danke ich Klaus und Christian sowie Dr. Julia Sedlmair für die hilfreichen Ratschläge und die Geduld bei der Generalprobe der Disputation.

Jochen Herbst und Thorsten Gronemann danke ich für ihre Hilfe bei Fragestellungen und Problemen technischer Natur, insbesondere der Wartung der Diffraktometer und der Probenpräparation. Jochen danke ich außerdem für die Anfertigung der Polypropylenfenster, die ein sehr untergrundarmes Signal ermöglicht haben. Peter Nieschalk und Carsten Wulf danke ich für die hervorragende Unterstützung durch die Werkstatt. Allen vieren danke ich für ihr großes Engagement insbesondere kurz vor den Messzeiten, was entscheidend zu deren Gelingen beigetragen hat.

Bei Christina Emser und Sabine Balder möchte ich mich ganz herzlich für die Unterstützung bei organisatorischen Fragen aller Art bedanken.

Schließlich gilt mein großer Dank allen Mitarbeitern des Instituts für Röntgenphysik für die ausgesprochen freundschaftliche und hilfsbereite Atmosphäre, die das Arbeiten hier sehr angenehm macht. Dies ist sicher ein entscheidender Grund, warum ich und viele andere ehemalige Diplomanden gerne für die Doktorarbeit hier geblieben sind.

Der *Göttingen Graduate School for Neurosciences, Biophysics, and Molecular Biosciences*, kurz GGNB, und dem verantwortlichen Gremium danke ich für die Auszeichnung mit einem GGNB-Stipendium über den Großteil meiner Promotionszeit. Außerdem haben die Methodenkurse und weitere Veranstaltungen für ein sehr abwechslungsreiches Rahmenprogramm gesorgt.

Dem Sonderforschungsbereich 803 *Funktionalität kontrolliert durch Organisation in und zwischen Membranen* und damit verbunden der Deutschen Forschungsgemeinschaft danke ich für die finanzielle Unterstützung des Projekts. Außerdem trägt der SFB entscheidend zu einem hervorragenden und inspirierenden Umfeld für die Membranbiophysik in Göttingen bei, was beispielsweise bei den Winterschulen oder Symposien stets zu spüren ist.

Abschließend möchte ich meinen Eltern, meiner Schwester und meinen Großeltern dafür danken, daß sie mich immer und in jeder Hinsicht unterstützt und ermutigt sowie an meinen Erfolg geglaubt haben.

Curriculum Vitae

Personal data

name	Sebastian Aeffner
date of birth	August 28, 1981
place of birth	Hannover
citizenship	German

Education and professional experience

since 12/2007	PhD student and scientific employee, Institute for X-ray Physics, Georg-August-Universität Göttingen, and member of the “International Max Planck Research School for Physics of Biological and Complex Systems” (IMPRS-PBCS) within the “Göttingen Graduate School for Neurosciences, Bio- physics, and Molecular Biosciences” (GGNB)
10/2007	Diploma in physics (Dipl.-Phys.), thesis title: “X-ray Structural Analysis of Phospholipid Membrane Systems: Chain Correla- tions and Fusion Intermediates”
01/2006–10/2007	Studies of physics, Georg-August-Universität Göttingen
08/2005–12/2005	Studies of physics, University of Jyväskylä, Finland
10/2002–07/2005	Studies of physics, Georg-August-Universität Göttingen
07/2001–04/2002	Zivildienst, DRK-Altenzentrum Nienburg/Weser
06/2001	Abitur
08/1994–06/2001	Albert-Schweitzer-Schule Nienburg/Weser
08/1992–07/1994	Orientierungsstufe Marklohe
08/1988–07/1992	Grundschule Wietzen

Stipends and awards

12/2008–05/2011	GGNB Excellence Stipend
06/2001	Award by the German Physical Society (Deutsche Physikalische Gesellschaft, DPG)

The fusion of two biological membranes is an important step in many processes on the cellular and sub-cellular level. Understanding the involved interplay of different lipid species, a specialized protein machinery and water on length scales of few nanometers poses a significant challenge to current structural biology. Among several complementary approaches, one strategy is to study the structural rearrangements of the lipid matrix. As the initial step, lipid bilayers must be forced into close contact to form a non-bilayer intermediate termed a stalk. This has been the subject of numerous theoretical studies and simulations, but experimental data on stalks are largely lacking. Currently, the only way to obtain structural information at the required sub-nanometer resolution is x-ray diffraction on the recently discovered "stalk phase" formed by certain lipids. We apply this method to elucidate the effect of lipid composition on stalk geometry and the repulsive forces between lipid bilayers prior to stalk formation. An approach based on differential geometry of electron density isosurfaces is introduced to analyze the curvatures and bending energies of the lipid monolayers. For the first time, this connects experiment-based structures of stalks and the associated bending and hydration energies. In addition, this thesis aims to provide a self-contained introduction to the required background in x-ray diffraction on lipid mesophases and electron density reconstruction.



ISBN 978-3-86395-043-9
ISSN 2191-9860

Universitätsverlag Göttingen